AD NUMBER

AD800398

NEW LIMITATION CHANGE

TO

Approved for public release, distribution unlimited

FROM

Distribution authorized to U.S. Gov't. agencies and their contractors; Administrative/Operational Use; Sep 1966. Other requests shall be referred to Commanding General, US Army Electronics Command, Attn: AMSEL-HL-CT-P, Fort Monmouth, NJ.

AUTHORITY

US Army Electronics Command ltr dtd 15 Jun 1972

8003398

(Form 1117)

①

TECHNICAL REPORT / ECOM-01354-F ⑱ ⑲

⑥ IONIZATION AND ELECTRON LOSS SIMULATION

IN ATMOSPHERIC GASES .

Report No. 3

1 December to 1 March 1966

⑮

Contract No. DA-28-043-AMC-01354(E)

⑨ Report. no. 3 (Final) 1 Dec 65 - 1 Mar 66,

⑭ Report R-109-3

M. N. Hirsh
G. M. Halpern
J. A. Slevin
N. S. Wolf

⑪ September 1966

② 228 p.

THE G.C. DEWEY CORPORATION
331 East 38 Street
New York, New York   10016

U.S. Army Electronic Command
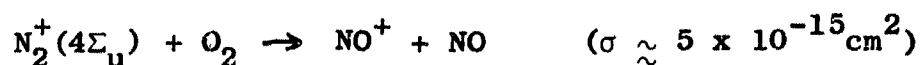Fort Monmouth, New Jersey 07703
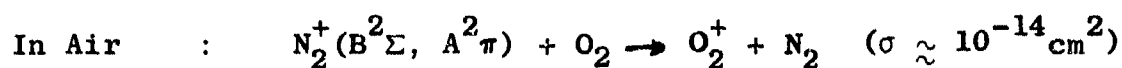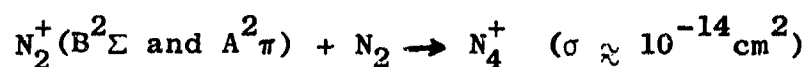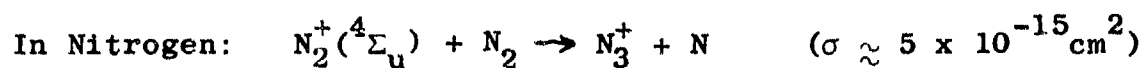⑯ DA Project No. 5900-21-830-4600

where α_{ei} (O_2^+, NO^+ in air) = (3 ±2) x $10^{-7} cm^3$/sec

f)   Ion-Molecule Reactions

In Nitrogen: $N_2^+(^4\Sigma_u) + N_2 \rightarrow N_3^+ + N$ ($\sigma \sim 5$ x $10^{-15} cm^2$)

$N_2^+(B^2\Sigma$ and $A^2\pi) + N_2 \rightarrow N_4^+$ ($\sigma \sim 10^{-14} cm^2$)

In Air   : $N_2^+(B^2\Sigma, A^2\pi) + O_2 \rightarrow O_2^+ + N_2$ ($\sigma \sim 10^{-14} cm^2$)

$N_2^+(^4\Sigma_u) + O_2 \rightarrow NO^+ + NO$ ($\sigma \sim 5$ x $10^{-15} cm^2$)

Optical studies of the fluorescent emission from irradiated nitrogen and air show collisional quenching of the $N_2(B^3\pi_g \rightarrow A^3\Sigma_u^+)$ Second Positive System and $N_2^+(B^2\Sigma_u^+ \rightarrow X^2\Sigma_g^+)$ First Negative System, with cross sections given by:

State	Quencher	σ (x$10^{-16} cm^2$)
$N_2:B^3\pi_g(v' = 0)$	N_2	1.2 ±-.6
$B^3\pi_g(v' = 0)$	O_2	39 ±11
$(v' = 1)$	O_2	52 ±18
$(v' = 2)$	O_2	81 ±32
$N_2^+:B^2\Sigma_u^+(v' = 0)$	N_2	69 ±10
$B^2\Sigma_u^+(v' = 0)$	O_2	123 ±21

ACKNOWLEDGEMENTS

TABLE OF CONTENTS

TABLE OF CONTENTS (continued)

TABLE OF CONTENTS (continued)

LIST OF ILLUSTRATIONS (continued)

LIST OF ILLUSTRATIONS (continued)

LIST OF ILLUSTRATIONS (continued)

viii

LIST OF TABLES

I. INTRODUCTION

A. Purpose of the Experimental Program

This report summarizes work performed during the period
1 July 1961 to 31 March 1966 on a program entitled "An Experi-
mental Investigation of the Effects of Radiation on the Propa-
gation of Electromagnetic Signals in Air." This work was
performed for the Defense Atomic Support Agency at the G. C.
Dewey Corporation Space Physics Laboratory in New York City,
under the technical supervision of the Atomics Branch of the
Applied Physics Division, U. S. Army Signal Research and
Development Laboratories at Fort Monmouth, New Jersey.

There are two traditional approaches to an experimental
study of the processes occurring in the upper atmosphere. One
can try to deduce atmospheric reaction models from _in situ_
observations of the chemical, ionic, and electronic composition
of the atmosphere obtained with rocket-borne instruments or
ground-based measurements. Alternatively, one can create a
situation in the laboratory in which a specific reaction is
dominant, then study this reaction as a function of the various
parameters at the control of the experimenter. Each method has
its advantages and limitations. Thus, the interpretation of
direct atmospheric measurements suffers from the incompleteness
of our knowledge of the composition of the atmosphere and the
nature of all the external influences exerted on it in general,
and at the time and location of the experiment in particular.
Also, the complexity of atmospheric processes is so great that
it is difficult to correlate a given observation with a particular
process. Finally, the experimenter cannot control the pressure,

temperature, and chemical composition independently, to study the
dependence of the process under investigation on these parameters.
Despite these difficulties, direct atmospheric measurements are
still attractive and important in that they represent the
ultimate in relevance, that is, they relate directly to the
phenomena which are to be explained. In the laboratory, on the
other hand, one has nearly complete control over the chemical
composition, pressure, and temperature of the gas being studied,
and can choose these parameters so that a given reaction will
dominate the observed phenomena. One can then study this reaction
in great detail. It is well known, however, that not only the
rates, but even the mechanisms, of many charged particle reactions
depend strongly on the internal energy states of the reactants.
Due to the dissimilarities between most laboratory experiments
and the atmospheric environment, it is unreasonable to assume
that the excited state distribution is characteristic of the
upper atmosphere. Hence, one cannot know a priori the relevance
of a given reaction studied in the laboratory to the upper
atmosphere.

In July, 1961, the G. C. Dewey Corporation began work on
an experimental program designed to study ionization and deioni-
zation processes in the upper atmosphere arising from prolonged
irradiation by beta particles from trapped fission debris
subsequent to the detonation of a nuclear device at high
altitudes. The objectives of the program were to create a
laboratory environment which closely resembles the beta-irradiated
upper atmosphere, then to study the processes common to the
laboratory and ionospheric situations as closely as possible.
The experiment was visualized as an approach to ionospheric
reactions which stands midway between direct atmospheric measure-

ments and traditional laboratory studies. By suitable choices
of experimental parameters, one could study individual reactions
in typical laboratory detail, then vary the parameters to produce
a close approximation to the ionospheric situation, and determine
the relevance of these reactions to the phenomenology of the
ionosphere. Thus the experimental program was planned to combine
the best features of the traditional approaches described above.
As the results to be presented in this report indicate, the
experimental program has been extremely successful in both
aspects of the problem.

B.   Nature of the Experiment   .

The ionosphere differs from any laboratory simulation in
several ways. Most obvious is the necessity of confining the
laboratory environment in some sort of container. The container
walls can then modify the test environment by various means,
including the removal of electrons and ions by surface recom-
bination and the de-excitation of otherwise long-lived states
by wall collisions. The laboratory experiment is never completely
free from system-contributed impurities which are not present in
the ionosphere, but which may participate in the laboratory
phenomenology. These dissimilarities are greatly minimized in
the present experiment, the first by the use of an extremely
large reaction chamber, four feet in diameter and two feet long,
to provide a large volume-to-surface ratio, and the second by
the use of   ultrahigh vacuum techniques and clean gases.

Three diagnostic techniques are used to study the irradiated
gas. The densities of free secondary electrons are deduced by
resonant cavity methods. A mass spectrometer studies the

4.

positive and negative ions which diffuse to the container walls.
An optical spectrometer examines the light emitted by the
fluorescing gas. The simultaneous application of these three
techniques provides unusually detailed information on the
instantaneous state of the irradiated gas.

C.   Summary of This Report

Chapter II describes the experimental equipment and techniques
in detail. In Chapter III, the various processes which can occur
in weakly ionized atmospheric gases are discussed, along with
means for treating experimental data obtained from the measure-
ments. Chapters IV and V contain the results obtained to date.
Chapter IV describes the optical studies in nitrogen, while
Chapter V presents the results of electron density and mass
spectrometric studies in pure oxygen, pure nitrogen and airlike
mixtures. The report closes with Chapter VI, which includes a
summary of experimental results and suggestions for further work.

D.   Administrative Details

The work described in this report was conducted over the
period between 1 July 1961 and 31 March 1966, under the
following contracts:

Contract Number	Dates
DA-36-039-SC-87318	1 July 1961 - 30 June 1963
DA-36-039-AMC-03278(E)	1 July 1963 - 31 June 1964
DA-28-043-AMC-00457(E)	1 July 1964 - 28 February 1965
DA-28-043-AMC-01354(E)	1 June 1965 - 31 March 1966

The following G. C. Dewey Corporation personnel contributed
to the project for the approximate fraction of the total
available time indicated:

Merle N. Hirsh, Senior Associate (Project Director)	75-100%
Philip N. Eisner, Research Associate	75-100%
James A. Slevin, Research Associate	50- 75%
David R. Maerz, Senior Technical Assistant	50- 75%
Alexander S. Walker, Jr., Senior Technical Assistant	50- 75%
Walter G. Chesnut, Senior Associate	0- 25%
Gerald M. Halpern, Research Associate	0- 25%
Neil S. Wolf, Research Associate	0- 25%
J. Warren Blaker, Reasearch Associate	0- 25%
Howard Zwiren, Technical Assistant	0- 25%

6.

II.   EXPERIMENTAL TECHNIQUES

A.   General Description

The present experiment is a study of electron production
and loss in air and atmospheric gases subjected to ionizing
radiation, under conditions approximating those at altitudes in
the atmosphere between 40 to 100 km.   Three diagnostic tools are
used for these studies.   The density of free electrons for a wide
variety of experimental conditions is determined by the measure-
ment of the radio-frequency properties of a resonant cavity
containing the ionized gas, and mass and optical spectrometry
provide information on the ions present and the density
distribution of excited states.   All three techniques are applied
simultaneously to the study of the ionized gas, thereby providing
as detailed a characterization of the state of the gas as possible.

A schematic diagram of the experimental system is shown in
Figure 2.1.   A divergent beam of 1.5 Mev electrons from a Van de
Graaff accelerator traverses a thin foil window which serves as
one end of a cylindrical uhf cavity containing the gas to be
studied.   The cavity has been made extremely large, four feet in
diameter, two feet in length, to minimize the role of diffusion
in the charged particle removal processes.   The geometry of the
beam divergence is chosen to provide a flux of electrons which is
nearly uniform throughout the volume of the cavity, so that the
gas contained in the cavity is ionized by a spatially uniform
source.

Two types of experiments are performed.   In one, the electron
beam irradiates the gas continuously, setting up a steady-state
distribution of charged particles and excited neutral species.

Electron and ion densities and optical emission intensities are
measured as functions of the pressure and chemical composition
of the gas and of fast electron beam current. In the second type
of experiment, the electron beam is pulsed on and off periodically,
and time-resolved measurements of electron density are made
during the approach to in-beam equilibrium and during the
radiation afterglow. These two types of experiments provide
complementary information as will be seen in Chapters V and VI.

Because of the high gamma intensity in the Van de Graaff
room, it is necessary for the operator to be located some distance
away from the experimental area. All parts of the experiment
which require adjustment, tuning, or observation during the course
of an experiment are therefore located in an adjacent room also
containing the operator. This room is shielded from the Van de
Graaff irradiation area by $4\frac{1}{2}$ foot thick walls of extremely
dense bluestone masonry. In the operator area, radiation surveys
are unable to detect any radiation in excess of normal background
during an experiment.

B.   The Electron Beam

The source of electrons for the irradiation experiments is
a Van de Graaff electron accelerator, Model GS (horizontal),
produced by High Voltage Engineering Corporation, Burlington,
Massachusetts. The accelerator produces 1.5 Mev electrons at
currents up to 1.7 milliamperes. The electrons emerge from the
accelerator in a collimated beam of roughly elliptical cross
section, 3 mm long by 1 mm wide. This collimated beam maintains
a cross-sectional dimension of less than 10 mm after traversing a
path 10 meters in length in vacuum of the order of 10^{-5} Torr. The

energy spread of the beam is guaranteed by the manufacturer to
be no more than 40 kev; since ionization cross-sections for fast
electrons in gases are quite insensitive to electron energy in
the Mev range, there was no attempt made to measure the actual
energy spread.

Upon emerging from the accelerator, the beam passes into
a beam switching section, shown in Figure 2.2, which consists of
a straight-through arm of 2" diameter tubing to which a second
tube at an angle of 12° from the beam axis is attached. A
Helmholtz coil, capable of producing a field of 300 Oersteds
quite uniform over a cylindrical volume 3" in diameter by 1" in
height, is located at the junction of the two tubes. A Faraday
cup is attached to the side arm through an insulating flange.
To read total current from the Van de Graaff one switches the
beam into this side arm by applying the magnetic field. With the
help of a second Faraday cup located at the end of the straight-
through section (E' in Figure 2.2) it was determined that the
current into the side arm with the field on is equal to the
straight-through current observed in the absence of a magnetic
field to within about 1%.

The collimated beam emerging from the Van de Graaff is
passed through a thin metallic foil, which diffuses it by multiple
scattering. For small scattering angles, the electrons can be
described by the angular distribution function

$$P(\theta) = K e^{-\theta^2/\bar{\theta}^2} \qquad (21.)$$

Here $\bar{\theta}$ is the rms scattering angle characteristic of the thickness
and composition of the foil, and is determined by

10.

$$\bar{\theta}^2 = \left(\frac{21}{E}\right)^2 \frac{x}{x_o} \tag{2.2}$$

Here E is the energy of the electron in Mev, x the "thickness" of the foil in gm/cm^2, and x_o a characteristic "length" for the foil material given by

$$1/x_o = 1.37 \times 10^{-3} \frac{Z(Z+1)}{A} \log_e 183Z^{-1/3} \quad gm/cm^2 \tag{2.3}$$

Foils are chosen so that only a small central spread in θ strikes the cavity, providing a nearly uniform flux across the cavity face. Electrons scattered through larger angles are removed at the collimator C. The length of the beam tube (10 meters) has been chosen to keep the r^{-2} loss in flux due to the beam divergence less than 10% from front to back of the cavity (0.6 meters).

Direct measurements of the spatial distribution and absolute flux of the Van de Graaff beam within the cavity were made with a Faraday cup which could be scanned along vertical and horizontal diameters of the cavity. Figure 2.3 shows the Faraday cup itself, which is made from a cylinder of aluminum 12" long and 1 1/8" in diameter, so that the collection area of the cup is 1 square inch. The back of the cylinder is closed with a 1/8" thick aluminum disc, and the open front end is guarded by a fine wire repeller grid insulated from the body of the cup, to which a large negative voltage is applied. The combination of the repeller grid and the large ratio of length to diameter of the cup prevents the loss of secondary electrons from the cup. To avoid electron collection on the outer walls, the cup is enclosed in a 1 3/4" diameter grounded aluminum tube, and the front edge of the cup is guarded from the direct beam by a $3\frac{1}{2}$" diameter grounded frontal disc. Collected electron current is measured with an electrometer-

tube microammeter and chart recorder.

The cup is driven at constant speed along the rod by means of a motor assembly which automatically reverses at each end of the travel. The cup thus scans continually back and forth, each traversal requiring about three minutes. At one end of the rod, the Faraday cup moves behind a heavy shield which blocks the incident beam. The residual current observed with the cup behind the shield is due to the collection of backscattered electrons at the cable feedthrough; this background is subtracted from all readings.

Beam profiles were measured with the scanning Faraday cup along the vertical and horizontal diameters of the cavity, for a beryllium foil scatterer 0.004" thick. The current distributions are shown in Figure 2.4. From these data, the total current to the cavity has been computed for a 100 μ amp beam from the Van de Graaff. It was found that this current amounts to 28.7% of the total incident beam. It will be noticed that the current distribution along the vertical axis is quite nonuniform. It is believed that the bottom of the scattered electron distribution is shadowed by an obstacle in the collimating section. A new collimator has been designed, and will be incorporated into subsequent experiments.

Indirect measurements of the foil scattering were also made. The geometry of the second Faraday cup E' and the collimator C in Figure 2.2 is chosen so that the collection area of E' intercepts the same solid angle at the foil as does the cavity in its normal position. The total current intercepted by E' should then be the same as the total current incident on the cavity.

Measurements made in this manner for the 0.004" beryllium foil used above give a value of 28.8% of the total incident beam, in fortuitously good agreement with the total current obtained above. Because of their simplicity, the indirect measurements were used for relative calibrations between foils.

Because of inadequate filtering in the pentode emission control circuit, the amplitude of the electron beam has a small 400 cps modulation, of the order of 5%. This normally presents very little difficulty in the experiments, particularly when the electron loss frequency is small compared to 400 $\sec^{-1}$. At high pressures in oxygen, however, some difficulty is encountered in the transient measurements due to the arbitrary phasing of the 400 cps modulation relative to the beam switching times, to which the afterglow densities show a marked response. It is planned to improve the beam stability in the near future. During the present program, however, there was considerable reluctance to open and repair an otherwise well-functioning accelerator, for fear of the time which could be lost in getting the Van de Graaff operating well again.

C.   Electron Density Measuring System

Figure 2.5 is a block diagram of the circuit used for the measurement of electron density. A uhf oscillator, crystal-controlled at 387 Mcps ±400 cps, is fed into the rf input of a General Radio 1000 - P6 crystal modulator. A General Radio Model 1211B low frequency oscillator drives the modulator at a frequency f_m, typically on the order of 1 to 6 Mcps. The output of the modulator then occurs at 387 Mcps $\pm f_m$. The high-frequency sideband is used to drive a hybrid ring bridge which contains the cavity

and an adjustable reference impedance in opposite arms. The
reference impedance is balanced for maximum output at frequencies
off cavity resonance. In the vicinity of cavity resonance, the
voltage reflection coefficient of the cavity decreases, thus
unbalancing the bridge so that the output signal goes through a
minimum at the cavity resonant frequency. The signal from the
rf bridge is detected by a crystal diode, and the resulting
envelope is displayed on an oscilloscope. Balancing the bridge
for maximum signal off resonance biases the crystal onto a
sensitive part of its characteristic, and optimizes the signal
observed at cavity resonance. This scheme allows one to measure
all frequency shifts in the cavity in terms of changes in f_m, due
to the stability of the 387 Mcps oscillator. Changes in f_m are
measured with a digital counter to an accuracy of 1 kcps.

The heart of the rf circuit is the resonant cavity in which
the gas is contained. The cavity has been made large, to minimize
the loss of charged particles to the walls by diffusion. The
principal concern of the present experiments lies with processes
occurring in the volume of the gas, away from the walls. Therefore,
a cavity mode was chosen which has vanishing electric fields at
the walls, thus weighting the electrons in the volume more heavily.

In the measurements, the cylindrical TE_{011} is used; the
electric field lines in this mode are azimuthal circles with the
intensity variation

$$E = E_o \, J_1 \left(3.832 \frac{r}{R} \right) \sin \frac{\pi z}{h} \quad . \tag{2.4}$$

Here R, h are the radius and height of the cavity, both equal to
60 cm. A false electrical end plate, in the form of a circular

14.

disc set off on legs from the back of the cavity structure,
separates this mode from the TM_{211}, with which it would be
degenerate in an ideal cylindrical resonator. The cavity has
a loaded Q of about 16,000.

The presence of a distribution of $n(r, z)$ free electrons
per cm^3 in a gas contained in a microwave resonant cavity changes
with the resonant frequency and quality factor from their electron-
free values ν_o, Q_o by an amount [Van Lint et al, 1965]

$$\Delta\left(\frac{1}{Q}\right) - 2i\frac{\Delta\nu}{\nu_o} = \frac{1}{2\pi\epsilon_o\nu_o}\frac{\int_v \sigma E^2 dv}{\int_v E^2 dv} \tag{2.4}$$

Here $\Delta\left(\frac{1}{Q}\right) = \frac{1}{Q_e} - \frac{1}{Q_o}$, $\Delta\nu = \nu_e - \nu_o$, the subscript "e"
referring to values in the presence of free electrons. E is the
rf electric field in the cavity, and r is the complex conductivity
of the free electrons, given by

$$\sigma = \frac{ne^2}{m}\frac{\nu_c - i\omega}{\nu_c^2 + \omega^2} \tag{2.5}$$

where ν_c is the electron-neutral atom collisional frequency, ω
the radian frequency of the applied rf field, and e and m are the
charge and mass, respectively, of the electron. The integrals in
2.4 extend over the volume of the resonant cavity. If we write
$n(r, z) = n_o f(r, z)$, then 2.4 becomes

$$\Delta\left(\frac{1}{Q}\right) - 2i\frac{\Delta\nu}{\nu_o} = \frac{n_o e^2(\nu_c - i\omega)}{2\pi m\epsilon_o\nu(\nu_c^2 + \omega^2)}\frac{\int_v f E^2 dv}{\int_v E^2 dv} \tag{2.6}$$

where the ratio of integrals is the effective "filling factor"
of the electrons in the cavity, which for convenience can be
abbreviated ϕ. For ν_o = 390 Mcps and ν_c = 1.35 x 10^8p sec^{-1}
[Van Lint, 1959], 2.6 can be written

$$\nu_0 \, \Delta\left(\frac{1}{Q}\right) - 2i \, \Delta\nu = \frac{(0.054\,p + i)\,0.1\,\phi\,n_0}{1 + (0.054\,p)^2} \qquad (2.7)$$

Thus a uniform distribution of electrons ($\phi = 1$) of density $n_0 = 10^7 \text{cm}^{-3}$ at 10 Torr in oxygen gives $\Delta\nu = 770$ kcps, $Q_e = 500$. At low pressures, where $Q_e \approx Q_0$, $\Delta\nu = 0.1\,\phi n_0$.

With no gas in the cavity, it is not possible to detect a shift in the resonant cavity due to the beam electrons alone. Since the velocity of these electrons is so high (effectively equal to the speed of light), the density of beam electrons in the cavity at the highest available current is only about 100 cm^{-3}, which is two orders of magnitude below the detection limit of the instrumentation. Thus, during continuous irradiation of the gas-filled cavity, one can relate all observed charges in resonant frequency to secondary electrons and ions produced in the gas.

The usual precautions have been taken to prevent heating of the free electrons by the rf probing field. Measurements of electron density have been performed at various probe power levels. The results indicate that the power levels used in all measurements reported here (about 0.1 μ watt) is at least 15 db below those required to produce detectable changes in the measured electron densities.

Direct measurements of cavity Q have not been made because of the beam modulation mentioned above. The noise observed in the oscilloscope display off cavity resonance is severe enough to prevent an accurate measurement of the inflection points of the cavity resonance curve. The cavity band width, from which the Q is deduced, is the small difference between the two large frequencies at the inflection points. With even a small error on each inflection frequency, the Q value is quite seriously in error.

D.   Timing Circuits and Transient Measurements

Time-resolved electron density measurements have been
performed in experiments in which the electron beam is repetitively
switched on and off the cavity. Time intervals are selected at
fixed positions within the beam switching sequence; the electron
density measurements are performed at these intervals. The
circuit also possesses a manual operating mode to be used in
steady-state measurements.

A block diagram of the timing system is shown in Figure 2.6.
The cycle is initiated by a one second time mark from a Tektronix
Model 180 A Time Mark Generator, which initiates the beam
irradiation and recycles the Berkeley Preset Counter. The
electron beam is switched off at a subsequent 10 or 100 msec
time mark selected by the coincidence circuit, so that the beam
on and off times are rigidly fixed to within about $1\,\mu$sec.

The selection of a time interval during the sequence at
which measurements are to be made is accomplished by the preset
counter. $100\,\mu$sec time marks are counted up to a number preselected
on the front panel, at which time a trigger pulse is delivered to
the oscilloscope used to observe the output of the uhf bridge
used for electron density measurements. The counter is recycled
by the next one second pulse and the process is then repeated.
In this manner, the oscilloscope sweep is activated at integral
numbers of $100\,\mu$sec intervals after the one second time mark.
The duration of the oscilloscope sweep is kept short compared
with the time over which the cavity resonance frequency changes
appreciably. Measurements are then made by adjusting f_m to

produce a minimum signal on the oscilloscope, which then gives
the cavity resonant frequency at that time.

E.   Mass Spectroscopy

Ions from the volume of the gas diffuse to the container
walls under the influence of ambipolar space charge fields (see
Chapter III). If a small aperture is placed in one of the walls,
a representative sample of the ions arriving at the walls can be
drawn off and injected into a mass analyzer to determine and
identify the   densities of the various ionic species produced
in the irradiated gas.

A common technique of ion sampling makes use of an
accelerating field at the aperture which attracts ions of a
given polarity, to increase the collection efficiency of a given
aperture.   It was feared that this technique would produce
disastrous results in the present experiment. Even a few volts
of energy opens many new channels to the ions for chemical reactions
which are not representative of those occurring in the volume of
the gas for thermal ions [Keller et al, 1965]. It was therefore
decided to forego ion acceleration in the relatively high pressure
cavity, reserving it for use in the low-pressure regions of the
mass analyzer where collisions are infrequent enough to minimize
the distortion of the ion spectra by chemical reactions.

A very important, but quite elusive, aspect of the mass
spectroscopy involves the detailed prediction of the ion sampling
efficiency as a function of charge density and gas pressure. If
the ions were sampled strictly by diffusion, they would enter the
aperture at a rate proportional to their diffusion loss rate,
that is, roughly proportional to the central density of the ions
in the cavity divided by the gas pressure. In fact, the data

18.

indicate that the inverse p dependence is not observed, and
the measured ion currents vary as the central ion densities. To
interpret this result requires detailed consideration of the
space charge field at the walls, and the neutral gas flow field
in the region of the aperture. Sufficient data do not exist
at this time to warrant such an an lysis.

Mass analyses of ions are performed with an rf monopole
mass filter [Von Zahn, 1963]. The monopole, which is actually
one quadrant of the Paul quadrupole spectrometer [Paul and Raether,
1955], consists of a circular cylindrical rod electrode and an
electrode in the shape of a "vee" (Figure 2.7). In principle,
the quadrupole field requires that the rod electrodes have a
hyperbolic cross section, but a correctly designed circular pole
piece can approximate the hyperbolic field quite well [Dayton et
al, 1954].

ROD ELECTRODE

VEE ELECTRODE
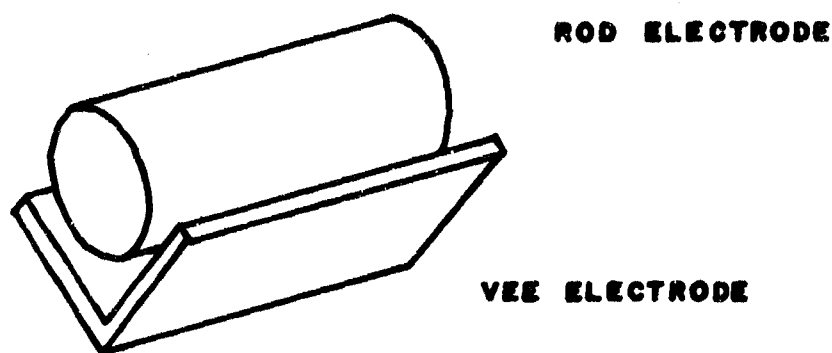
Figure 2.7   R.F. MONOPOLE

Figure 2.8 is a simplified cross-sectional view of the spectrometer, showing the salient features of its design. The front chamber A is defined by the entrance aperture plates into the cavity and the monopole housing B. This region provides the first stage of differential pumping required to maintain the necessary low pressures in the monopole and detector sections. Chamber A contains a simple aperture lens for focussing ions into the analyzing region, and an electron gun of conventional design for use in the study of neutral species. Great care has been taken to remove all insulating surfaces from Chamber A. These insulators were found to be particularly troublesome because they accumulate charge in the gamma field produced by the Van de Graaff electrons which defocusses the ion beam entering the spectrometer.

The monopole housing contains the analyzing electrodes. A ceramic ring seal C insulates the front section of the housing, which is at the potential of the Vee electrode, from the rear section, which is maintained at ground potential.

The rear chamber of the spectrometer houses the detector and a nude ionization vacuum gauge. This chamber is evacuated by its own diffusion pump and is maintained at the lowest pressure in the spectrometer system. The ion detector is mounted on the flange at the rear of the chamber. Electrical feedthroughs in the flange make connection to the electrodes of the detector.

The vacuum system for the mass spectrometer consists of two 4" NRC oil diffusion pumps isolated from the spectrometer by a combination water cooled chevron-molecular sieve baffle manufactured by Kane Engineering Labs. The pumps are connected

to the main foreline used by the diffusion pumps on the cavity
and beam tube. Without baking, the detector section of the mass
spectrometer reaches an ultimate pressure of 2×10^{-8} Torr.
This vacuum system enables the spectrometer to maintain a low
internal pressure despite high cavity pressure. For example,
with a gas flow of 150 micron-liters/sec through the entrance
aperture the pumping system maintains a pressure of 10^{-3} Torr in
the lens chamber, 3×10^{-6} Torr in the monopole section, and
5×10^{-7} Torr at the detector. (This gas flow is obtained with
an entrance aperture of 0.0135 inch diameter and a cavity
pressure of 10 Torr)

Figure 2.9 is a block diagram of the electronics for the
mass spectrometer. The rf oscillator is a Hartley type tunable
from 730 kcps to 9.39 Mcps, with a peak rf voltage of 1100 volts
over the entire frequency tuning range. The rf oscillator is
rigidly but demountably attached to the mass spectrometer by a
brass coaxial coupler between the oscillator chassis and the rf
feedthrough on the monopole housing. This arrangement minimizes
the capacitance seen by the oscillator yet provides good rf shielding.

The mode of operation for this spectrometer maintains
constant amplitudes of the electric fields, but changes the
frequency of the rf field to scan the range of mass-to-charge
ratios. The oscillator is tuned remotely from the operator by
a selsyn drive which changes the capacitance and inductance in the
tank circuit simultaneously. The selsyn master is itself driven
by a multispeed motor to permit mass scans to be made at various
speeds. Oscillator frequency is continuously monitored on a
digital counter for mass identification.

An additional output from the oscillator is rectified to produce the dc potential required for the rod electrode; the polarity of this potential can be chosen by means of a front panel switch, depending on the polarity of the ion being studied. After suitable voltage division, the same rectified output is also used to supply the required voltages for the focussing electrodes. Derivation of the dc voltages from the rf output provides a first-order stability correction for variations in oscillator output power.

The ion detector is a 10-stage Dumont electron multiplier with copper-beryllium dynodes. Dynode voltages are supplied from a regulated Keithley high voltage supply. In the detection of negative ions the entire Keithley supply is floated 1000 volts positive with respect to ground by means of an additional voltage supply. The detector is typically operated at 350 volts per stage.

Two detection schemes have been employed. In the first, the output from the electron multiplier is measured on a Keithley Model 600 A electrometer, and, after suitable integration, is displayed on a strip chart recorder. In the second, the ion lens is driven by a square wave at several hundred cycles per second. The output from the electron multiplier is amplified by an electrometer amplifier with a frequency response flat to 1 kcps and then capacitively coupled to the input of a Princeton Applied Research Model JR-5 Lock-in Amplifier. The lock-in has an internal Oscillator which provides both the reference signal for the detector and a modulation signal which is applied to the ion lens. The ion current is thus coherently modulated at the reference frequency.

The largest source of noise results from the bremsstrahlung generated by the electron beam, which produce photoelectrons within the electron multiplier. The signal-to-noise ratios for the ac and dc techniques outlined above were found to be about the same. However, since the electron multiplier must be biased to a high positive potential for the detection of negative ions, the ac technique must be used in this case.

F.   Optical Spectroscopy

The optical spectrometer used is a Jarrell-Ash 0.5 meter Fastie-Ebert monochromator [Fastie, 1952]. This instrument provides good resolution (0.3 Å in the visible first order) and a relatively high geometrical speed (f/10) for moderate cost. Other advantages include its ability to scan the entire spectral range without being refocussed, and the linearity of its wavelength drive with time.

Figure 2.10 shows the optical system of the monochromator. Light from the entrance slit is collimated by the spherical mirror, and strikes the plane grating as a plane wave. Depending on the angle between the direction of propagation of the light and the normal to the grating, light at a particular wavelength is reflected back to the spherical mirror, where it is refocussed to pass through the exit slit and strike the detector. Wavelength scanning is accomplished by rotating the grating about a vertical axis while maintaining fixed light paths in space. The grating is equipped with a motor drive which produces wavelength scans linear with time, at any of eight speeds from 2 Å/min to 500 Å/min, as well as a manual drive for setting by hand to any given wavelength. Wavelength indications are displayed on a counter to within the nearest Angstrom, both alongside the spectrometer

itself and on a remote servo-driven counter located in the operator area. Two modes of operation are possible with the monochromator. First, the grating can be scanned at some fixed rate through a given wavelength range to determine the general appearance of the spectrum. Alternatively, the grating rotation and slit widths can be set to transmit a given wavelength interval and the variation of intensity at that wavelength can be measured as a function of external parameters such as time or beam current.

The grating used for the work reported below is a Bausch and Lomb plane replica grating with 30,000 lines per inch, blazed for maximum intensity in the first order at 5,000 Å. The grating is 52 mm square.

The detector is an RCA Type 1P21 photomultiplier contained in a light-tight housing. As in the mass spectrometer detecting system, bremsstrahlung generated by the electron beam from the Van de Graaff accelerator produce photoelectrons within the photomultiplier, and reduce the overall sensitivity of the system. Consequently, it is necessary to shield the photomultiplier with lead in order to reduce the beam-contributed signal. To obtain the necessary 4π shielding, the photomultiplier housing was removed from the exit slit of the spectrometer, and mounted some distance away from it.

The complete optical system is shown in Figure 2.10. Light from the cavity falls on the entrance slit of the spectrometer with no intervening optical elements. (It can be shown [Nielsen, 1930; 1947] that the geometry of the extended source of light provided by the cavity affords optimum illumination of the spectrometer which cannot be improved by the use of focussing lenses.) After traversing the spectrometer, the light is collimated by a convex

lens A and falls onto plane mirrors B and C. The light is then
focussed by lens D onto the photocathode of the photomultiplier,
which is contained in a light-tight housing. All optical
elements are mounted in a brass tube which is in turn rigidly
attached to the spectrometer. By surrounding the light pipe on
all sides with lead, it is possible to reduce the bremsstrahlung
signal to zero. The photomultiplier output is measured with an
electrometer amplifier, then displayed on a strip-chart recorder.

The relative response of the optical system versus wave-
length was measured in the following way. Measurements (described
in Chapter IV below) were made of the intensity distribution of
several molecular band systems in nitrogen, and of the relative
intensities of several multiplets from a mercury capillary
discharge. The detailed distribution of excited states in a
radiating system depends very critically on the nature of the
excitation process and the physical environment of the system.
In the absence of selective absorption, however, the relative
intensities of lines or bands arising from a common upper state
depend only on the density of that state, and not on external
conditions. The ratios of measured photocurrents to theoretical
intensities for these lines or bands are then determined by the
transmission of the optical system.

Ratios of measured photocurrents to theoretical intensities
were plotted as a function of wavelength for various bands in the
First Negative and Second Positive Systems in nitrogen, and for
several multiplets in mercury. Values of relative intensities in
nitrogen were obtained from Bates [1949], and those in mercury
from Crosswhite and Dieke [1957]. Intensity ratios for bands or
lines arising from the same upper level were found to lie on
smooth curves. By appropriate normalization of groups of

transitions arising from different upper states, it was possible to construct a smooth curve covering the entire wavelength region between 3000 and 6000 A. The resulting curve is shown in Figure 2.11.

G. Vacuum and Gas Handling Systems

It is well known that concentrations of certain impurities in atmospheric gases as small as one part per million may cause marked alterations in the electron removal processes occurring in the pure gas. Standard ultra-high vacuum techniques are employed in order to reduce to a minimum the contamination of the experimental gas by outgassing of the vacuum system.

In addition to the clean system, an evacuated region is provided for the diverging electron beam. The beam tube vacuum and the uhf chamber are separated by a thin metal foil to avoid distortions of the beam homogeneity by multiple Coulomb scattering. The beam tube is operated at about 10^{-5} Torr, somewhat below the pressure required from considerations of beam dynamics alone, in order to reduce the chance of contamination of the experimental gas through possible pinhole leaks in the foil.

A schematic of the vacuum system is shown in Figure 2.1. A Kinney fore-pump with a speed of 80 cfm is used to rough out both the cavity and the beam tube. A 1500 liters/sec NRC diffusion pump followed by a water cooled chevron baffle and 6" gate valve is used to evacuate the beam tube and beam scattering section. The clean experimental chamber is evacuated by an 1800 liters/sec Dresser diffusion pump isolated from the chamber by a water cooled baffle and sorbent trap containing zeolite. The net pumping speed at the cavity is reduced to about 150 liters/sec by the

26.

various traps.

The rf cavity and gas handling system are constructed from
non-magnetic type 304 stainless steel. Due to the difficulty of
of machining flanges of the order of 48" I.D. to sufficient
accuracy for crush metal seals, the foil window is sealed to the
cavity and beam tube with double viton O-rings. The space between
the two O-rings is evacuated through a connection to the beam tube.
A 6" Granville-Phillips valve is used to seal off the cavity from
the pump when the latter is filled with gas during experiments.
The 4" optical window, made from Spectrosil quartz to prevent
color-centre formation in the intense radiation field, is sealed
to the cavity opposite the optical port, is attached to the
cavity by a Varian Conflat seal.

The gas handling system, constructed from $\frac{1}{2}$" diameter
stainless steel tubing, is evacuated separately by a 200 liters/
sec CVC diffusion pump equipped with a water-cooled baffle and
zeolite sorbent trap. The system is attached to the cavity through
a GE 1.5" bakeable valve, and a similar valve is used to seal it
off from the pump when gas is to be admitted to the cavity. The
gases used in the experiments are research grade oxygen and
nitrogen contained in steel cylinders filled to 500 psi, and
supplied by the Matheson Corporation, New Jersey. Gas from the
bottles is admitted to the cavity through a pressure regulator
and Granville-Phillips variable-leak pressure controller. The
variable leak is capable of controlling flow rates from more than
100 standard cc per second to less than 10^{-8} standard cc per sec,
and is used to admit gas continuously to the cavity to compensate
for that lost through the mass spectrometer aperture.

All seals are made with Varian conflat flanges, and the entire gas handling system is bakeable to 450° C.

Figure 2.12 shows the system used for the measurement of gas pressures. A Granville-Phillips capacitance manometer is mounted onto the cavity with its reference side connected, as shown in the figure, to a system containing an oil manometer, a CVC McLeod Guage, and a needle valve air inlet. The system, which is constructed from Pyrex, is evacuated by a Cenco diffusion pump and Welsh forepump, which provide an ultimate pressure of less than 10^{-5} Torr. With the cavity and reference system both evacuated, the capacitance bridge is balanced. Air is then admitted to the reference side at the pressure at which the cavity is to be filled, which unbalances the capacitance bridge. This pressure is then determined on the McLeod Guage between 10^{-3} Torr and 10 Torr, and on the oil manometer, which uses Octoil as the working fluid, at pressures greater than 10 Torr. Alternatively, two Hastings-Raydist thermocouple pressure guages, calibrated against the McLeod Guage, are used as rough monitors of this pressure. Gas is then admitted slowly to the cavity and the bridge is rebalanced. This technique permits pressure measurements to be made with absolute manometers without allowing the clean experimental gas to come in contact with the manometric fluid.

To minimize the effects of wall-occluded impurities, it is necessary to bake the cavity at high temperatures while evacuating prior to filling with experimental gas. A serious wall contaminant in the cavity is water released from the zeolite sorbent trap during its activation. To remove water effectively from steel surfaces, a wall temperature of at least 200°C is required.

The oven used to bake the experimental chamber consists
of twelve 2.5 kilowatt Calrod heaters wound around the cavity,
and twelve 0.5 kilowatt Calrod heaters attached to the back.
Several chromel-alumel thermocouples are attached to various
parts of the cavity in order to monitor the temperature during
bakeout. The cavity is insulated thermally by wrapping it with
a thick layer of fibre glass wool. The temperature of the oven
is controlled by varying the current through the Calrods by means
of variacs. Heating tapes are used to bake the gas handling
system. Because of the various Viton O-rings, the cavity cannot
be baked at temperatures higher than 250°C. The gas handling
system, however, which is baked separately can withstand
termperatures up to 450°C.

After cavity bakeout at 250°C for 24 to 48 hours, the
background pressure in the cavity is on the order of 1.0×10^{-8}
Torr or less, with a rate of rise of about 1.0×10^{-8}Torr/minute
when the cavity is shut off from the pumps. For a gas load of
5×10^{-3} Torr the cavity contributed impurity level is about 1
part in 10^4 after thirty minutes, which represents the least
favorable conditions under which the data on the following pages
were collected.

REFERENCES (Chapter II)

Bates, D.R., Proc. Roy Soc. (Lon.) 190, 217 (1949)

Crosswhite, H.M., and G.H. Dieke, "American Institute of Physics Handbook," Section 7, pp 120 f. (McGraw Hill, 1957)

Dayton, I.E., F.C. Shoemaker, and R.F. Mozley, Rev. Sci. Instr. 25, 485 (1954)

Fastie, W.G., Jour. Opt. Soc. Amer. 42, 641 (1952)

Keller, G.E., D.W. Martin, and E.W. McDaniel, Phys. Rev. 140, A1535 (1965)

Nielsen, J.R., Jour. Opt. Soc. Amer. 20, 101 (1930); 37, 494 (1947)

Paul, W., and M. Raether. Z . Physik, 140, 262 (1955)

Van Lint, V.A.J., J. Parez, D. Trueblood, and M.E. Wyatt Rev. Sci. Instr. 36, 521 (1965)

Von Zahn, V., Rev. Sci. Instr. 34, 1 (1963)
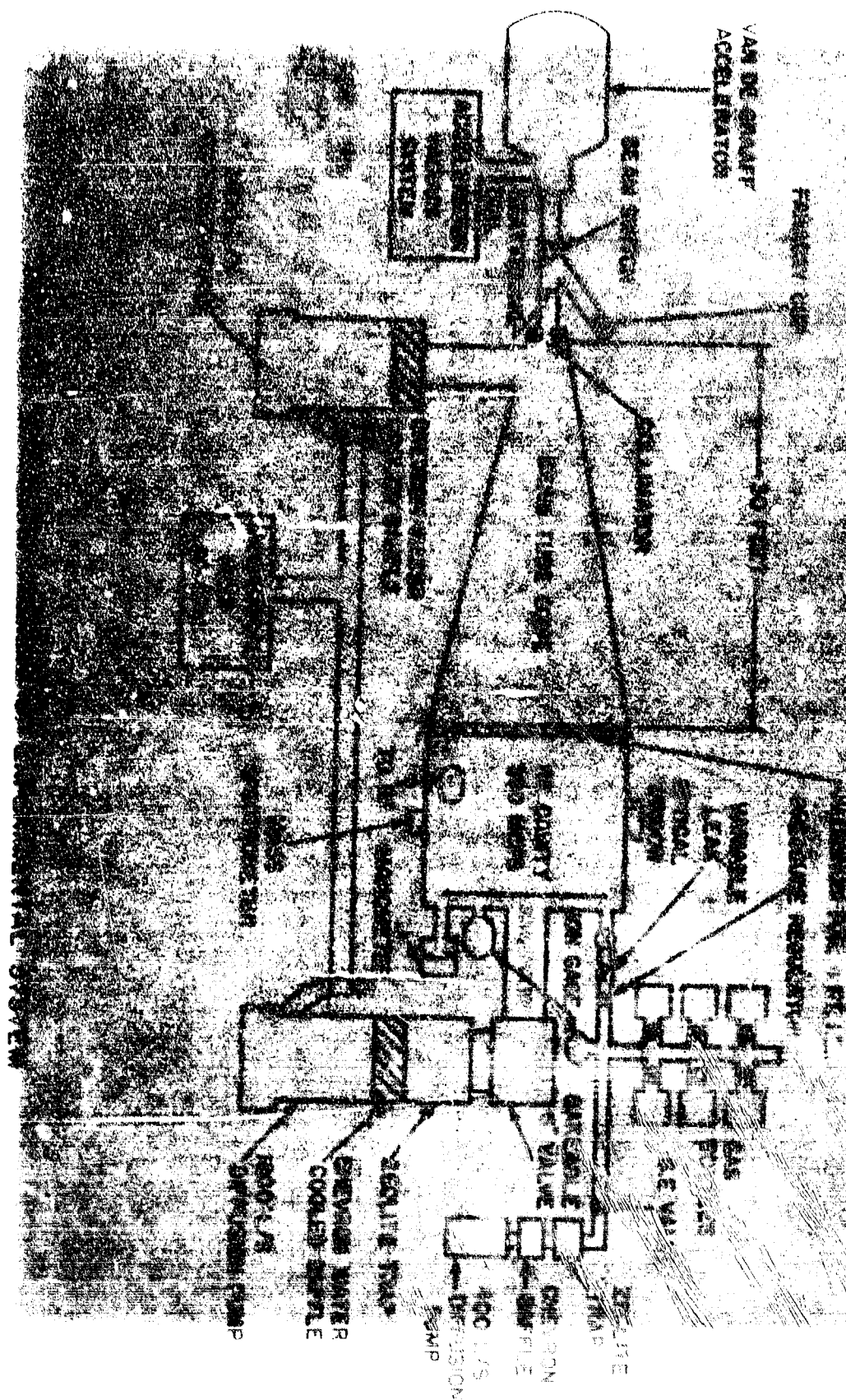
30.

A — HELMHOLTZ COILS

B — GAS DIFFUSER

C — COLLIMATOR

D — INSULATING FLANGES

EE' — FARADAY CUPS

VAN DE GRAAF ACCELERATOR

C.G.

NYLON SLIDE

1/8" ALUMINUM
SHIELD

FARADAY CUP

BNC

TUNGSTEN
SCREEN

CROSS SECTION OF CUP

6" FLANGE

NYLON CORD
DRIVE
SLIDE

3/8" x 3/8"
ALUMINUM
BAR

LIMIT
SWITCH

6" FLANGE

FARADAY
CUP

1/8" ALUMINUM
SHIELD

SHIELD

SUPPORT

VACUUM
FEEDTHROUGH

DRIVE MECHANISM
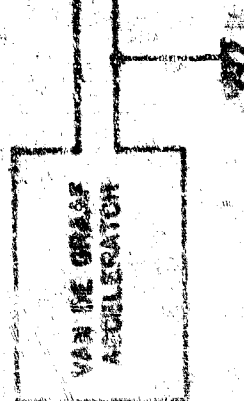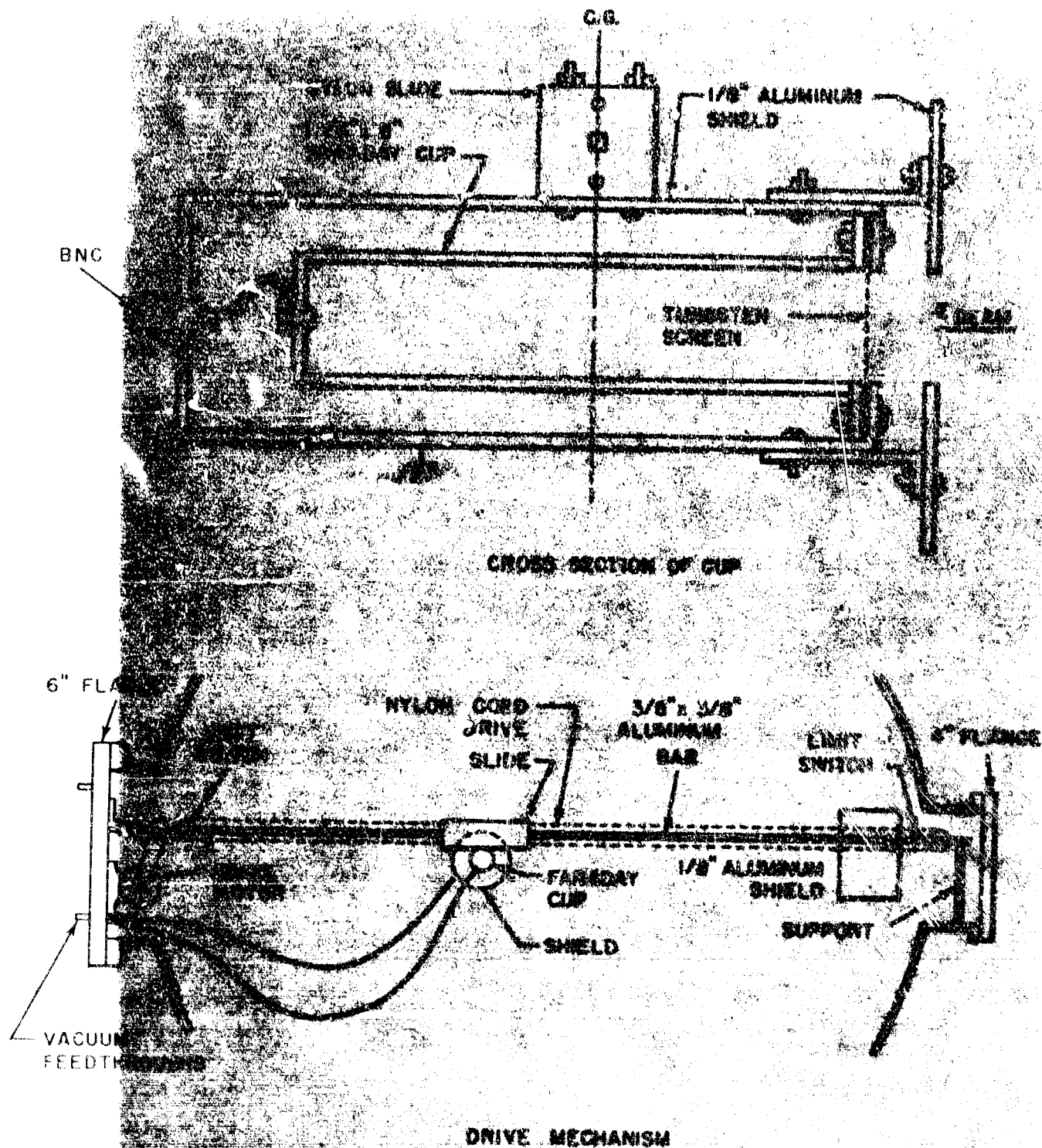
FIGURE 2.3- FARADAY CUP FOR BEAM CALIBRATION

MASS
SPECTROMER
PORT
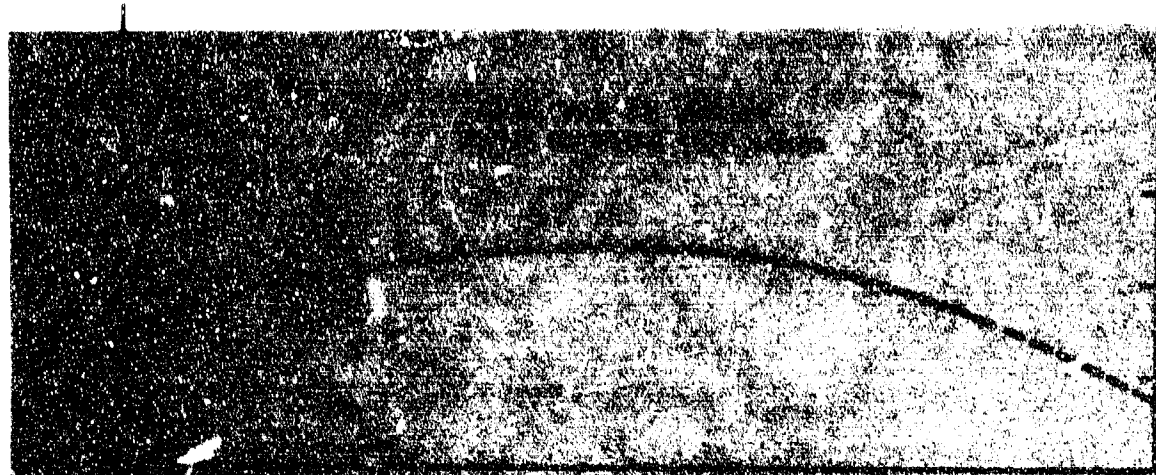
HORIZONTAL PROFILE OF ELECTRON BEAM

DENSITY
TOP

TOTAL MAG 2% GAUSS
BEAM CURRENT = 100 AMPS
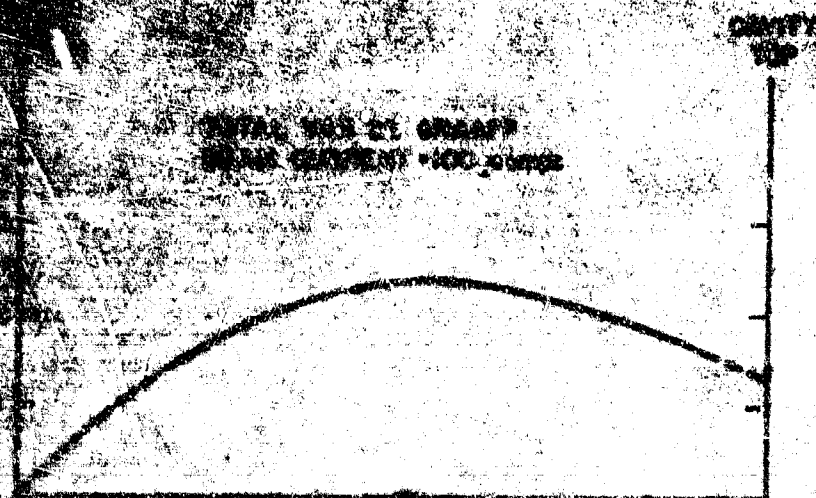
VERTICAL PROFILE OF ELECTRON BEAM

FIGURE 2.4

FIGURE — RF CIRCUITS

FREQUENCY CONTROL

DETECTOR

HYBRID

TO CAVITY

MASTER TIMING PULSE 1 sec.

TIME
MARK
GENERATOR

100 μ secs

RECYCLING
PULSE

PRESET
COUNTER

100 msecs

TRIGGER AT
PRESET DELAY

INPUT-B
COINCIDENCE
CIRCUIT

OUTPUT 9

EXTERNAL
TRIGGER
TYPE 545

SIGNAL FROM
UHF BRIDGE

INPUT-A INPUT-B
MULTIVIBRATOR

TEKTRONIX
OSCILLOSCOPE

TO
BEAM SWITCH
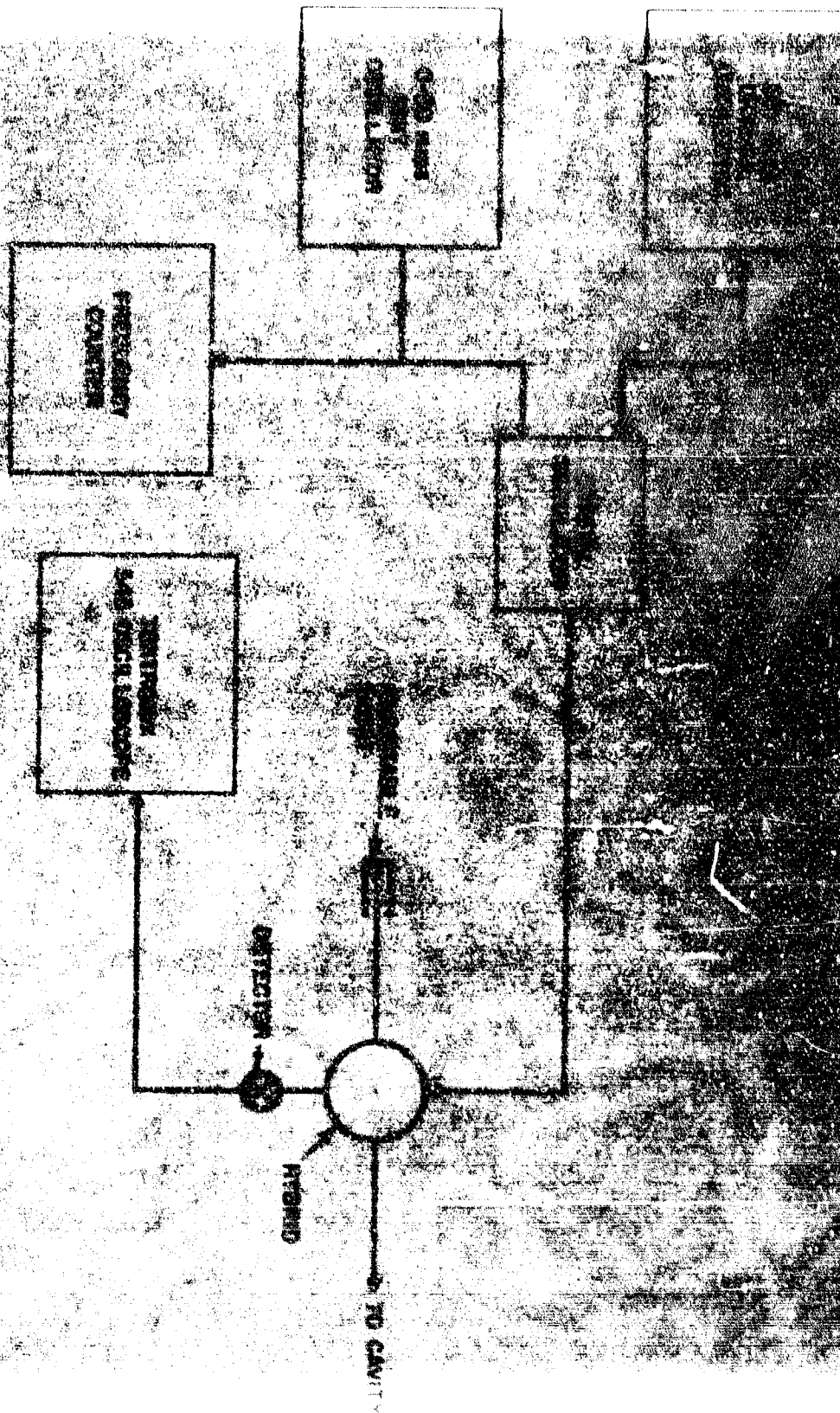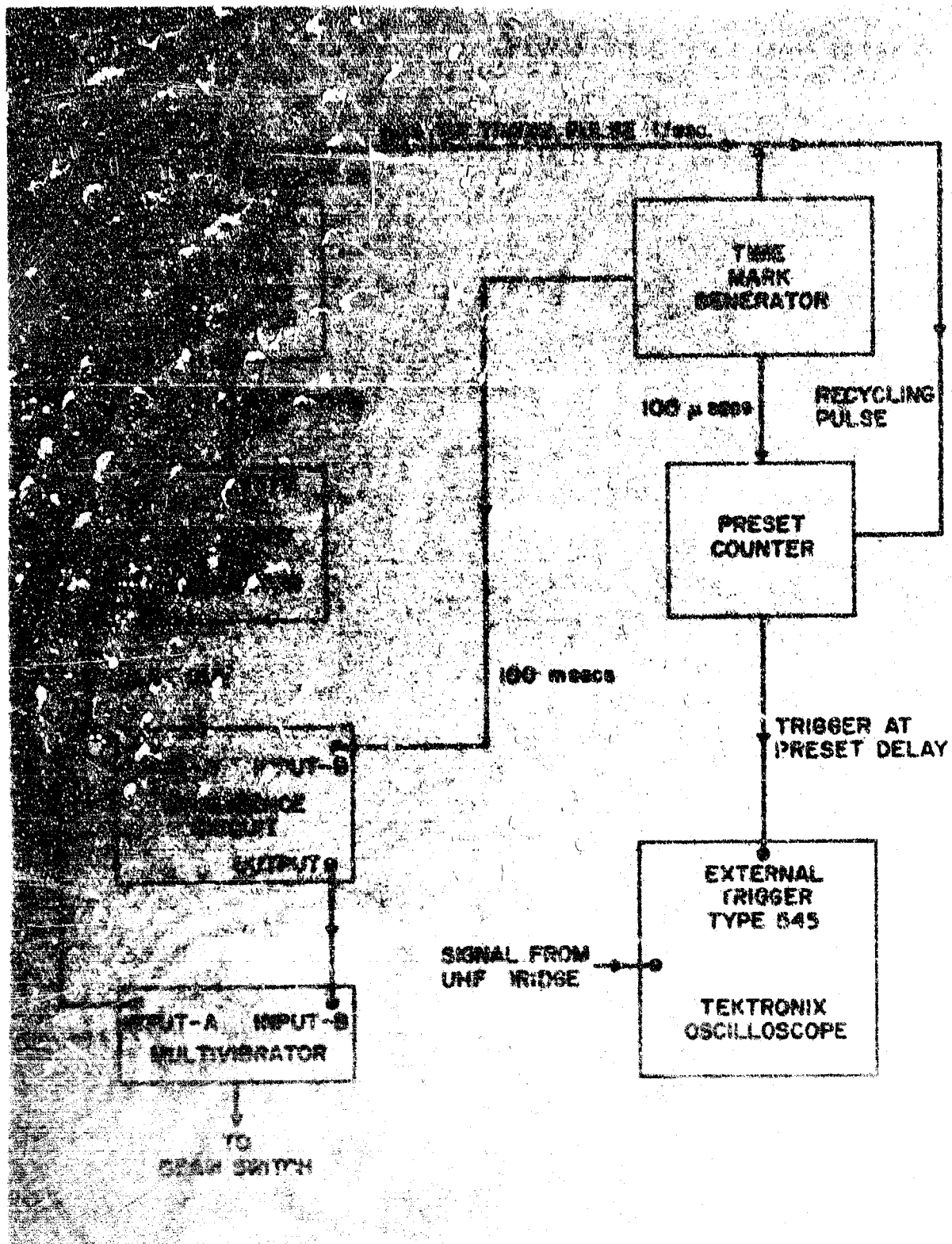
FIGURE 26- BLOCK DIAGRAM OF TIMING CIRCUIT
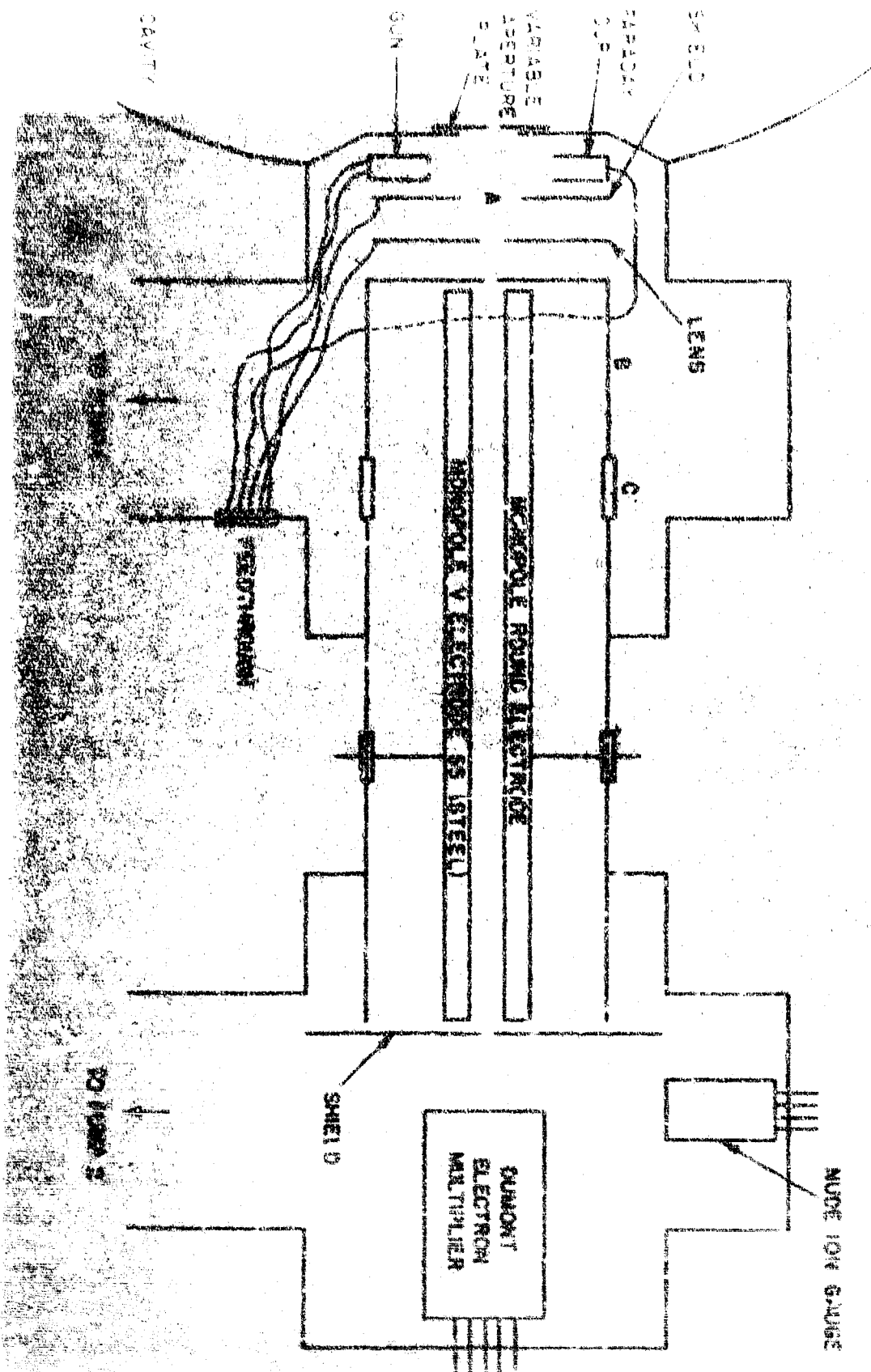
FIGURE 2.8 CROSS SECTION SCHEMATIC OF MONOPOLE STRUCTURE AND HOUSING
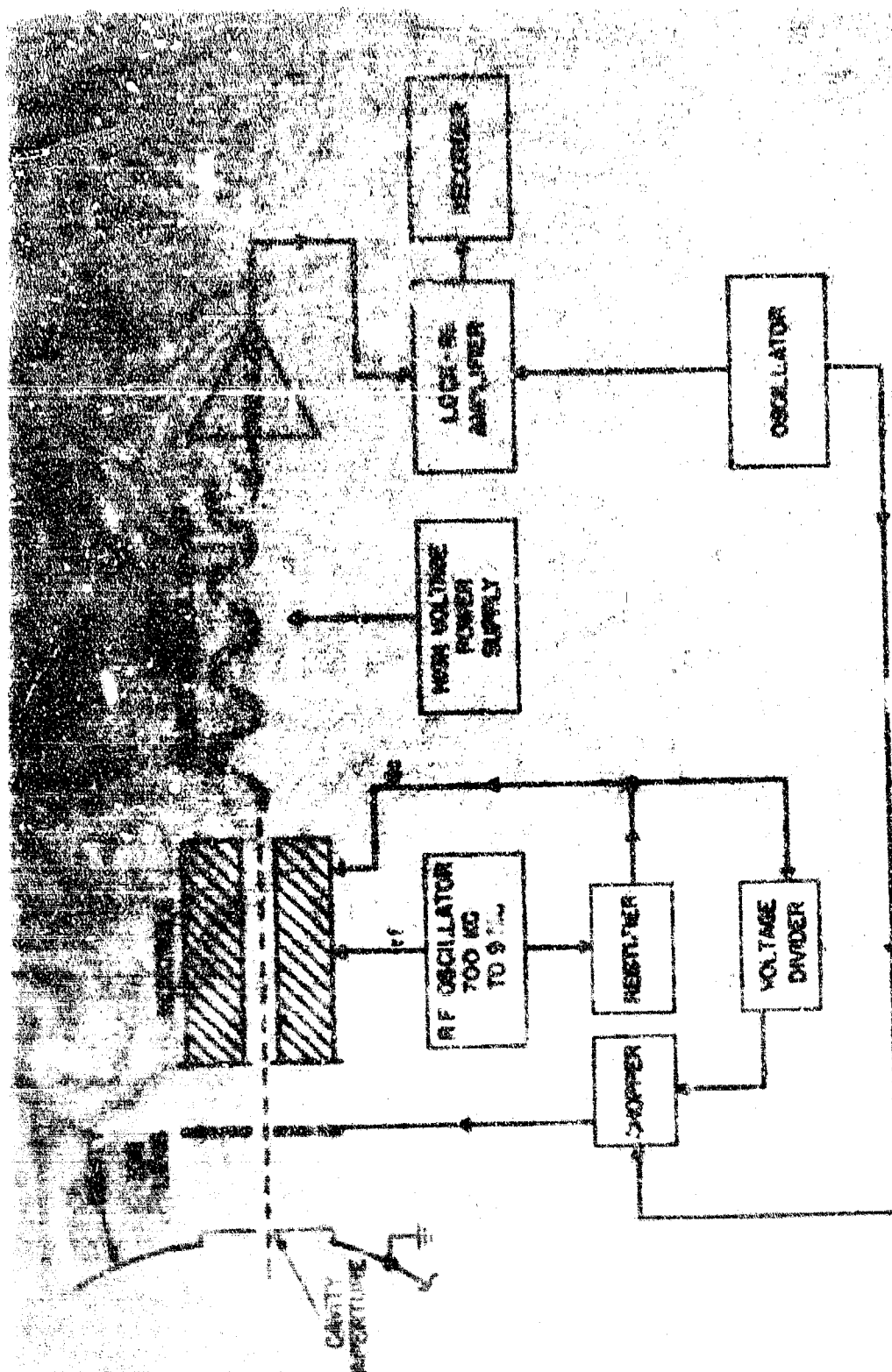
FIGURE 2.9- ELECTRONICS FOR MASS SPECTROMETER
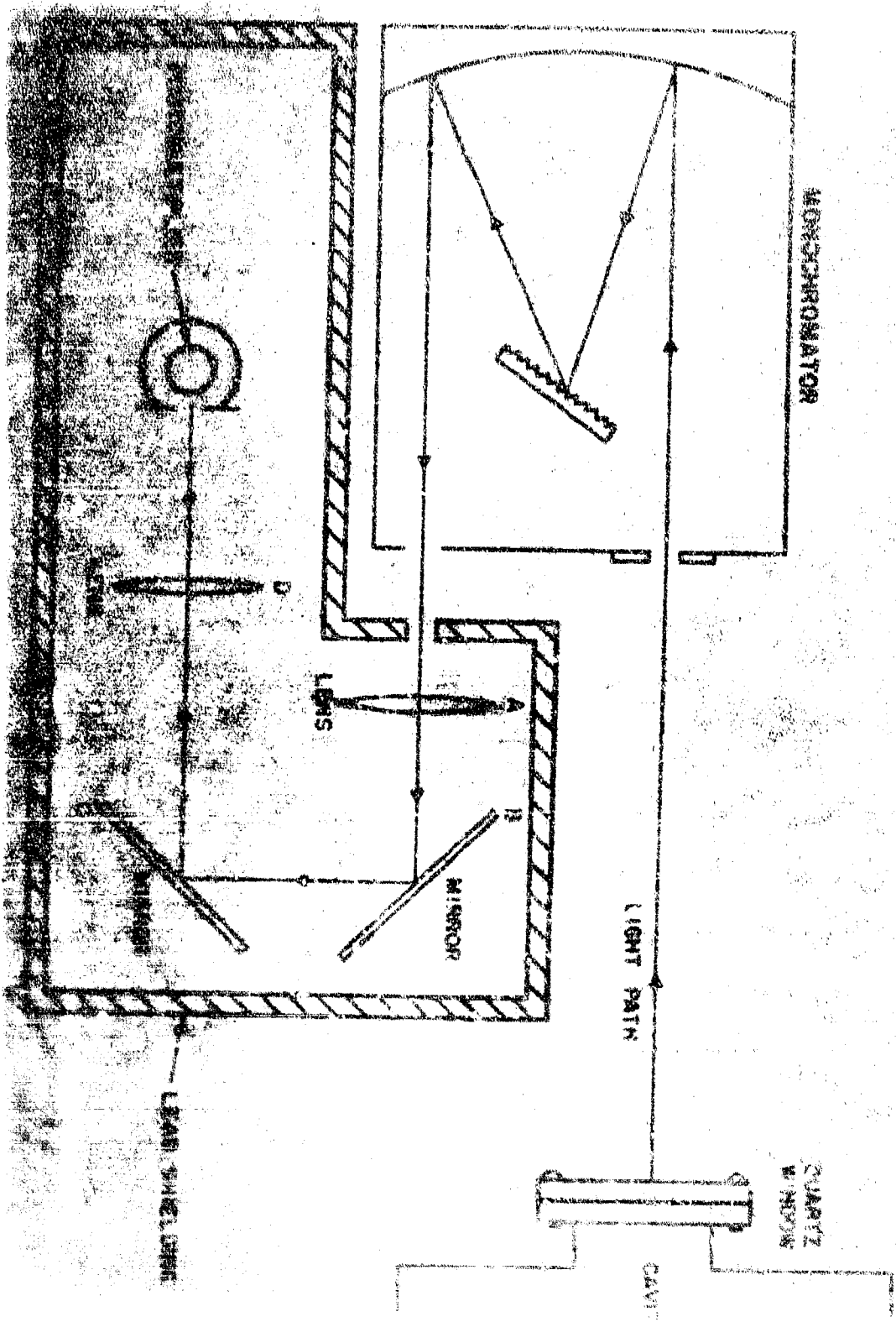
FIGURE 2.10 OPTICAL SYSTEM

Legend in figure:

N_2^+ in:
- ■ $v' = 0$
- ◇ $v' = 1$
- ● $v' = 2$
- ▲ $v' = 0$

Hg:
- ○ 6^3D_1
- × 6^3D_2
- + 7^3S

↓ = OVERLAPPED;
ACTUAL INTENSITY
LOWER THAN INDICATED

λ (Å)
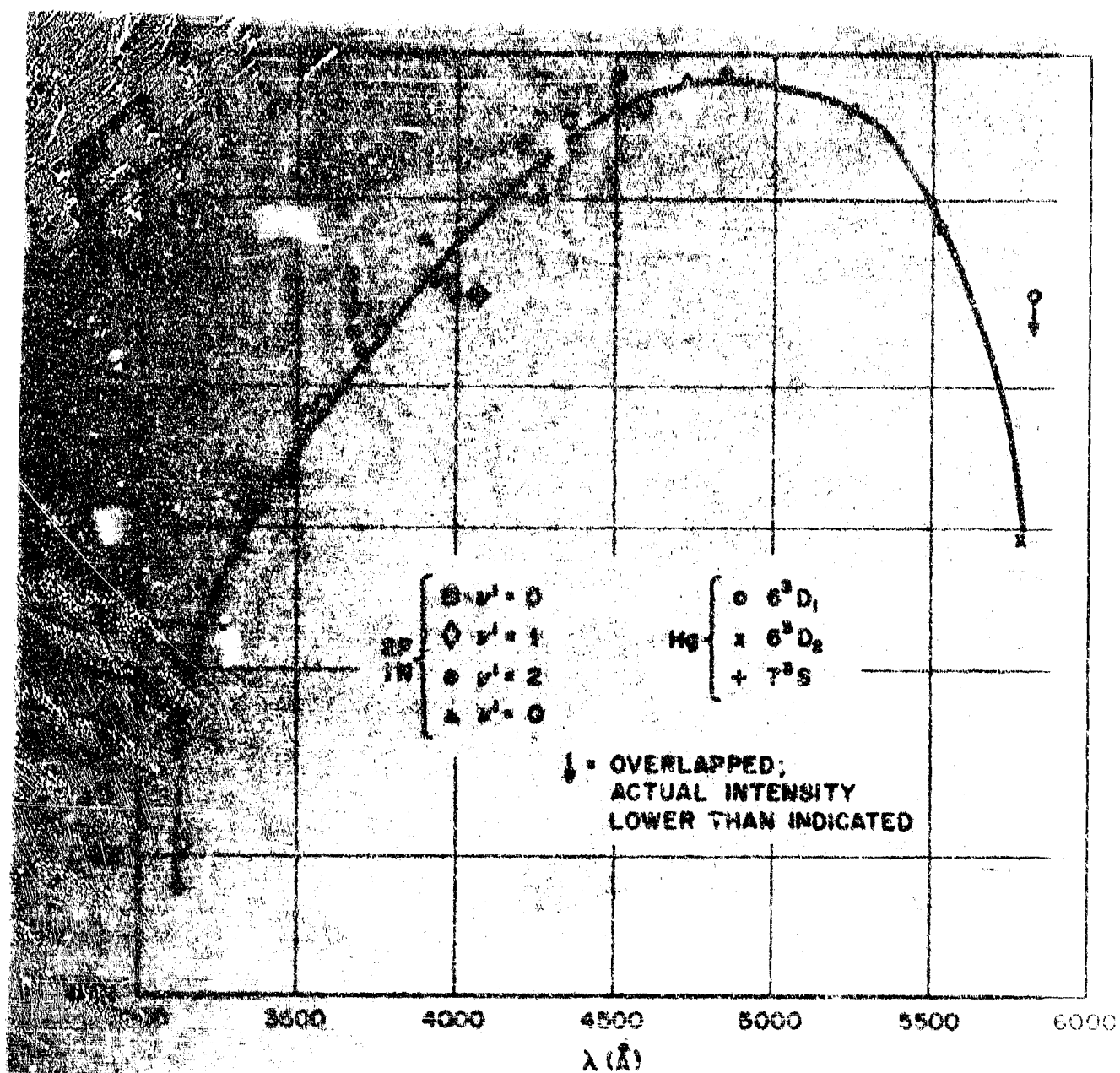
FIGURE 2.11 - RELATIVE RESPONSE OF SPECTROMETER
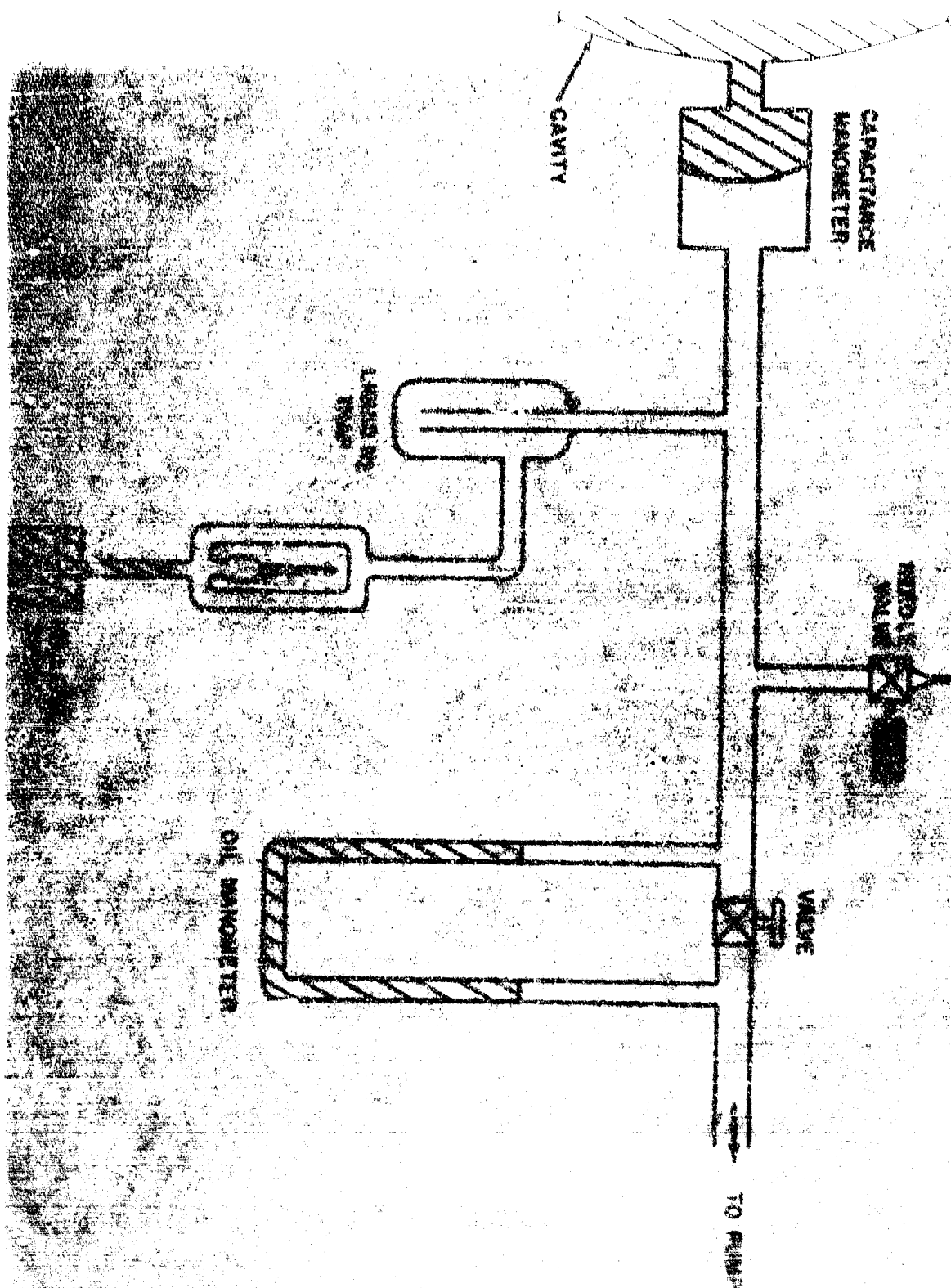
FIGURE 2.12- REFERENCE PRESSURE MEASURING SYSTEM

III.   THEORETICAL BACKGROUND

A.   Introduction

This chapter provides the theoretical framework in which
to view the experimental results presented in the remainder of
this report. The chapter includes descriptions of the various
processes by which charged particles and excited neutral species
are created and destroyed in atmospheric gases subjected to
irradiation by 1.5 Mev electrons. The discussion will be on an
empirical level, aimed at developing a phenomenological
description of the behavior of a gas in which the various
reactions are occurring. In addition, experimental tests will
be derived by which the data can be examined for evidence that
a given type of reaction is taking place. Detailed accounts of
the reaction mechanisms will not be included, for reasons of
brevity; for these, the reader is referred to the excellent
treatises by McDaniel [1964], Hasted [1964], and Bates [1962].
The chapter concludes with a description of the problems in
extrapolating laboratory results to ionospheric situations.

B.   Ionization by Beam Electrons

A relativistic electron traversing a molecular gas can
interact directly with one of the bound electrons of a neutral
gas molecule, imparting sufficient energy to it to excite it
to either a higher bound state or the ionization continuum. A
calculation by Bethe [1936] of the distribution of various kinds
of collisions for electrons in the Mev range with hydrogen
molecules suggests that approximately 50% of the collisions
produce molecules excited into electronic states with principal
quantum number 2, 8% into states with quantum number 3, and 5%

into all higher states; 4% of the collisions are elastic. The
remaining 33% of the collisions result in ionization, in which
the molecular ion may be left in an excited state. Figure 3.1
shows the calculated energy spectrum of secondary electrons
produced by 1 Mev electrons incident on H_2. It can be seen
that many of the secondary electrons are sufficiently energetic
to produce further excitation and ionization in the gas. It
is reasonable to expect that the calculation for hydrogen should
display the general features which can be expected for other
diatomic gases. Although the cross-sections for various
processes may vary somewhat differently with energy.

The production of electron-ion pair in a gas by electron
impact can be written as a binary collision between the incident
electron and a gas molecule. For convenience in comparison
with laboratory measurements, this reaction can be expressed by
the rate equation

$$\frac{\partial X^+}{\partial t} = \frac{\partial n}{\partial t} = K p i \tag{3.1}$$

where X^+ is the number density of ions produced per cm^3, n the
number density of the electrons per cm^3, p the pressure of the
target gas in Torrs, and i the beam current density in micro-
amperes/cm^2. For an a priori calculation of the rate coefficient
K, one must resort to a mixture of theory and experiment. If a
fast electron loses V volts in traversing one centimeter of a
gas at STP, and if an expenditure of W volts of primary electron
energy results in one ion pair under condition where all secondaries
are stopped in the gas, then $K = 7.55 \times 10^9$ W/V at 25°C. From

a calculation by Nelms [1957], the stopping power V/ρ where ρ is the gas density in gram cm^{-3}, is 1.66 Mev cm^2/gm in air, N_2, and O_2 for electrons at 1.5 Mev. Because of the complication of ionization by energetic secondary electrons, it is difficult to compute W from first principles. However, values of W have been determined experimentally for these gases by Jesse and Saudauskis [1953] and Jesse [1958] under conditions in which all secondary electrons are stopped in the gas. Table I presents these results, together with the calculation for K.

Laboratory measurements are frequently complicated by the presence of back-scattered and secondary electrons produced at the chamber walls, in addition to those in the primary beam. For the aluminum back plate used in the reaction chamber, one can expect about 7% of the incident electron beam to be back-scattered with energies of 50 ev or greater [Bakish, 1962]. The last column in Table I includes the full 7% correction on K; this correction provides an upper limit for K, since many of the back-scattered electrons have insufficient energy to traverse the cavity completely. "True" secondary electrons in the energy range below 50 ev are also emitted from the back plate, but it is expected that their total number above the ionization potential of the gas is not significant.

Of particular interest in the present experiment is the rate of energy relaxation of the secondary electrons. In some of the measurements reported below, a steady-state electron distribution is established in equilibrium between continuous ionization (hence production at high energies) and electron removal and energy relaxation processes. For this distribution to approximate gas temperatures, the free electron removal rates must be low compared to the energy relaxation frequencies, so

T A B L E I

GAS	$U/\rho \left(\dfrac{\text{Mev cm}^2}{\text{gm}}\right)$	$\rho \left(\dfrac{\text{gm}}{\text{cm}^3}\right)$	$U \left(\dfrac{\text{kev}}{\text{cm}}\right)$	W eV/ion pr	U/W $\dfrac{\text{ion pr}}{\text{cm}}$	K $\dfrac{\text{ion pr}}{\text{cm}^3\text{ Sec}} \dfrac{\text{cm}^2}{\text{Torr uamp}}$	K + Back Scattering
Air	1.66	1.19 x 10⁻³	1.98	33.9	58	4.4 x 10"	47 x 10"
N₂	1.66	1.15	1.91	35.0	54.5	4.1 x 10"	4.4 x 10"
O₂	1.65	1.31	2.16	30.9	70	5.3 x 10"	5.7 x 10"

CALCULATION OF RATE COEFFICIENT FOR IONIZATION
by BEAM ELECTRONS

that the electrons spend most of their free lifetimes at thermal
energies. The correct approach to the analysis of this problem
requires a solution to the Boltzmann transport equation for the
secondary electrons, in which elastic and all pertinent inelastic
collisions are included. This would be a staggering task even if
all relevant cross-sections were known over the energy range of
interest, which they in fact are not. A very promising approximate
approach in the current literature is a technique described by
Frost and Phelps [1962]. In this work the frequency of energy
exchange collistions is obtained from comparisons of theoretical
and experimental values for mobility and diffusion coefficients,
by adjusting a set of assumed elastic and inelastic collision
cross-sections for optimum fit. For nitrogen, their value for the
frequency of energy exchange collisions at thermal energies is
$\nu_u \approx 6.5 \times 10^5 p$, where p is the gas pressure in Torr. This is to
be compared with the ordinary elastic collision-frequency model
for energy echange, defined by

$$\frac{\partial u}{\partial t} = \frac{2m}{M} \nu_c u \tag{3.2}$$

where u is the electron energy in excess of that corresponding
to the ambient gas, m and M are the masses of electrons and
neutral molecules, respectively, and ν_c is the frequency for
elastic collision with energy transfer. For nitrogen, this gives
an elastic rate of about $3 \times 10^3 p$, which is considerably smaller
than the rate obtained by Frost and Phelps. One ordinarily expects
inelastic collisions to bring the electrons very quickly down to
energies below the lowest available state of the neutral molecule.
The major part of the electron cooling time is then assumed to be
spent in elastic collisions as described by Equation (3.2). As
will be reported below, however, observations have been made in

which the electrons are apparently thermal although their life-
times are shorter than the elastic-collision cooling time, but
are still within the lifetime specified by the results of Frost
and Phelps.

C.   Electron and Ion Loss Mechanisms

The charged particles produced by the primary ionization
of O_2 - N_2 mixtures are subject to various possible loss mechanisms.
These loss mechanisms can be conveniently classified into three
general types: attachment, recombination and diffusion.

1.   Electron attachment

Electrons can be removed from the volume of certain
gases by combining with neutral molecules to form negative ions.
Various mechanisms are available to stabilize the resulting
negative ion by removing the excess binding energy from the
electron-molecule system.   The energy may be radiated as a photon;
This process, referred to as radiative attachment, is written

$$e + O_2 \longrightarrow O_2^- + h\nu$$
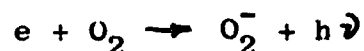
If the electron energy and the inter-nuclear distance in the
neutral molecule are appropriate, the electron may be captured
into an excited state of the ion from which it very rapidly makes
a transition to a repulsive ionic state.   This process, called
dissociative attachment, produces a neutral atom and a negative
atomic ion, the excess energy being carried off as kinetic energy

of the atomic fragments. Thus

$$e + O_2 \longrightarrow O^- + O + \text{kinetic energy}.$$
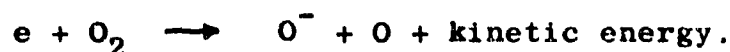
Finally, a ternary (3-body) collision may occur between an electron, a neutral molecule to which the electron will ultimately attach, and a second molecule (not necessarily of the same species) which carries off the excess energy. Thus

$$e + O_2 + X \longrightarrow O_2^- + X + \text{kinetic energy}.$$
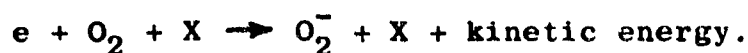
Electron attachment losses are described quantitatively by the rate equation

$$\left(\frac{\partial n_e}{\partial t}\right)_{\text{attachment}} = -\nu_\alpha\, n_e \quad, \tag{3.3}$$

where ν_a is the net attachment frequency, and is the sum of contributions from the radiative, dissociative, and three-body processes. For thermal electrons in pure oxygen, the best current estimates in the literature give:

$$\nu_{rad.} \cong 4 \times 10^{-21}\, [O_2] \quad sec^{-1} \qquad \text{[Archer, 1963]}$$
$$\nu_{3\text{-body}} \cong 2 \times 10^{-30}\, [O_2]^2 \quad sec^{-1} \qquad \text{[Pack and Phelps, 1966]} \tag{3.4}$$
$$\nu_{diss.} \cong 0 \qquad \qquad \qquad \qquad \text{[Pack and Phelps, 1966]}$$

[Dissociative attachment becomes important only for electron energies above ~ 1.3 ev.] Thus three-body attachment is the only important process at pressures above 10^{-5} Torr.

In mixtures of oxygen with nitrogen, the ground-state N_2 molecule can also serve as a stabilizing third body:

48.

$$e + O_2 + N_2 \longrightarrow O_2^- + N_2 + \text{kinetic energy.}$$
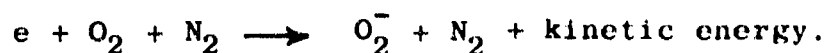
The total three-body attachment rate equation in nitrogen-oxygen mixtures can be written

$$\left(\frac{\partial n}{\partial t}\right)_{3\text{-body}} = -\beta_o \,[O_2]\left([O_2] + \xi\,[N_2]\right) \tag{3.5}$$

where ξ, the efficiency of an N_2 molecule in stabilizing the negative ion relative to an O_2 molecule, is of the order of a few percent [Chanin et al, 1962].

2. Recombination

Electrons can recombine with positive ions to form neutral molecules in various stages of excitation. The energetics of the disposal of binding energy in the recombination process are similar to the attachment reactions described above. Radiative, dissociative and three-body recombination are all at least theoretically possible. For the low ionization levels which we encounter, three-body recombination in which the third body is a charged particle is very unlikely. A process such as

$$e + NO^+ + x \longrightarrow NO + X,$$
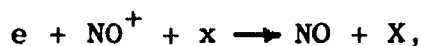
however, in which the stabilizing third body is a neutral molecule, may be expected to dominate the recombination mechanisms at sufficiently high pressures. Radiative recombination seems to have a very small probability; a theoretical estimate of the rate of the reaction

$$e + O_2^+ \longrightarrow O_2 + h\nu$$

yields the result [McDaniel, 1964]

$$\frac{\partial n_e}{\partial t} \sim 10^{-12} P n_e$$

where P is the density of positive ions. It is presently believed that dissociative recombination is an important electron-ion process in the upper atmosphere [Kasner and Biondi, 1965]. For this case we write

$$e + P_{2j}^+ \longrightarrow P_j + P + kinetic\ energy \qquad (3.6)$$

$$and \quad \left(\frac{\partial n_e}{\partial t}\right)_{recomb.} = \left(\sum_j \alpha_{je}\right) n_e$$

where P_j is the density of the "jth" positive ion and α_{je} is the pertinent two-body coefficient for its recombination with electrons.

In addition to the electron-positive ion reactions described above, negative ions may also charge-exchange with positive ions. Here there can be a two-body process in which the excess energy appears as excitation of the resulting species:

$$X^+ + Y^- \longrightarrow X^* + Y^*$$

A three-body ion-ion recombination also occurs, and is of great importance in ionized air at low altitudes. The loss of negative ions from oxygen by recombination can be written [Sayers, 1938]

$$\frac{\partial N}{\partial t} = -\left[10^{-[8\pm0.5]} + 7.2 \times 10^{-[9\pm0.5]} p\right] P N \qquad (3.7)$$

50.

3. Diffusion

Charged particles can be removed from the volume of a
gas by diffusion to the walls of the experimental container.
Experiments indicate that the charge species readily recombine
at the walls by utilizing the latter as an efficient medium for
energy and momentum disposal. This imposes the boundary
conditions that all charged particle densities vanish at the walls
[cf. however McDaniel, 1964 pp 496 ff]. The vanishing of the
particle densities at the walls guarantees the existence of a
concentration gradient for the charge species, which makes
diffusion possible.

The equation describing the current of the jth
particle species under the combined influence of a concentration
gradient and an electric field E is

$$\Gamma_j = -D_j \nabla n_j + \mu_j n_j E \quad , \tag{3.8}$$

where D_j and μ_j are the free diffusion and mobility coefficients
of the jth species. These quantities satisfy the Einstein Relation
[Jeans, 1954]

$$\frac{D_j}{\mu_j} = \frac{k T_j}{e} \tag{3.9}$$

where T_j is the "temperature" of the jth species. The diffusion
coefficient is defined for a Maxwellian distribution by the
equation

$$D_j = \frac{1}{3} \lambda_j \overline{V_j} \quad , \tag{3.10}$$

where λ_j is the mean free path of the jth species for elastic collisions with momentum transfer with gas molecules and $\bar{v}$ is the mean thermal speed of the jth species. As a result, D_j and $_j$ are both inversely proportional to the gas pressure, and diffusion can dominate any volume process at sufficiently low pressures. Even in the absence of external electric fields E does not, in general, vanish. The initially unequal rates at which the various charged particle species diffuse out of the volume of the chamber sets up space charge fields (E) which profoundly influence further diffusion. To study this influence in greater detail, one must consider specific plasmas containing the kinds and numbers of ion species of interest. In the work to be described in the body of this report, three situations are of particular interest:

a) Plasmas containing electrons and a single species of positive ions;

b) Plasmas containing electrons and two species of positive ions;

c) Plasmas containing electrons and one species each of positive and negative ions.

Case a) represents the situation leading to the well-known ambipolar diffusion problem [Biondi and Brown, 1949]. As long as n = P everywhere in the plasma, both electrons and positive ions will diffuse at a common rate according to the equation

$$\frac{\partial n}{\partial t} = \frac{\partial P}{\partial t} = D_a \nabla^2 n = D_+ \left(1 + \frac{T_e}{T_i}\right) \nabla^2 n \tag{3.11}$$

where D_a is the ambipolar diffusion coefficient, $T_e = T_i$, as the electron and ion temperatures, respectively. If $T_e = T_i$, as

52.

appear to be the case in the work discussed below, then D_a $2D_+$
[cf. however, Allis and Rose, 1954].

Case b) represents a more complex situation, in that
charge neutrality considerations above do not fix the relative
spatial distribution of the electrons and the two ion species,
P_1, P_2, as they did in Case a). If one imposes the assumption
of spatial congruence [Phelps, 1952], that is, that

$$\frac{\nabla n}{n} = \frac{\nabla P_1}{P_1} = \frac{\nabla P_2}{P_2}$$

then

$$\left.\begin{array}{l} \dfrac{\partial P_1}{\partial t} = D_{a1} \nabla^2 P_1 \\[2mm] \dfrac{\partial P_2}{\partial t} = D_{a2} \nabla^2 P_2 \\[2mm] \dfrac{\partial n}{\partial t} = \dfrac{\partial P_1}{\partial t} + \dfrac{\partial P_2}{\partial t} \end{array}\right\} \qquad (3.12)$$

where D_{a1}, D_{a2} are the ambipolar diffusion coefficients which
would be obtained if each ion species were diffusing in the absence
of the other. In some cases, particularly those involving strong
recombination of electrons with one of the ion species, the
assumption of a spatial congruity is difficult to justify, and a
more complete theory must be used [McDaniel, 1964].

Case c) presents a similar complexity, in that
relatively simple solutions can be obtained only with the
assumption of spatial congruence of all species. In this latter
case, one finds for the effective diffusion coefficients for the
electrons, positive ions, and negative ions [Oskam, 1958]

$$D_{e,eff} = 2D_+ \left(1 + N/n\right)$$

$$D_{+,eff} = 2D_+$$

$$D_{-,eff} \cong 0 \tag{3.13}$$

As will be seen in Chapter V, the assumption of spatial congruence of all the particle species is frequently difficult to justify on physical grounds. In this case, one must go back to the set of Equations 3.8, and find the complete self-consistent solution for the currents subject to the conditions

$$\sum_j n_{j+} = \sum_k n_{k-} \quad ; \quad \sum_j \Gamma_{j+} = \sum_k \Gamma_{k-} \quad , \tag{3.14}$$

that is, that the total local positive and negative charge and current densities vanish. This then leads to a rate equation for the diffusion of each particle species of the form

$$\frac{\partial N_j}{\partial t} = -\nabla \cdot \Gamma_j \quad , \tag{3.15}$$

which in general must be solved numerically on a high-speed electronic computer.

For many situations of interest, it is sufficiently accurate to make the replacement

$$\nabla^2 n_j \Rightarrow \frac{1}{\Lambda_{\parallel}^2} n_j$$

where $\Lambda_{\parallel}$, the fundamental diffusion length, is the largest eigen-value of the equation

$$\frac{\partial n_j}{\partial t} = D_j \nabla^2 n_j \tag{3.16}$$

subject to the boundary conditions that n_j vanish at the container

54.

boundary. For a right circular cylindrical container of radius R, height h,

$$\frac{1}{\Lambda_{\parallel}^{2}} = \left(\frac{2.405}{R}\right)^{2} + \left(\frac{\pi}{h}\right)^{2} \tag{3.17}$$

D.   Production and Loss of Excited States

In this section, the mechanisms by which excited states of neutral and ionic species can be created or destroyed is considered. One must know the excited state distribution in the irradiated gas, both to interpret the observed optical emission from these states, and to account for the profound effect that excited states can have on measured rate coefficients [McDaniel, 1964, pp. 250,255].

The rate equation governing the population N_j of the jth excited states is [Fowler, 1954]

$$\frac{\partial N_j}{\partial t} = P_j + D_j \nabla^2 N_j + B_{oj}\rho_{oj}N_o - \sum_{k=o}^{j-1} A_{jk}N_j + \sum_{k=j+1}^{\infty} A_{kj}N_k \tag{3.18}$$

Here D_j is the diffusion coefficient for state j, B_{oj} the Einstein absorption coefficient for radiation corresponding to transitions between state j and the ground state (denoted by the subscript "o"), ρ_{oj} is the flux density of this radiation, and A_{jk} is the Einstein spontaneous emission coefficient for a downward transition from state j to state k. P_j includes all other mechanisms for the production and loss of N_j from the volume of the gas. The diffusion term in Equation 3.17 is only significant when state j is metastable; for short-lived states, diffusion is a negligible

loss mechanism relative to the radiative processes. For a weakly ionized gas, only the ground state is present in sufficient density to produce appreciable population of upper states by absorption; the only states which can be affected by the process described by the third term are therefore those for which $B_{oj} \neq 0$. The first summation in Equation (3.17) represents the radiative loss out of N_j to all lower states; it is convenient to define the radiative lifetime $\tau_{\kappa j}$ of the state by

$$\tau_{\kappa j}^{-1} = \sum_{i=0}^{j-1} A_{ji} \equiv A_j .$$ (3.19)

The second summation represents the population of N_j by radiative cascading from all higher states N_k; the relative importance of this term must be examined separately in each experimental situation.

Consider now the term P_j. A binary inelastic collision between an energetic electron and a gas molecule will produce an excited state of either the neutral molecule or the molecular ion, so that the reaction can be represented by one of the following:

$$e + X_2 \longrightarrow X_2^* + e$$

$$e + X_2 \longrightarrow (X_2^+)^* + e + e$$
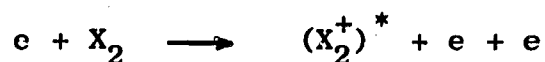
The rate equation for this process can be written

$$\left(\frac{\partial N_j}{\partial t}\right)_{impact} = K_j n_i$$ (3.20)

Excited molecular states may also be populated by the recombination of a molecular ion in a radiative or three-body process:

$$X_2^+ + e \longrightarrow X_{2j}^*$$

if the recombination mechanism is dissociative, an excited atomic state may result:

$$X_2^+ + e \longrightarrow X^* + X$$

In either case, the population of an excited state by recombination is proportional to the recombination rate:

$$\left(\frac{\partial N_j}{\partial t}\right)_{recomb.} = \alpha_j \left[X_2^+\right] n \tag{3.21}$$

The proportionality constant obviously satisfies

$$\sum_{j=0}^{\infty} \alpha_j \leqq \alpha \tag{3.22}$$

where α is the electron-ion recombination coefficient, since not all of the recombination events may populate excited states.

It should be noted that dissociative recombination may also populate a molecular state indirectly, by way of a reassociation reaction such as the process

$$X^* + X \longrightarrow X_2^*.$$

If this reaction occurs rapidly enough, its rate is still con-
trolled by the rate of the initial dissociative recombination
(Equation 3.20).

Excited molecules can also be lost to the volume of the
gas by collisions with ground state neutral molecules. These
collisions can result in the transfer of excitation (either
rotational, vibrational or electronic) from the excited molecule
to the neutral molecules, leaving the former in some lower state
i:

$$N_j + M \longrightarrow N_i + M^* + \text{kinetic energy.}$$
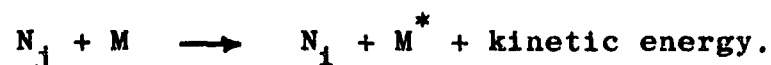
If M is the ground state of the neutral molecule from which N_j
was produced, then the resonant exchange

$$N_j + N_o \longrightarrow N_o + N_j$$
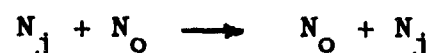
makes no change in N_j. Another type of collision which can remove
excitation is one which changes the identity of the excited
molecule in a chemical reaction, such as

$$X_2^* + M \longrightarrow MX_2$$

$$X_2^* + M \longrightarrow MX + X$$

$$X_2^* + M \longrightarrow M + 2X$$
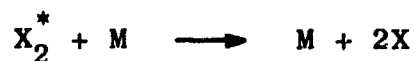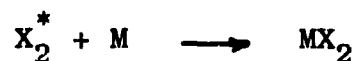
All these collision processes compete with radiation as the
depopulating mechanism of N_j, and are therefore referred to as
quenching reactions, for which the rate eqaution can be written

58.

$$\left(\frac{\partial N_j}{\partial t}\right)_{quenching} = - C p N_j \tag{3.23}$$

The optical measurements to be presented in this report are concerned with band systems originating on one of two electron states, the First Negative System of N_2^+, resulting from the transition $B^2\Sigma_u^+ \longrightarrow X^2\Sigma_g^+$, and the Second Positive System of N_2, $C^3\pi_u \longrightarrow B^3\pi_g$. Neither initial state is radiatively coupled to the ground state of the neutral molecule, and both are sufficiently short-lived that diffusion is negligible. For the $B^2\Sigma$ level of N_2^+, radiative cascading can almost certainly be ignored [Stewart, 1956]. For lack of specific information to the contrary, it will be assumed that cascading can be neglected for the $C^3\pi_u$ state of N_2 as well. If the measurements are confined to a regime of ionization levels where recombination can be ignored, then

$$\frac{\partial N_j}{\partial t} = K_j p i - A_j N_j - C p N_j \tag{3.24}$$

This equation is easily generalized to the case of a gas mixture. If the parent gas of the excited molecule (or ion) is denoted by subscript a and the other constituents of the mixture by b, c,...., then

$$\frac{\partial N_j}{\partial t} = K_j p_a i - \left(C_a p_a + C_b p_b + ... \right) N_j - A_j N_j \tag{3.25}$$

where p_a, p_b,..... are the respective partial pressures.

For a binary mixture in steady-state,

$$N_j = \frac{K_j \, p_a \, i}{C_a p_a + C_b p_b + A_j} \qquad (3.26)$$

The intensity of light emitted during a transition from state j
to a given lower state will be proportional to the population N_j.
Consequently

$$\frac{p_a}{I_j} \propto C_a p_a + C_b p_b + A_j \qquad (3.27)$$

where I_j is the intensity of the radiation under consideration.
The quenching coefficients can be determined by an analysis of
(P_a/I_j) versus p_a plots for various values of p_b. In particular,
a pure gas plot $(p_b = 0)$ should yield a straight line for which
the ratio of slope to intercept is given by

$$R_a = \frac{C_a}{A_j} \qquad (3.28)$$

with C_a thus determined, C_b can be found in an entirely analogous
manner.

To conclude this section, consider how K_j can be calculated
in terms of known quantities. By definition K_j, p_i gives the
number of molecules per cm^3 raised to a specific state j in one
second. The designation j fixes both the electronic and vibra-
tional configurations; rotational fine structure may be included
if desired. If p is sufficiently low that collisional quenching
is negligible, the steady-state population reduces to

$$N_j = \frac{K_j \, p \, i}{A_j} \qquad (3.29)$$

60.

The number of photons ϕ_{je} emitted from each cm^3 of the gas per second in a downward transition from state j to some specific state 1 is then given by

$$\phi_{j\ell} = A_{j\ell} \, N_j \;\; = \;\; \frac{A_{j\ell}}{A_j} \, K_j \, p \, \lambda \tag{3.30}$$

In the absence of an absolute intensity calibration for the optical spectrometer, ϕ_{je} cannot be evaluated directly. One can relate ϕ_{je}, however, to the total energy U deposited in one cm^3 in the gas per second by the beam if the fluorescence efficiency N_{je} for the excitation of the specific transition is known. N_{je} is defined by

$$\eta_{j\ell} = \phi_{j\ell} \, h \, \nu_{j\ell} \, / \, U \tag{3.31}$$

U can be evaluated for the present experiment by a measurement of the ionization production rate (Section III.B):

$$U = K p \lambda W \, , \tag{3.32}$$

where K is the rate coefficient for ionization by the beam. This yields

$$K_j = \frac{\eta_{j\ell} \, A_j \, W \times K}{A_{j\ell} \, h \, \nu_{j\ell}} \tag{3.33}$$

One can then determine the absolute density of excited state N;; from this one can determine quantities such as the total number of quenching collisions per cm^3 per second for state j:

$$\left(\frac{dN_j}{dt} \right)_Q = - C \, p \, N_j \tag{3.34}$$

E.   Treatment of Experimental Data

In this section some of the techniques by which information
is extracted from the basic measurements are developed. In
addition to afterglow measurements, which have been widely treated
in the literature, the experiment employed here permits the study
of thermal electrons and ions in the steady state during
continuous irradiation. Several techniques not described else-
where in the literature have been applied to the data analysis,
and are therefore included here.

The results of electron density measurements appear as a
set of frequency shifts which are functions of the experimental
parameters. These frequency shifts can be related to local
electron density in the cavity only if the spatial distribution
of electrons is known. To do this, one must have a model which
describes the various processes occurring in the gas, from which
the spatial dependence can be deduced. In order to arrive at a
model, the individual reactions occurring in the gas must be
identified. We have proceeded by first making the assumption
that the electron density differs from the measured frequency
shift by a constant factor, then studied the variations of the
density which results from this assumption with experimental
parameters. When the processes have been identified qualitatively,
they are then assembled into a complete mathematical model from
which the correct spatial dependences can be obtained. This
model is then solved accurately, at least in principle, for the
correct frequency shift - electron density relation.

62.

The steady-state density n_S can be written

$$n_s = K p i / \nu_s \qquad (3.34)$$

where the loss frequency in the steady-state is, in general, a function of gas pressure and temperature, beam current, and electron and ion densities and their gradients. (In the following, the gas temperature will be considered constant at 300° K.) For ν_s a function only of pressure, which is taken as a power law dependence,

$$\nu_s = a p^b \qquad (3.35)$$

then

$$n_s / i = K p / \nu_s \sim p^{1-b} \qquad (3.36)$$

The ratio n_S/i is found from the slope of the linear plot of n_S vs i at a fixed pressure, then b is evaluated from a plot of log (n_S/i) vs log p. Cases have been observed in which ν_s is constant for low ionization levels, but is a function of n_S at larger n_S. Then the data have been found to obey a relation of the form

$$i = A n + B n^c \qquad (3.37)$$

where A is the reciprocal of n_S/i in the linear regime. With this relationship, the entire beam current dependence at a fixed pressure can be characterized by only three number, the coefficients A and B and the exponent c.

In the linear regime, the time-resolved electron density rises toward n_S after the irradiation has begun according to

$$n_R(t) = n_s(1 - e^{-\nu_R t}) .$$

(3.38)

Following a beam pulse of duration T, the density in the after-glow falls according to

$$n_A(t) = \left\{ n_s(1 - e^{-\nu_R T}) \right\} e^{-\nu_A (t-T)}$$

(3.39)

If n_S is sufficiently large to lie in the non-linear regime, Equations 3.38 and 3.39 are no longer valid. One can evaluate $_\theta$ in this case by studying the early portion of the electron density rise. This is done by replacing n_S in 3.38 with the extrapolation of the linear density to the beam current actually employed in the transient experiment:

$$n_R(t) = i/A \ (1 - e^{-\nu_R t})$$

(3.40)

ν_R is then found from the characteristic frequency at early times, that is, for t' such that $n_2(t < t')$ is linear.

The transient frequencies are evaluated from the time-resolved densities by the usual graphical techniques. If $\nu_j ,(j=A,R)$ varies as p^b, where b is evaluated from the steady-state data, one is tempted to identify that transient frequency with ν_s . To establish this identity, calculate K_j, which is defined by

$$K = \nu_j \ n_s/ip$$

(3.41)

64.

(<u>Cf</u>. Equation 3.36). If K_j is independent of pressure, and has
a numerical value in reasonable agreement with the predictions
of K given in Table I, then one may safely assume $\nu_j = \nu_e$, $K_j = K$.
All subsequent distinctions between the transient and steady-state
values may then be used without further distinction.

If ν_4 is a strong function of electron temperature, then
the result $\nu_4 = \nu_e$ implies a common temperature (T_{gas}) for the
electrons in both the steady-state and afterglow experiments
(Section III.B). In fact, if the electrons were epithermal in
the steady-state, one could expect ν_4 to change with time in the
afterglow as the electrons cool; thus the afterglow decay of
electron density would not appear to be exponential.

The complete general equations describing the production
and loss of charged particles in the cavity may be written for
ions as

$$\frac{\partial X_j}{\partial t} = P_j + D_{j,eff} \nabla^2 X_j - \alpha_{ej} n_e X_j - \alpha_{ij} X_j X_k \qquad (3.42)$$

and for electrons as

$$\frac{\partial n_e}{\partial t} = P_e + D_{e,eff} \nabla^2 n_e - \nu_a n_e - \alpha_{ej} X_j n_e \qquad (3.43)$$

Here X_j is the j<u>th</u> species of ion, P_j and P_e are production rates
for ions and electrons. $D_{j,eff}$ and $D_{e,eff}$ are the effective
diffusion coefficients for ions and electrons, and the other terms
are as defined in earlier sections. Equations 3.42 for each X_j

and 3.43 form a set of simultaneous non-linear partial differential equations which cannot in general be solved in closed form. Solutions can be obtained by rewriting these equations as difference equations, then solving the set numerically as a function of space and time on a high-speed electronic computer. In general, computer programs of this magnitude were outside the scope of the present contract, so that other means have had to be devised to obtain information from the measurements.

The technique used most frequently in the present work has been based on the approximation that the spatial distribution of all particles is characteristic of the fundamental diffusion mode; thus

$$X_j \approx X_{jo} \, J_o \left(2.405 \frac{r}{R} \right) \, \sin \frac{\pi z}{h} \tag{3.44}$$

where R,h are the radius and height, respectively, of the experimental cavity. This technique allows 3.42 and 3.43 to be rewritten as total differential equations:

$$\frac{d X_{j,o}}{dt} = P_{jo} - \frac{D_{j,eff}}{\Lambda_{11}^2 p} \cdot p \, X_{jo} - \alpha_{ej} n_{eo} X_{jo} - \alpha_{ij} X_{jo} X_{ko} \tag{3.45}$$

$$\frac{d n_{e,o}}{dt} = P_{eo} - \frac{D_{e,eff}}{\Lambda_{11}^2 p} \cdot p \, n_{eo} - \nu_a n_{eo} - \alpha_{ej} X_{jo} n_{eo} \tag{3.46}$$

66.

The subscript "0" applied to a quantity is defined by

$$N_o(t) = \frac{\int_c N(\vec{r},t) \, J_o(2.405\frac{r}{R}) \, \sin \frac{\pi z}{h} \, dv}{\int_c J_o^2(2.405\frac{r}{R}) \, \sin^2 \frac{\pi z}{h} \, dv} \qquad (3.47)$$

where the integrals extend over the volume of the cavity.

To evaluate a specific reaction rate coefficient, one chooses experimental conditions which cause the desired reaction to predominate. Thus at high pressures and low ionization levels, the electron equation (3.46) reduces to

$$\frac{dn_{eo}}{dt} = P_{eo} - \mathcal{V}_a \, n_{eo}, \qquad (3.48)$$

which, by virtue of its linearity, can be extended to all other coefficients in the Fourier-Bessel expansion and eventually to the summation of these coefficients into the original quantities:

$$\frac{dn_e}{dt} = P_e - \mathcal{V}_a \, n_e . \qquad (3.49)$$

For a spatially uniform source term, as is the case in the present experiments, n_e is also uniform, and the relationship between Δf and n_e is given by

$$n_e \; (cm^{-3}) = 10^4 \, \Delta f \; (kcps) \qquad (3.50)$$

From transient measurements $\mathcal{V}_a$ can be determined; steady-state measurements then give P_e.

At higher ionization levels at high pressures, electron-positive ion recombination can also be studied. The pertinent

rate equation still refers to uniform spatial distributions of particles, since recombination will not destroy the spatial uniformity:

$$\frac{dn_e}{dt} = P_e - \gamma_a n_e - \alpha_{ei} X_j n_e \qquad (3.51)$$

In these measurements, the actual ion density X_j is usually not identical with n_e, due to the presence of other ions. A useful technique for steady-state measurements involves the use of mass spectrometer ion currents, in the following way. From (3.51) in the steady-state,

$$\frac{P_e}{n_e} = \gamma_a + \alpha_{ei} X_j \qquad (3.52)$$

A plot of the ratio P_e/n_e vs X_j can be made, using measured values of n_e and X_j, and computed values of P_e (usually Kpi). If the mass spectrometer ion current is known only in relative units, then such plots at least identify electron-ion recombination as the responsible process. If an absolute calibration of the ion current has been obtained, so that X_j is known in units of ions per cm^3, α_{ei} can be evaluated from the ratio of slope to intercept of the straight-line plot resulting from (3.52).

At low pressures, where diffusion becomes important, the particles have a spatial distribution midway between the uniform distribution imposed by the beam and that of the fundamental diffusion mode. In the absence of the complete calculation, we have resorted to the fundamental-mode approximation (Equation 3.44). This is particularly justified for electrons, since the measured frequency shift is dominated by the contribution from the funda-

mental-mode component of the actual electron distribution. To
see this in more detail, consider a fictitious electron density,
$n(\bar{r},t)$ expressed as a Fourier-Bessel series with equal coefficients.
The net frequency shift is then given by $\Delta f = \sum_{k\ell} \Delta f_{k\ell}$ where

$$\Delta f_{k\ell} = C \int_0^h \int_0^R J_3(\alpha_k \tfrac{r}{R}) \, J_1^2(3.832 \tfrac{r}{R}) \, \sin(\tfrac{\ell \pi z}{h}) \sin^2(\tfrac{\pi z}{h}) r \, dr \, dz \quad (3.54)$$

α_k is the kth zero of $J_0(x)$ and C is a constant. The Table
below gives $g_{k1} \equiv |\Delta f_{k\ell} / \Delta f_{11}|$. Consideration of this table
along with the fact that the Fourier-Bessel coefficient for the
fundamental mode $(k = \ell = 1)$ of a physically realizable density
distribution is always larger than any of the higher order
coefficients justifies the inclusion of only fundamental-mode
contributions to the frequency shift.

TABLE II

RELATIVE FREQUENCY SHIFT CONTRIBUTIONS FROM
WEIGHTED FOURIER-BESSEL MODES

k \ ℓ	1	3	5	7	
1	1.000	.200	.029	.001	(Symmetry requires
2	.230	.046	.007	.000	that even-ℓ contributions
3	.146	.029	.004	.000	vanish)
4	.001	.000	.000	.000	

REFERENCES (Chapter III)

Allis, W.P. and D. J. Rose, Phys. Rev. 93, 84 (1954)

Archer, D.H., General Electric Company, Tempo RM 63 TMP-45, November (1963)

Bakish, R., Introduction to Electron Beam Technology, (John Wiley, 1962) p. 436

Bates, D.R., Proc. Roy. Soc. (London) 190, 217 (1949)

Bethe, D.A., Handbuch der Physik XXIV, 517 (Springer, 1936)

Biondi, M.A. and S.C. Brown, Phys. Rev. 75, 1700 (1949)

Chanin, L.M., A.V. Phelps and M.A. Biondi, Phys. Rev. 128, 219 (1962)

Fowler, R.G. Handbuch der Physik XXII, 209 (Springer, 1956)

Frost, L.S. and A.V. Phelps, Phys. Rev. 127, 1621 (1962)

Hasted, J.B., Physics of Atomic Collisions, Butterworth, Washington (1964)

Jeans, J., The Dynamical Theory of Gases, Fourth Edition, Dover, New York (1954)

Jesse, W.P., Phys. Rev. 109, 2002 (1958)

Jesse, W.P. and J. Sadauskis, Phys. Rev. 90, 1120 (1953)

Kasner, W.H. and M. Biondi, Phys. Rev. 137, A317 (1965)

McDaniel, E.W., Collision Phenomena in Ionized Gases, John Wiley, New York, (1964)

Nelms, A.T., U.S. Bureau of Standards, Circular No. 577 (1957)

Oskam, H.J., Philips Research Report 13, 335, 401 (1958)

Pack, J.L. and A.V. Phelps, J. Chem. Phys. 44, 1870 (1966)

Phelps, A.V. and S.C. Brown, Phys. Rev. 86, 102 (1952)

Sayers, J., Proc. Roy. Soc. (London) A-169, 83 (1938)

Stewart, D.T., Proc. Phys. Soc. (London) A-69, 437 (1956)

70.

TABLE III

Observed Bands and Their Identification

λ (observed)	Identification	λ observed	Identification
3120	2P (3,2)	3999	2P (1,4)
3135	2P (2,1)	4059	2P (0,3)
3159	2P (1,0)	4091	2P (4,8)
*3275	2P (4,4); 2P(3,3)	4141	2P (3,7)
*3309	2P (2,2); 1N(2,0)	4200	2P (2,6)
3340	2P (1,1)	4239	1N (1,2)
3371	2P (0,0)	4278	1N (0,1)
*3463	2P (4,5); 2P(3,4)	4346	2P (0,4)
3501	2P (2,3)	4415	2P (3,8)
3537	2P (1,2)	4488	2P (2,7)
3578	2P (0,1)	4574	2P (1,6)
3660	Unidentified	4656	1N (1,3)
3671	2P (3,5)	4667	2P (0,5)
3710	2P (2,4)	4709	1N (0,2)
3755	2P (1,3)	4813	2P (2,8)
3804	2P (0,2)	5230	1N (0,3)
3894	2P (3,6)		
3914	1N (0,0)		
3943	2P (2,5)		

the wavelength at the peak intensity is given, and both over-
lapping bands are identified. All other bands are degraded to the
violet, and are listed by the wavelength of the bandhead. Except
for a single unidentified band at 3630 Å, all other bands have
been assigned to either the N_2 Second Positive or the N_2^+ First
Negative system. The absence of N_2 First Positive bands is in
keeping with the observations of other workers [Davidson (1964),
Fan (1956)] on the low intensity of the N_2 First Positive bands
excited by fast electron bombardment.

As a further verification of the band identifications, the
relative response of the system as a function of wavelength has
been determined from the measured intensity distributions using
a technique described in Section II.F. The identified nitrogen
bands, when compared with the theoretical intensity distributions,
can be made to lie on a smooth curve by a suitable normalization of
of each of the common upper vibrational levels. Figure 2.11 shows
data from a high pressure nitrogen beam experiment together with
a similar treatment of several multiplets measured in a mercury
capillary discharge, using published intensity ratios [Crosswhite
(1957)], as a secondary verification of the reasonableness of the
results. The smoothness and general agreement of the shape of
the curve with expectations based on the known photomultiplier
response and grating blaze suggest that the identifications are
correct.

C. Emission Intensities

The only published quantitative experimental data with which one can compare the emission intensities reported here are from Davidson and O'Neil (1964). Air-like mixtures of N_2: O_2 at 5 Torr and higher total pressures were bombarded by 50 kev electrons at high current densities in their experiment. Their reported intensities are integrated intensities rather than peak heights as in the present report. However, the ratio of peak height to integrated intensity should be reasonably constant over the limited wavelength interval of a given band system. This fact has been confirmed for a few bands in this laboratory as well as by Brocklehurst [1964]. Therefore the intensity comparisons of the various 2P bands between Davidson's results and those pre- sented here can properly be made. Furthermore, one would expect the excitation due to 50 kev electrons to be similar to 1.5 Mev electrons, [Davidson, 1964].

From the air data shown in Figure 4.3, emission intensities at 5 Torr have been determined and are listed in Table IV. The 2 P intensities observed by Davidson have been normalized to agree at the 2P (0,0) band (3371 $\overset{o}{A}$) and are also tabulated there. The last column of Table IV lists the relative intensities predicted by Bates [1949] under the assumption that the parent state concerned is populated by direct electron excitation from the ground state of the neutral molecule. Bates' 2_oP intensities are also normalized to the 5 Torr data at 3371 $\overset{o}{A}$.

RELATIVE INTENSITIES OF SECOND POSITIVE BANDS

TABLE IV

Identification	$\lambda(\overset{o}{A})$	5 Torr Intensities	Davidson	Bates
2P(1,0)	3159	2600	–	2340
2P(0,0)	3371	3200	3200	3200
2P(1,2)	3537	690	668	634
2P(0,1)	3577	2250	2260	1970
2P(2,4)	3710	155	132	127
2P(1,3)	3755	600	566	514
2P(0,2)	3804	770	821	710

In order to compare 1N and 2P intensities with those of Davidson, it is necessary to compute the ratio of the peak intensity to the area under the band for each of the band systems and correct Davidson's intensities accordingly. This has been done from measurements made in the laboratory; the ratios of peak heights to integrated area are 0.4 for the 3371 $\overset{o}{A}$ 2P band and 0.28 for the 1N band at 3914 $\overset{o}{A}$. With this information Davidson's integrated intensites have been converted to peak heights and are listed in Table V. Bates' values for electron excitation from the ground state of the neutral molecule are also listed in Table V , after normalization to the measured 3914 $\overset{o}{A}$ intensity for this table.

The rather good agreement, especially in the 2 Positive intensities, with both the measured values from Davidson and the theoretical values from Bates displayed in Tables IV and V suggests several conclusions.

RELATIVE INTENSITIES OF FIRST NEGATIVE BANDS

TABLE V

Identification	$\overset{o}{A}$	5 Torr Intensities	Davidson	Bates
1N(0,0)	3914	1700	2090	1700
1N(1,2)	4237	32	-	63.5
1N(0,1)	4278	330	-	480
1N(0,2)	4709	45	100	71

First, the procedure outlined above for the computation of the relative spectral response curve, Figure 2.11, is reasonably valid. Second and more important, the agreement lends credence to the theory that the light observed from both the 2 P and 1 N band systems is produced by direct excitation of ground state neutral molecules.

Another test for the direct excitation mechanism was made by examining the afterglow of both the 1 N and 2 P emission. The output of the photomultiplier was applied directly to the 1 Megohm input of a Tektronix 545 oscilloscope. The Van de Graaff beam was pulsed periodically on for 15 milliseconds, off for 10 milliseconds. From photographs of the traces it would have been possible to detect afterglows with decay times of 2 milliseconds or longer. Measurements in pure nitrogen (no oxygen added) at 5 and 12 Torr failed to reveal any afterglow light from nitrogen band systems which decayed at least this slowly. (The cyanogen bands, however, were observed to have afterglow lifetimes of the order of one second at 12 Torr.) Thus it must be concluded that the B $^2\Sigma$ and C $^3\pi$ states are not populated by long-lived

processes, in keeping with their assumed excitation by the
electron beam.

D. Collisional De-excitation of $B\ ^2\Sigma$ and $C\ ^3\pi$ States

Measurements have been made of the dependence of the peak
intensities of various bands as a function of pressure and
chemical composition of the irradiated gas and of Van de Graaff
beam current. From these measurements one can expect to obtain
some indication of the processes by which a given excited state
is populated and depopulated.

The intensity of the 3914 Å First Negative (0,0) band has
been measured in nitrogen and 4:1 ("airlike") mixtures of $N_2:O_2$
as a function of beam current and gas pressure. In nitrogen, the
intensity is linear with Van de Graaff current up to the highest
currents used, 1 milliampere, over the pressure range 1 to 10 Torr,
as illustrated in Figure 4.4. At a fixed beam current, the
intensity increases smoothly with pressure, as shown in Figure 4.5,
and exhibits the well known non-linear behavior associated with
collisional quenching [Mitchell, 1961].

The 3914 Å band has also been studied in 4:1 mixtures of
$N_2:O_2$. At 10 Torr, the intensity is also linear with beam currents
less than 1 milliampere, but departs from linearity in this
current range at lower pressures, as shown in Figure 4.6. The
variation of intensity in the linear region with total "air"
pressure at a fixed beam current is shown in Figure 4.7.

From the theory developed in III.D one can extract col-
lisional de-excitation coefficients from data such as those

shown in Figures 4.5 and 4.7. The intensity I_{jk} of a given band of frequency ν_{jk} was shown to be given by (Equation 3.25)

$$I_{jk} = A_{jk} N_j = \frac{K_j \, p_N \, i}{A_j + C_N \, p_N + C_o \, p_o} \tag{4.1}$$

where

A_{jk}	=	Einstein spontaneous emission coefficient for the transition
N_j	=	Population density of state j
K_j	=	Production coefficient for state j
p_n, p_o	=	Partial pressures of N_2, O_2
A_j	=	Reciprocal of radiative lifetime of state j
$C_n p_n$, $C_o p_o$	=	De-excitation frequencies for collisions with N_2, O_2 molecules.

In pure N_2 (and in N_2 with a trace of O_2 for cyanogen quenching) the quenching coefficients for the 2P and 1N systems are found from the ratio of slope to intercept R_n of a plot of p_n/I vs p_n, such as Figure 4.8; (Equation 3.26).

$$\frac{p_N}{I} \sim A_j + C_N \, p_N \tag{4.2}$$

From Equation 3.27, this yields

$$\tag{4.3}$$

$$C_N = R_N \, A_j$$

In binary $N_2:O_2$ mixtures

$$\frac{p_N}{I} \sim A_j + C_N \, p_N + C_o \, p_o \tag{4.4}$$

In airlike mixtures, for which $p_n = 4p_o$, so that the total pressure $p_t \cong p_n + p_o$ can be written

$$p_N = 0.8\, p_T \quad , \qquad p_o = 0.2\, p_T \tag{4.5}$$

Equation 4.4 becomes

$$\frac{p_N}{I} \sim A_j + (0.8\, C_N + 0.2\, C_o)\, p_T \tag{4.6}$$

Thus the ratio of slope to intercept for the airlike mixtures, R_a, can be written

$$R_\alpha = \frac{0.8\, C_N + 0.2\, C_o}{A_j} \tag{4.7}$$

so that

$$C_o = \frac{A_j\, R_\alpha - 0.8\, C_N}{0.2} \tag{4.8}$$

Substituting for C_n its value determined from the pure N_2 data (Equation 4.3), one obtains

$$C_o = 5 A_j (R_\alpha - 0.8\, R_N) \tag{4.9}$$

This analysis has been applied to the observed band intensities of the 2P and 1N systems of N_2. Figure 4.9 presents the results which have been obtained for the $v' = 0$ level of the N_2^+ 1N system, with both N_2 and O_2 as the quenching molecule, for the

$v' = 0$ level of the N_2 2P system with N_2 as the quenching molecule, and the $v' = 0, 1, 2$ levels of the 2P system with O_2 as the quenching molecule. Although other bands were observed, their relative intensities were too weak for accurate quantitative study. Values for A_j were obtained from Bennet and Dalby [1958].

There has been some confusion in the literature as to an appropriate definiation of the effective cross-section for quenching, $\sigma_{o,n}$. The definition used in this report is:

$$C_a p_a = \sigma_a \overline{V}_a N$$

where

$$\overline{V}_a = \left(V_N^2 + V_a^2 \right)^{1/2}.$$

The values for N_2 and O_2 as the quenching gases at 25° C and 1 Torr are

$$\overline{V}_N = 6.71 \times 10^4 \quad cm \cdot sec^{-1}$$
$$V_o = 6.50 \times 10^4 \quad cm \cdot sec^{-1}$$
$$N = 3.24 \times 10^{16} \quad cm^{-3}$$

yielding

$$\sigma_N = \frac{C_N p_N}{\overline{V}_N N} = \frac{C_N}{2.17 \times 10^{21}} \quad cm^2 \; ; \qquad \sigma_o = \frac{C_o p_o}{V_o N} = \frac{C_o}{2.11 \times 10^{21}} \quad cm^2.$$

The cross-section results of Davidson and O'Neil are of the form $\sigma = \pi \, r^2/4$, and therefore should be multiplied by 4 for $\pi r^2/4$ comparison with our data. If this same procedure is applied to Brocklehurst's data, then all three sets of results are substantially in agreement. There is a discrepancy between Brocklehurst and this laboratory of a factor of two in the cross-section for O_2 quenching of the 1 Negative (0,0) band. A possible cause of this discrepancy may be the effects of impurities present in Brocklehurst's unpurified O_2.

Some comments must be made regarding the very large cross-sections tabulated in Figure 4.9 for collisional de-excitation. First, quenching cross-section of this magnitude $(2 \times 10^{-14} \text{ cm}^2)$ have been reported for N_2 on the A $^2\pi$ state of N_2^+, the upper state of the transition responsible for the Meinel bands [Sheridan et al, 1962]. It is not too surprising to find these two states of N_2^+ behaving similarly. Second, evidence is offered in Chapter V, Section B.3, that the rate of quenching collisions between N_2 and N_2^+ (A $^2\pi$) is quite nearly equal to the rate at which N_4^+ ions appear to be produced from the reaction

$$N_2^+ + N_2 \rightarrow N_4^+ .$$
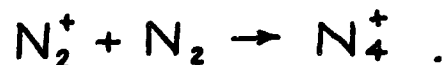
This suggests that the quenching mechanism may be a chemical reaction, rather than a simple excitation transfer, which might account for the large cross-section.

REFERENCES (Chapter IV)

Bates, D.R., Proc. Roy. Soc. (Lon.) 190, 217 (1949)

Bennet, R.G. and Dalby, F.W., J. Chem. Phys. 31, 434 (1959)

Brocklehurst, B., Trans. Faraday Soc. 60, 2151 (1964)

Crosswhite, H.M. and Dieke, G.H., "American Institute of Physics Handbook," Section 7, 120 ff (McGraw-Hill, 1957)

Davidson, G. and O'Neil, R., J. Chem. Phys. 41, 3946 (1964)

Fan, C.Y., Phys. Rev. 103, 1740 (1956)

Mitchell, A.C.G. and Zemansky, M.W., "Resonance Radiation and Excited Atoms" (Cambridge, 1961)

Sheridan, W.F., Oldenberg, O., and Carleton, N.P., "Atomic Collision Processes" ed. McDowell, M.R.C. (John Wiley, 1964)
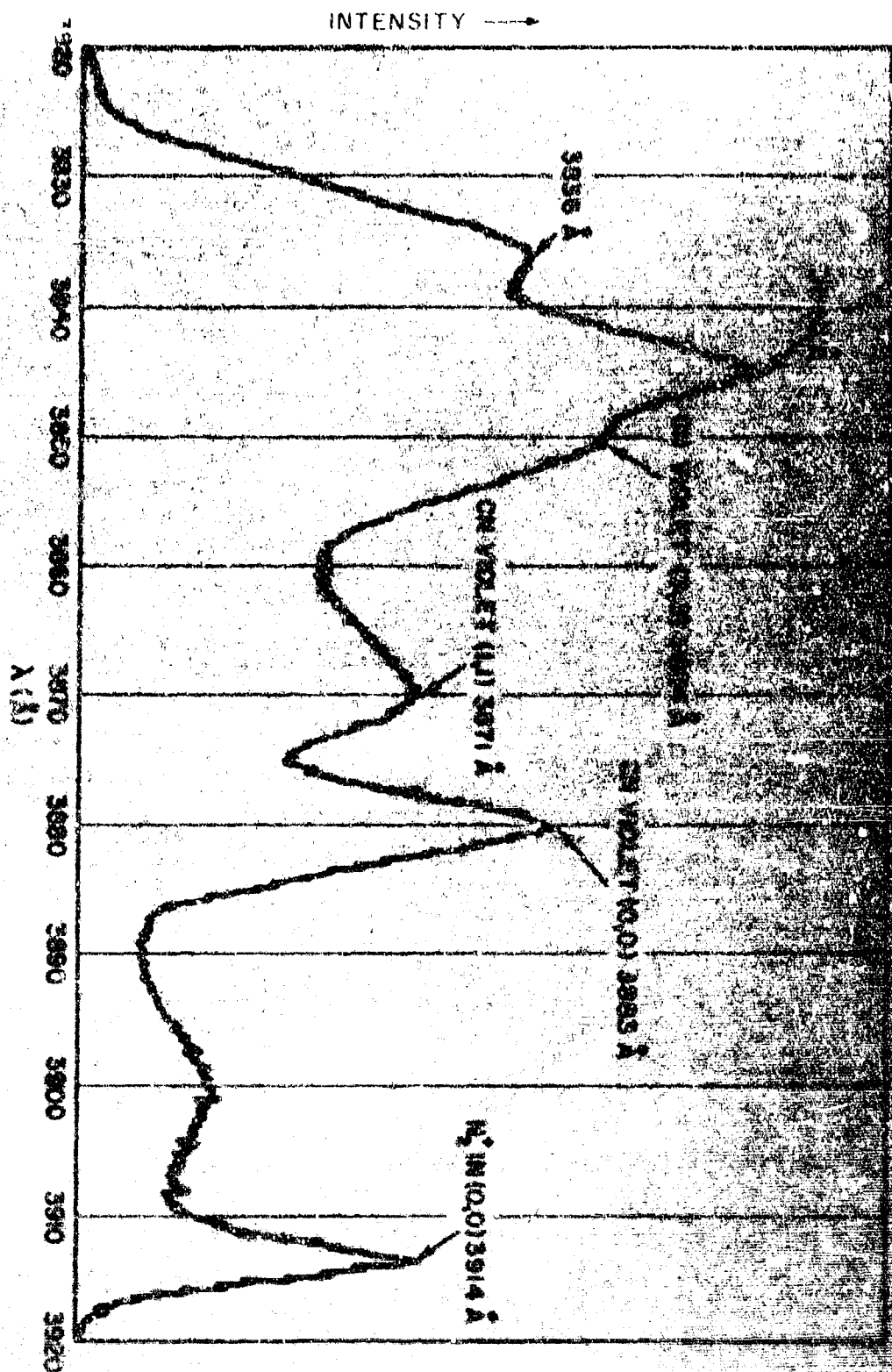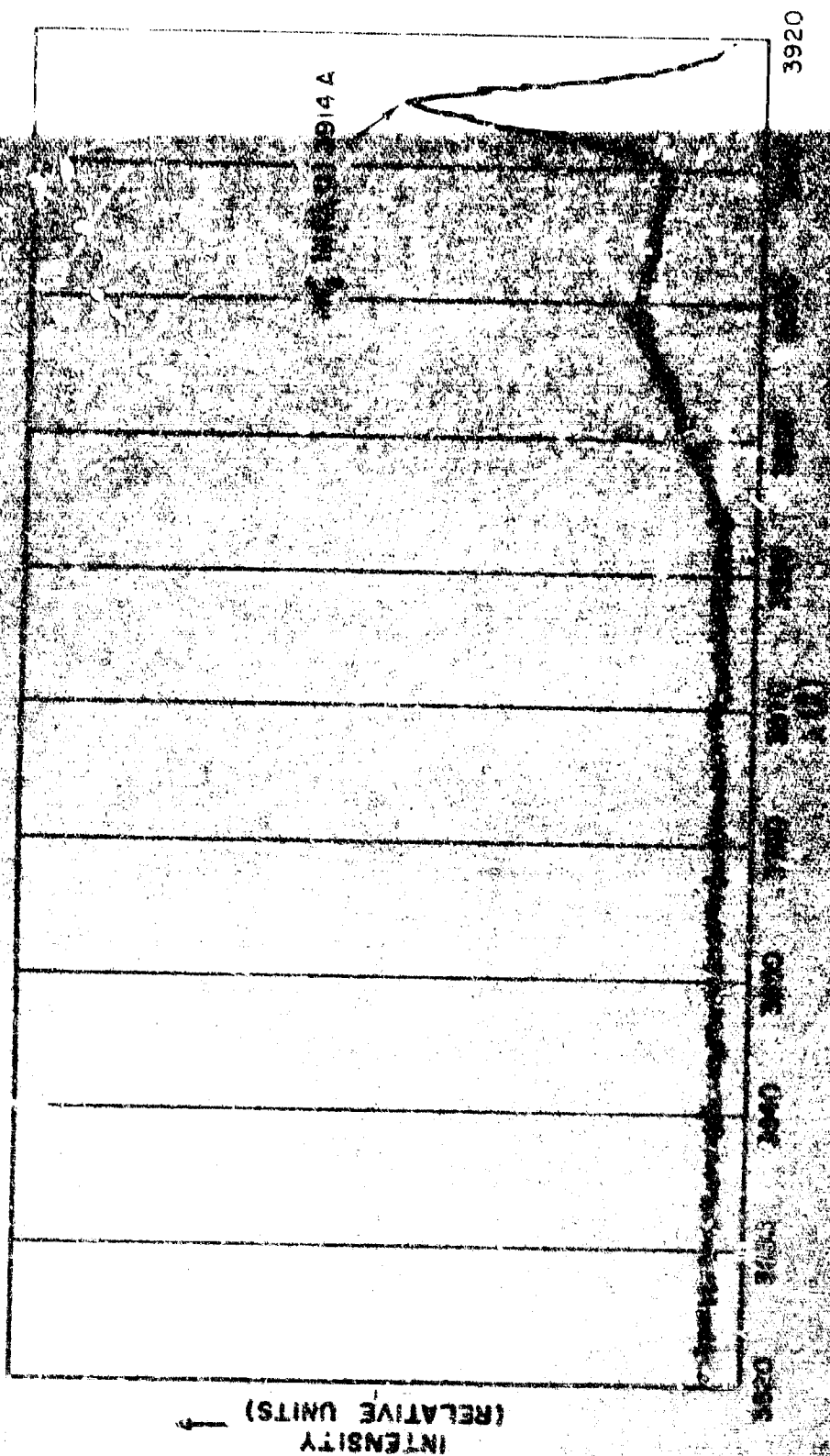
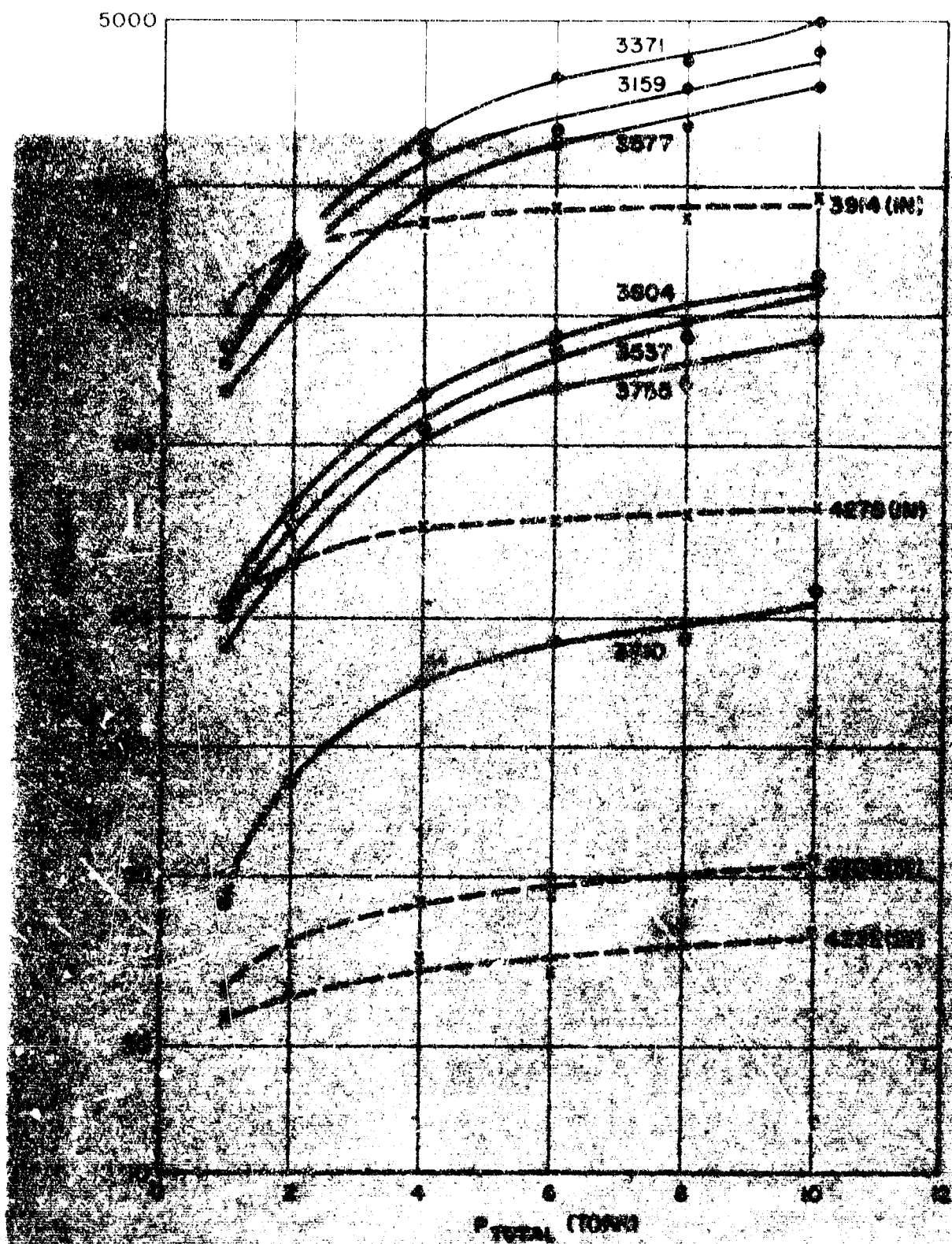FIGURE 4: SPECTRAL SCAN IN 10.5 TORR OF N_2 (3920 Å - 3820 Å)

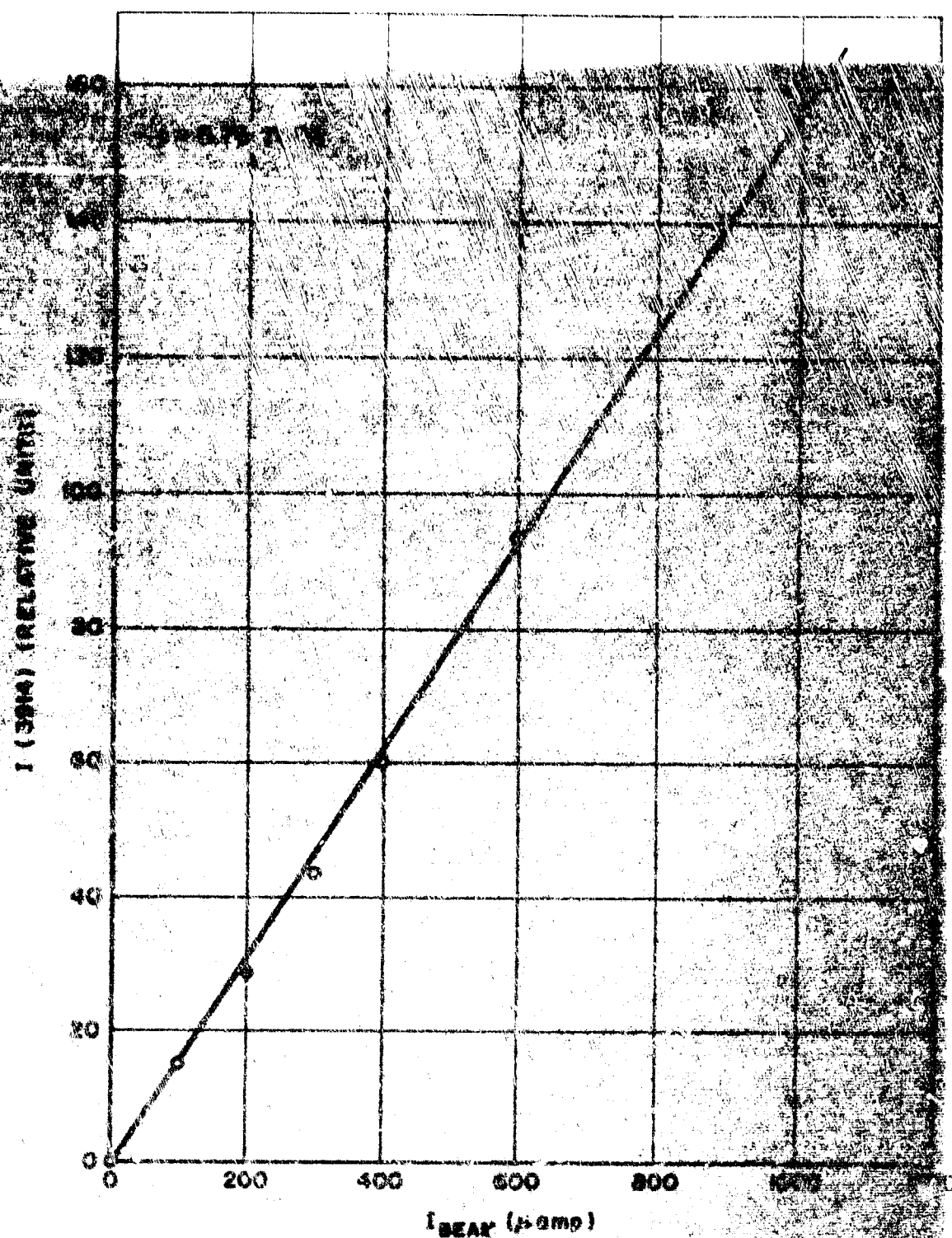FIGURE 4.2. RELATIVE INTENSITIES OF PROMINENT BANDS VS. PRESSURE IN MIXTURES $N_2 O_2$

FIGURE 4.4 — I (3914Å) VS. BEAM CURRENT IN NITROGEN

88.

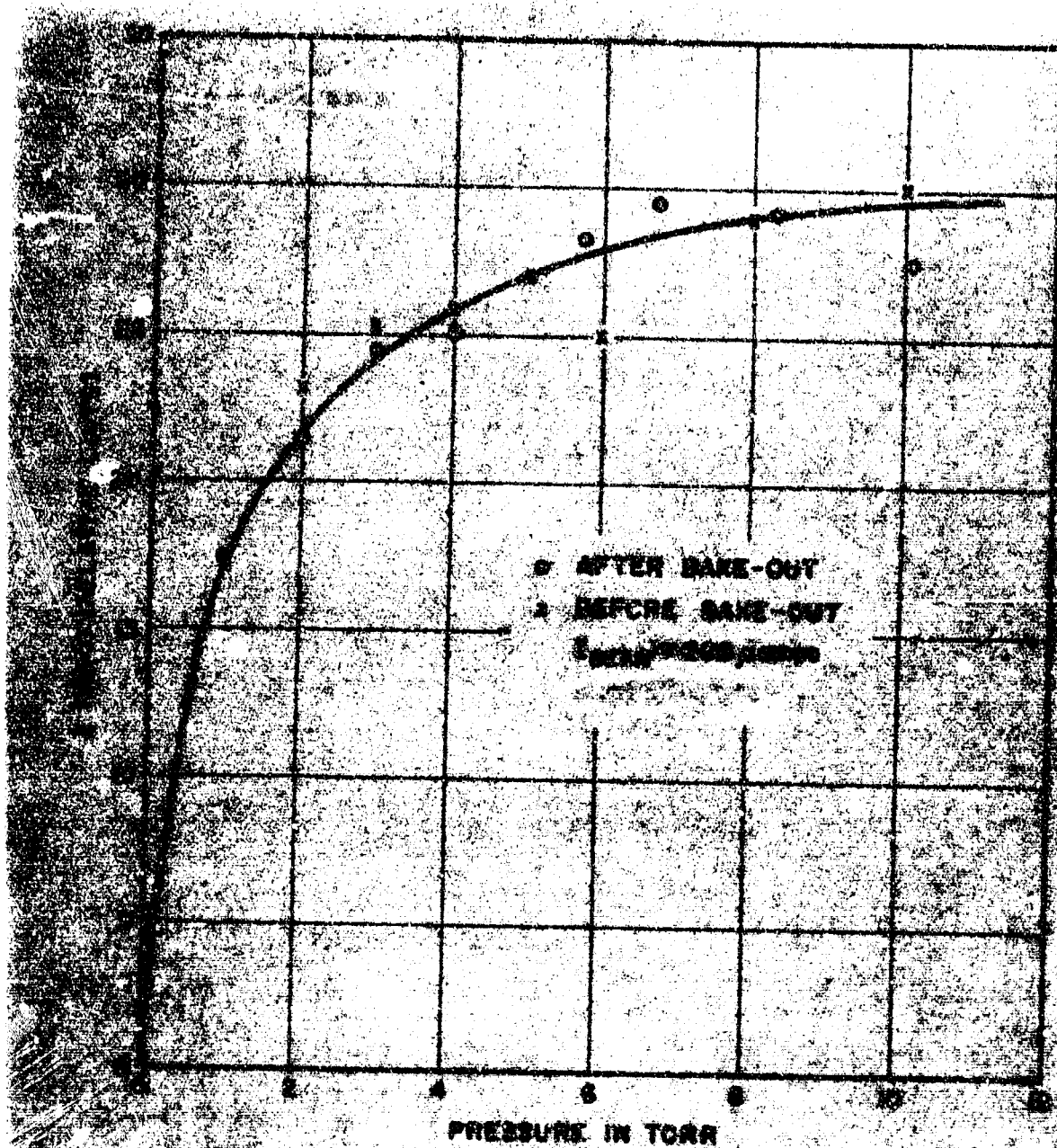FIGURE 4.5— I (3314) VS. PRESSURE IN "PURE" N_2
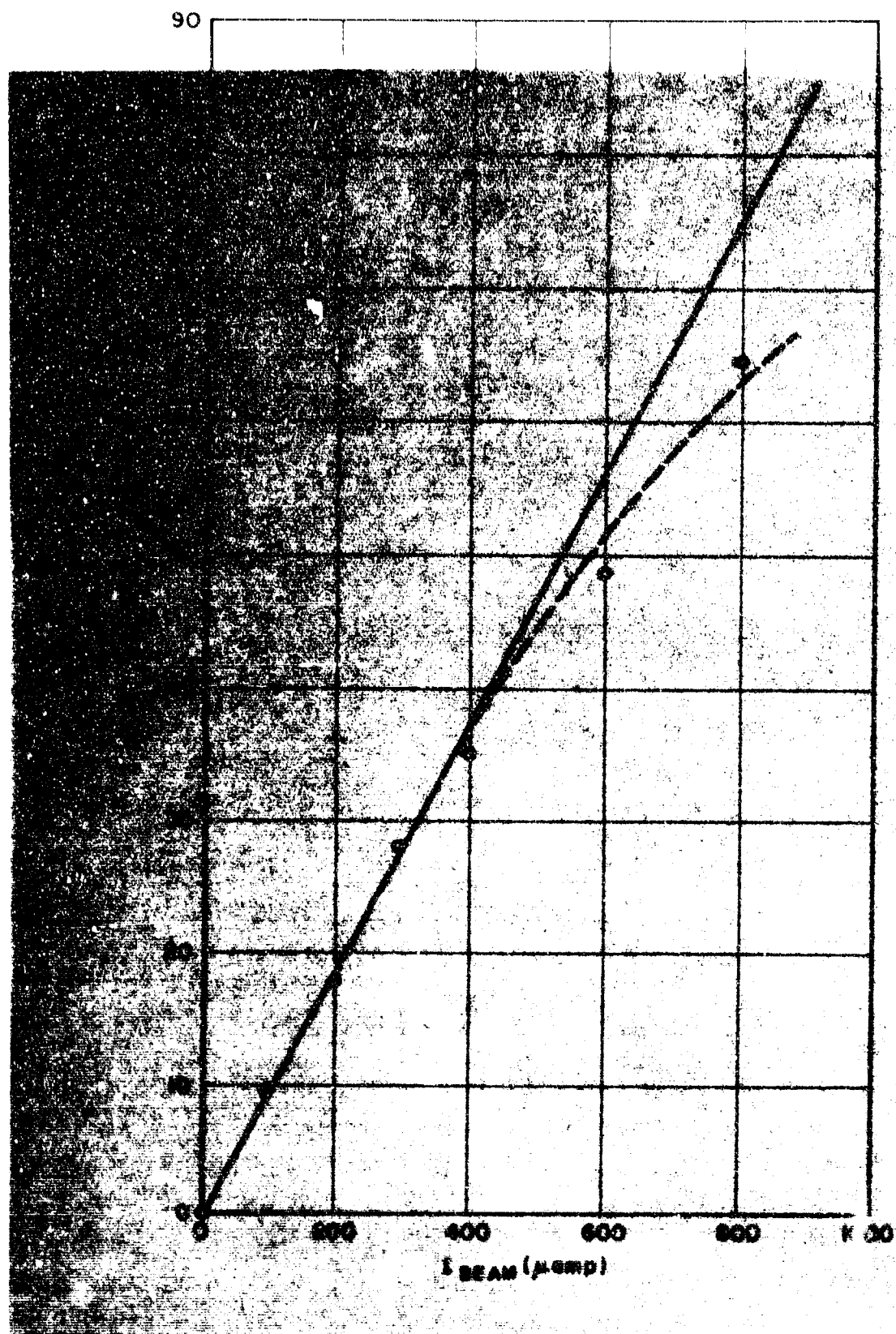
FIGURE 4.6 - I (3914) VS. I$_{BEAM}$ IN 4:1 N$_2$:O$_2$

FIGURE 4.7 - I (3914) VS. PRESSURE IN 4:1 $N_2:O_2$
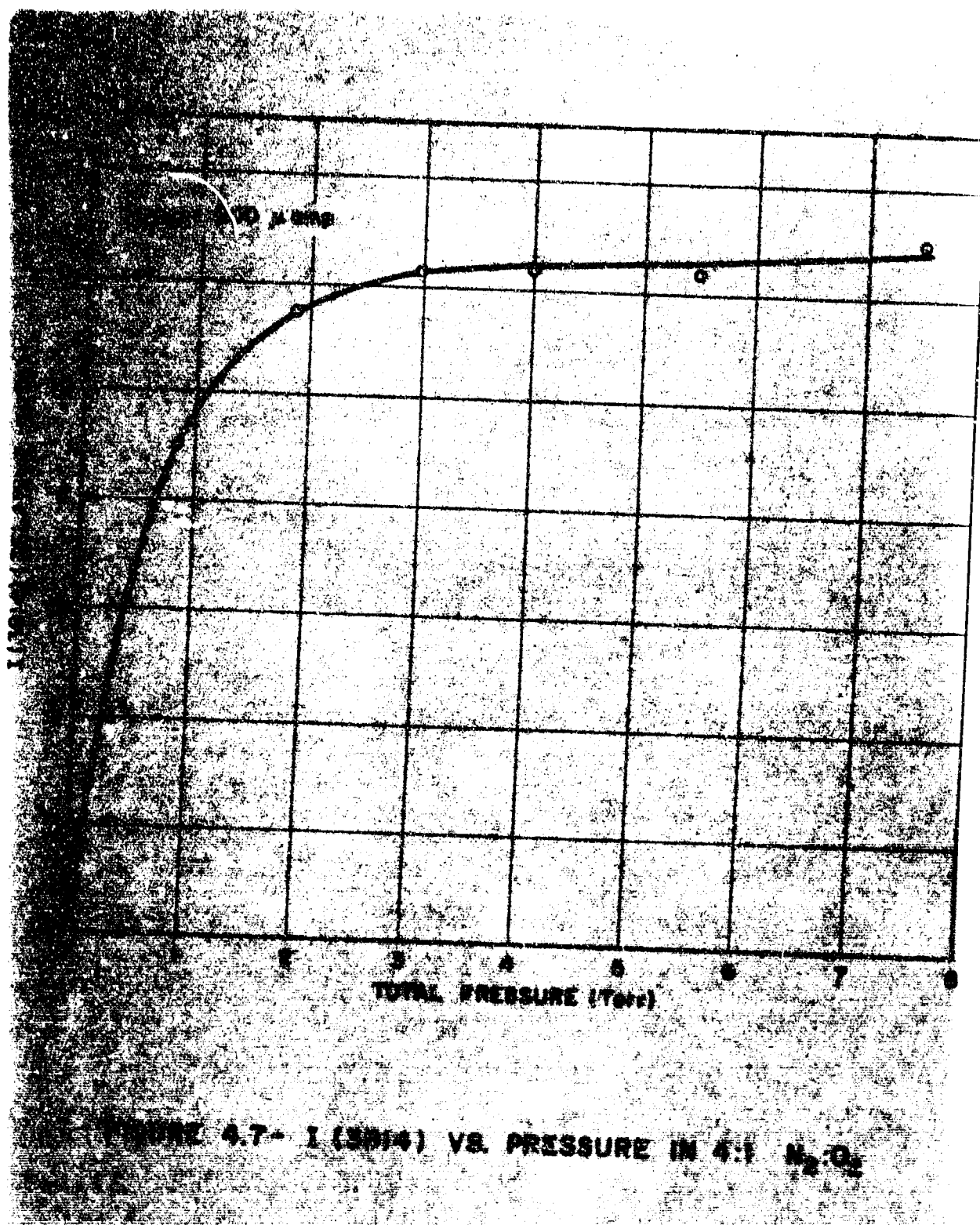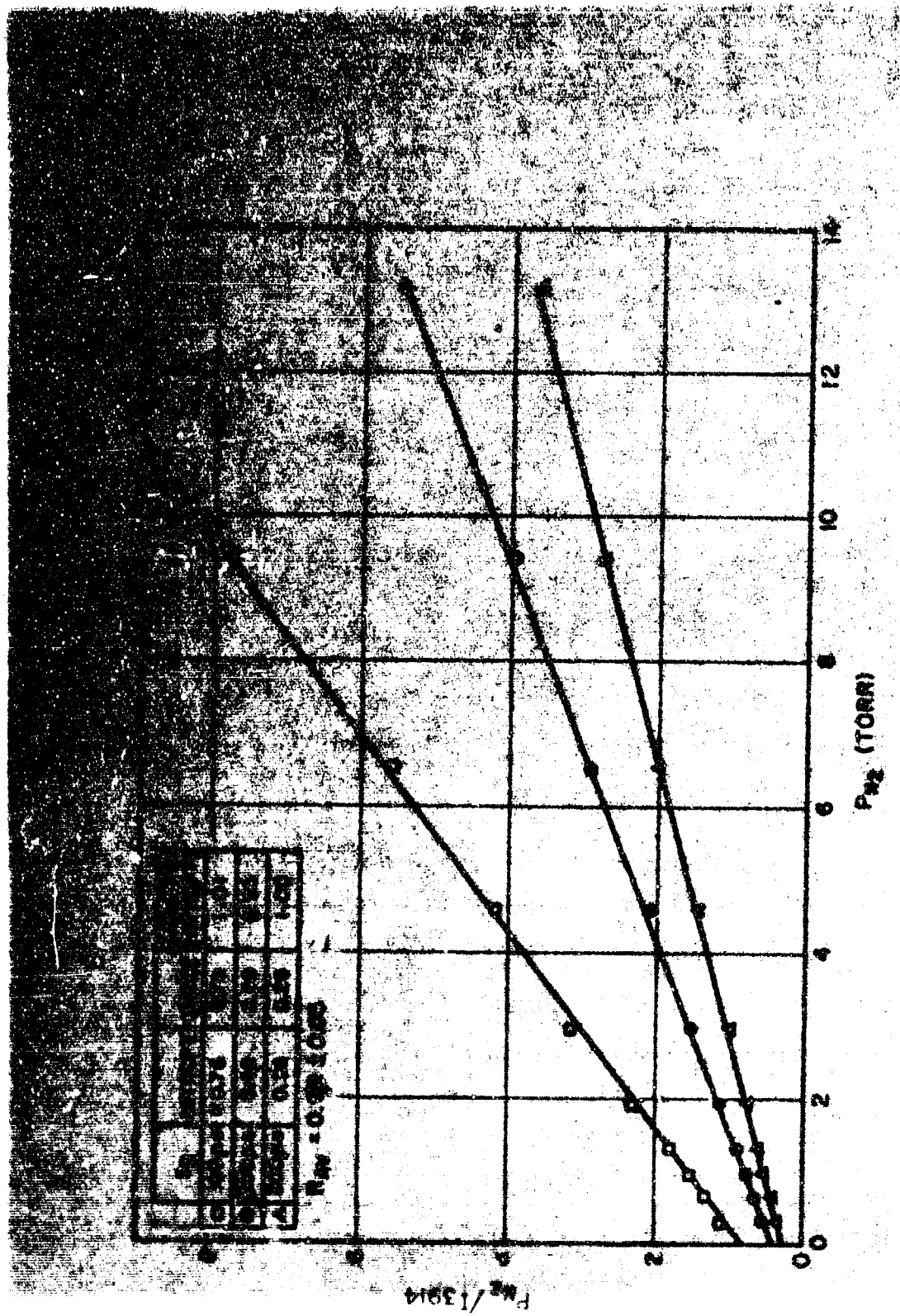
FIGURE 4.8 - 3914 Å QUENCHING PLOT IN NITROGEN

QUENCHER	k_q (10^9 sec^{-1})	k_q/k_o	τ (10^{-9} cm^3)	k_o/k_q	k_q (10^{-9} cm^3) (k_x)	k_o (10^{-9} cm^3) (k_x)
H₂	255 ± 34	400 ± 110	15 ± 0.9	200 ± 5010	191 ± 9	
		100 ± 0.4	38 ± 11	212 ± 10	50 ± 48	
O₂		0.5 ± 0.0	28 ± 18			
O₂		0.125 ± 2.5	18 ± 36			
H₂	80 ± 120	1.1 ± 0.1	151 ± 133	0.089	60 ± 50	
O₂		5 ± 3.1	15 ± 51	0.180	85 ± 85	

V.   EXPERIMENTAL RESULTS AND INTERPRETATIONS

A.   Introduction

This chapter presents the results of laboratory studies
of electron and ion densities in pure oxygen, pure nitrogen, and
4:1 (airlike) mixtures of $N_2:O_2$ subjected to ionizing radiation.
From these measurements and the optical studies described in
Chapter IV, many specific reactions which participate in the
deionization of the disturbed ionosphere have been identified,
and their mechanisms and rates have been determined. These
gases have afforded a relatively simple medium in which the
techniques developed for the lumped-parameter experiment were
tested. By avoiding the full complexity of atmospheric chemistry
at the early stages of this program, it has been possible to
concentrate on the techniques themselves, and on the kinds of
information which can be expected from these measurements. As
a result, the pure gas and simple mixture studies have established
the range of validity of the lumped-parameter measurements more
thoroughly, and more rapidly, than would have been possible had
the experiments been confined to air from the outset.

B.   Measurements in Oxygen

1.   Electron density measurements

Steady-state electron densities have been measured
during continuous irradiation in oxygen over the pressure range
0.025 to 10 Torr. Figure 5.1 shows several measurements of
the shift of resonant frequency in the cavity as a function of Van

de Graaff beam current, which typify the observations made at pressures above 0.3 Torr. The measured points lie on straight lines passing through the origin. The slopes of these lines, in kcps/μ amp, are shown as a function of pressure in Figure 5.2. The data for Figure 5.2 have been obtained under various conditions, including the use of both 0.0015" beryllium and 0.0005" titanium foil beam scatterers (corrected for relative transmission) with the cavity both baked and unbaked prior to the measurements. All data obtained in the baked cavity were reproducible even after prolonged irradiation of the gas at high beam currents. Similar experiments in the unbaked cavity show a permanent decrease in the ionization per unit beam current following the irradiation of a given gas load at high currents, probably due to contamination by the evolution of occluded impurities from the chamber walls.

From Figure 5.2 it can be seen that the measured values of the specific ionization are well approximated by a p^{-1} dependence at pressures greater than 0.9 Torr. From Section III.E, this implies that $\nu_s \sim p^2$.

Below 0.3 Torr, n_s is not linear with beam current. Instead, the measured frequency shifts appear as shown in Figure 5.3. At high beam currents, the data lie on straight lines which do not, however, intersect the origin. The low current data have been examined carefully to insure that the offset of the straight-line fit is not due to instrumental errors, but is in fact a reproducible, pressure-dependent phenomenon. The inherently non-linear nature of the electron loss process at low pressures is borne out in the transient results as well, as will be described below.

Transient electron density measurements were made in oxygen at both high and low pressures, using a pulsed beam with a repetition rate of either 10 or 1 per second. For the measurements described below, the beam remained on the cavity for times which varied between 10 and 90% of the beam switching cycle.

Measurements above 0.7 Torr were originally made with a beam duty cycle of 50%, that is, 0.05 seconds into the cavity and 0.05 seconds off. A typical afterglow decay obtained from these measurements is shown in Figure 5.4. The frequency shifts appear to fall exponentially early in the afterglow, but then deviate into a long-lived "tail." The frequency shift at which this deviation occurs is related, although erratically, to the pressure and to the gas history of the cavity since its most recent bakeout. If these measurements are repeated in the afterglow of a 0.01 second beam pulse, the tail disappears and the frequency shifts decrease exponentially for well over a decade, as shown by the circles in Figure 5.5. Furthermore, one can duplicate the short-pulse measurements by subtracting a constant frequency shift from the data obtained in the afterglow of the long pulse, such as those in Figure 5.4, as shown by crosses in Figure 5.5. This suggests that the afterglow frequency shifts can be described as the sum of an exponentially decaying component independent of beam duty cycle and a constant, or at least much more slowly varying, component related to the the duty cycle.

The loss frequencies obtained from the exponential decays at high pressures are shown in Figure 5.6 as a function of oxygen pressure, after correction for the cavity bandwidth.

Above 0.9 Torr, the data are well approximated by a p^2-dependence, as had been predicted from the steady-state measurements of specific ionization. The decay frequency can be expressed as

$$\nu = (2.12 \pm 0.15) \times 10^{-30} [O_2]^2 \; sec^{-1} \qquad (5.1)$$

It would be more desirable to have a much wider pressure range over which to deduce the decay frequency. Unforunately, the p^2 dependent loss process no longer controls the electron lifetimes below 0.9 Torr, and the decay frequencies above about 2.0 Torr are as large as or larger than the cavity bandwidth, thus restricting the range over which data may be obtained. From the steady-state measurements, however, one can infer that the p^2 process dominates the electron removal at least at pressures up to 10 Torr. Indirect evidence also exists for the persistence of the p^2 process at pressures as low as 25 millitorr with the same coefficient as that deduced from the data in Figure 5.6. This is discussed below in connection with the interpretation of the low pressure transient data.

The nonlinearity observed in the low-pressure steady-state data is seen in the transient measurements as well. Figure 5.7 shows typical time resolved measurements of electron density during the in-beam phase of a repetitively pulsed beam switching cycle; in this cycle, the beam spends 0.5 seconds in the cavity, 0.5 seconds off. The overshoot at early times characterizes all the measurements below 0.3 Torr, although the peak is more pronounced at the lower pressures, as can be seen from the figure. Following the overshoot, the electron density

decays toward the equilibrium value obtained in the steady-state
measurements. The decay of electron density in the afterglow
at low pressures is typified by the data shown in Figure 5.8.
At early times, the densities decay more or less exponentially
with time, but soon break away and fall at an increasingly rapid
rate at the late times.

The detailed behavior of the transient in-beam measure-
ments at low pressures is a very sensitive function of the duty
cycle of the electron beam. Figure 5.9 shows the effect of
varying the duty cycle from 10 to 90% at 0.1 Torr. In general,
the ratio of peak overshoot height to equilibrium in-beam density
decreases as the afterglow period is shortened.

2. Mass spectrometric observations

Ion measurements have been made in oxygen during
continuous electron irradiation over the pressure range 0.01
to 10 Torr. Studies above 1 Torr were performed early in the
experimental program. At that time, the mass spectrometer data
were not quantitatively reproducible, due to the presence of
inadequately shielded insulators in the ion lens chamber. These
insulators accumulated charge during the Van de Graaff irradiation
which defocussed the slow incident ions in an unpredictable way.
No quantitative information could be obtained concerning the
pressure and beam current dependence of the various ions during
that period, although the ion identifications appear to be
reliable. Not until the last quarter of the present program was
it possible to arrive at a design for the front end of the
spectrometer which was free of these charging problems, yet
provided the necessary operating characteristics. The quantitative

studies of mass-identified ions presented in this report have all
been performed during the last month of this program. These
latter studies were performed at pressures below 0.3 Torr; re-
examination of the high-pressure regime was not possible during
the time remaining on this contract.

Two detection systems were used during the earlier mass
spectrometer measurements. The dc current from the electron
multiplier could be read directly with an electrometer-tube
picoammeter. Alternatively, the ion current could be modulated
by a square-wave voltage applied to the ion lens, then the
modulated component of the ion current ac amplified and syn-
chronously detected. Both techniques were used for the positive
ion studies, and gave comparable results. For studies of negative
ion spectra, only the ac scheme could be employed because of the
high dc voltage (about 4.5 kv) on the electron multiplier dynode
with the spectrometer operating in the negative-ion mode.
Following the elimination of the spectrometer charging problem
mentioned above, there was insufficient time remaining to set up
the ac detection system, so that only positive ions were studied
during the last series of measurements.

At pressures in the range 1 to 10 Torr, several
positive ions were observed in pure oxygen. The largest ion
currents were observed for O_4^+ at these pressures. O_3^+ appeared
with about one-third to one-fourth the ion current observed for
O_4^+. Traces of O_2^+ were also observed during these measurements.
On several occasions at the higher pressures, possibly the
first observations of O_5^+ reported in the literature were made.

During this early period, mass scans were also made
in the pressure range 0.01 to 0.30 Torr. O_2^+ was the only
positive ion observed in this pressure range. Similar scans
for negative ions were also made during this period. A single
ion, O_2^-, was observed with a signal-to-noise ratio of about
5. It is possible that other negative ions were present in
appreciable density which were not seen due to the low sensitivity
which the instrument then had for negative ions. There is,
however, no reason to believe that other ions were indeed
present.

Since the modification of the mass spectrometer,
a series of measurements of positive ions was made in oxygen
below 0.1 Torr. As was the case earlier, only O_2^+ was observed
during continuous irradiation over this pressure range. Figure
5.10 shows several measurements of the O_2^+ ion current as a
function of beam current, shown on a logarithmic plot. It
can be seen that O_2^+ is not linear with beam current, which
would then be evidenced by a straight line of unit slope on
the graph, except for an "accidental" linearity somewhere
between 25 and 50 millitorr.

3. Discussion of Oxygen results

Consider first the electron density measurements at
high pressures. From the agreement between the pressure
dependence measured in the afterglow ($\nu_a \sim p^2$) and that
deduced from the steady-state n_s/i plots, it is reasonable to
assume that the dominant electron loss mechanism in both time
domains is the same. The afterglow decay frequencies yield
the value

$$\nu_a = (2.12 \pm 0.15) \times 10^{-30} [O_2]^2 \quad sec^{-1} \tag{5.1}$$

This is in excellent agreement with the value obtained by
Pack and Phelps [1966] for the frequency of three-body attach-
ment of electrons to neutral O_2 molecules at 300° K, of
$(2.0 \pm 0.2) \times 10^{-30}[O_2]^2 sec^{-1}$, and with that of Van Lint [1959]
of $2.1 \times 10^{-30}[O_2]^2 sec^{-1}$. From this numerical agreement, it
is reasonable to conclude that the reaction being studied is

$$e + O_2 + O_2 \rightarrow O_2^- + O_2 \tag{5.2}$$

The identification of O_2^- as the negative ion at low pressures
supports the reaction proposed in 5.2. This does not imply that
O_2^- is also the dominant ion at high pressures, for subsequent
ion chemistry may alter the identity of the ion produced in the
attachment process.

From the measured value of the decay frequency, the
ionization production coefficient can be evaluated as discussed
in Chapter III. From Figure 5.2, the specific ionization over
the pressure range 0.9 to 10 Torr is given by $(1.35 \pm 0.14) \times 10^3/p$

electrons/cm^3 μ a, referred to total current from the Van de
Graaff accelerator. In terms of actual flux of electrons at
the cavity, the specific ionization should be corrected by the
factor appropriate to the scattering foil used:

$$\frac{\lambda_{CAVITY} \ (\mu a/m^2)}{\lambda_{V.d.G.} \ (\mu a)} = 0.58 \pm 0.02 \tag{5.3}$$

This yields a corrected specific ionization at 1 Torr of

$$\left(\eta_{\lambda}\right) = (2.33 \pm 0.33) \times 10^5 \ electrons \left[cm^2 \ \tfrac{\mu a}{m^2}\right]^{-1} \tag{5.4}$$

From the decay frequency given by Equation (5.1) the production
coefficient is now evaluated; one finds

$$K = \frac{\nu_b \ (\eta/\lambda)}{p} = (5.1 \pm 0.1) \times 10^7 \left[cm^3 \ sec \ Torr \left(\tfrac{\mu a}{m^2}\right)\right]^{-1} \tag{5.5}$$

With the assumption of the value W = 30.9 ev/ion pair measured
by Jesse and Saudauskis [1953], the energy loss rate of 1.5 Mev
electrons per unit path length in oxygen at STP (Section III.B)
is

$$U = (2.1 \pm 0.4) \ kev/cm \tag{5.6}$$

which is to be compared with the theoretical value 2.2 kev/cm
computed by Nelms (1957).

At pressures above 0.9 Torr, it has been shown that
diffusion does not play an important role in electron removal.
As a consequence, for a spatially uniform electron-beam excitation
function the electron density will also be spatially uniform,

both during irradiation and in the afterglow. This justifies
the conversion of cavity frequency shifts to electron densities
by the relation

$$\eta = 10^{4} \times \Delta f(\text{kcps}) \qquad [\text{cm}^{-3}] \qquad (5.7)$$

implicit in which is the assumption of uniform electron density
(Section II.C).

As the pressure is reduced, one expects diffusion
to play an increasingly important role in electron removal.
Three-body attachment can be expected to persist down to the
lowest pressures, although it is no longer the dominant electron
removal mechanism. Nevertheless, the attachment process should
still produce appreciable densities of negative ions even at
the lowest pressure employed in these experiments. This
necessitates the use of the positive ion-negative ion ambipolar
diffusion treatment for oxygen (Section III.C), and the model
of the low-pressure oxygen plasma used to interpret the data
must follow the density of negative ions as well as of electrons
and positive ions.

From the mass spectroscopic results, it is apparent
that the only significant positive ion at pressures below 300
millitorr is O_2^+. The mass data also suggest that O_2^- is the
only negative ion to be considered. If a complete account of
the density of O_2^- is to be kept, some assumption must be made
regarding the lifetime-controlling processes for O_2^-. It is
reasonable to assume that O_2^- is produced by three-body attachment.
From Equation 3.13, diffusion cannot be the limiting removal
mechanism for the negative ion. Also, from the variation of

electron density with beam current, it is apparent that the negative ions must be lost in a non-linear process. This non-linear process is assumed to be mutual neutralization with O_2^+, that is

$$O_2^+ + O_2^- \rightarrow 2 O_2 \ . \tag{5.8}$$

For the purposes of the model, the production coefficient K and the three-body attachment frequency ν are assumed to have the values found at high pressures.

The model defined by the above consideration can be described by the system of equations

$$\frac{\partial n_e}{\partial t} = K p i - \beta p^2 n_e + D_a \left(1 + \frac{[O_2^-]}{n_e} \right) \nabla^2 n_e \tag{5.9}$$

$$\frac{\partial [O_2^-]}{\partial t} = \beta p^2 n_e - \alpha [O_2^+][O_2^-] \tag{5.10}$$

$$[O_2^+] = [O_2^-] + n_e \tag{5.11}$$

This set of equations can now be solved numerically on an electronic computer for the electron and ion densities as functions of space and time, using assumed values for D_a and $\alpha_{O_2^+;O_2^-}$. The electron densities obtained from the solution should then be convoluted with the square of the rf measuring field in the cavity, from which the frequency shifts are predicted which can then be compared with experiment. A computation of this magnitude was felt to be beyond the scope of the present program, so that exact solutions have not yet in fact been obtained. The complete numerical solutions are included in plans for future work, however.

104.

A great deal of information can be extracted from a
simplified analysis which proceeds from the substitution
$\nabla^2 n_e \rightarrow -n_e/\Lambda_{\scriptscriptstyle \parallel}^2$, where $\Lambda_{\scriptscriptstyle \parallel}$ is the fundamental diffusion
length for the cavity. (In this work, $\Lambda_{\scriptscriptstyle \parallel}^2 = 230$ cm^2.) With
this substitution, the steady-state model becomes

$$K p \lambda = \frac{D_a p}{\Lambda^2 p}\left(1 + \frac{[O]}{n_e}\right) n_e + \beta p^2 n_e \tag{5.12}$$

$$\beta p^2 n_e = \alpha_{\lambda\lambda}[O_2^+][O_2^-] \tag{5.13}$$

$$[O_2^+] = [O_2^-] + n_e \tag{5.14}$$

The error inherent in the assumption that all charged particles
are distributed in the fundamental diffusion mode can be seen
from Equation 5.13, where in essence a single species is assumed
proportional to the product of the other two. The error intro-
duced by this simplification can only be evaluated by comparison
of the solutions of the approximate model with the complete
solutions, when the latter have been obtained.

From the measurements of Sampson and Weissler [1965]
of the drift velocity of O_2^+ in oxygen, the zero-field mobility
of O_2^+ is 2.4 cm^2/volt sec. This corresponds to an ambipolar
diffusion coefficient D_a p = 110 Torr cm^2/sec at 300° K, or a
free diffusion coefficient for O_2^+ just half that value
(D_+ p = 55 Torr cm^2/sec), which is the value used in the
following computations. With the help of 5.14, Equation 5.12
can be written

$$\frac{D_a p}{\Lambda_{\scriptscriptstyle \parallel}^2 p}[O_2^+] = K p \lambda - \beta p^2 n_e \equiv G(\lambda) \tag{5.15}$$

G(i) has been calculated at 88 millitorrs from measured
electron densities. Using the D_a p given above, one can
then predict $[O_2^+]$ in density   units. This prediction is
compared with the values of O_2^+ ion current measured simul-
taneously with the electron densities used in the above
computation in Figure 5.11, where it can be seen that tne
linearity is excellent. This implies that the values for K
and β determined at high pressures are still reasonable below
100 millitorr.

Equations 5.12 and 5.13 can be combined to yield an
expression for the beam current as a function of electron
density:

$$\dot{\lambda} = \left[\frac{\beta \dot{\gamma}}{K} + \frac{D_a p}{2 \Lambda_n^2 p^x K} \right] n_e + \frac{D_a p}{2 \Lambda_n^2 p^x K} n_e \left(1 + \frac{4 \beta p^2}{\alpha_{ii} n_e} \right)^{1/2} \qquad (5.16)$$

A value for α_{ii} has been determined for one pressure and for a
single beam current. Figure 5.12 is a plot of Δf <u>versus</u> beam
current for oxygen at a pressure of 0.17 Torr. For i_b = 30 μ amp,
Δf = 106 kcps. Substitution of these values into 5.16 yields
a value α_{ii} = 9.86 X 10^{-8} cm^3/sec. Equation 5.16 can now be
plotted, as shown in Figure 5.13. The electron beam currents
required to produce electron densities of 5 X 10^5, 10^6, and
5 X 10^6 cm^{-3} have been calculated and are shown in Figure 5.13.
Experimental data are shown by open circles. The agreement
between experiment and calculation is quite good over the
pressure range shown with the use of a single value of α_{ii},
considering the inadequacies of the simplified model. The value
$\alpha_{ii} \approx$ 9.86 X $10^{-8} cm^3$/sec is in agreement with numbers reported
in the literature [Sayers, 1962]. The process is probably a

two-body recombination since the calculations agree so well
with the data over nearly two decades of pressure.

The values of the coefficients obtained from the
steady-state data can now be applied to the transient situation.
The time-dependent simplified model can be written

$$\frac{dn_e}{dt} = K p i - \frac{D_a p}{\Lambda_{\shortparallel}^2 p}\left(1 + \frac{[O_2^-]}{n_e}\right)n_e - \beta p^2 n_e \tag{5.17}$$

$$\frac{d[O_2^-]}{dt} = \beta p^2 n_e - \alpha_{ii}[O_2^+][O_2^-] \tag{5.18}$$

$$[O_2^+] = [O_2^-] + n_e \tag{5.19}$$

These equations apply when electrons are present as well as
positive and negative ions. From the increasingly rapid
electron removal rate in the afterglow, it is apparent that the
ratio $[O_2^-]/n_e$ becomes large as the electrons disappear. When
$[O_2^-]/n_e \gg \mu_e/\mu_- \approx 10^4$, Equations 5.17 through 5.19 are no
longer appropriate. Instead, one must set $n_e = 0$, then permit
the residual positive and negative ions to diffuse freely; thus,
for late times in the afterglow, Equations 5.18 and 5.19 must
be replaced by

$$\frac{d[O_2^+]}{dt} = \frac{d[O_2^-]}{dt} = \alpha_{ii}[O_2^+][O_2^-] - \frac{D_a p}{\Lambda_{\shortparallel}^2 p}[O_2^-] \tag{5.20}$$

Equations 5.17 through 5.20 have been programmed and
solved numerically on an IBM 1620 electronic computer for the
case of a transient experiment with a 50% electron beam duty
cycle (500 msec on, 500 msec off). Calculations were performed
for a beam current of 100 μamperes and oxygen pressures of 50,
100, 200, and 300 millitorrs, for the initial conditions

$n_e = [O_2^-] = [O_2^+] = 0$. The calculations trace n_e vs time during the in-beam phase of the cycle, then into the electron afterglow, using Equations 5.17, 5.18, and 5.19 . When $[O_2^-]/n_e \approx 10^4$, the calculation switches over to Equation 5.20 to compute the ion density decays. The residual ion densities at the end of the afterglow are then used as initial conditions for the next beam cycle. It was found that the calculations converged after two cycles for all cases tried.

The results of the calculations for the in-beam electron density are shown in Figures 5.14 through 5.17, for two pairs of values for α_{cc} ans $D_a p$. Agreement between theory and experiment is surprisingly good. In addition to supplying general qualitative agreement, the model capably predicts both the location and height of the electron density overshoot over the entire pressure range. There are still some limitations to the model, however, as can be seen from the afterglow results shown in Figures 5.18 through 5.21. Perfect agreement can hardly be expected, in light of the following weaknesses of this calculation:

(a) There is no reason to believe that n_e, $[O_2^+]$, and $[O_2^-]$ are spatially congruent. In fact, the differential equations indicate that they are not.

(b) The spatial variation of the electron beam has not been properly taken into account.

(c) It must be remembered that the solution

to the electron equation must be
convoluted with the square of the
cavity field before comparison
with experiments can be made.

The variation of the in-beam behavior of the time-resolved electron density at low pressures with electron beam duty cycle has been referred to in Section V.B.1 and Figure 5.9. The origin of this variation can now be understood immediately. As long as the afterglow time is short compared to the positive and negative ion lifetimes, the second and all subsequent beam cycles begin with a finite density of negative ions. This changes the initial diffusion coefficient from its value $2D_+$ at $t = \Delta t$ during the first cycle to $2D_+\left(1 + \frac{[O_2^-(R)]}{n_e(\Delta t)}\right)$, where $[O_2^-(R)]$ is the residual negative ion density at the end of the preceding pulse. This is illustrated by the computation shown in Figure 5.22, in which the early behavior of the electron density is calculated for initial ion densities $[O_2^-] = 0$, $[O_2^-] = 1.5 \times 10^7 cm^{-3}$, and $[O_2^-] = 2 \times 10^7 cm^{-3}$ for an oxygen pressure of 80 millitorr. These assumptions are compared with experimental measurements made for afterglow times of 20 and 100 milliseconds, respectively. It can be seen that, with a correct calculation of electron density in oxygen as outlined above, it should be possible to determine the time variation of negative ion density in the afterglow by terminating the afterglow at selected times and studying the early-time behavior of the next in-pulse electron density measurement.

An important consequence of the duty cycle effects reported above is the fact that the negative ions survive for at least one second in the wall-controlled laboratory environment. In the atmosphere, where the diffusion loss rate is greatly reduced, one can expect the ions to survive for a considerably longer period. Thus, even if the recombination coefficient is in fact as large as $10^{-7} cm^3/sec$, then

$$\nu_{eff} = \alpha_{ii} \, [O_2^+] \tag{5.21}$$

At an ion density of $10^6 cm^{-3}$, the effective loss frequency of O_2^- is $10^{-1} sec^{-1}$; at $10^5 cm^{-3}$, the loss frequency is reduced to $10^{-2} sec^{-1}$. Densities of positive and negative ions as high as $10^4 cm^{-3}$ can last for times the order of 15 to 20 minutes following the disappearance of electrons by attachment. If he correct computation proves that α_{ii} is lower than $10^{-7} cm^3/sec$, the ions will last even longer. The military consequences of this persistence of negative ions in the atmosphere will be discussed in Chapter VI.

In summary, it has been shown that the behavior of oxygen over the pressure region 0.025 to 10 Torr can be explained by the following processes, using the indicated rate coefficients:

(a) Production of electrons and O_2^+ ions in binary collisions between beam electrons and O_2 molecules in the ground state.
   Production rate = Kpi ion pairs/cm^3 sec,

   where

$$K = (5.1 \pm 0.1) \times 10^7 \; [cm^3 \, sec \, Torr \, (\tfrac{\mu amp}{meter^2})]^{-1}$$

At the higher pressures O_2^+ is rapidly converted to O_4^+; O_3^+ is also observed, although its origin is uncertain. At pressures below 0.3 Torr, O_2^+ and O_2^- appear to be the only ions present.

(b) Loss of electrons and production of O_2^- ions by three-body attachment. The reaction is

$$e + O_2 + O_2 \rightarrow O_2^- + O_2$$

with a rate constant

$$\eta_e = (2.12 \pm 0.15) \times 10^{-30} \, [O_2]^2 \, sec^{-1}$$

(c) Diffusion controlled by the space-charge field of electrons, positive ions, and negative ions. For the O_2^+ ions, a value

$$D_a \, p \approx 110 \quad cm^2 \, Torr/sec$$

is consistent with the measurements.

(d) Loss of O_2^+ and O_2^- by two-body mutual neutralization, via the reaction

$$O_2^+ + O_2^- \rightarrow 2 \, O_2$$

$$\alpha_{ii} \approx 1 \times 10^{-7} \ cm^3/sec$$
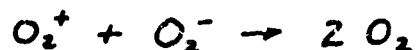
is consistent with the measurements.

(e)   Duty-cycle effects on the in-beam
       densities at low pressures can be
       interpreted as the effect of residual
       ions left over from the preceding
       afterglow on the initial rate of
       electron diffusion. Negative ions
       persist for more than 1 second in
       the laboratory environment.

112.

C.   Measurements in Nitrogen

1.   Electron density measurements

Measurements of electron densities in nitrogen were
made over the pressure range 6 to 300 millitorr. The results
were reproducible and consistent to a degree not usually
encountered in experiments with pure nitrogen.

During the measurement of steady-state electron densities
in oxygen, it was necessary to wait for about a minute after each
beam current setting to allow the frequency shift to reach its
equilibrium value. Figures 5.23 and 5.24 show results of several
measurements of these equilibrium cavity frequency shifts as a
function of total electron current from the Van de Graaff. At low
currents, the measured points lie on straight lines which inter-
sect the origin. At higher currents, the data break away from the
extrapolation of these lines, suggesting the onset of another loss
mechanism at the higher ionization levels. The frequency shift at
which the breakaway occurs decreases with increasing pressures,
as can be seen from the figure.

Figure 5.25 shows a compilation of the slopes of the
linear portions of the steady-state measurements, in units of
electrons/cm^3 μamp, where the slopes have been corrected for the
transmission of the foil scattering system. For this graph, it
has been assumed that the electron density has a uniform spatial
distribution in the cavity, so that f(kcps) has simply been
replaced by $10^4 \Delta f \dfrac{\text{electrons}}{\text{cm}^3}$. It can be seen that the data display
a p^2 variation up to about 100 millitorr. From equation 3.36,
this suggests that the rate coefficient for the controlling
electron removal process in the linear regime varies as p^{-1}.

Figure 5.26 shows a typical decomposition of the electron density into an expression of the form (Equation 3.37).

$$i = An + Bn^c \qquad (5.22)$$

This expression fits all the steady-state measurements quite accurately. From graphs such as Figure 5.26 the exponent c has been determined as well as the electron density at which the linear and the non-linear terms are equal, that is, n_{int} such that

$$B n_{int.}^{c-1} = A \qquad (5.23)$$

(From Figure 5.25, $A = 9.5 \times 10^{-9} p^{-2}$ μamp cm^3, where p is in Torr.) Figure 5.27 is a summary of the values of c and of n_{int} for nitrogen which characterizes the measurements at all beam currents used.

Time-resolved measurements of the rise of the electron density to in-beam equilibrium, and of its decay in the radiation afterglow, were also made over the pressure range 5 to 300 millitorr in switched-beam experiments. Typical afterglow measurements are shown in Figure 5.28. Data at lower pressures are linear throughout the entire afterglow period, beginning with the time the beam is switched off. At higher pressures, the electron densities at late times show an exponential decay as well, although at earlier times the data lie above the backward extrapolation of the late-time linear decay. The early data at high pressures seem to follow a relationship of the form

$$\frac{1}{n} = \frac{1}{n_o} + \alpha t \qquad (5.24)$$

114.

the well-known "recombination plot" (See Chapter III), as shown
in Figure 5.29. From the data, the slopes are given by
$\alpha = (6 \pm 2) \times 10^{-7} cm^3/sec$. Unfortunately, the range of
electron densities over which the data appear to satisfy
Equation 5.24 is less than a factor of 2, so that it is dangerous
to draw inferences from this plot about both mechanisms and rates.
See Section C.3 below, however.

From the exponential afterglow decays one can compute
lifetimes for the linear loss mechanism at various pressures.
The   data are summarized in Figure 5.30 in which the product of
decay frequency and nitrogen pressure is shown as a function of
pressure (solid circles).

Time-resolved measurements have also been made of the
buildup of the electron density following beam turn-on. As
mentioned in Section III.E, one must be careful in the analysis
of the early-time data. Plots of the exponential rise toward
equilibrium in-beam density should be referred not to the actual
steady-state density characteristic of the beam current used,
but to an extrapolation to the density which would occur if only
linear processes were operating. When this is done according to
Equation 3.40,   one obtains plots of Δn vs time following beam
turn-on which at least at ealy times characterize the linear
process in-beam, as shown in Figure 5.31. This non-linearity
at large $n(t)$. hence small $\Delta n(t)$, is exactly analogous to the
early-time nonlinear behavior in the afterglow. The products of
the gas pressures and characteristic frequencies of the
exponential rise are shown in Figure 5.30 as open circles.

2. Mass spectrometric measurements

Mass spectrometric studies of positive ions in nitrogen have been made over the pressure range 0.005 to 10 Torr. These measurements have the same general history as those in oxygen (See Section V.B.2). At pressures between 1 and 10 Torr, only ion identifications have been made; quantitative results have been confined to the region below 0.1 Torr.

Between 1 and 10 Torr, several positive ions were seen in pure nitrogen. The largest ion currents were observed for N_4^+, with N_3^+ appearing at currents about 0.2 to 0.3 times as large. At the highest pressures, traces of N_5^+ have also been seen. Small currents corresponding to ions of mass $44(N_2O^+$ or $CO_2^+)$, $46(NO_2^+)$, and $30(NO^+)$ have also been detected at various times, as well as a broad unidentified peak in the neighborhood of mass 72. As mentioned in Section IV.A, when 0.1 to 1% O_2 is added to the nitrogen to quench cyanogen emission, peaks are observed at masses $48(O_3^+)$ and $52(C_2N_2^+?)$. N_2^+ is not observed in pure nitrogen at these pressures.

Below about 0.1 Torr, the positive ion spectrum observed during continuous irradiation is dominated by N_2^+, N_3^+, N_4^+. Near 0.1 Torr, NO^+ and NO_2^+ have also been observed, but their intensities decrease more rapidly at lower pressures than do those of N_2^+, N_3^+ and N_4^+. Most of the quantitative data which have been collected relate to these latter three ions, and the remainder of this section will be devoted to their discussion.

A series of measurements was performed of the relative ion currents for N_2^+ and N_4^+ at fixed pressures as a function of

Van de Graaff beam current. Figure 5.32 shows typical results for the N_2^+ currents at several pressures. The ion currents are linear with bombarding current over the range of beam currents employed. In Figure 5.33 the results of similar measurements for N_4^+ are shown. These data are linear at low beam currents, but depart from linearity at higher Van de Graaff flux, in a manner reminiscent of the high-current electron density behavior shown in Figure 5.24 . The similarity between the N_4^+ and electron densities is borne out by Figure 5.34, in which logarithmic plots of N_4^+ ion current and electron density are shown at several pressures.

Another set of experiments was performed in which ion currents were measured at a fixed beam current as a function of gas pressure. Figure 5.35 shows the results of these measurements for N_2^+ at a beam current of 100 μ amperes. The N_2^+ ion currents vary as p^2 at low pressures, but approach a constant value at pressures above 0.035 Torr. At the highest pressures a slight decrease in ion current is observed, corresponding to the departure from linearity of the N_2^+ vs i data at 100 μ amperes. This behavior is quite different from the N_4^+ pressure dependence at 100 μ amperes, shown in Figure 5.36. There is no evidence of saturation at high pressures in the N_4^+ current, so that the N_2^+ saturation seen in Figure 5.35 is not due to instrumental limitations. The ratio of N_4^+ current to N_2^+ current at 100 μ amperes is shown in Figure 5.37 as a function of pressure. Below 40 millitorr the ratio varies as p^2, but at higher pressures the ratios are smaller than predicted by the p^2 dependence. Included in Figure 5.37 are values of the N_4^+/N_2^+ ratio at 10 μ amperes, at which the individual N_4^+ measurements are linear. These ratios are somewhat larger at high pressures than those obtained at

100 μamperes, but are still too small to agree with the p^2 dependence extrapolated from lower pressures.

The behavior of N_3^+ can be described simply by the statement that, for all cases observed, the ion current due to N_3^+ is exactly one-fourth the N_4^+ current. Thus N_3^+ varies with both pressure and beam current in the manner indicated above for N_4^+, except for the absolute magnitude of the ion current. At the highest pressures studied, at which N_4^+/N_2^+ is largest, $I(N_2^+)$ is still more than twice as large as $I(N_3^+)$.

3. Discussion of nitrogen results

The principal experimental facts to be explained are summarized below.

    a) The steady-state electron densities can
        be expressed as

$$i_{beam} = An + Bn^c$$

        where $A = 9.5 \times 10^{-9}/p^2$ $\mu amp\ cm^3$
        and $C \gtrsim 2$.

    b) In transient measurements in the linear
        regime, the electron densities rise
        exponentially in-beam, and decay expo-
        nentially in the afterglow. Between
        0.1 and 0.3 Torr, the rise and decay
        frequencies are equal, and satisfy the
        relation

$$\nu p = (0.65 \pm 0.03)\ Torr\ sec^{-1}.$$

At low pressures, the product of
transient frequency and pressure is
smaller than this value, with the
rise frequency smaller than the after-
glow decay frequency at the lowest
pressures.

c) For beam-current in the non-linear regime,
the early afterglow electron densities
satisfy a relation of the form

$$\frac{1}{n} - \frac{1}{n_0} = (6 \pm 2) \times 10^{-7} \times t \; ,$$

but only over a range of densities
smaller than a factor of two.

d) Below 0.1 Torr, three positive ions, N_2^+,
N_3^+, and N_4^+ dominate the mass spectrum in
the steady-state. The N_2^+ ion currents
are linear with Van de Graaff beam current.
At a fixed beam current, $I(N_2^+)$ varies as
p^2 at the lowest pressures then appears
to flatten off at about 0.035 Torr. The
N_4^+ ion current is linear with beam current
at low currents, then breaks away from
linearity at high beam currents. The
ratio N_4^+/N_2^+ varies as p^2 below 0.040 Torr.
$I(N_3^+)$ is always one-quarter of $I(N_4^+)$ under
all conditions investigated.

From the results summarized above, it is possible to identify
several processes occurring in the nitrogen plasma.

Consider the following model of the low-pressure nitrogen plasma. The plasma consists of electrons and N_2^+, N_3^+, and N_4^+ ions as well as neutral N_2 molecules. N_2^+ is produced by binary collisions between beam electrons and neutral molecules, and is removed from the plasma by ambipolar diffusion and ion-molecule reactions producing N_3^+ and N_4^+. The latter two ions are produced by the ion-molecule reactions which remove N_2^+, and are lost by ambipolar diffusion and by recombination with electrons. To simplify the treatment of the diffusion controlled by several positive ion species, the assumption is made that all charged particle species are spatially congruent, that is, that

$$\frac{\nabla N_2^+}{N_2^+} = \frac{\nabla N_3^+}{N_3^+} = \frac{\nabla N_4^+}{N_4^+} = \frac{\nabla n_e}{n_e} \qquad (5.25)$$

Then Equations 3. may be used for the effective diffusion coefficients. The model can then be described by

$$\frac{\partial N_2^+}{\partial t} = K p i + D_{a,2} \nabla^2 N_2^+ - \left\{ C_3(p) + C_4(p) \right\} N_2^+ \qquad (5.26)$$

$$\frac{\partial N_3^+}{\partial t} = C_3(p) N_2^+ + D_{a,3} \nabla^2 N_3^+ - \alpha_{3,e} n_e N_3^+ \qquad (5.27)$$

$$\frac{\partial N_4^+}{\partial t} = C_4(p) N_2^+ + D_{a,4} \nabla^2 N_4^+ - \alpha_{4,e} n_e N_4^+ \qquad (5.28)$$

$$n_e = N_2^+ + N_3^+ + N_4^+ \qquad (5.29)$$

Here D_{aj} is the ambipolar diffusion coefficient which would be observed for the ion N_j^+ in the absence of all other ions. $\alpha_{j,e}$

is the electron-N_j^+ recombination coefficient, and $C_j(p)$ is the frequency of ion-molecule reaction producing N_j^+. Equations 5.26 to 5.29 are non-linear partial differential equations which cannot be solved in closed form. A numerical solution can be obtained through the use of a high-speed electronic computer. A computer program of sufficient complexity to provide accurate solutions was beyond the scope of the present contract, however, although it is included in plans for future work.

Much information can be obtained from the model without an exact solution, if we make an additional approximation. Assume not only spatial congruence, but that the ions and electrons are all distributed spatially according to the fundamental diffusion mode:

$$n_e, N_j^+ \sim J_0 \left(2.405 \frac{r}{R}\right) \sin \frac{\pi z}{h} \qquad (5.30)$$

Then the equations reduce to

$$\frac{dN_2^+}{dt} = K pi - \left(\frac{D_{a,2} \, p}{\Lambda_{\shortparallel}^2 \, p} + C_3(p) + C_4(p)\right) N_2^+ \qquad (5.31)$$

$$\frac{dN_3^+}{dt} = C_3(p) N_2^+ - \left(\frac{D_{a,3} \, p}{\Lambda_{\shortparallel}^2 \, p} + \alpha_{3,e} \, n\right) N_3^+ \qquad (5.32)$$

$$\frac{dN_4^+}{dt} = C_4(p) N_2^+ - \left(\frac{D_{a,4} \, p}{\Lambda_{\shortparallel}^2 \, p} + \alpha_{4,e} \, n\right) N_4^+ \qquad (5.33)$$

$$\frac{dn_e}{dt} = K pi - \frac{1}{\Lambda_{\shortparallel}^2 \, p} \sum_j D_j \, p \, N_j^+ - \sum_j (\alpha_{j,e} \, N_j^-) n_e \qquad (5.34)$$

In the above equations n_e, N_j^+ are the amplitudes of the fundamental-mode distribution, and $\underline{i}$ is the coefficient of the first term in the expansion of the uniform current in a Fourier-Bessel series. In the remainder of this treatment, the density coefficients are identified with the measured particle densities. Equations for the steady-state are derived from 5.31 - 5.34 by setting all time derivatives equal to zero.

Consider first the steady-state equations in the limit of low ionization, so that electron-ion recombination can be neglected. Then Equations 5.32 and 5.33 give

$$\frac{N_3^+}{N_2^+} = \frac{p\,C(p)}{\dfrac{D_{a,3}\,p}{\Lambda_{\shortparallel}^{\,2}}} \quad ; \quad \frac{N_4^+}{N_2^+} = \frac{p\,C_4(p)}{\dfrac{D_{a,4}\,p}{\Lambda_{\shortparallel}^{\,2}}} \qquad (5.35)$$

Since $D_{aj}\,p/\Lambda_{\shortparallel}^{\,2}$, is independent of pressure, then the pressure dependence of the indicated ion current ratios can be used to deduce the pressure dependence of $C_j(p)$. From the low-pressure p^2 dependence of N_4^+/N_2^+ shown in Figure 5.37,

$$C_4(p) = \xi_4\,p \qquad (5.36)$$

from the similarity of N_3^+ and N_4^+ it is also apparent that

$$C_3(p) = \xi_3\,p \qquad (5.37)$$

This linear dependence of the ion-molecule reaction rates on gas pressure implies that the reactions are of the form

$$N_2^+ + N_2 \xrightarrow{\xi_3} N_3^+ \; ; \; N_2^+ + N_2 \xrightarrow{\xi_4} N_4^+ \qquad (5.38)$$
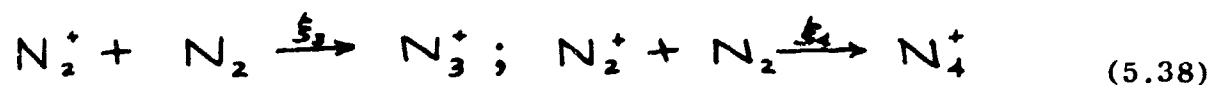
For further confirmation of 5.36 and 5.37, and for evaluation
of the rate coefficients, Equation 5.31 is rewritten

$$\frac{p^2}{N_2^+} = \frac{1}{K_i} \left\{ \frac{D_{a,2}\, p}{\Lambda_{||}^2} + (\xi_3 + \xi_4)\, p^2 \right\}$$ (5.39)

A plot of p^2/N_2^+, at fixed beam current $\underline{vs}$ p^2 should yield a
straight line, for which the ratio of slope to intercept is

$$\frac{Slope}{Intercept} = \frac{\xi_3 + \xi_4}{\dfrac{D_{a,2}\, p}{\Lambda_{||}^2}}$$ (5.40)

Figure 5.38 shows the N_2^+ $\underline{vs}$ p data of Figure 5.35 replotted in
accordance with Equation 5.39. The data below 0.04 Torr lie
on a straight line; from the data and Equation 5.43,

$$\xi_3 + \xi_4 = 4 \times 10^3\, \frac{D_{a,2}\, p}{\Lambda_{||}^2} \quad.$$ (5.41)

The data at pressures above 0.04 Torr are well approximated by
a straight line on the p^2 plot which passes through the origin.
This high pressure behavior of the data has not yet been
explained. It may represent a change in the mode of ion
sampling by the mass spectrometer, since at 0.04 Torr the gas-
kinetic mean free path is equal to the aperture diameter 1.25 mm.
This problem requires more detailed study with apertures of
various sizes, to determine the role of the aperture on ion
sampling. Below 0.09 Torr, however, it appears that the ion
current is representative of the central ion density. Gas-kinetic
considerations of ion sampling should not be a problem in

coefficient through its effect on the excited state populations.
Cress et al [1966] have also measured the lifetime of the excited
state responsible for the two-body N_3^+ production. T'   obtain a
value on the order of 6×10^{-6} sec.

Two reactions have been proposed in the literature for
the production of N_4^+ from N_2^+. The first is the Hornbeck-Molnar
process,

$$N_2^* + N_2 \rightarrow N_4^+ + e \qquad (5.44)$$

proposed by Curran [1963] to explain his observed ion chemistry
in nitrogen; the excited state of N_2 involved in 5.44 is not
specified. At higher pressures, an additional source of N_4^+ is
the three-body process

$$N_2^+ + 2 N_2 \rightarrow N_4^+ + N_2 \qquad (5.45)$$
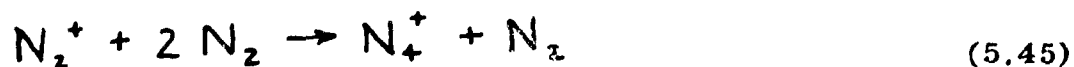
[Munson et al, 1962; Knewstubb and Tickner, 1962]. The present
result show no evidence for the three-body process below 0.1
Torr. It is somewhat more difficult to make a definitive statement
concerning the applicability of 5.44 to the present situation.
Several points should be made, however. First, the similarity of
the pressure variation of the N_3^+ and N_4^+ ion currents suggest that
these ions arise from states having similar pressure dependences.
Second, as will be mentioned in the next section, the addition of
oxygen to nitrogen to 20% partial pressure depletes N_2^+ through the
rapid charge exchange reaction

$$N_2^+ (A^2\pi) + O_2 \rightarrow N_2 + O_2^+ \qquad (5.46)$$

[Stebbings et al, 1966]. Traces of N_2^+, but no N_3^+ or N_4^+ are seen in the nitrogen-oxygen mixtures. The latter fact suggest that N_4^+ production must be related to N_2^+ rather than to neutral N_2. From the former, it is possible to relate the N_4^+ production to a definite state of the N_2^+ ion, as follows.

First, we observe N_4^+ currents four times as large as the N_3^+ currents; Cermak and Cress do not observe N_4^+ from binary collisions. Hence it would appear that N_3^+ and N_4^+ arise from two different states, the relative excitation of which is different in this experiment from that which results from low-energy electrons. The state from which N_4^+ is derived must be lost by radiation at low pressures and by ion-molecule reaction at high pressures; the ratio of the reaction rate coefficient to the spontaneous emission probability for this state must be the same as for the $^4\Sigma_u$ state. Sheridan et al [1964] have shown that the $A^2\pi$ state of N_2^+ has a radiative lifetime of the order of 3×10^{-6} sec, much the same as the result of Cress et al for $^4\Sigma_u$. Since no estimate of the rate coefficient for $^4\Sigma_u$ conversion to N_3^+ is forthcoming it is not possible to compare the rate with that for $A^2\pi$. One can estimate, however, the number of quenching collisions suffered by $A^2\pi$ in one second, then compare this with the observed production rate of N_4^+.

The quenching coefficients obtained by Sheridan et al for $A^2\pi$, as well as our own results for $B^2\Sigma$, are of the order of 5×10^{-9} cm^3/sec, referred to the excited state density. We observe N_2^+ destruction at a rate of the order of 5×10^{-14} cm^3/sec, so that these rates give equal numbers of events for values of the ratio

$$\frac{[A^2\pi]}{N_2^+} \approx 10^{-5}$$

(5.47)

This ratio in the steady-state can be estimated from a knowledge of the fluorescence efficiency for one of the Meinel bands (which arise from $A^2\pi$) in the following manner. The density of $A^2\pi$ states is given by (Equation 3.26)

$$[A^2\pi] = \frac{K_A\, p\, i}{A_A + C_A\, p} \tag{5.48}$$

where $C_A = 130\ A_A$, the ratio $[A^2\pi]/N_2^+$ is then given by

$$\frac{A^2\pi}{N_2^+} = \frac{K_A}{K}\ \frac{D_{0,2}\,p/\Lambda^2\,p + (\xi_2 + \xi_4)p}{A_A + C_A\, p} \tag{5.49}$$

From 3.33 ,

$$\frac{K_A}{K} = \frac{\eta_{(2,0)}\, A_A\, W}{A_{(2,0)}\, h\, \nu_{(2,0)}} \tag{5.50}$$

The various symbols are as defined in Chapter III. From Davidson [1966]. $\eta_{(2,0)} \approx 1 \times 10^{-3}$, the ratio $A_A/A_{(2,0)}$ is of the order of 2; for nitrogen, $W = 35$ ev; $h\,\nu_{(2,0)} \approx 1.5$ ev. Then

$$\frac{K_A}{K} \approx 0.05\ ; \tag{5.51}$$

since $A \approx 3 \times 10^5$ sec^{-1} this gives [Sheridan et al, 1964]

$$\frac{A^2\pi}{N_2^+} \approx 1.7 \times 10^{-7}\ \frac{[D_{0,2}\,p/\Lambda^2\,p + (\xi_2 + \xi_4)p]}{1 + 130\, p} \tag{5.52}$$

Over the pressure range 0.01 t0 0.1, the quantity in brackets

varies from 70 sec^{-1} at 0.01 Torr to 200 sec^{-1} at 0.1 Torr, so that

$$\frac{A^2\pi}{N_2^+} \approx 10^{-5} \text{ to } 10^{-6} \,. \tag{5.53}$$

Hence the number of $A^2\pi$ quenching reactions is nearly equal to the observed production rate for N_3^+ and N_4^+ ions, to within the accuracy of the calculation. This suggests the reactions

$$N_2^+ (A^2\pi) + N_2 \xrightarrow{\xi_4} N_4^+ \tag{5.54}$$

$$N_2^+ (^4\Sigma_u) + N_2 \xrightarrow{\xi_3} N_3^+ \,. \tag{5.55}$$

The assignment of $A^2\pi$ to the reaction 5.54 is consistent with Varney's [1953] estimate of the binding energy of N_4^+ of 0.5 ev ($A^2\pi$ lies 1 ev above the $X^2\Sigma$ ground state of N_2^+). The apparent rates for these reactions, without corrections for mass spectometer relative sensitivty for N_3^+ and N_4^+, or difference in $D_{a'3}$ p and $D_{a'4}$ p. are

$$\xi_3 \approx 6 \times 10^{-15} \quad cm^3/sec \tag{5.56}$$

$$\xi_4 \approx 2.4 \times 10^{-14} \quad cm^3/sec \,. \tag{5.57}$$

The observation of such small rate coefficients compared with those observed by Crese. must be attributed to the different experimental

considerations of the <u>ratio</u> of two ion currents, however, unless specific chemical reactions occurring at or in the aperture are involved.

Although a numerical evaluation of the rate coefficients ξ_3 and ξ_4 requires a knowledge of $D_{a,2}\, p$, several considerations concerning the reaction are in order at this point. First, a two-body rate coefficient for the reaction

$$N_2^+ + N_2 \rightarrow N_3^+ + N \tag{5.42}$$

has been reported [<u>Cress et al</u>, (1966)]; its value is about 5 X 10^{-11} cm^3/sec. From 5.41 and the knowledge that $D_{a,2}\, p$ cannot be much different from 100 Torr cm^2/sec, the total conversion coefficient is of the order of

$$\xi_3 + \xi_4 \approx \frac{2 \times 10^3 \; [\overline{\text{Torr...sec}}]^{-1}}{3.2 \times 10^{16} \; \frac{\text{Molecules}}{\text{cm}^3 \text{ - Torr}}} \approx 6 \times 10^{-14} \; cm^3/\text{sec} \tag{5.43}$$

The rate constant reported by Cress for the reaction 5.42 which is believed to proceed from the $^4\Sigma_u$ state of N_2^+ [<u>Cermak</u> <u>and Herman</u>, 1962] is referred to the total density of N_2^+. Thus in the present experiment in which the ions are observed during continous irradiation by fast electrons, it appears that the $^4\Sigma_u$ state (or whichever state of N_2^+ is in fact involved in 5.42) has a fractional density some three orders of magnitude lower than in Cress's work. This illustrates the difficulties encountered in the characterization of reactions which proceed through excited states; the experimental technique employed for ionization can control the apparent rate

conditions employed here. The high energy electrons which
are used for the excitation, may be   less likely to induce
the spin transition required for $^4\Sigma$ excitation. Also, the
observations were made during continuous irradiation; thus
whatever $^4\Sigma$ was produced could be destroyed in collisions with
the beam electrons.   Any of the proposed reactions 5.42,
5.44 and 5.45 could be occurring in the afterglow, although the
similarity of the electron density turn-on and turn-off rates
suggests that nothing unusual happens in the afterglow.

To summarize, it appears that N_3^+ is produced from N_2^+
in the $^4\Sigma$ state by binary collisions with ground-state N_2
molecules, with a rate of 1 X $10^{-14} cm^3$/sec, N_4^+ is produced from
the $A^2\pi$ state of N_2^+ in similar collisions; both excited states
behave in a similar manner with pressure. The ion-molecule
reaction is responsible for the observed optical quenching of
$A^2\pi$. From the equality of the cross-sections for $A^2\pi$ and $B^2\Sigma$
quenching, it appears reasonable to assign the $B^2\Sigma$ quenching
to N_4^+ production, as well. The cross-sections for the quenching
collisions are also the ion-molecule cross-sections referred to
the excited state, of the order of $10^{-14} cm^2$.

For several reasons, we are hesitant to deduce ambi-
polar diffusion coefficients from the electron density data.
First, the transient decay frequencies do not vary inversely as
the pressure, as the steady-state slopes suggest they should.
The high-pressure asymptote of $\not\!\! p$ = 0.65 Torr sec^{-1} (Figure 5.30)
is consistent with a $D_a p$ of about 150 ±10Torr cm^2/sec. If this
is used in Equation 3.41 , a value for the production coefficient
K = 6.8 X $10^{11} (cm^3$ Torrsec $\frac{}{cm^3})^{-1}$ is obtained from the steady-
state slopes shown in Figure 5.25 . From air measurements to be

presented in the next section, a value of $K = 5.7 \times 10^{11}$ $(cm^3 \text{ Torrsec } (\frac{ions}{cm^3}))^{-1}$ is found corresponding to a $D_a p$ of about 110 Torr cm^2/sec which agrees with the low pressure limit of $\mathcal{D} p$. In no case does the transient electron decay follow an exponential plot for significantly more than a decade of electron density, so that these plots may be gravely misleading. In view of the recent dispute over ionic mobilities in nitrogen [Keller et al, 1965] it is desirable to avoid entering the controversy until better measurements are obtained. At this point it will suffice to say that the measurements are consistent with a value of $D_a p$ between 110 and 150 Torr cm^3/sec, which can probably be attributed to the N_3^+ and N_4^+ ions. For N_2^+, the best estimate from mobility measurements [Keller et al, 1965; Saproschenko, 1965] give $D_{a,2} p$ $\approx (60 \pm 20)$ Torr cm^2/sec. This value may explain the apparently low $\mathcal{D} p$ observed in the turn-on at low pressures, before the N_2^+ has had an opportunity to convert to N_3^+ and N_4^+ in any significant amounts.

To summarize the results in nitrogen, the following should be listed:

a) The dominant electron loss mechanism at low pressures is ambipolar diffusion. The following coefficients are consistent with the measurements:

$$D_{a,2} p \approx (60 \pm 20) \text{ Torr } cm^2/sec$$

$$D_{a,3} p, \ D_{a,4} p \approx 110 \text{ to } 150 \text{ Torr } cm^2/sec$$

The steady-state data suggest that $D_{a,4} p$ is probably 110 Torr cm^2/sec.

b) N_2^+ is produced directly by the beam, and
is lost by diffusion and conversion to
N_3^+ and N_4^+.
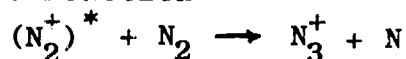
c) The reaction
$$(N_2^+)^* + N_2 \longrightarrow N_3^+ + N$$
has been observed. The evidence is consistent
with the assignment of the $^4\Sigma_u$ metastable
state of N_2^+ as the one participating in the
reaction. The cross-section for the reaction
is on the order of $5 \times 10^{-15} cm^2$.

d) The reaction
$$(N_2^+)^* + N_2 \longrightarrow (N_4^+)^*$$
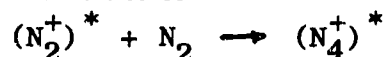
has been observed. It is suggested that the
dominant excited state involved is the $A^2\pi$,
and that the conversion to N_4^+ is responsible
for the observed optical quenching of both
$A^2\pi$ and $B^2\Sigma$. The cross-section for the
reaction, as deduced from optical quenching
measurement, is about $10^{-14} cm^2$.

D. Measurements in Airlike Mixtures of N_2 and O_2

1. Introduction

A series of measurements of electron and ion densities has been performed in 4:1 mixtures of $N_2:O_2$ subjected to bombardment by 1.5 Mev electrons. Optical emission studies in these gas mixtures have also been performed, and are presented in Chapter IV. The measurements described in this section were performed over the pressure range 0.035 to 10 Torr, which corresponds to the altitude range from 30 to 70 km in the atmosphere.

The gas mixtures used in this work, 80% N_2 and 20% O_2 by pressure, have been chosen as a first approximation to the complex chemistry of the upper atmosphere. As will be seen below, much of the gross phenomenology of the atmosphere deduced from weapon test data is reproduced by this simple mixture. Future work directed toward a study of the detailed aspects of the response of the atmosphere to ionizing radiation can use these binary mixtures as a starting point for more sophisticated chemical approximations to the atmosphere. The results of those measurements will probably consist of small changes in the results observed in the present work.

The section opens with a discussion of the measurements performed in the $N_2:O_2$ mixtures. This is followed by the interpretation of the results with reference to the laboratory environment. The section closes with an extrapolation of the laboratory results to the upper atmosphere, in which comparisons are made with current lumped-parameter models of the disturbed ionosphere.

132.

2. Electron density measurements

Electron densities were measured during continuous
irradiation of 4:1 mixtures of $N_2:O_2$ at fixed pressures between
0.035 and 10 Torr. Figure 5.39 shows several examples of these
measurements at pressures above 0.6 Torr. It can be seen that
the data are linear over the beam current range measured. The
slopes of these linear plots are compiled in Figure 5.40 as a
function of pressure; the measured slopes, in kcps/μ ampere,
have been converted to electrons/cm^3 μ ampere with the use of
Equation 2.7 . The correction for electron-neutral collisions
was made for the assumption $\nu c = 1 \times 10^8 p$ sec^{-1} [Phelps, 1962].
The slopes are referred to total beam current from the accelerator.
It can be seen that n_S/i varies as p^{-1} quite accurately for
pressures greater than 1.5 Torr. This implies that the electron
loss mechanism varies with pressure as p^2 (Equation 3.34).

Figure 5.41 shows several measurements of electron
density at pressures below 0.1 Torr. Here the curvature at
low beam currents is reminiscent of the steady-state oxygen data
at low pressures (Section V.B). At somewhat higher beam currents,
the electron densities fall onto a straight line which does not
intersect the origin, as was also observed in oxygen. At higher
currents and pressures, however, the electron density breaks away
below this line in the mixtures; in oxygen the straight line
represented the data up to the highest beam currents.

Transient measurements of electron density were
performed in the radiation afterglow at pressures above 0.6 Torr.
Figure 5.42 shows several examples of the observed decays, which
are quite accurately exponential over the pressure range inves-

tigated. The characteristic frequencies deduced from these
decays are compiled in Figure 5.43 as a function of gas pressure.
These frequencies accurately follow a p^2 dependence at least
down to 1.5 Torr, and can be represented in this range by

$$\nu_A = \left(1.10 \pm 0.05 \right) \times 10^{-31} \; [M]^2 \;\; sec^{-1} \tag{5.58}$$

where [M] is the number density of neutral air molecules.

3. Mass spectrometric measurements

Quantitative mass data have been obtained in 4:1
mixtures of $N_2:O_2$ over the pressure range 0.025 to 0.1 Torr.
Above 1 Torr, positive ions have been identified, but no
quantitative results are available at this time.

At pressures above 1 Torr, the positive ion spectra
observed in 4:1 mixtures are dominated by two species, N_2^+ and
NO^+. In addition, other ions have been seen from time to time,
particularly N_3^+, N_2O^+, and O_4^+, although at much smaller peak
currents.

Below 0.1 Torr, two peaks dominate the positive ion
spectrum, O_2^+ and NO^+. N_2^+ is also observed at these pressures,
but its peak current is about an order of magnitude smaller than
either NO^+ or O_2^+, and remains nearly constant over the pressure
range. Figure 5.44 shows O_2^+ peaks as a function of beam current
at several pressures. At low currents the data lie on straight
lines passing through the origin. The slopes of these lines are
linear with pressure, as shown in Figure 5.45. The deviation of

the ion currents from the straight line increases with increasing pressure.

In Figure 5.46 the NO^+ peak currents are shown as a function of beam current at several pressures. The data are linear at low beam currents, but show a departure from linearity at the highest pressure. In general, this departure is not as marked as that observed for O_2^+ under these conditions. The slopes of the straight-line portions are not linear with pressure, but vary as illustrated in Figure 5.45.

4. Interpretation of laboratory measurements

The coincidence of the p^2 dependence of the electron loss processes deduced from the steady-state and afterglow measurements at high pressures suggests that these in fact represent the same process. From the analogy with the measurements in oxygen, the dominant removal mechanism can be identified as three-body attachment of electrons to neutral O_2 molecules, with both O_2 and N_2 acting as third bodies. The attachment frequency

$$\nu_a = (1.10 \pm 0.05) \times 10^{-31} [M]^2 \quad sec^{-1} \qquad (5.58)$$

deduced from the measurement is in excellent agreement with the value quoted by other workers [Pack and Phelps, 1966] for electron attachment in airlike mixtures of nitrogen and oxygen. The efficiency of N_2 relative to O_2 as a third body in stabilizing the newly formed negative ion is given by (Equation 3.5)

$$\eta = (3 \pm 1) \times 10^{-2} \qquad (5.59)$$

From the measured slopes of the linear n_s _vs_ i plots, a value for the ionization production coefficient K may be deduced. From Equation 3.34,

$$K = \frac{\eta_a \, n_s}{p \, i} = \frac{\eta_a}{p} \, S \tag{5.60}$$

where S is the value of the slope referred to incident beam current density. From Figure 5.40, the slope referred to total beam current from the accelerator is

$$S_T = 1.45 \times 10^5 \cdot p^{-1} \qquad (cm^3 \, \mu amp)^{-1} \tag{5.61}$$

After correction for the scattering foil used in these measurements, (foil transmission = 0.288), this yields

$$S = (5.0 \pm 0.2) \times 10^9 \cdot p^{-1} \qquad (cm^3 \, \frac{\mu amp}{cm^2})^{-1} \tag{5.62}$$

Thus the production coefficient for the airlike mixture is given by

$$K_{air} = \frac{S \eta_a}{p} = (5.55 \pm 0.35) \times 10^{11} \tag{5.63}$$
$$\left[cm^3 \, \frac{\mu amp}{cm^2} \, Torr \cdot sec \right]^{-1}$$

This is to be compared with the value obtained for the production coefficient for oxygen (Section V.B):

$$K_{oxygen} = 5.1 \times 10^{11} \qquad (cm^3 \, \frac{\mu amp}{cm^2} \, Torr \cdot sec)^{-1} \tag{5.64}$$

From the relation

$$K_{air} = 0.8K_{nitrogen} + 0.2K_{oxygen},$$

it follows immediately that

$$K_{NITROGEN} = (5.6 \pm 0.4) \times 10^{11} \quad \left(cm^3 \frac{\mu amp}{cm^2} Torr\,sec\right) \quad (5.65)$$

These values are in general agreement with the calculated production coefficients shown in Section III.B, and in good agreement with each other.

From the mass spectrometer data at low pressures, several statements can be made concerning the origins of the positive ions observed during continuous irradiation. The primary ions produced by the electron beam are N_2^+ and O_2^+, in the ratios of the partial pressures of neutral N_2 and O_2, respectively. It is known that N_2^+ undergoes a rapid charge exchange with O_2 to produce O_2^+ (Equation 5.46). Referred to their total N_2^+ density, which was known to be very rich in $A^2\pi$, Stebbings et al [1966] deduce a rate coefficient for the charge exchange reaction given by

$$R_x = 2 \times 10^{-10} \quad cm^3/sec \quad (5.66)$$

Our measurements of the rate coefficient for the quenching of $B^2\Sigma$ by collisions with O_2 molecules (Chapter IV) gives a value when referred to $B^2\Sigma$ density of about $10^{-9} cm^3/sec$. This suggests

that similar rates should hold for the quenching of $A^2\pi$ by O_2 as well. Furthermore, both quenching reactions can probably be attributed to the charge exchange reaction. The origin of NO^+ in the experiments is somewhat uncertain. From the observation that NO^+ shows less departure from linearity with beam current than does O_2^+, reactions of the form

$$O_2^+ + mX \longrightarrow NO^+ + Y \qquad (5.67)$$
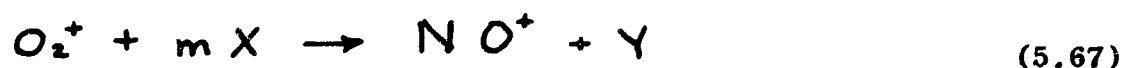
can probably be ruled out. NO^+ could be produced in an ion-molecule reaction of the form

$$\left(N_2^+\right)^* + O_2 \rightarrow NO^+ + NO \qquad (5.68)$$
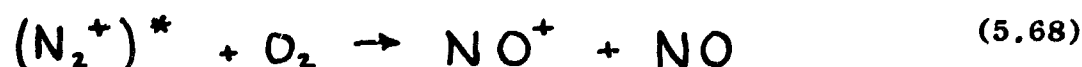
It is necessary to invoke an excited state for this reaction Stebbings and his group do not observe this reaction for ionizing electron energies of the order necessary to populate just the $A^2\pi$ and $X^2\Sigma$ states of N_2^+; 5.58 must therefore come from a higher-lying state that $A^2\pi$. Since N_3^+ is not observed in the air mixtures, the $^4\Sigma$ state responsible for N_3^+ production might be quenched by reaction 5.58.

NO^+ could also be produced from a modified Hornbeck-Molnar reaction

$$O_2^* + N_2 \rightarrow NO^+ + NO + e \qquad (5.69)$$

or

$$N_2^* + O_2 \longrightarrow NO^+ + NO + e \qquad (5.70)$$

138.
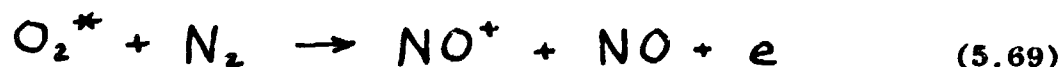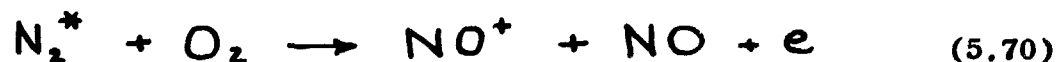
It would be very convenient to invoke Reaction 5.60 to explain the observed quenching of Second Positive Bands, which originate from the $C^3\pi$ state of N_2, by neutral oxygen. This reaction cannot however, be a major source of NO^+, since the resulting production of free electrons would be in disagreement with the electron density measurements, which show an electron production term which varies as p over the entire pressure range. Thus reactions 5.69 and 5.70 cannot explain most of the observed NO^+, which we therefore tentatively ascribe to 5.68.

To describe the mixture data in its most convenient form, a lumped-parameter model is used. This model assumes a single species each of "average" positive and negative ions, as well as electrons, so that it is very similar to the model used for oxygen (Section V.B). The equations for three-component plasma at low pressures will be presented for the steady-state, with the assumption that all particles are distributed in the fundamental diffusion mode. Then

$$K p i = \frac{D_a p}{\Lambda^2 p} P + \alpha_i N P + \alpha_e n P \qquad (5.71)$$

$$\beta p^2 n = \alpha_i N P \qquad (5.72)$$

$$P = N + n \qquad (5.73)$$

In the limit of low electron density, where the electron-positive ion recombination term in 5.61 can be neglected, the above equations can be rearranged to give

$$P = \frac{Kpi - \beta p^2 n}{\frac{D_a p}{\Lambda^2 p}} \tag{5.74}$$

$$N = P - n \tag{5.75}$$

$$\alpha_i = \frac{\beta p^2 n}{N P} \tag{5.76}$$

Both K and β have been evaluated from the high pressure data.
One can therefore arrive at a value for α_i by assuming a value
for $D_a p$ (say $\overline{D_a p}$) calculating P and N for this value, then
finally α_i . $\overline{D_a p}$ is then varied until the calculated ion
recombination coefficient is independent of beam current. The
ion densities predicted by one such calculation are shown in
Figure 5.47. From calculations of this type, all the data
obtained at low pressures have been found to be consistent
with the values

$$D_a p = (160 \pm 15) \quad Torr \cdot cm^2/sec \tag{5.77}$$

$$\alpha_i = (2.5 \pm 1.5) \times 10^{-7} \quad cm^3/sec. \tag{5.78}$$

A simple extension of the above technique permits an
estimate of the electron-positive ion recombination coefficient.
From Equations 5.71 and 5.72 one obtains

$$\frac{Kpi - \beta p^2 n}{P} = \frac{D_a p}{\Lambda^2 p} + \alpha_e n \tag{5.79}$$

Thus a plot of the quantity $(Kpi - \beta p^2 n)/P$ vs n should yield a
straight line; the ratio of the slope to intercept of this line

140.

is given by

$$\frac{Slope}{Intercept} = \frac{\alpha_e}{\frac{D_a p}{\Lambda^2 p}}$$

(5.80)

Figure 5.48 shows a plot of Equation 5.79 made for a mixture pressure of 0.083 Torr. From the limited data thus far available, α_e has been found to be consistent with

(5.81)

$$\alpha_e = (3 \pm 2) \times 10^{-7} \qquad cm^3/sec$$

Several comments should be made concerning the above computations of recombination coefficients. First, the techniques described above yield more consistent results in air than they did in oxygen (section B). This is because the lower attachment rate for air than for oxygen at the same pressure results in fewer negative ions, hence in a closer approximation to the true situation by the fundamental-mode model, Equations 5.71 to 5.73. Second, the predicted values of α_e are in very good agreement with other laboratory measurements for $\alpha_e(O_2^+)$ and $\alpha_e(NO^+)$ which can be summarized as

$$\alpha_e(O_2^+) = (2 \pm .5) \times 10^{-7} \ cm^3/sec \text{ [\underline{Kasner} \underline{and} \underline{Biondi}, 1965]} \quad (5.82)$$

$$\alpha_e(NO^+) = 4.6 \times 10^{-7} \ cm^3/sec$$

(5.83)

[\underline{Gunton} \underline{and} \underline{Shaw}, 1965]

Finally, the pair of numbers α_i, α_η obtained above is in good agreement with deductions made from analyses of the disturbed ionosphere [\underline{Knapp}, 1966], which are consistent with the sets of

values

$$\alpha_e = \alpha_i = 3 \times 10^{-7} \quad cm^3/sec$$

$$\alpha_e = 2^+ \times 10^{-7} \ cm^3/sec \ ; \quad \alpha_i = 1 \times 10^{-7} \ cm^3/sec$$

$$\alpha_e = 2^- \times 10^{-7} \ cm^3/sec \ ; \quad \alpha_i = 3 \times 10^{-8} cm^3/sec$$

$$\left. \right\} \quad (5.84)$$

From the results presented above, we are inclined to accept the first set of values, the so-called equal-coefficient model.

The laboratory measurements in air-like mixtures can be summarized as follows:

a) At pressures above 1.4 Torr, the linear
   electron loss process is dominated by the
   three-body attachment of thermal electrons
   to neutral O_2 molecules. The rate coeffi-
   cients for attachment and for production of
   electron-ion pairs by 1.5 Mev electrons are
   given by

$$\beta_{air} = \left(1.10 \pm 0.05 \right) \times 10^{-31} \quad cm^6/sec$$

   referred to the total density of neutral
   molecules, and

$$K = \left(5.55 \pm 0.35 \right) \times 10^{11} \ (cm^3 \ \frac{\mu amp}{cm^2} \ Torr\text{-}sec)^{-1}$$

   The attachment coefficient is consistent
   with a value of the efficienty of N_2
   relative to O_2 as the third body stabilizing
   the newly formed negative ion is

142.

$$\eta = (3 \pm 1)\ \%$$

b) At pressures below 0.1 Torr, three species
   of positive ions are found, NO^+, O_2^+, and N_2^+.
   The ion densities are consistent with the
   following scheme:

$$e + N_2 \rightarrow N_2^+ + 2e \qquad \text{(a)}$$

$$e + O_2 \rightarrow O_2^+ + 2e \qquad \text{(b)}$$

$$(N_2^+)^* + O_2 \rightarrow O_2^+ + N_2 \qquad \text{(c)}$$

$$(N_2^+)^* + O_2 \rightarrow NO^+ + NO \qquad \text{(d)}$$
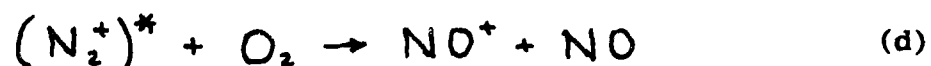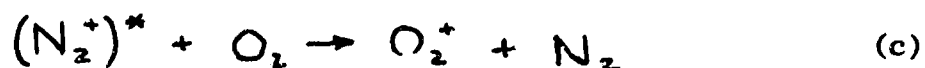
The charge-exchange reaction (c) has been
identified as the quenching mechanism
observed in the optical spectra from N_2^+
states, with a cross-section of the order
of $10^{-14} cm^2$.

c) The ionization at pressures below 0.1 Torr
   is controlled by electron diffusion in the
   presence of positive and negative ions, three-
   body attachment of electrons to O_2 molecules,
   electron-ion recombination, and ion-ion mutual
   neutralization. The apparent values for the
   various rate coefficients are

$$D_a P = (160 \pm 15) \ T_{orr} \cdot cm^2/sec$$

$$\alpha_i = (2.5 \pm 1.5) \times 10^{-7} \ cm^3/sec$$

$$\alpha_e = (3 \pm 2) \times 10^{-7} \ cm^3/sec$$

E.   Ionospheric Implications of the Laboratory Measurements

The phenomenology of airlike mixtures of nitrogen and oxygen reported in the previous section strongly resembles that observed in the disturbed ionosphere. The positive ion spectrum observed in the laboratory experiment, consisting of O_2^+, NO^+, and N_2^+, is the same as has been observed in the upper atmosphere [Narcisi, 1965]. The measured rate coefficient for three-body attachment is in agreement with that deduced from conductivity measurement in the O_2 dominated D region [Knapp, 1966]. Electron-ion and ion-ion recombination has been observed in the laboratory at simulated altitudes between 60 and 75 km, with rates which are in substantial agreement with atmospheric data [Knapp, 1966].

Several important ionospheric reactions have not yet been studied in the laboratory. First, since all experiments to date have been performed at 300° K, no information on temperature dependence of the various rate coefficients has been obtained. In particular, the collisional detachment of negative ions, the rate coefficient for which is negligible below 400° K, has not been observed. Second, no indications have been seen of the production of significant densities of free atoms over the

144.

pressure range investigated. Thus reactions depending on free
atoms, such as radiative attachment,

$$O + e \longrightarrow O^- + h\nu ,$$

associative detachment,

$$X^- + O \longrightarrow XO + e$$

and ozone formation,

$$O_2 + O \longrightarrow O_3 ,$$

have not been studied. The laboratory measurements are therefore
characteristic of the upper atmosphere at altitudes below about
80 km, where the neutral O density is negligible. Third,
measurements of ionic recombination have not been made for
simulated altitudes lower than 60 km; in particular, three-body
ionic recombination, which is expected to be of significance
below 45 km [Knapp, 1966] has not been studied. Finally, the
effects of minority constituents of the normal atmosphere are
not included in the laboratory experiments. These constituents
are expected to play a significant role in the phenomenology of
the disturbed atmosphere only at very low ionization levels
[Knapp, 1966]. Thus the laboratory measurements should be
substantially representative of the real atmosphere over the
altitude range 45 to 80 km.

Within the above limitations, it is possible to construct
a model of the ionosphere based on the laboratory measurements.
As before, a three-component "lumped-parameter" model (electrons,
positive ions, and negative ions) will be used. The equations
describing the simulated ionosphere are

$$\frac{dn_e}{dt} = P_e - \beta[M]^2 n_e - \alpha_e P n_e \qquad (5.85)$$

$$\frac{dP}{dt} = P_e - \alpha_e n_e P - \alpha_i N P \qquad (5.86)$$

$$\frac{dN}{dt} = \beta[M]^2 n_e - \alpha_i P N \qquad (5.87)$$

The production term P_e is the same for positive ions and electrons. For ionization due to a flux of ϕ beta particles/cm^2 sec in the energy range 1 to 2 Mev, which corresponds to a current density of relativistic electrons given by

$$J = 1.6 \times 10^{-13} \phi \quad \mu amp/cm^2 \qquad (5.88)$$

The production rate is (Equation 5.63)

$$P_e \equiv K_p J = 8.8 \times 10^{-2} p \phi \quad (cm^3 sec)^{-1} \qquad (5.89)$$

or, in terms of neutral molecule number density,

$$P_e = 2.7 \times 10^{-18} [M] \phi \qquad (5.90)$$

Figure 5.49 summarizes the production rate as a function of altitude for a uniform beta flux of $1(cm^2 sec)^{-1}$.

No information on the temperature dependence of the three-body attachment coefficient has yet been obtained in this experiment. Instead, we use the expression given by Knapp [1966], modified upward 10% to agree with our value of β at 300°K:

$$\beta = 2.2 \times 10^{-30} \left(\frac{300}{T}\right)^{1/2} exp\left[1.8\left(1 - \frac{300}{T}\right)\right] cm^6 sec^{-1} \qquad (5.91)$$

The resulting loss frequency due to three-body attachment is calculated from the U.S. Standard Atmosphere [1962], and is shown in Figure 5.50.

One can now calculate expected electron and ion densities from Equations 5.85 through 5.87 as a function of altitude and beta flux. From the results presented in Section V.D.3, $\alpha_e \approx \alpha_i$, so that 5.76 can be rewritten as

$$P = (P_e / \alpha_e)^{1/2} .$$

(5.92)

N and n_e can then be computed in a straightforward manner.

In a realistic situation in the disturbed upper atmosphere, a uniform beta flux is not to be expected. Instead, the production model given by Crain [1964a], is used. Assume a nuclear detonation at high altitudes with the fission debris spread into a circular area of radius R(km), all at altitudes above 90 km. Then the normalized production distribution P_e at lower altitudes is as shown in Figure 5.51. Ionization is due primarily to betas above 65 km, and to gammas below 30 km. Between 30 and 65 km, both betas and gammas contribute to the ionization.

The ionization at 65 km is related to weapon parameters by

$$P_e (65 \text{ km}) = \frac{5 \times 10^{13} \, Y}{R^2 t^{1.2}} \quad electrons/cm^2 sec$$

(5.93)

where Y is the fission yield of the weapon in megatons, and t is the time in seconds after the detonation. For a weapon with a fission yield of 1 megaton, with the debris spread over a radius

100 km, the production rate one hour after detonation is given by

$$P_e \, (65 \, km) = 2.5 \times 10^6 \quad electrons/cm^3 sec \qquad (5.94)$$

to which the curve in Figure 5.51 is normalized. The model then yields the particle densities shown in Figure 5.2. The rapid attachment of electrons to O_2 molecules below about 60 km is responsible for the strongly developed electron layer peaked at 75 km. At 45 km, the ratio of ion to electron density is sufficiently high that the propagation of electromagnetic signals through this region is controlled by the ions rather than by the electrons [Crain, 1946 ; Johler, 1965]. It should be remembered that the curve is valid only for night-time conditions, that is, in the absence of photodetachment.

If one includes the effects of three-body recombination with a coefficient given by [Crain, 1961]

$$\alpha_{i,3} \approx 6 \, p \, (atm) \, T^{-5/2} \qquad (5.95)$$

where the pressure is expressed in atmosphere, the ion densities are reduced at low altitudes, as shown by the dotted curve in Figure 5.52.

From atmospheric measurement, it is difficult to evaluate α_e and α_i separately. For both quantities one must study the ion densities at high ionization levels. It should be pointed out that in the laboratory it is possible to separate the effects of electron-ion and ion-ion recombination, in a rather surprising way. At low ionization levels, electron-positive ion recombination

can be neglected relative to the linear processes of attachment and diffusion. For the negative ions however diffusion is greatly suppressed by the electrons, so that their only available loss mechanism is ionic recombination, even at low ionization levels. In the laboratory, electron diffusion rates have been shown to be strongly dependent on the negative ion density, hence indirectly on the ionic recombination coefficient which controls the negative ion density. By studying electron diffusion at low ionization levels, one can deduce α_i (as was in fact done in the preceding section) without interference from electron-ion recombination. Thus the hither to "undesirable" diffusion of charged particles to the walls of the laboratory container is in fact a valuable diagnostic method for a process which cannot presently be studied directly in the atmosphere.

As mentioned in Section V.B, one can expect to find negative ions in a post-weapon environment at densities of $10^4 cm^{-3}$ or greater for times of the order of 30 minutes. One is tempted to inquire into the fate of these negative ions when subjected to the high rf field of a modern area-defense radar beam. The field strengths contemplated for such systems are certainly small enough to avoid breakdown in normal air. It is not difficult to contemplate that a small electron residuum could be heated in the radar field sufficiently to detach appreciable densities of electrons from the negative ions. Thus a premature resumption of radar surveillance following a period of weapon-induced blackout could result in the radar's blacking itself out again as soon as it is turned on. It is recommended that radar breakdown studies in air rich in negative ions be carried out to establish safe-working limits for radar field strengths.

In summary, the laboratory measurements have given general agreement with measurements obtained in the disturbed ionosphere over the altitude range between 45 and 80 km. It should be possible to extend the range of agreement by means of further work using the same general techniques described in the present report. In the next chapter, specific recommendations are made for experimental studies by which the reaction rates deduced from laboratory measurements can be extended to other altitude ranges and ionization conditions.

150.

REFERENCES (Chapter V)

Cermak, V. and Z. Herman, Collection Czech. Chem. Commvn. 27, 1493 (1962)

Crain, C.M., J. Geophysics Res. 66, 1117 (1961)

Crain, C.M., The RAND Corporation, Memorandum RM-4037-PR (March 1964)

Crain, C.M. and H.G. Booker, The RAND Corporation, Memorandum RM-4031-PR (March 1964)

Cress, M.C., P.M. Becker, and F.W. Lampe, J. Chem. Phys., 44, 2212 (1966)

Gunton, R.C. and T. M. Shaw, Phys. Rev. 140, A756 (1965)

Jesse, W.P. and J. Sadauskis, Phys. Rev. 90, 1120 (1953)

Johler, J.R. and T.A. Berry, N.B.S. Tech. Note No. 313 (June 1965)

Kasner, W.H. and M. Biondi, Phys. Rev. 137, A317 (1965)

Keller, G.E., D.W. Martin, and E.W. McDaniel, Phys. Rev. 140. A1535 (1965)

Knapp, W.S., J.B. Culbertson, P.G. Fisher and D.H. Archer, General Electric Company, TEMPO 66TMP-18 (March 1966)

Knewstubb, P.F., and A.W. Tickner, J. Chem. Phys. 37, 2941 (1962)

Munson, M.S.B., F.H. Field, and J.L. Franklin, J. Chem. Phys. 37, 1790 (1962)

Narcisi, R.S. and A.D. Bailey, Space Res., 5, 753 (1965)

Nelms, A.T., U.S. Bureau of Standards, Circular No. 577 (1957).

Pack, J.L., and A.V. Phelps, J. Chem Phys. 44, 1870 (1966)

Phelps, A.V., J. Appl. Phys. 31, 1723 (1960)

Samson, J.A.R. and G.L. Weissler, Phys. Rev., 137 A381 (1965)

Saporoschenko, M., Phys. Rev. $\underline{139}$, A352 (1965)

Sayers, J. in ATOMIC AND MOLECULAR PROCESSES, Ed. D.R. Bates
  New York; Academic Press(1962)

Sheridan, W.F., O. Oldenberg, and N. P. Carleton,in ATOMIC COLLISION
  PROCESSES, ed. by M.R.C. McDowell, Wiley & Sons, New York (1964)

Stebbings, R.F., B.R. Turner, and J.A. Rutherford, J. Geophys.
  Res., $\underline{71}$, 771 (1966)

U.S. STANDARD ATMOSPHERE, 1962, Prepared under sponsorship of
  NASA, U.S. Air Force, and U.S. Weather Bureau (December 1962)

Van Lint, V.A.J., E.G. Wicker, and D.L. Trueblood, Report No.
  59-43 (August, 1959), General Atomics Division of General
  Dynamics Corp., San Diego, California (Unpublished).

Varney, R.N., Phys. Rev.,$\underline{89}$, 708 (1953)
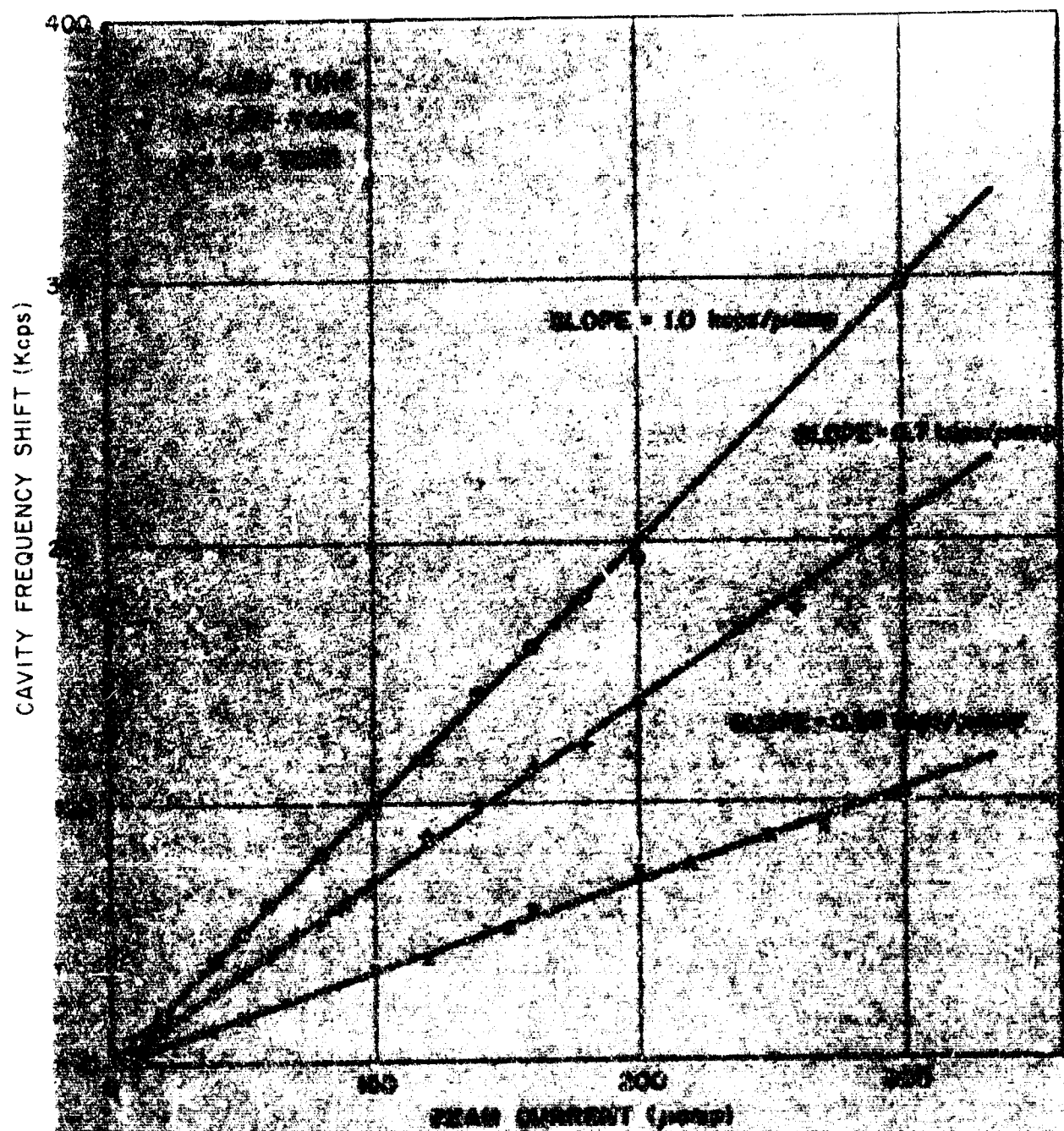
FIGURE 3.1 — EQUILIBRIUM ELECTRON DENSITY IN OXYGEN VS. BEAM CURRENT FOR HIGH PRESSURES

153.
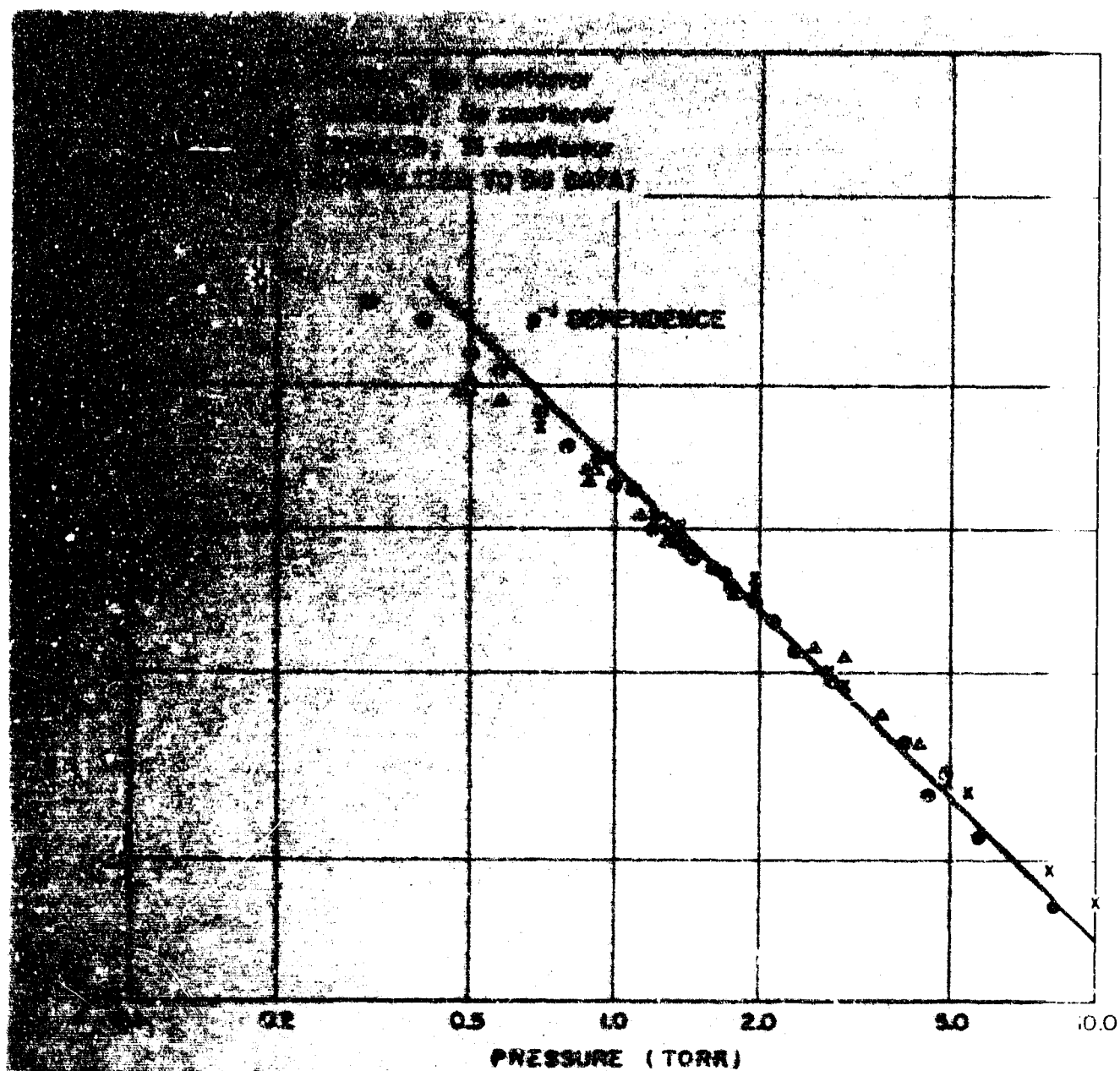
FIGURE 3.2. PRESSURE DEPENDENCE OF SPECIFIC IONIZATION IN PURE OXYGEN

154.
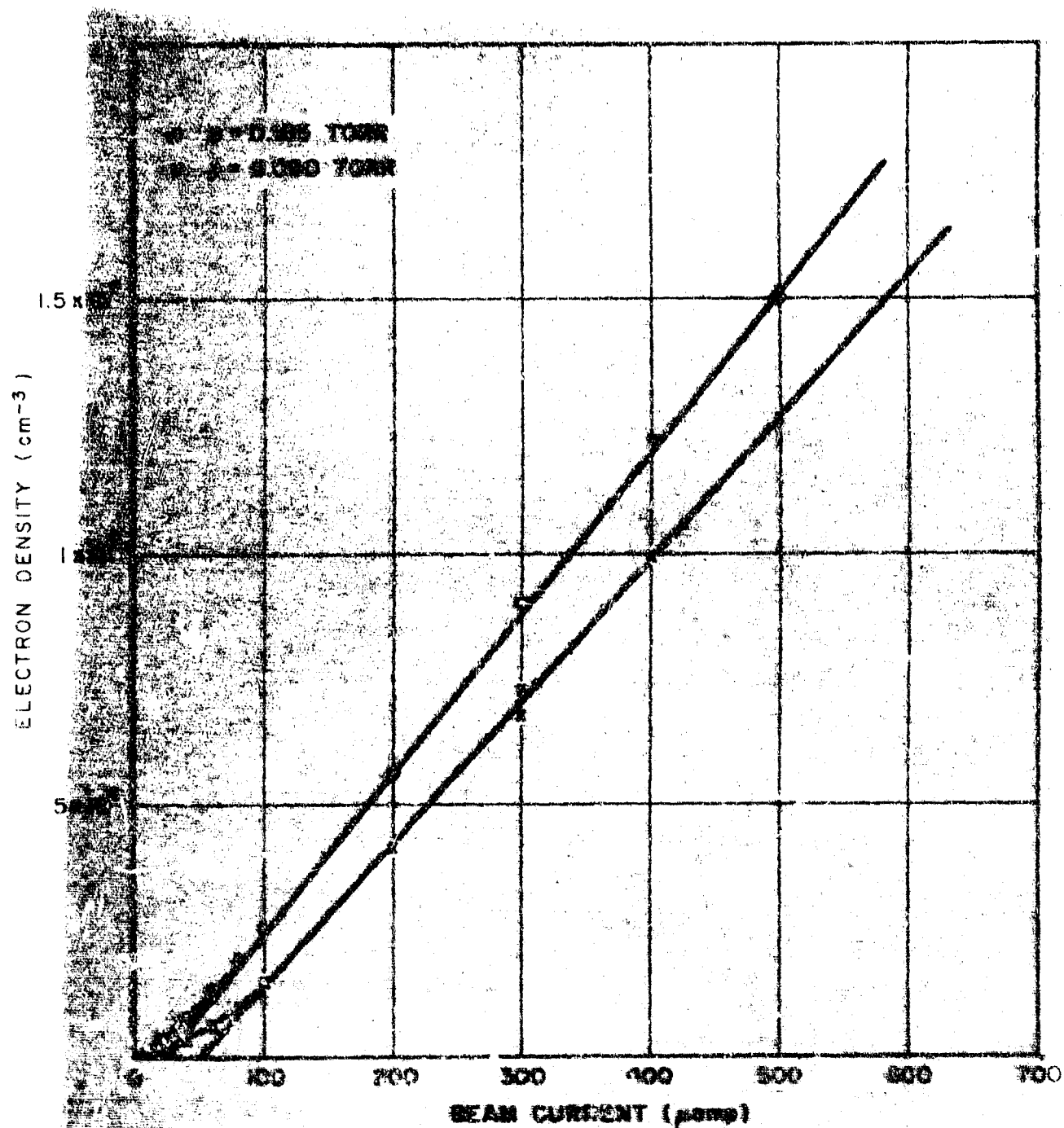
FIGURE 5.3 – EQUILIBRIUM ELECTRON DENSITY IN OXYGEN VS.
BEAM CURRENT FOR LOW PRESSURES
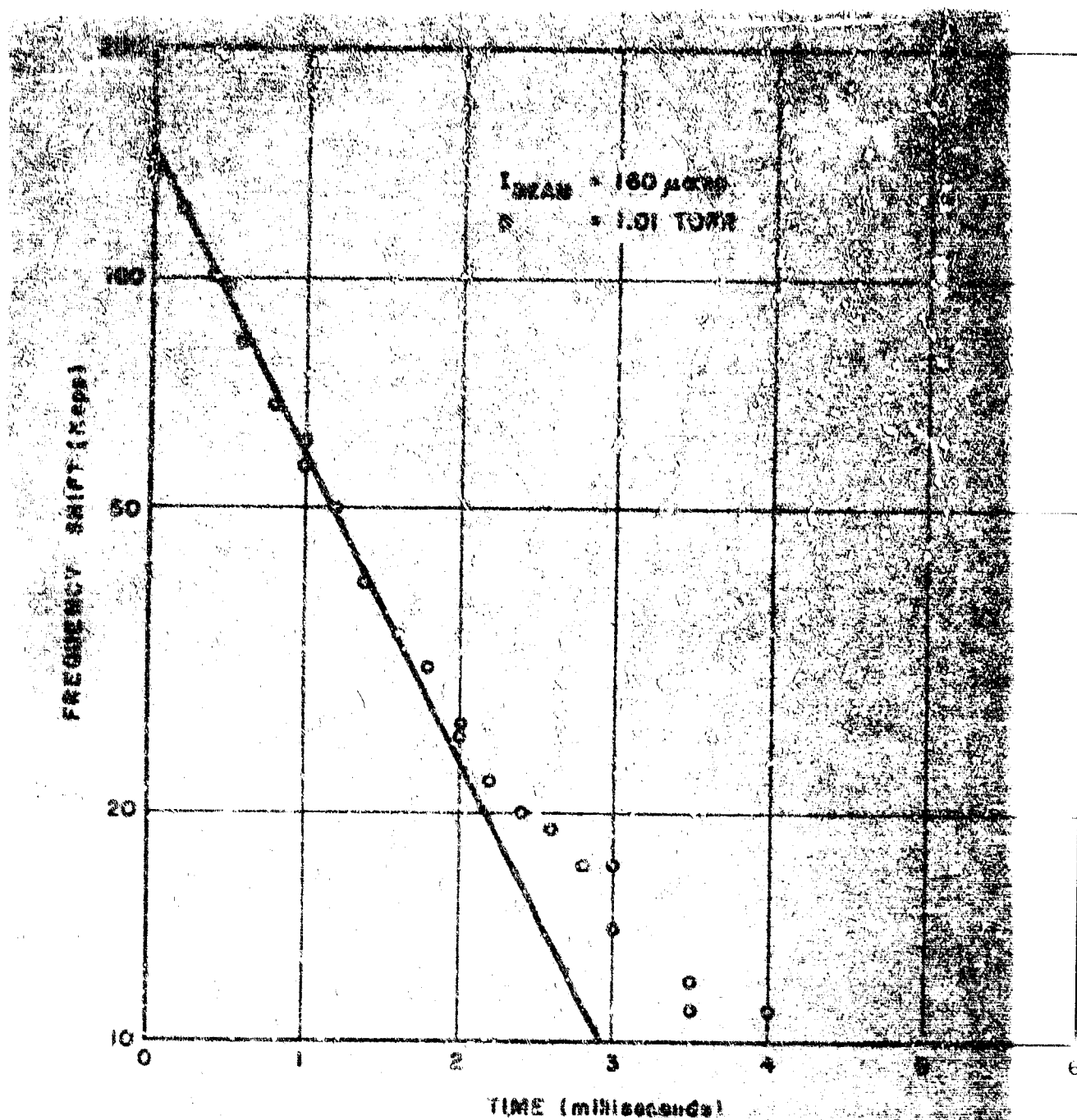
FIGURE 5.4 - CAVITY FREQUENCY SHIFT VS. TIME IN AFTERGLOW
OF 50 msec IRRADIATION IN OXYGEN

156.
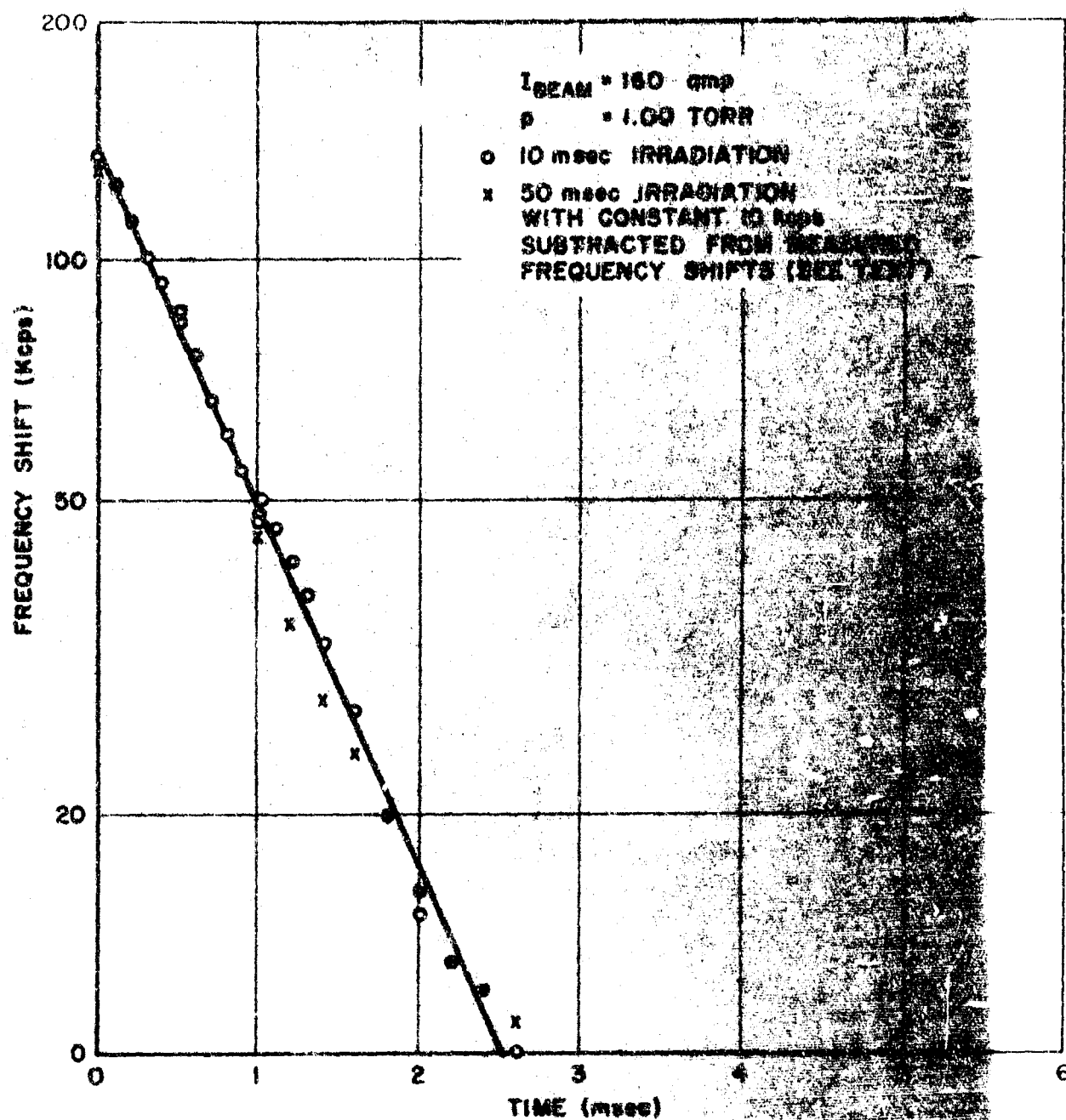
FIGURE 5.5- CAVITY FREQUENCY SHIFT VS. TIME IN AFTERGLOW
OF 10 msec IRRADIATION IN OXYGEN
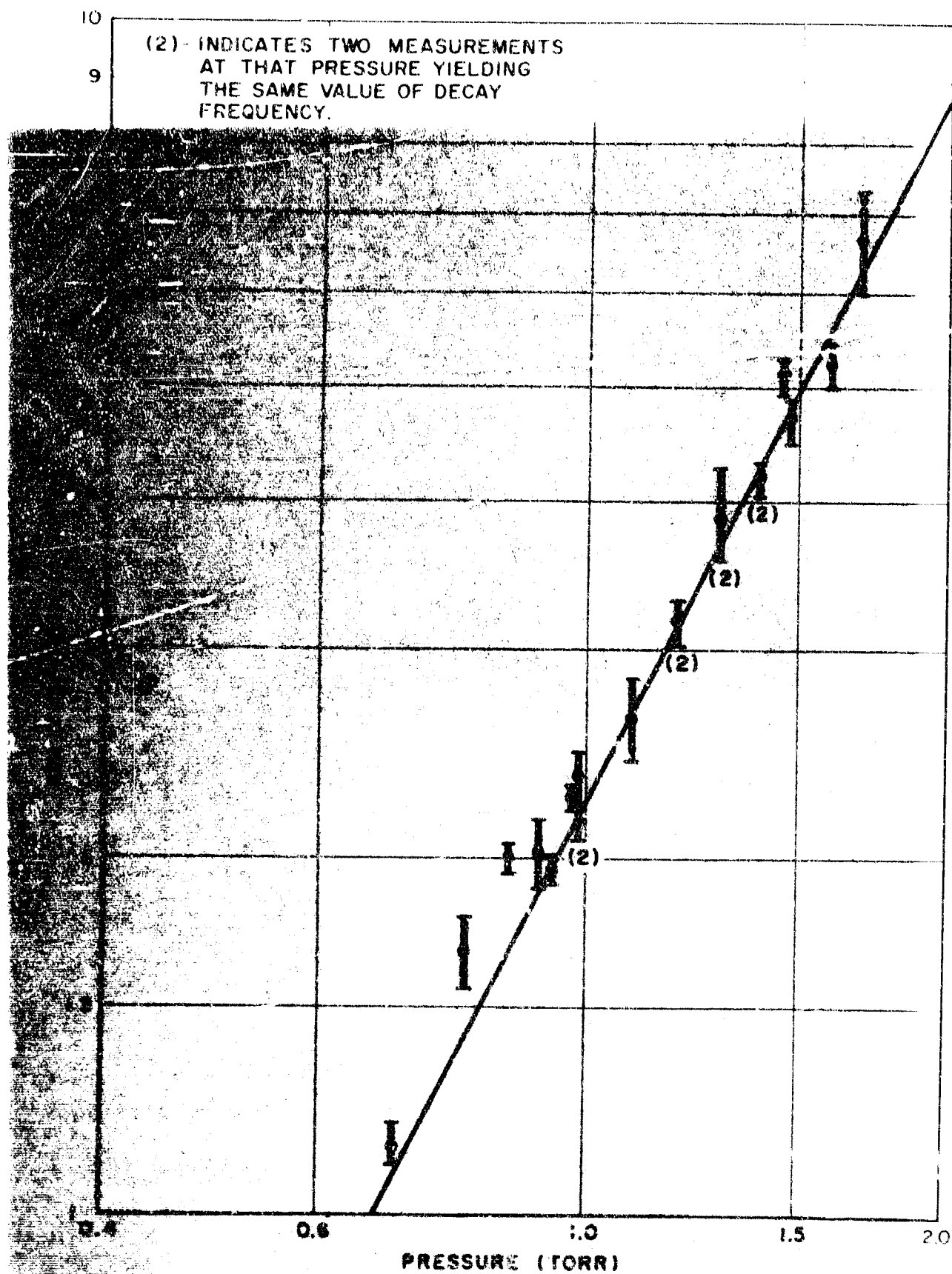
FIGURE 5.6 - AFTERGLOW DECAY FREQUENCY VS. PRESSURE
IN OXYGEN
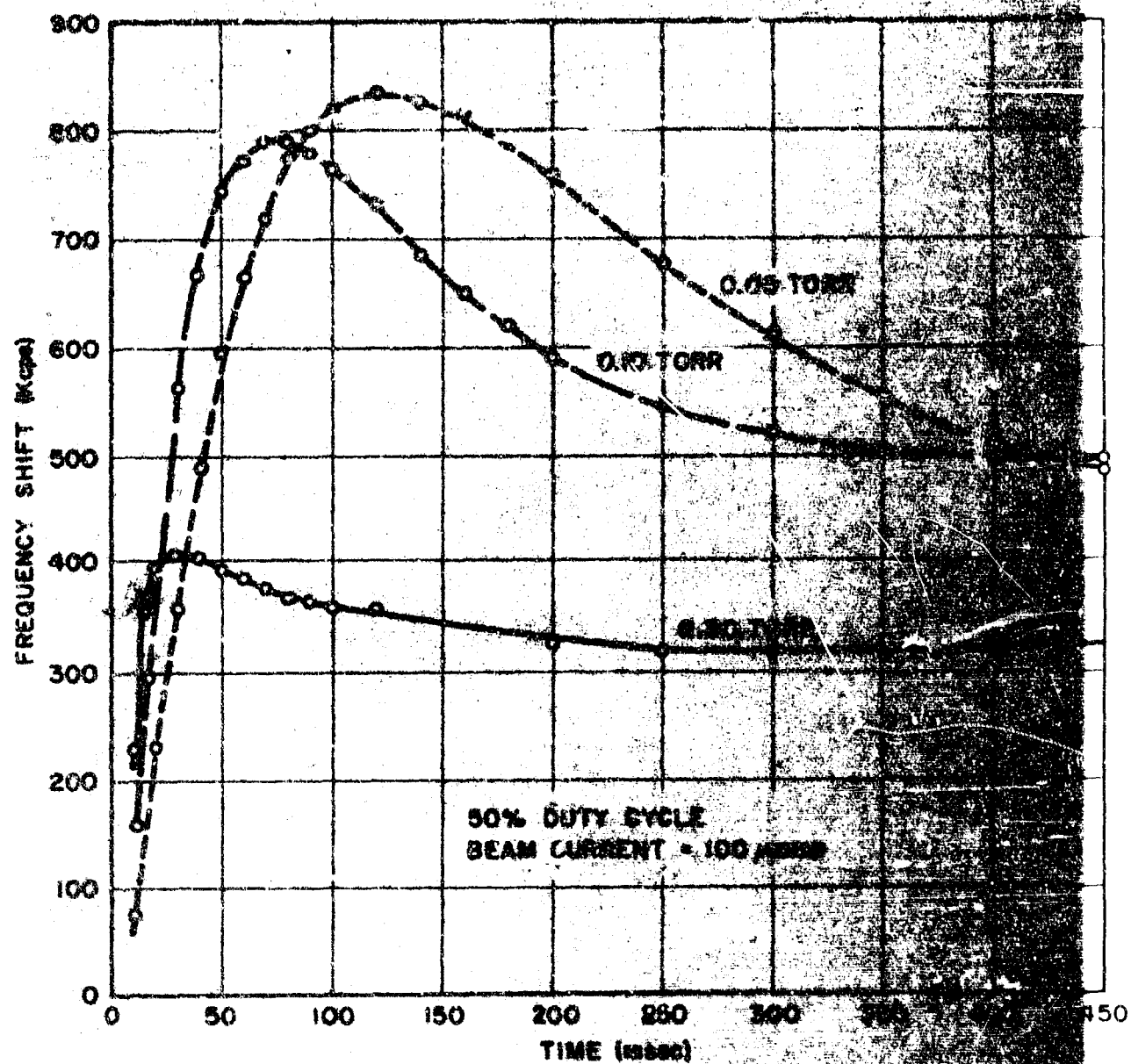
FIGURE 5.7 — TURN-ON DATA IN OXYGEN AT GIVEN
PRESSURES
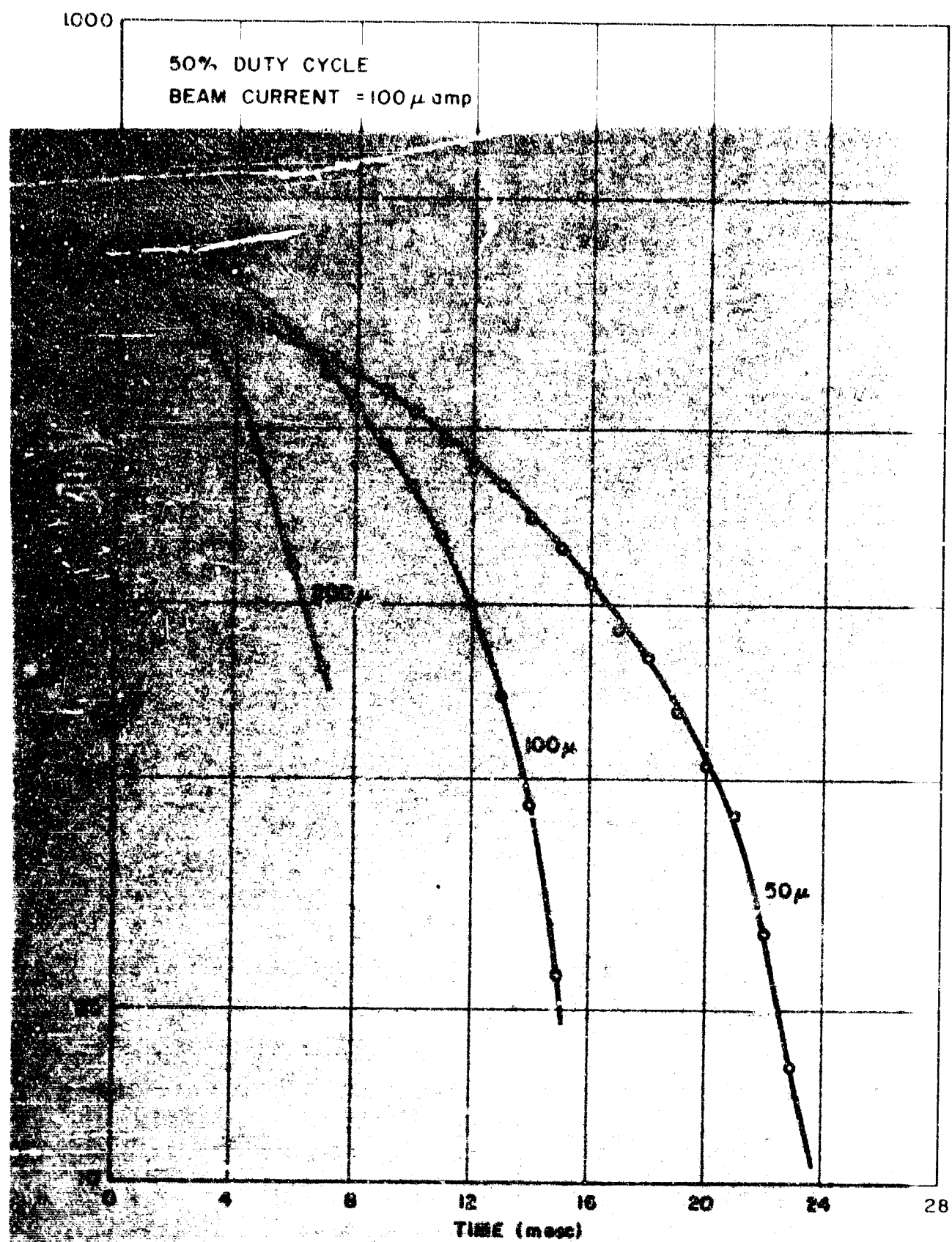
FIGURE 5.8- AFTERGLOW DATA IN OXYGEN AT LOW PRESSURES

Δf (Kcps)

200
400
600
800
1000

p = 100 microns OF O₂
Temp = 100 µ amps

20%

30%
40%

60%
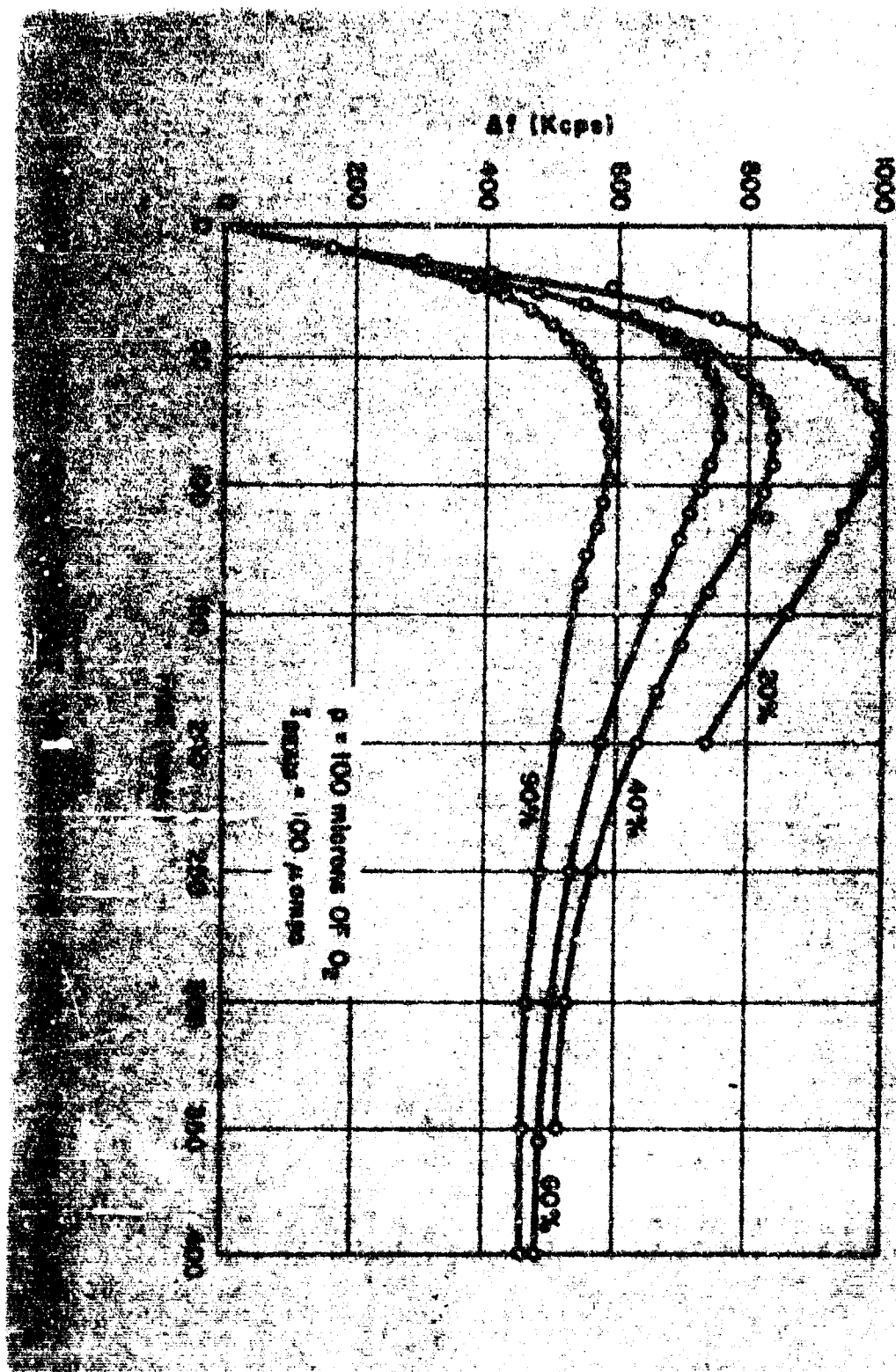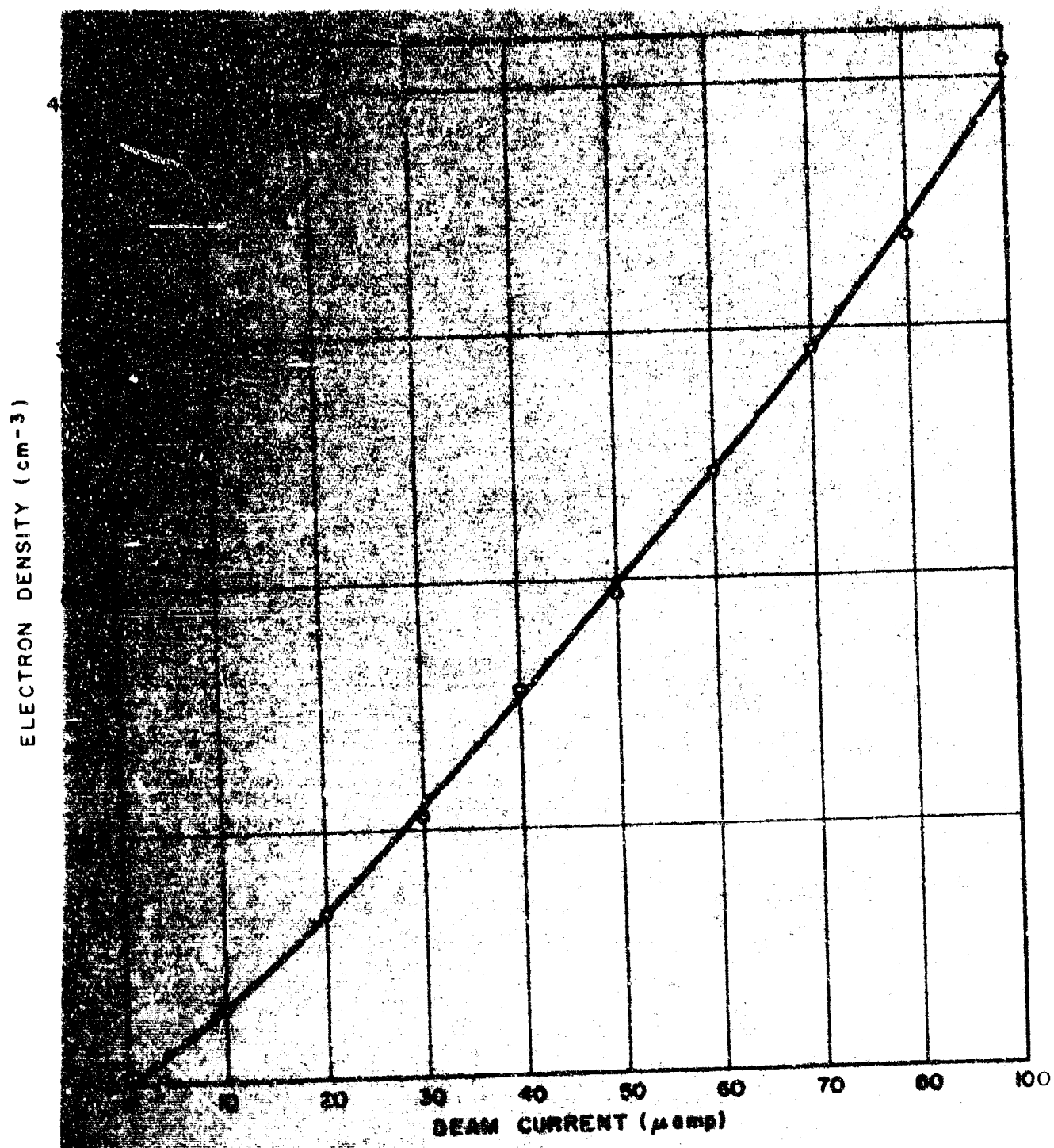
FIGURE 8.12 - ELECTRON DENSITY VS. BEAM CURRENT IN
OXYGEN
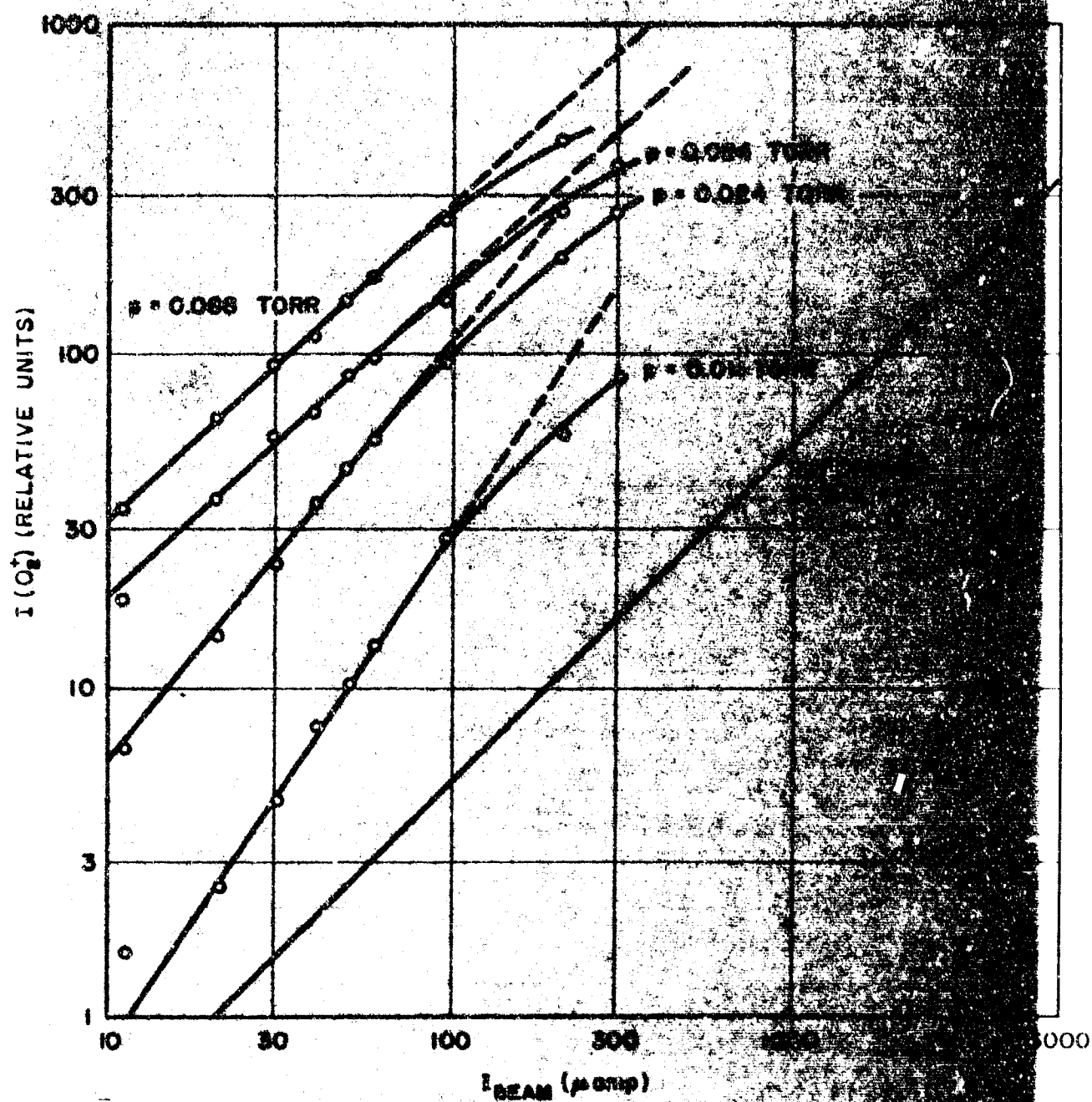
FIGURE 5.10- O_2^+ ION CURRENT VS. I_{BEAM}

162.
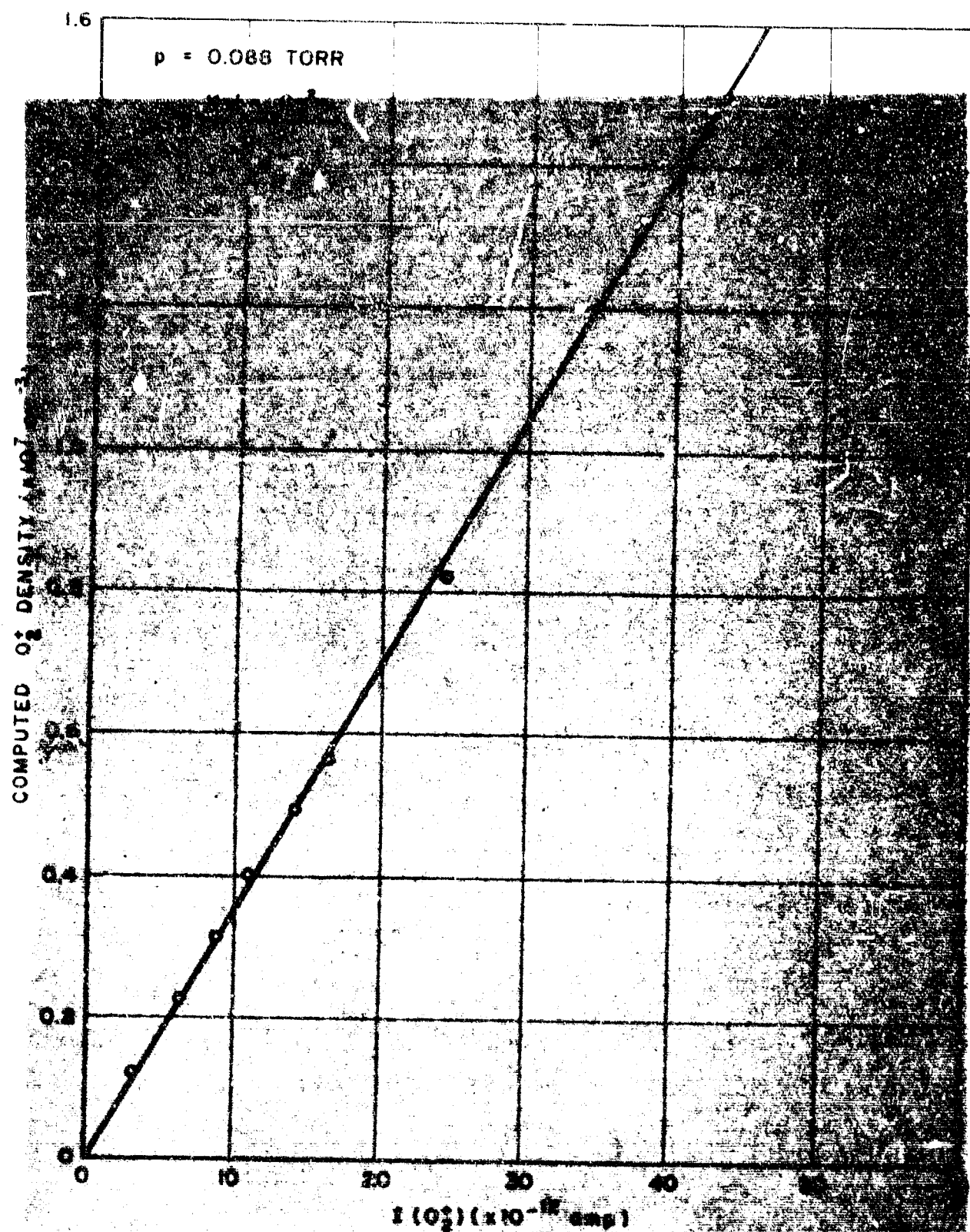
FIGURE 5.11 - COMPARISON BETWEEN MEASURED AND CALCULATED
O_2^+ DENSITIES FROM EQUATION 5.15

164.
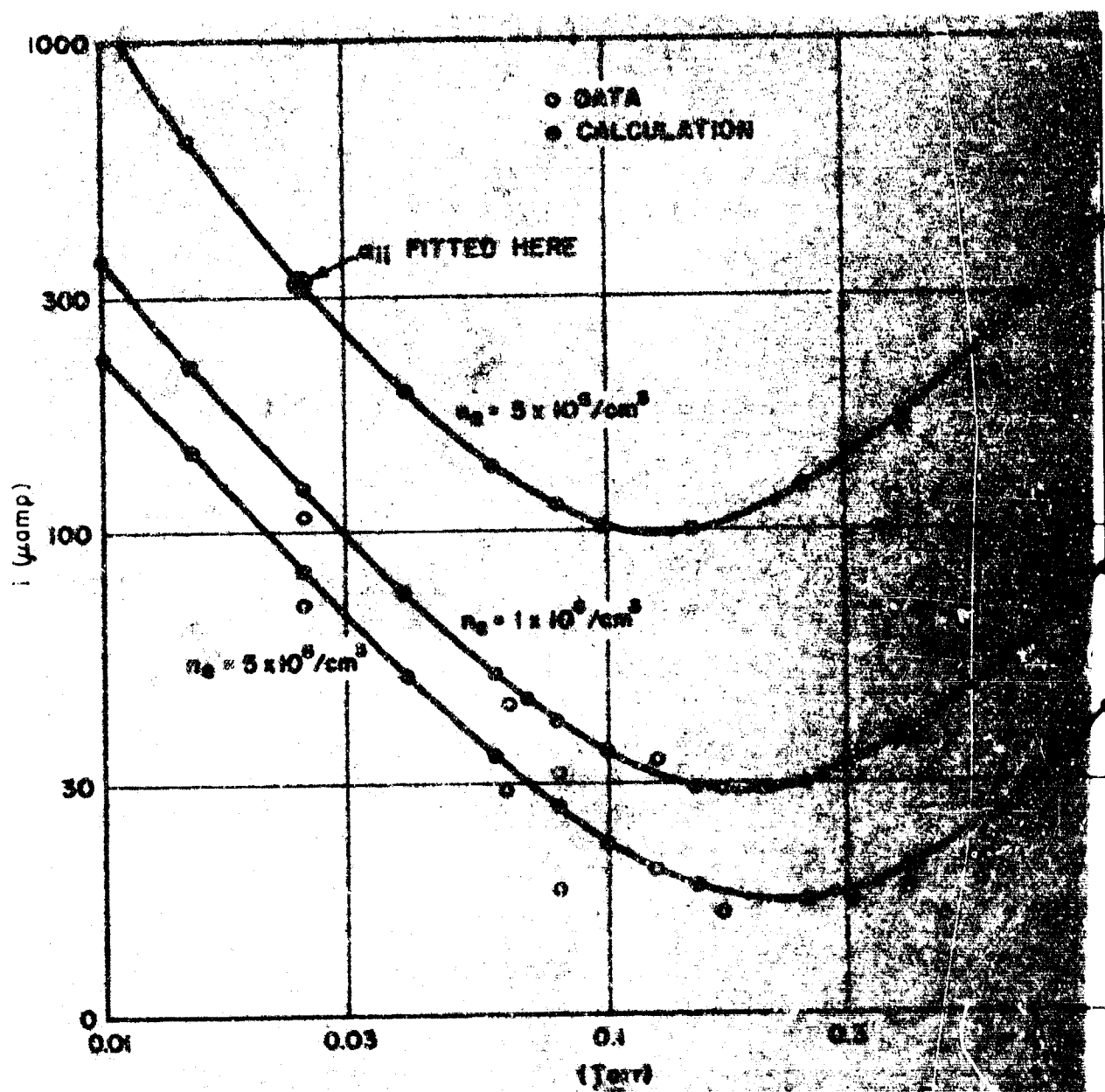
FIGURE 5.13- PLOT OF EQUATION 5.29 AND COMPARISON WITH DATA.
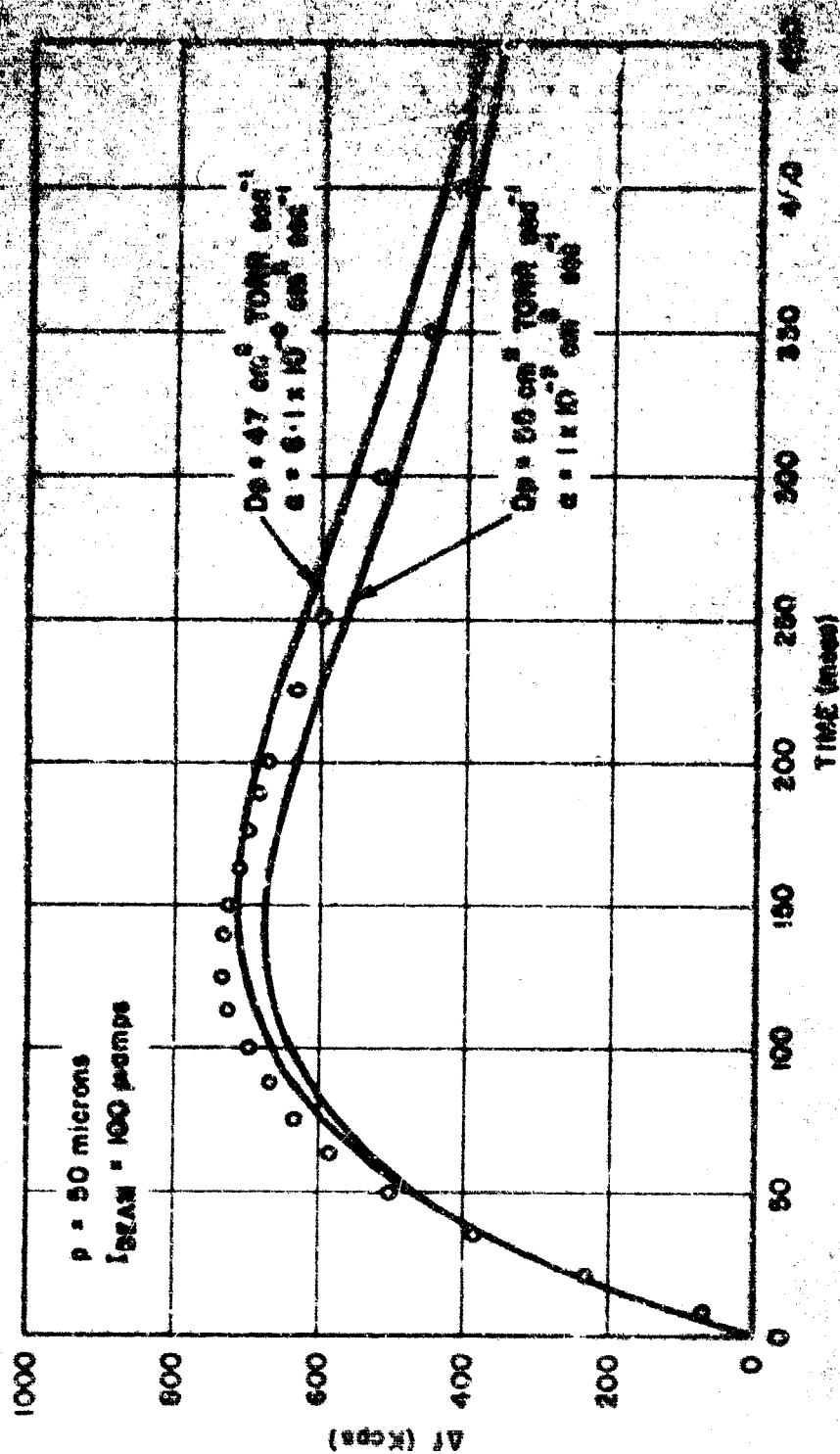
FIGURE 6.14 - FREQUENCY SHIFT VS. TIME AFTER BEAM TURN-ON IN O₂
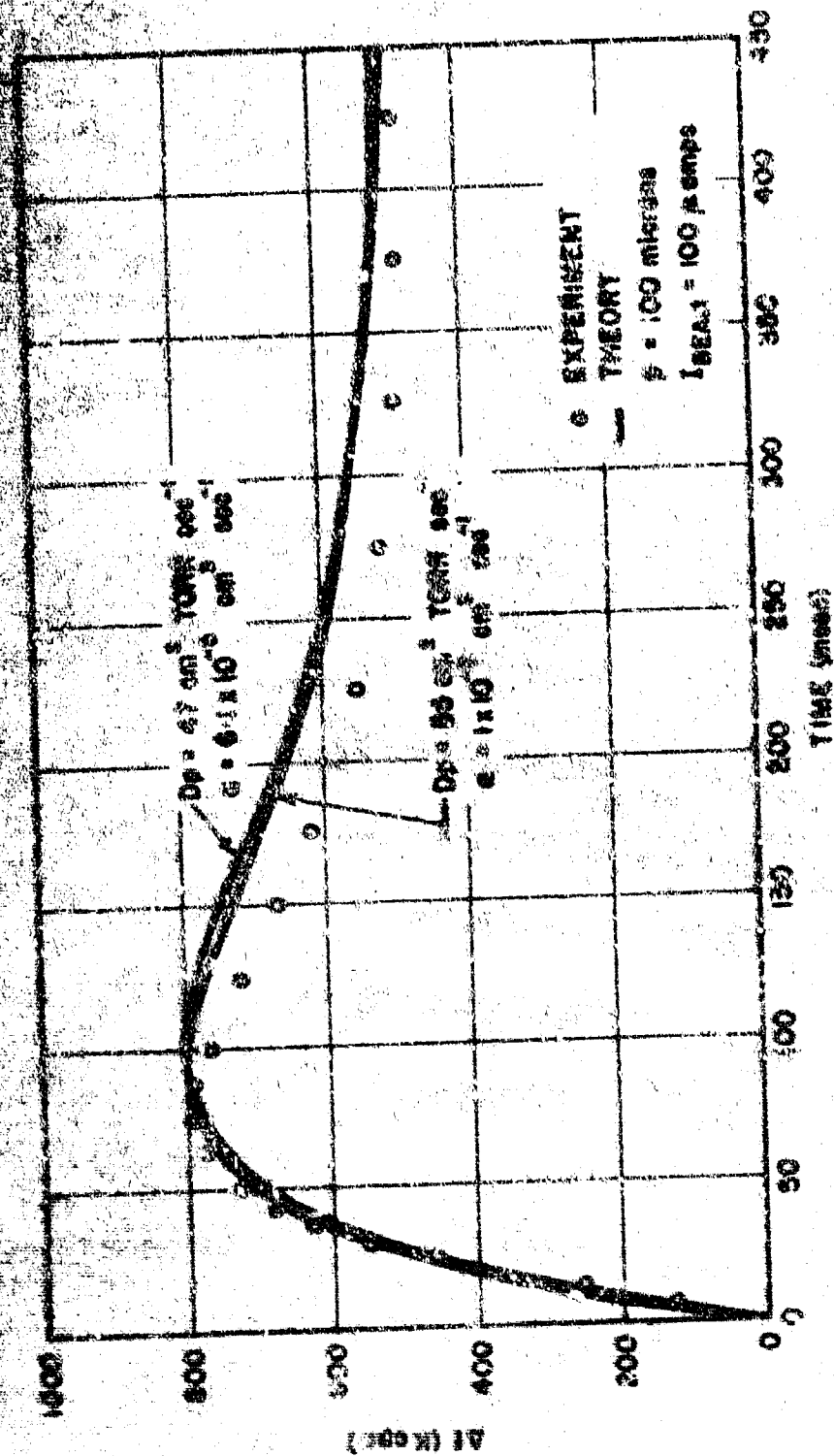
FIGURE D.15 - FREQUENCY SHIFT VS. TIME AFTER BEAM TURN-ON IN O_2
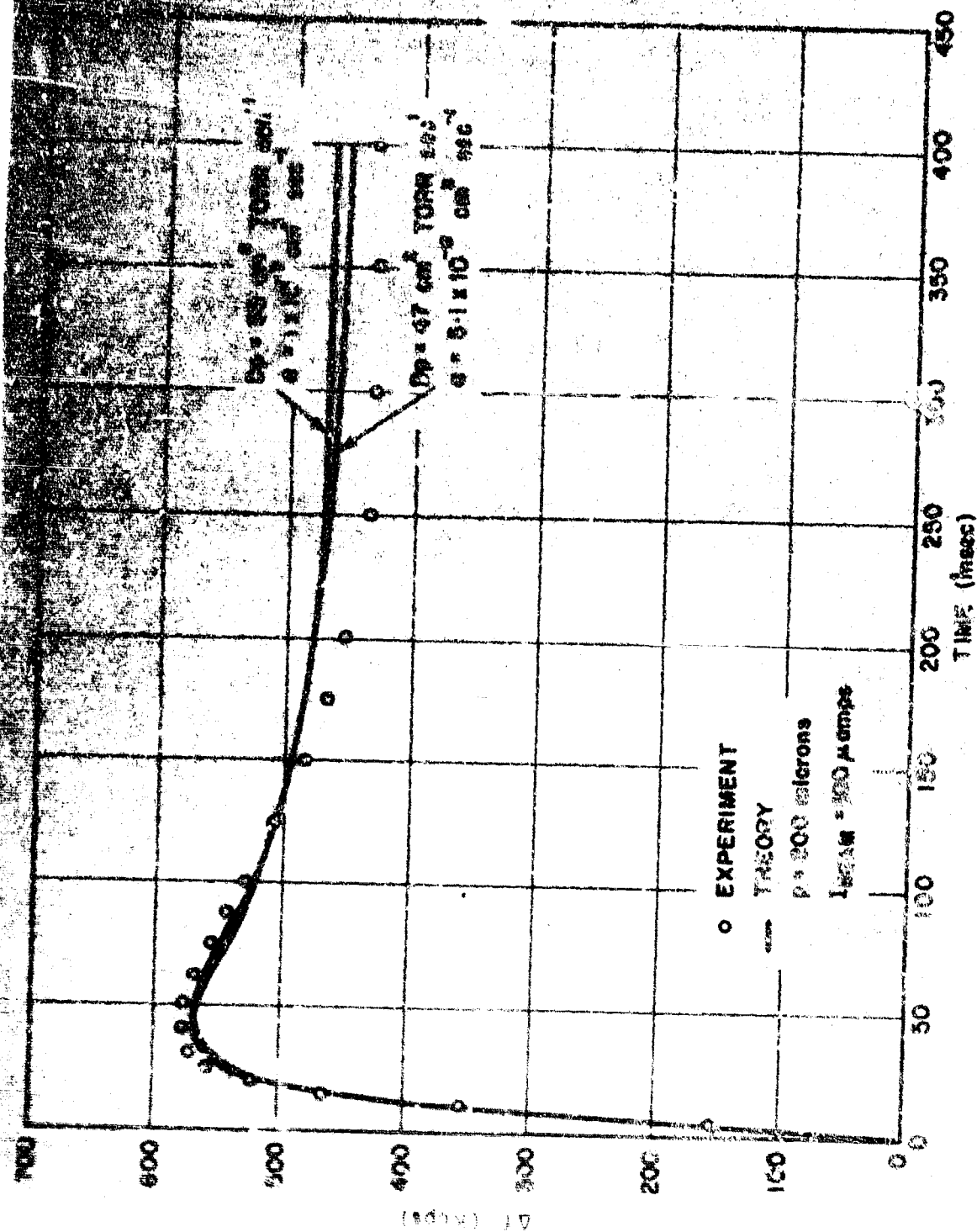
FIGURE 5.16- FREQUENCY SHIFT VS. TIME AFTER BEAM TURN-ON IN O_2
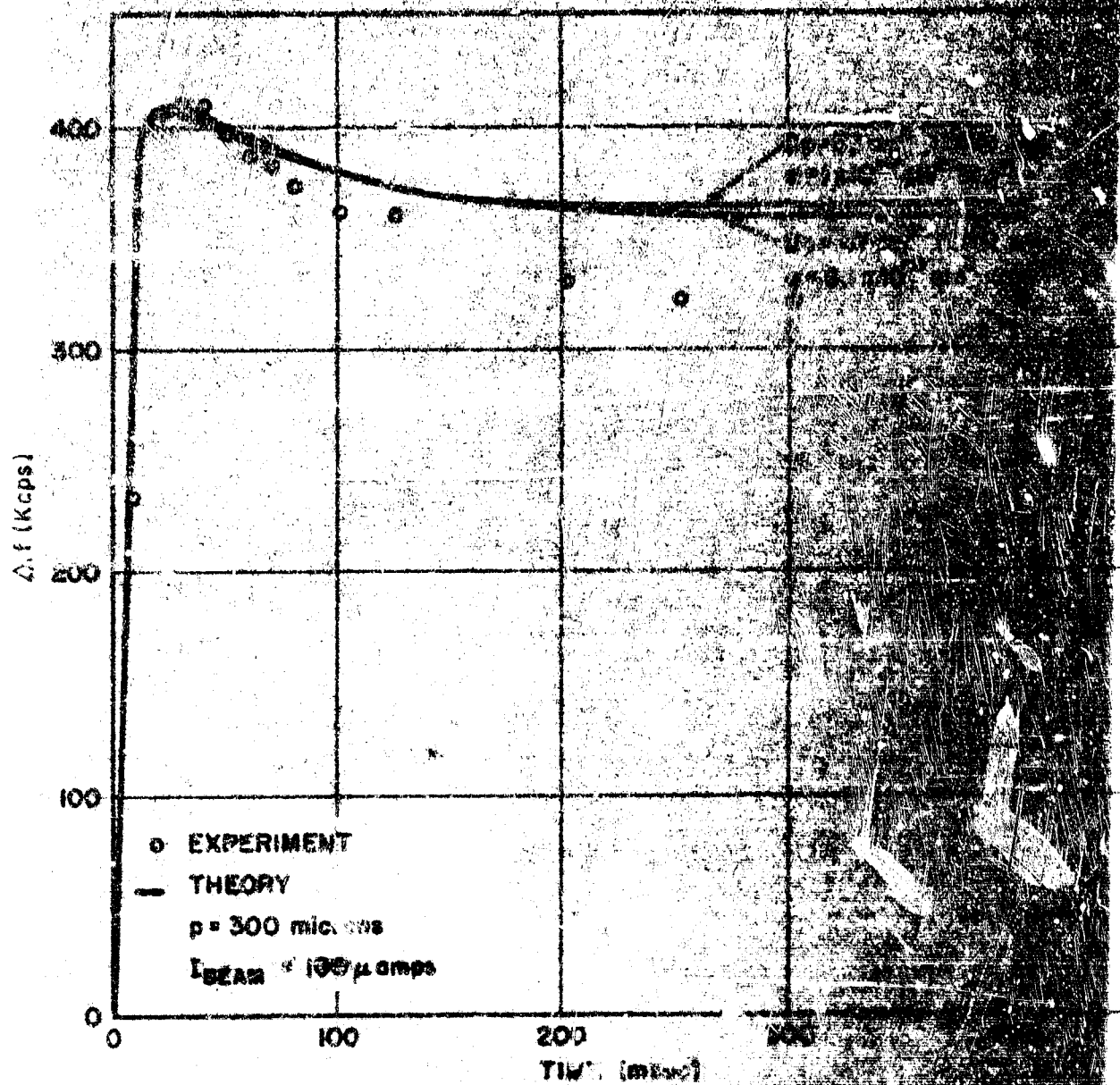
FIGURE 5.17- FREQUENCY SHIFT VS. TIME AFTER
TURN-ON IN O_2
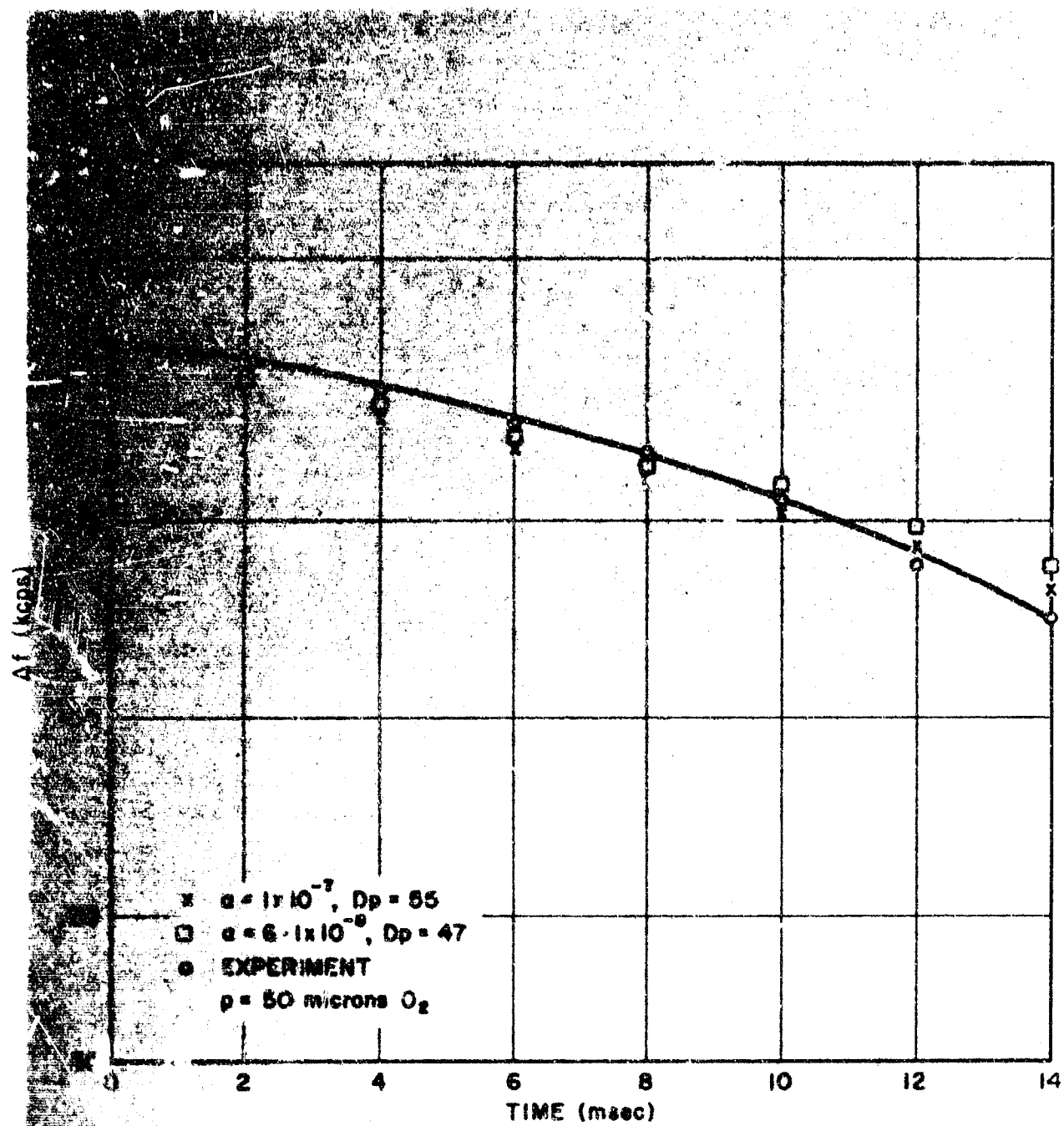
FIGURE 5.18 - ELECTRON AFTERGLOW
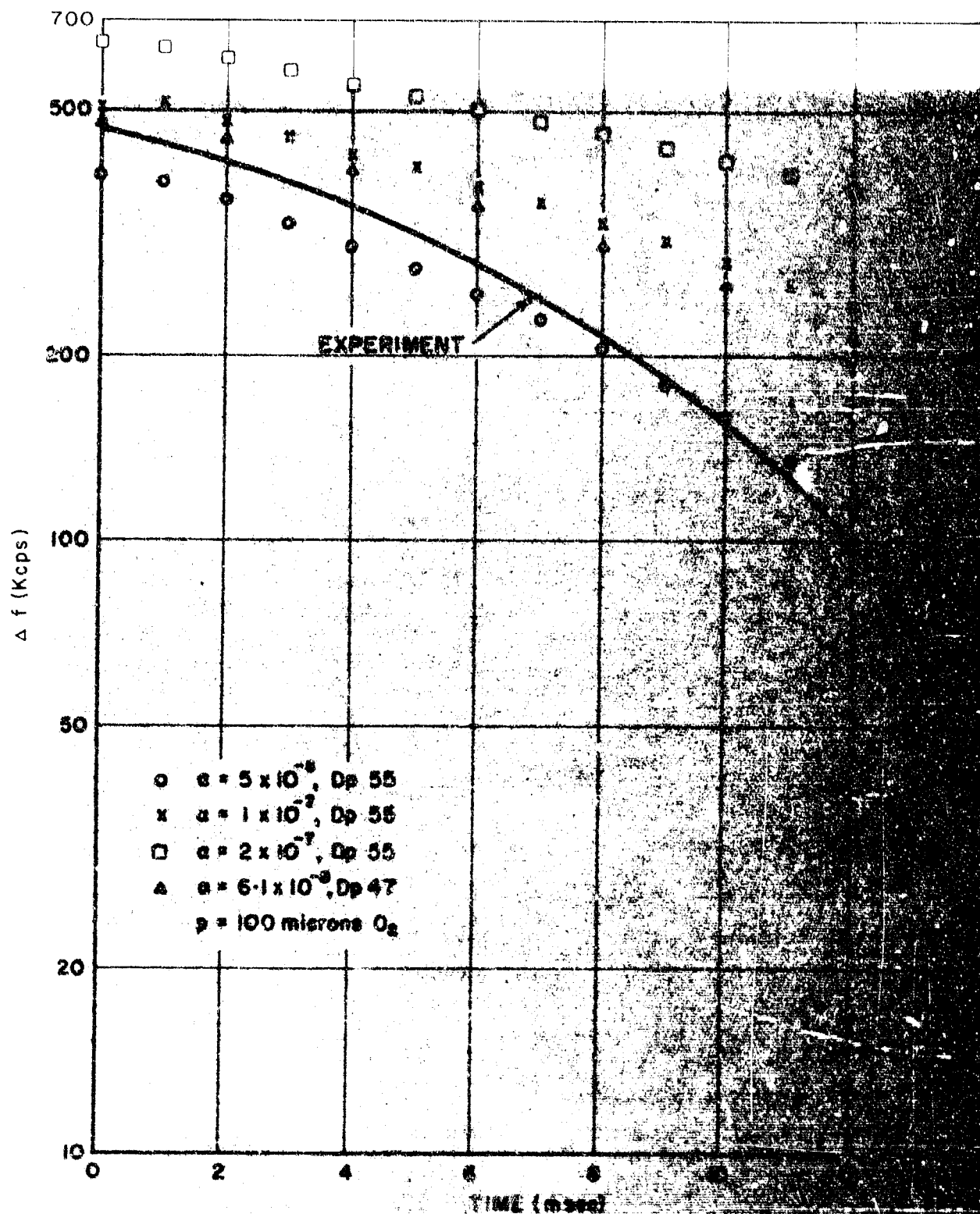
FIGURE 5.19- ELECTRON AFTERGLOW

171.
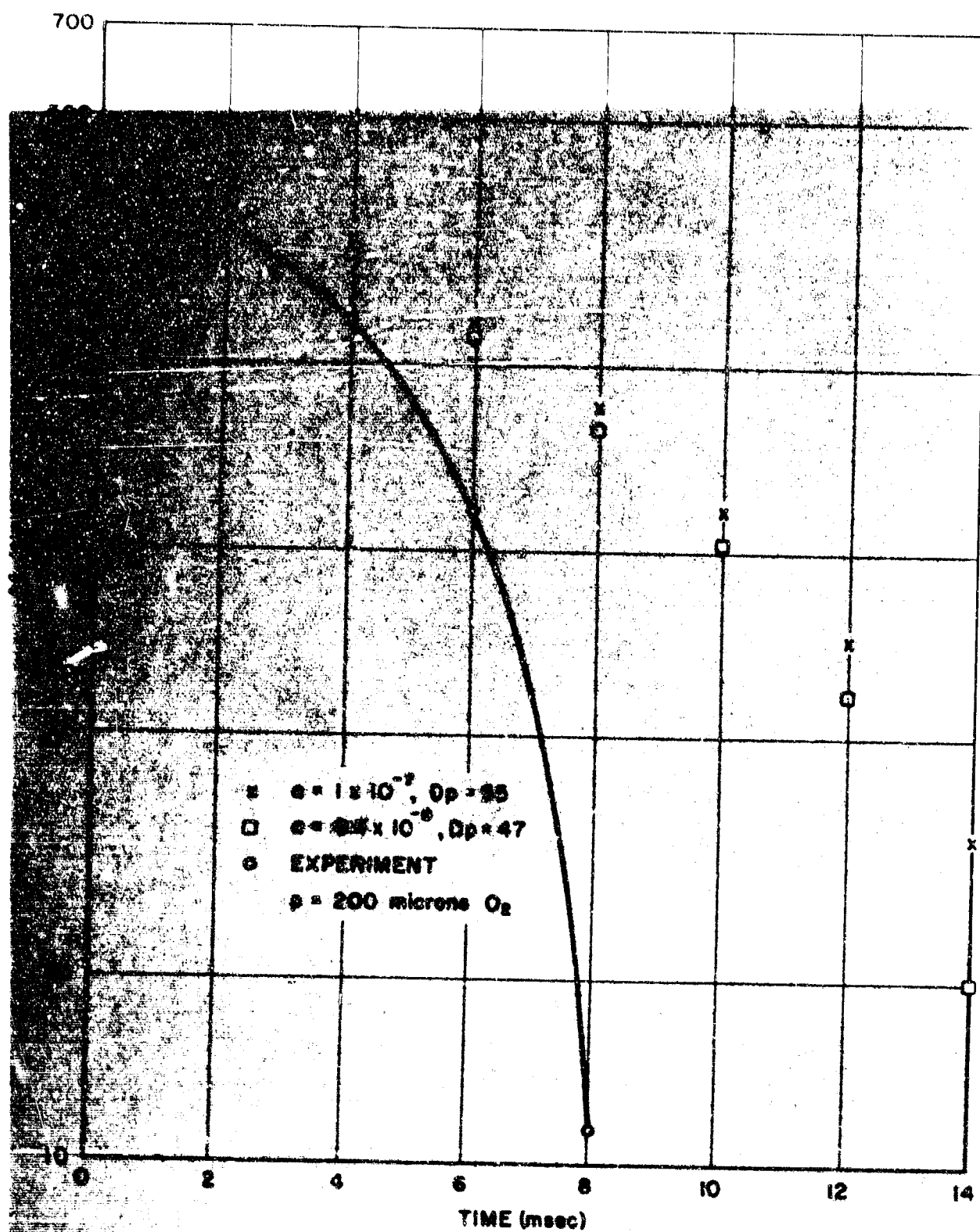
FIGURE 5.20- ELECTRON AFTERGLOW
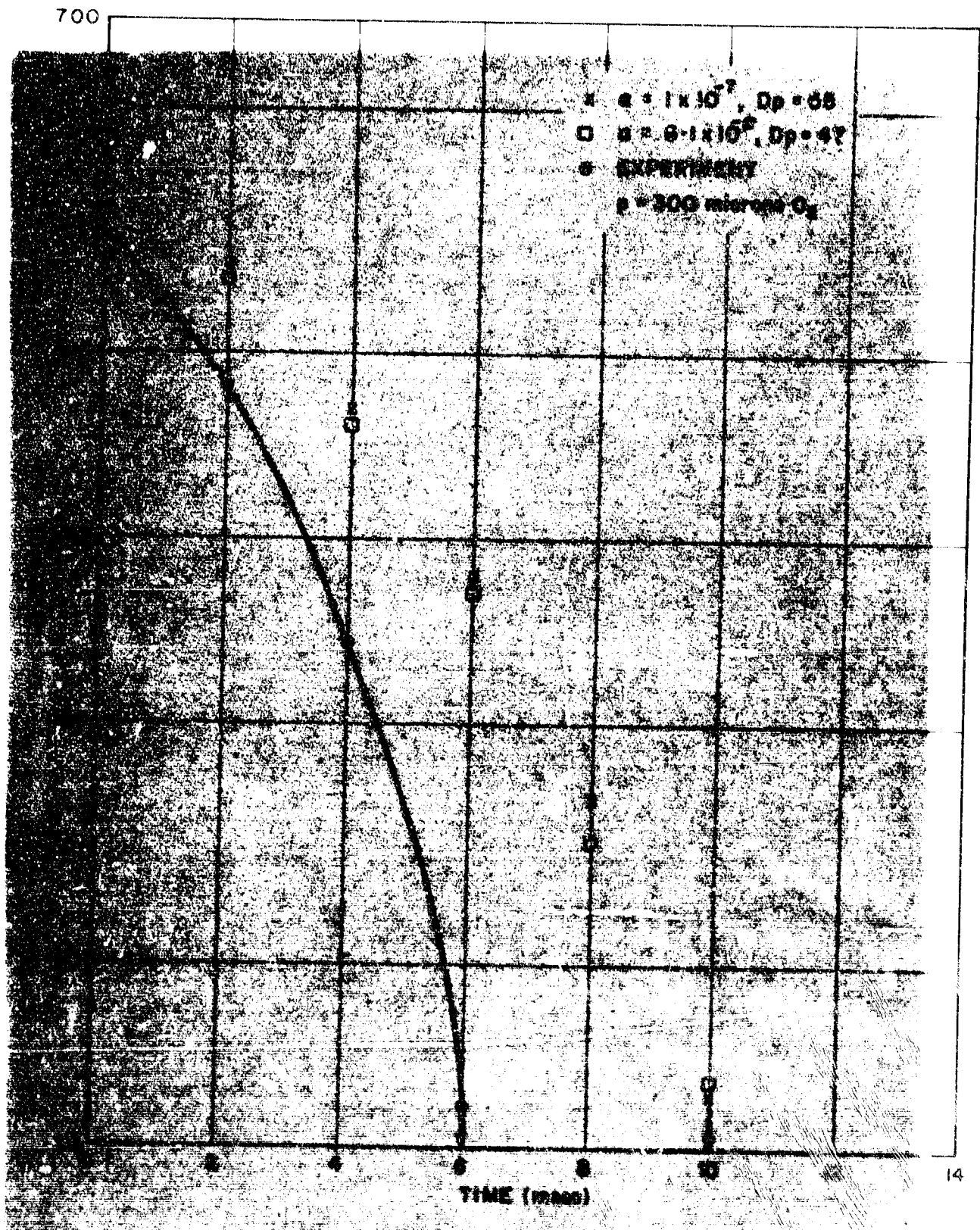
FIGURE 5.21- ELECTRON AFTERGLOW
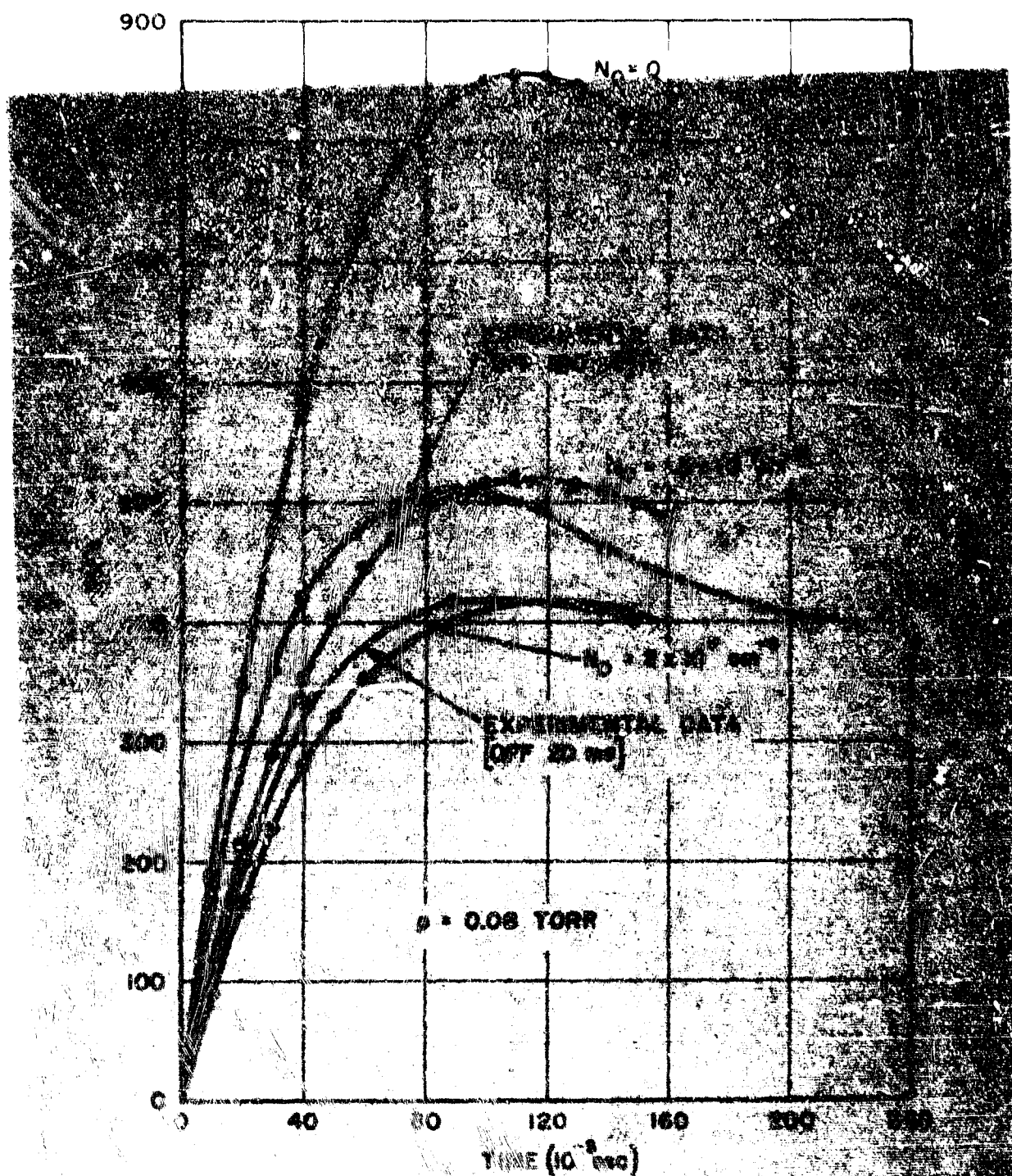
FIGURE 6.22 — EFFECT OF INITIAL NEGATIVE ION
DENSITY ON CALCULATED ELECTRON
DENSITIES DURING TURN ON IN
OXYGEN.

174.
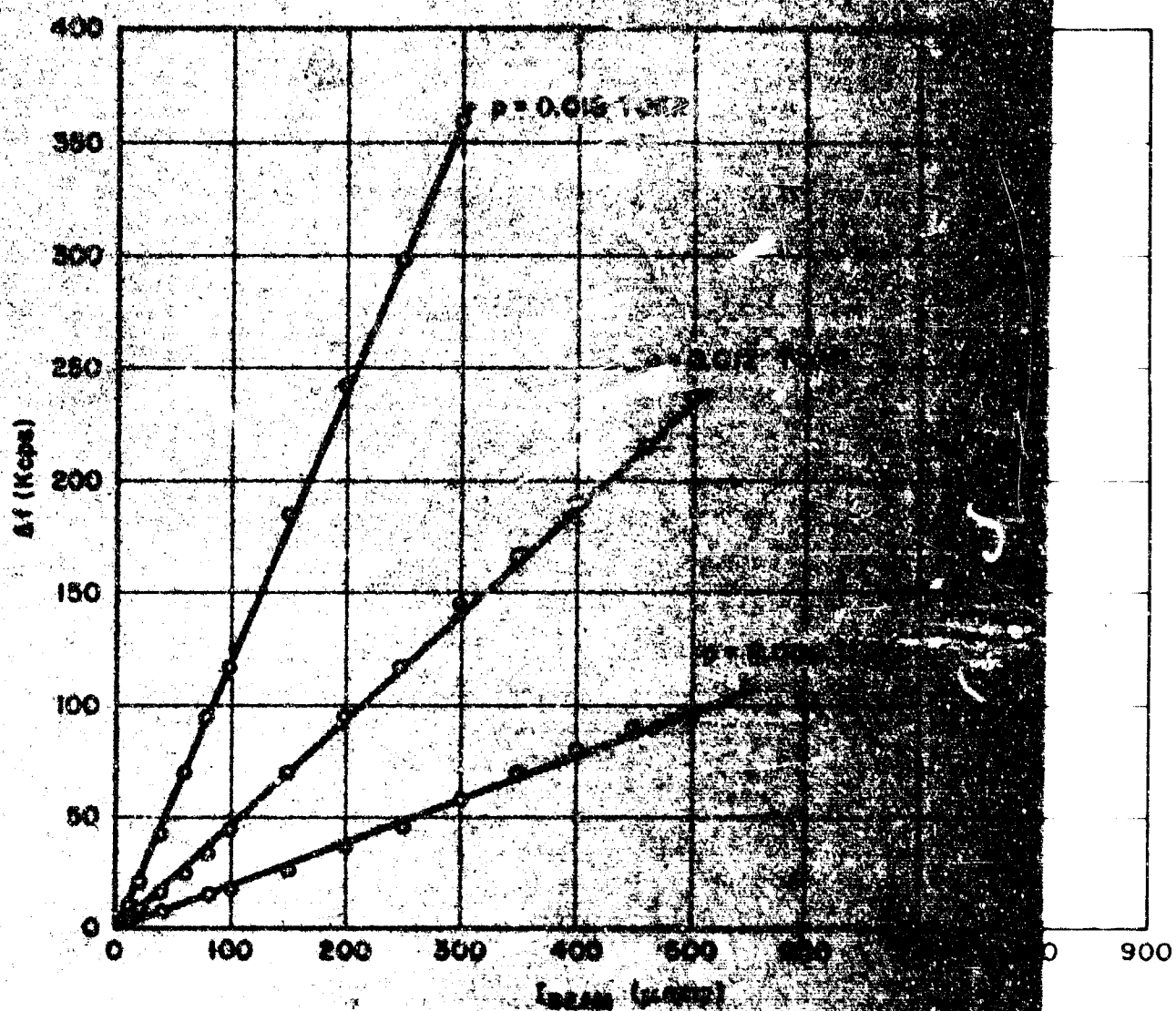
FIGURE 5.23- STEADY-STATE ELECTRON DENSITY vs BEAM CURRENT IN NITROGEN
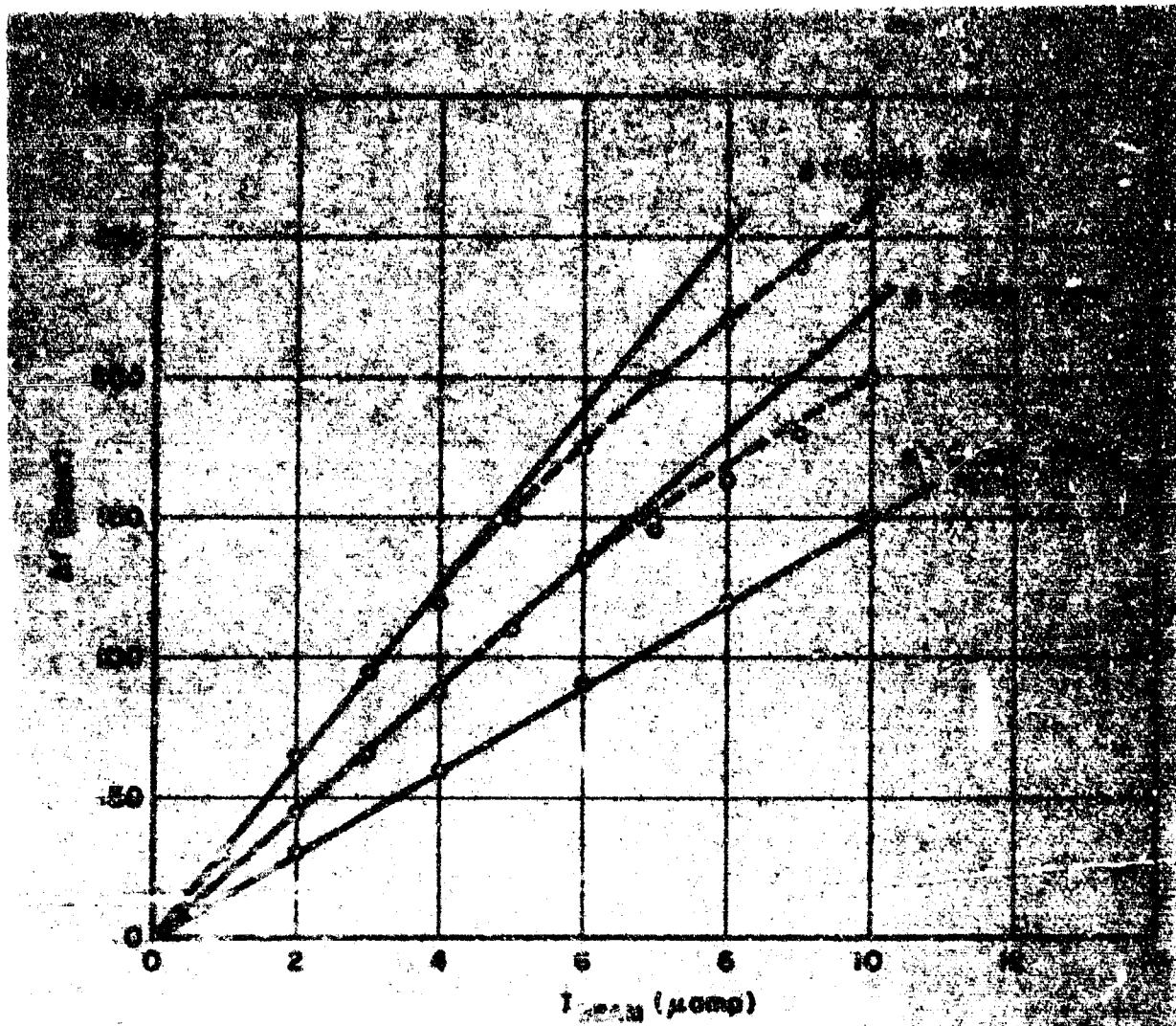
FIGURE 5.24 — STEADY-STATE ELECTRON DENSITY VS.
BEAM CURRENT IN NITROGEN

FIGURE 3.23 STEADY STATE SLOPES VS. PRESSURE IN NITROGEN
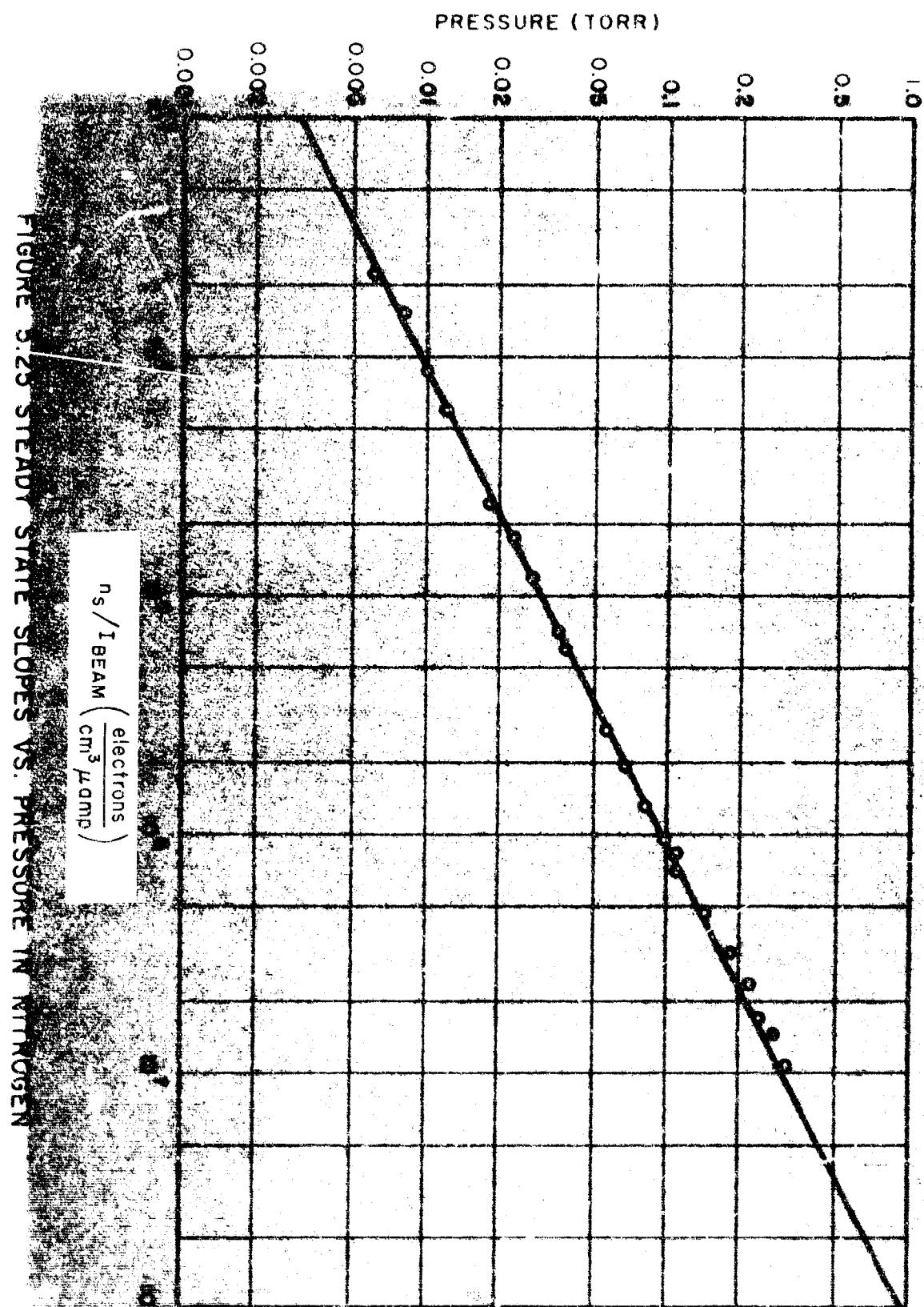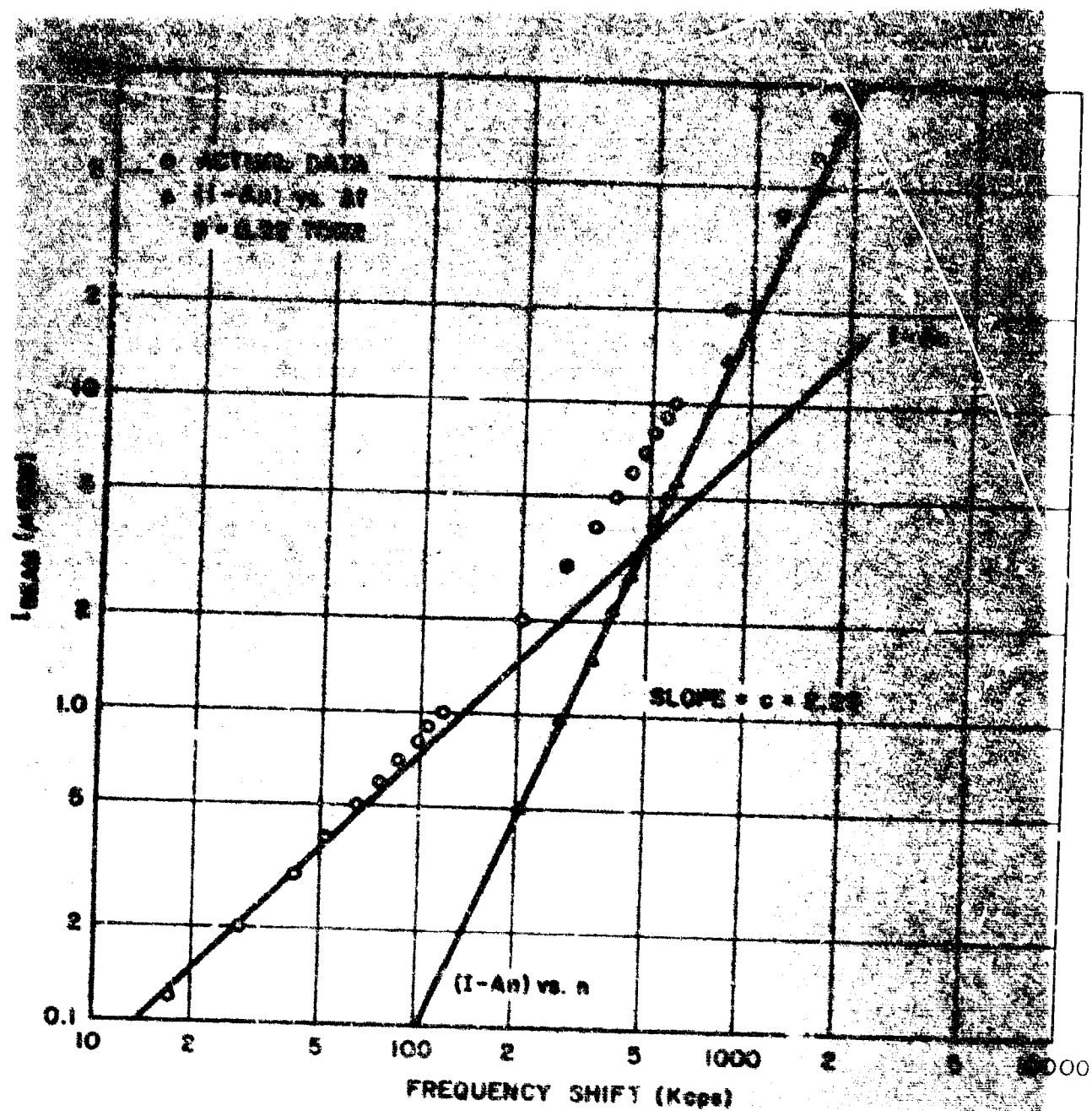
FIGURE 5.26— DECOMPOSITION OF ELECTRON DENSITY DATA INTO $Kp_i = An + Bn^c$

RESULTS OF DECOMPOSITION OF STEADY-STATE
ELECTRON DENSITIES INTO THE FORM

$$Kpi = A_n + B_n{}^c$$

PRESSURE (Torr)	$n_{intersection}$	c
0.057	1.25×10^7	2.07
0.067	1.25×10^7	2.20
0.081	7.7×10^6	2.60
0.098	9.4×10^6	2.26
0.110	8.2×10^6	2.24
0.145	9.5×10^6	2.24
0.185	9.5×10^6	2.92
0.220	5.5×10^6	2.38
0.240	8.5×10^6	2.32
0.275	9.0×10^6	2.53
0.310	8.1×10^6	2.50

NOTE: $(n_{intersection})^{c-1} = A/B$

FIGURE 5.27
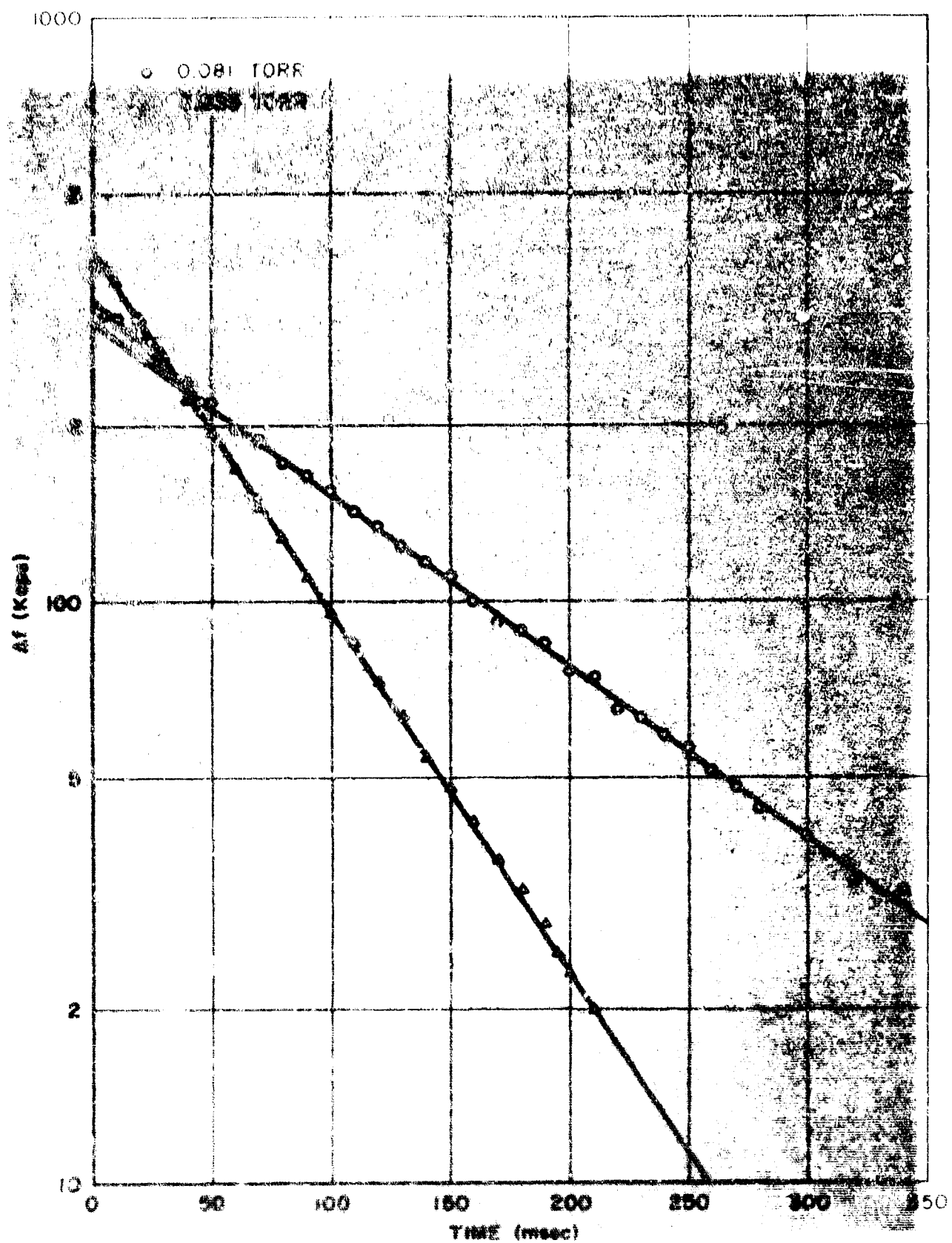
FIGURE 5 28 - ELECTRON DENSITY DECAY IN NITROGEN AT 0.081 TORR AND 0.035 TORR
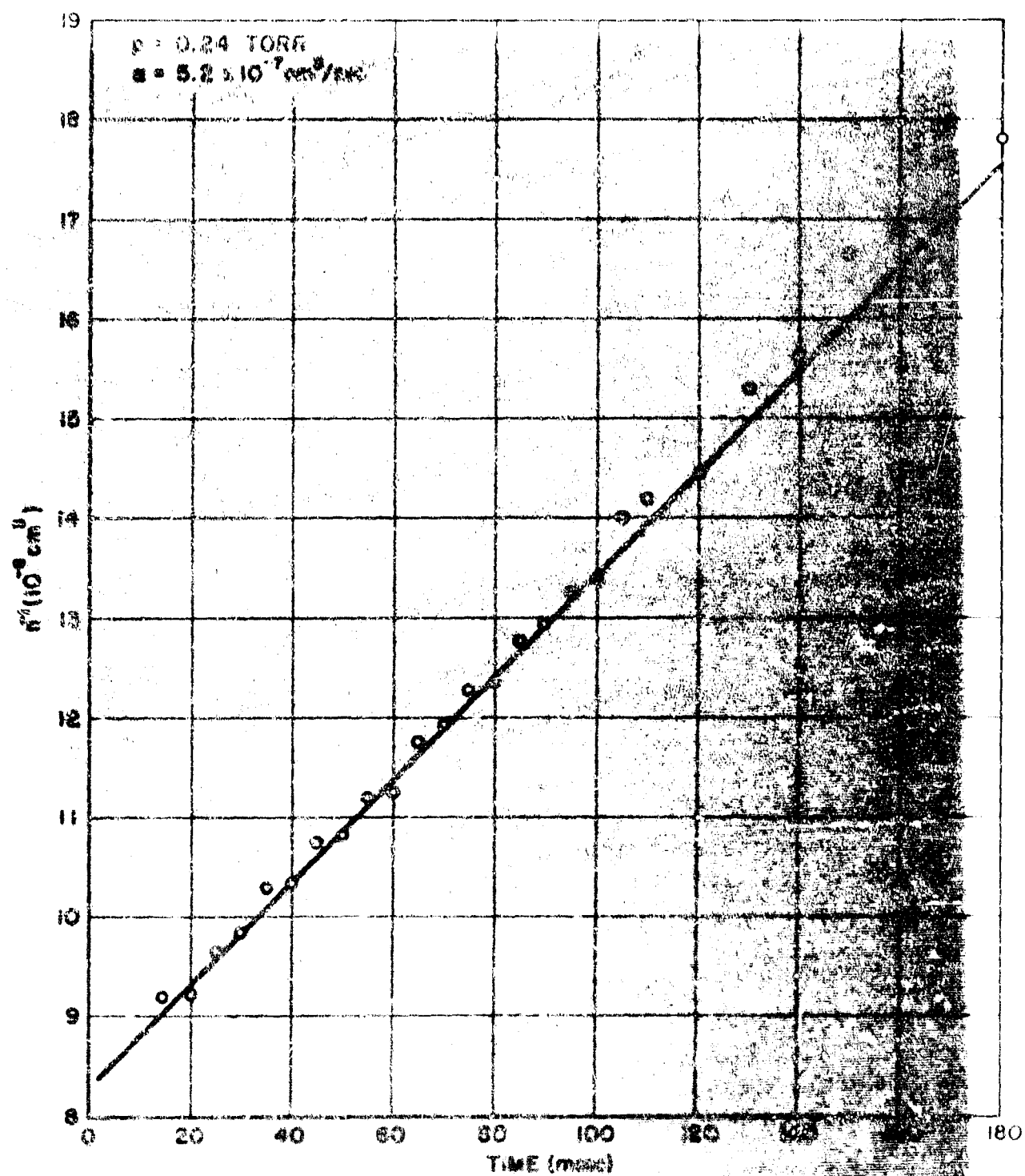
FIGURE 5.29 - RECOMBINATION PLOT FOR NITROGEN AFTERGLOW
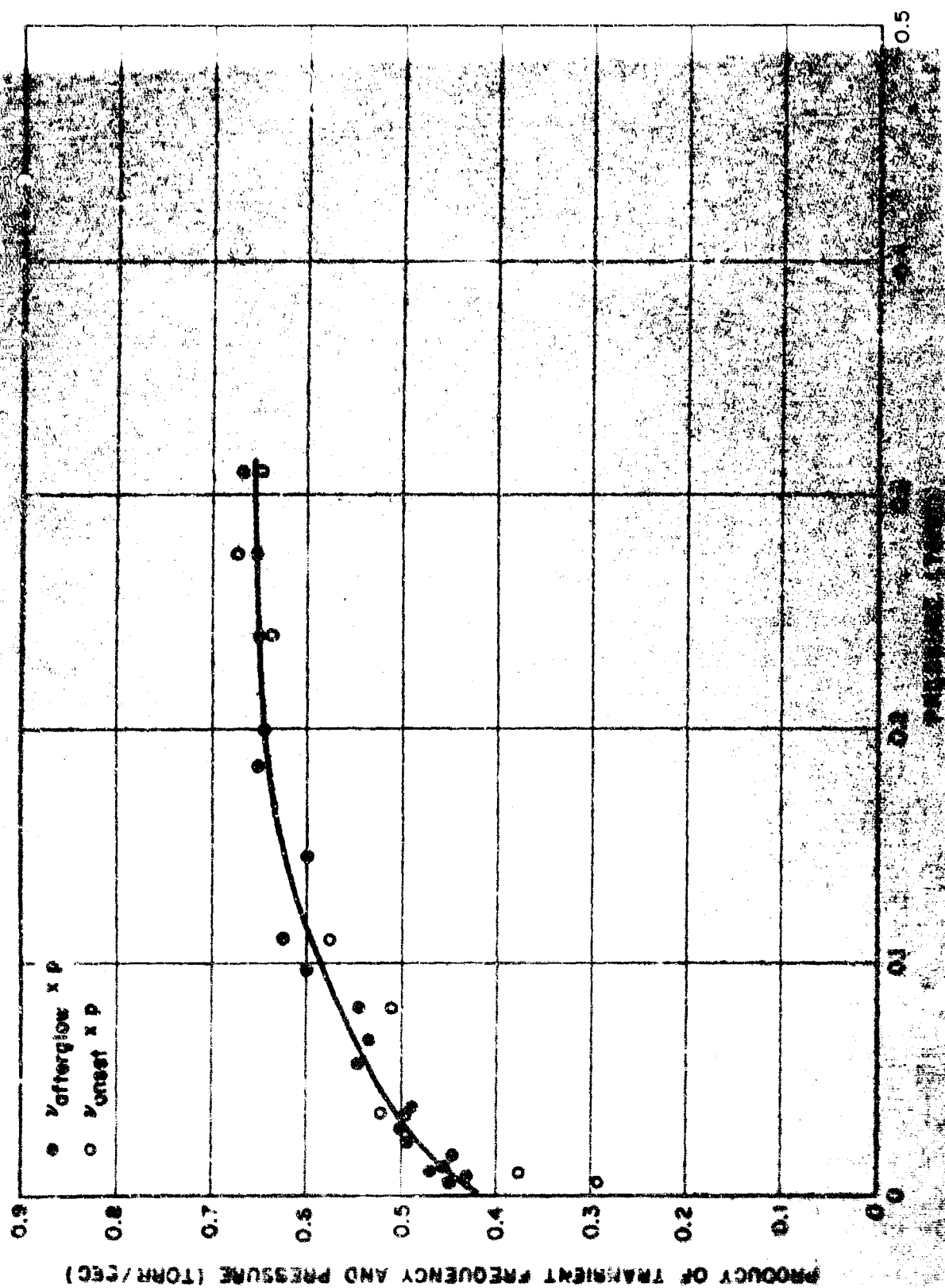
FIGURE 5.30- LINEAR BEHAVIOR OF TRANSIENT ELECTRON DENSITIES IN NITROGEN
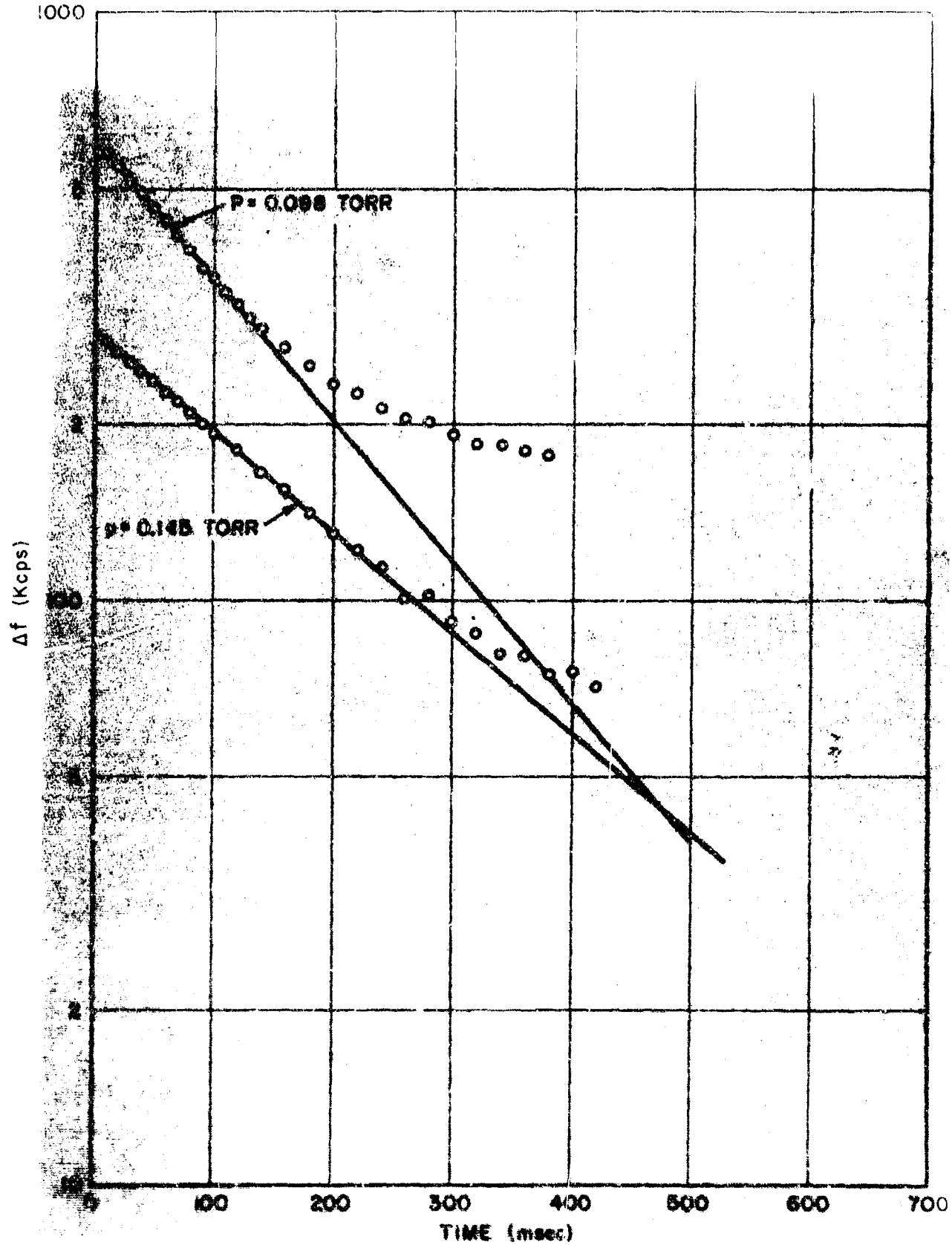
FIGURE 5.31 - ELECTRON DENSITY BUILD-UP IN NITROGEN
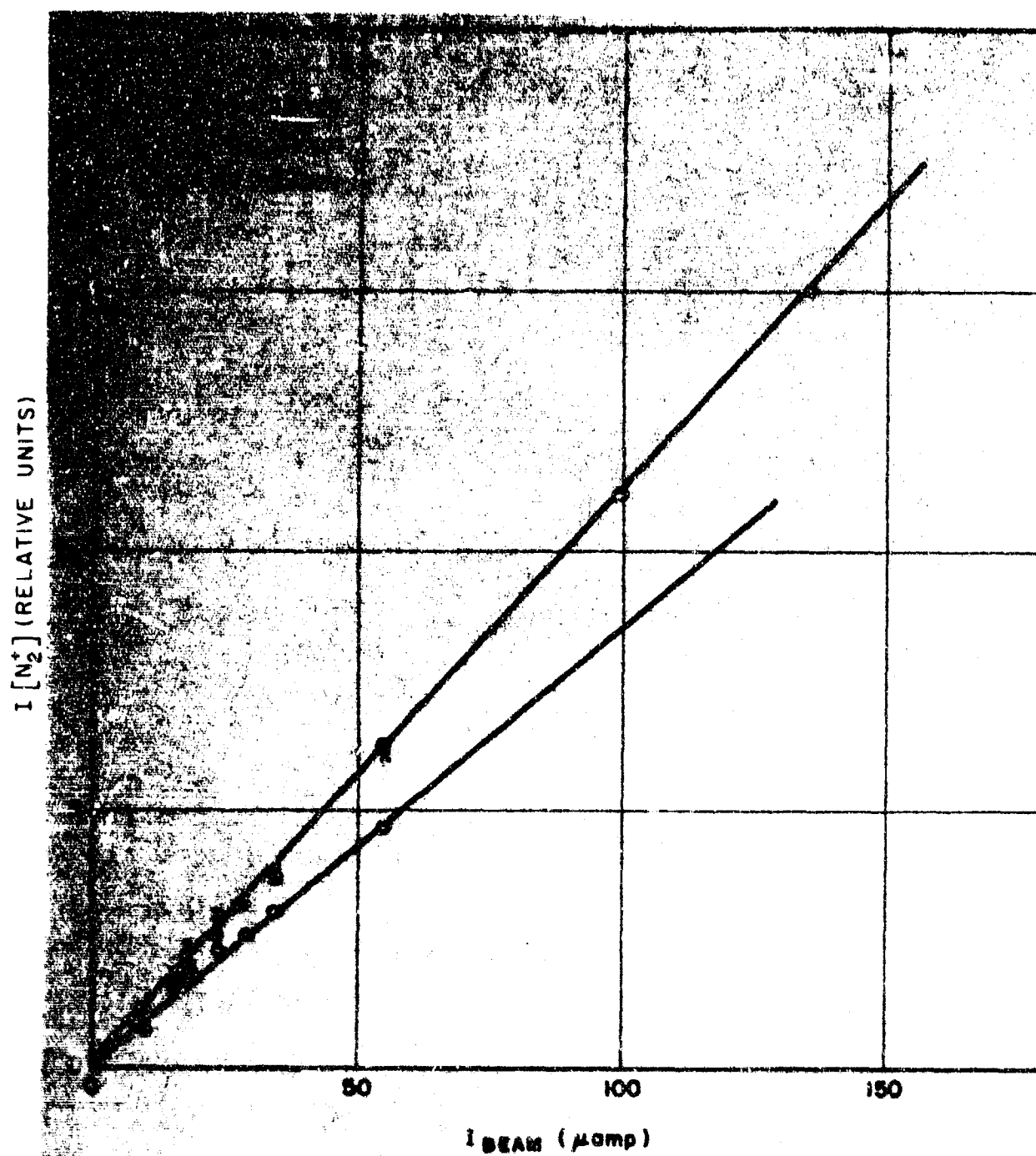
FIGURE 5.32- N$_2^+$ CURRENT VS. I$_{BEAM}$ AT SEVERAL PRESSURES
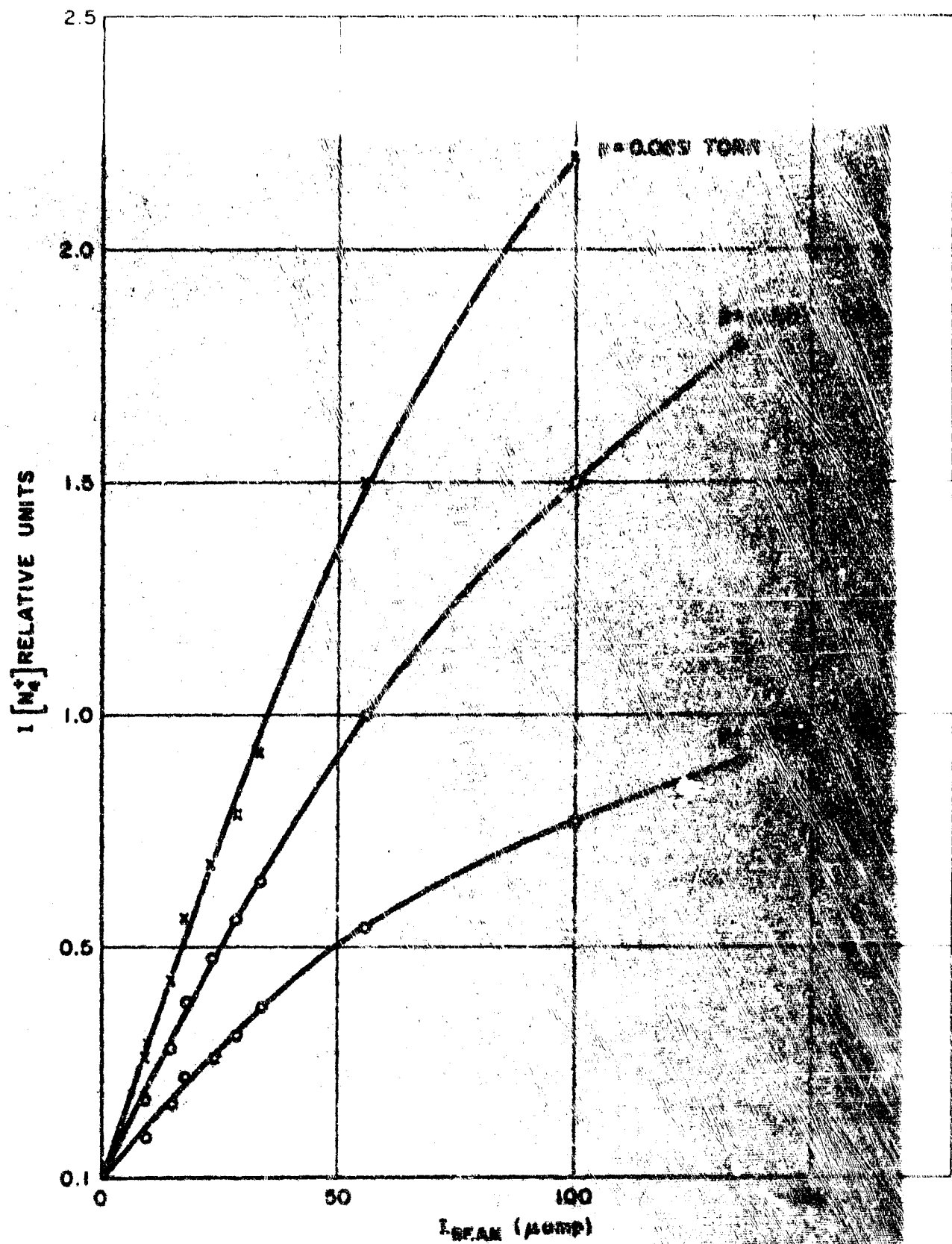
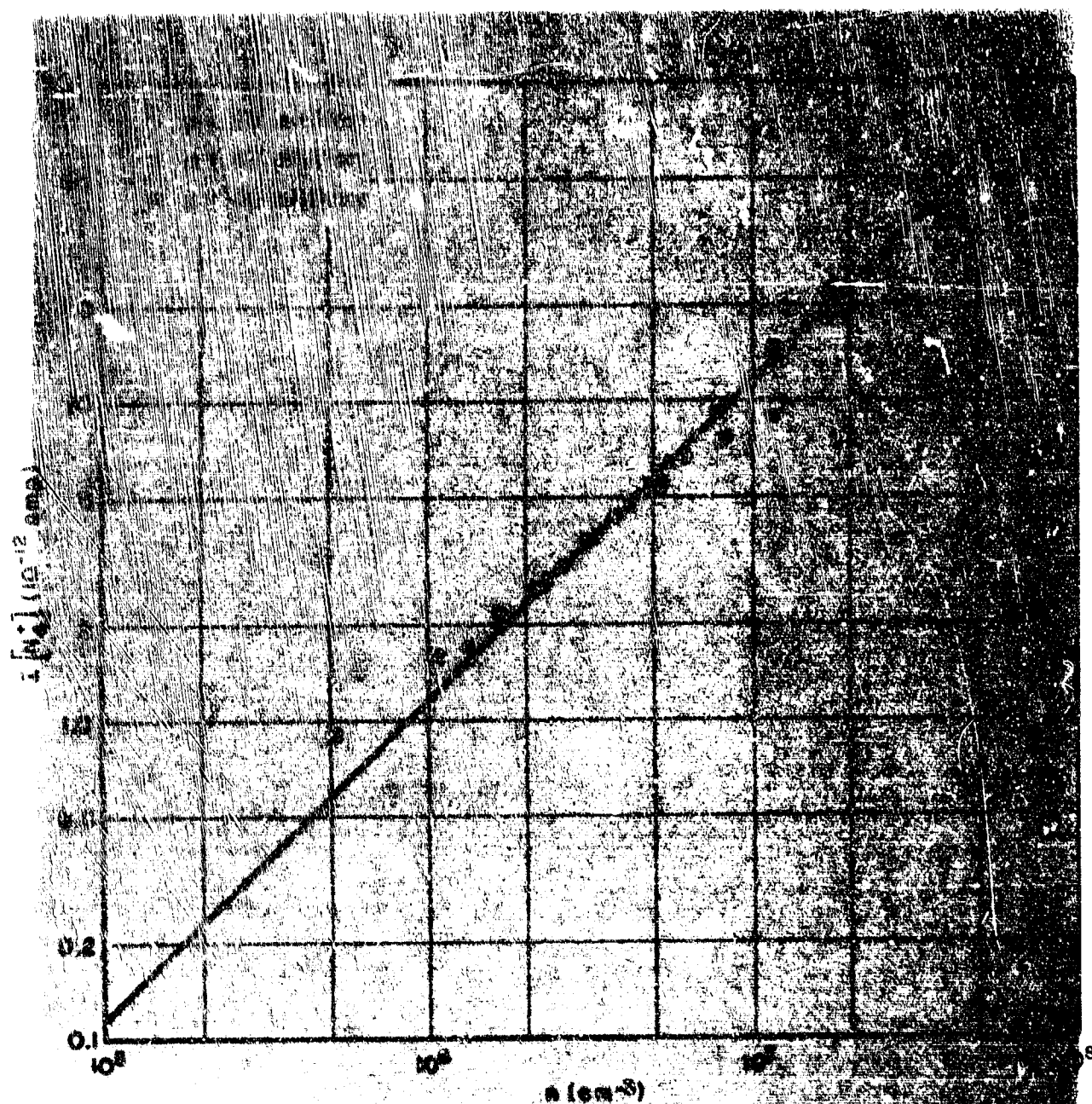FIGURE 5.33- N_4^+ CURRENT VS. I_{BEAM} AT SEVERAL PRESSURE

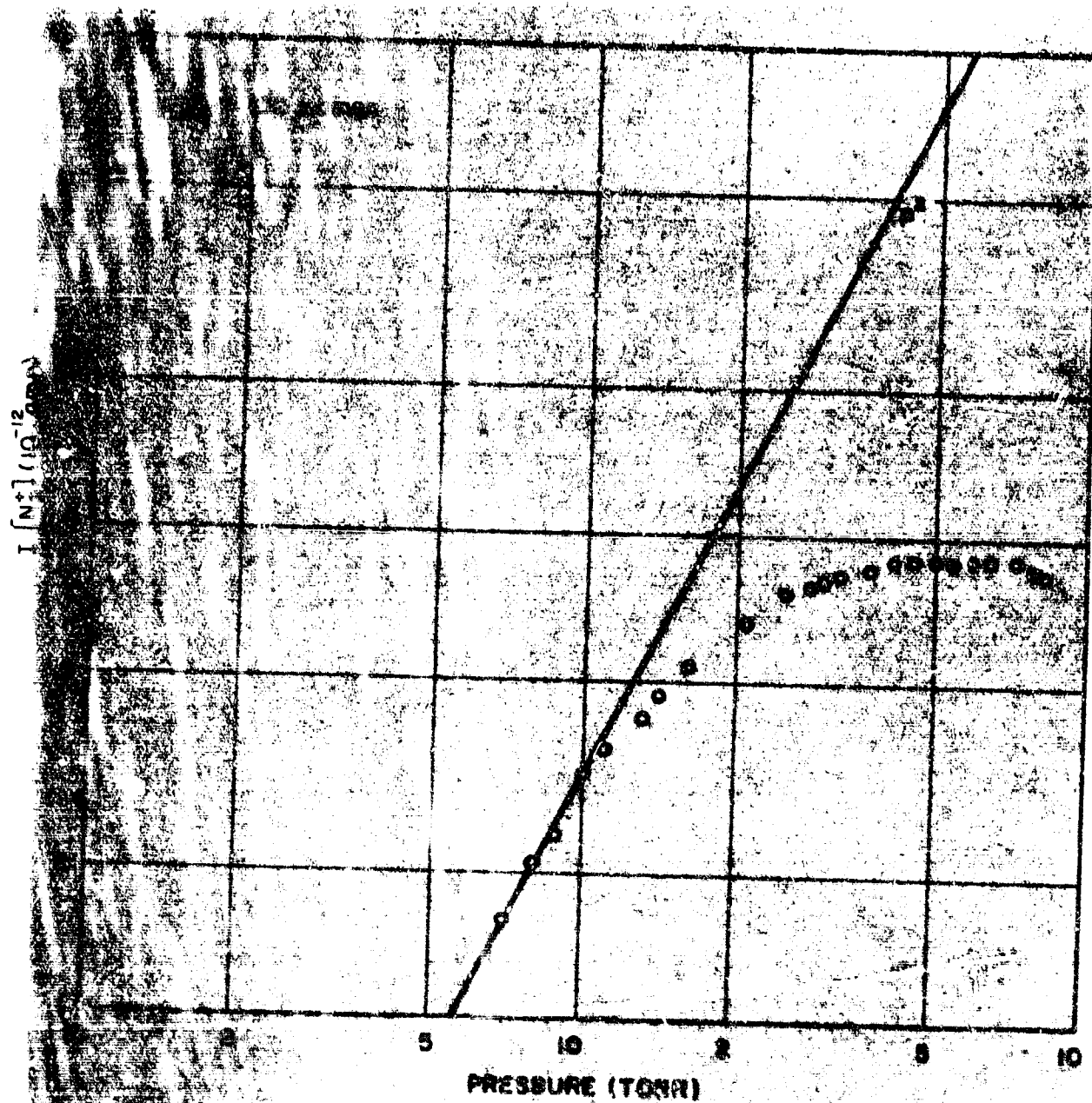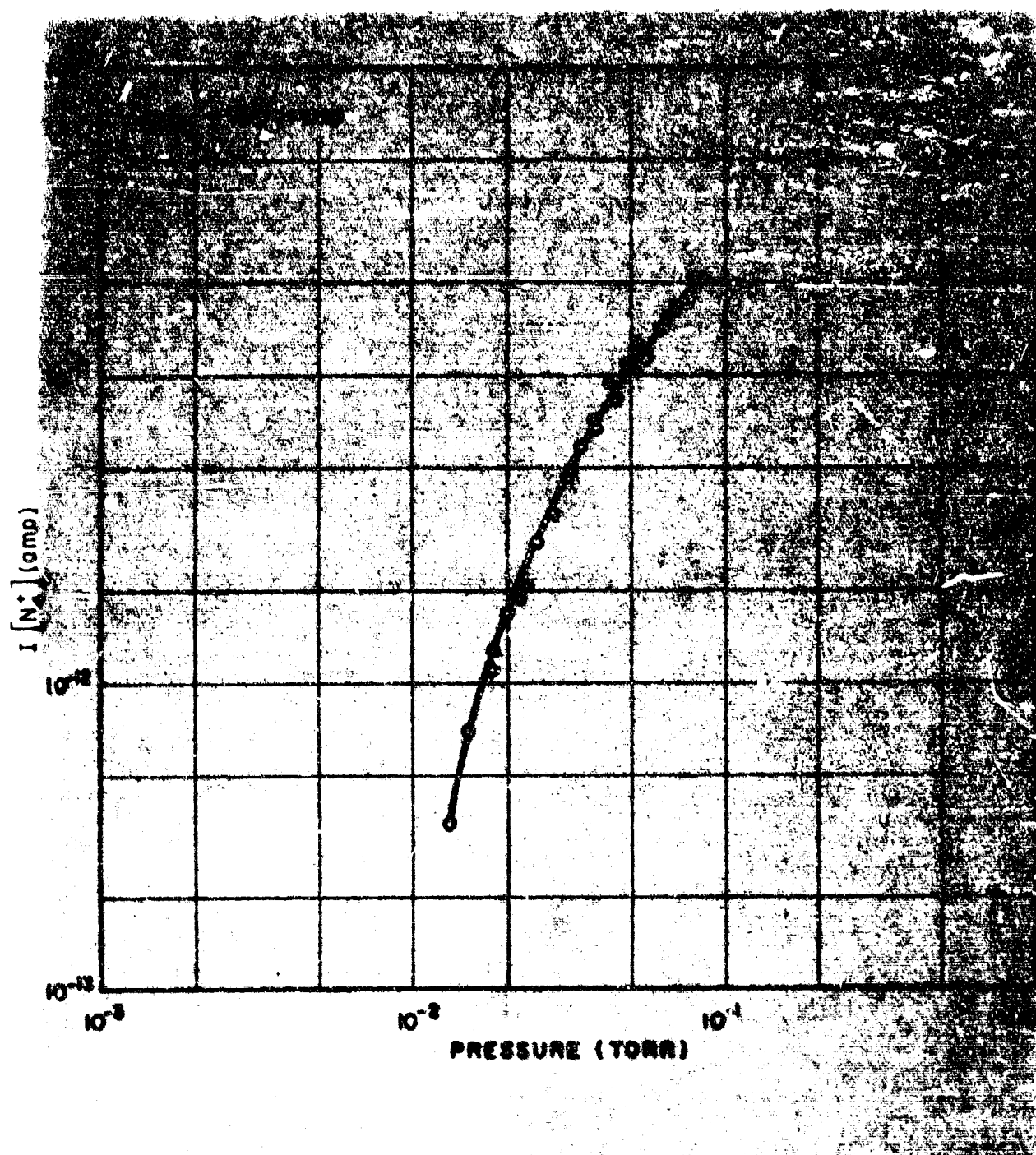FIGURE 5.34- N_2^+ ION CURRENT VS. ELECTRON ENERGY AT SEVERAL PRESSURES

FIGURE 5.35 — $I\left[N_2^+\right]$ VS. PRESSURE IN PURE NITROGEN

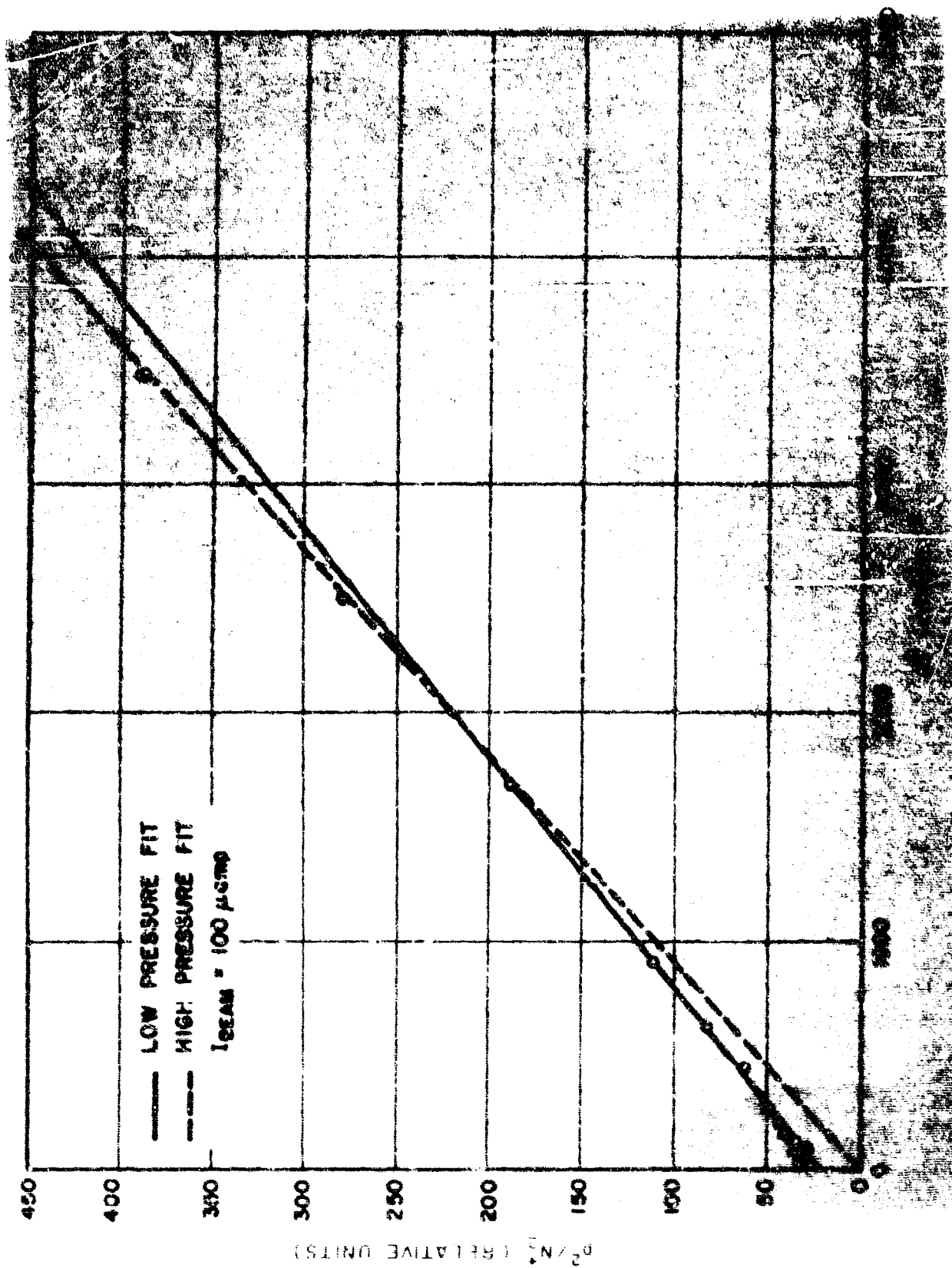FIGURE 5.36- $I[N_4^+]$ VS. PRESSURE IN PURE NITROGEN
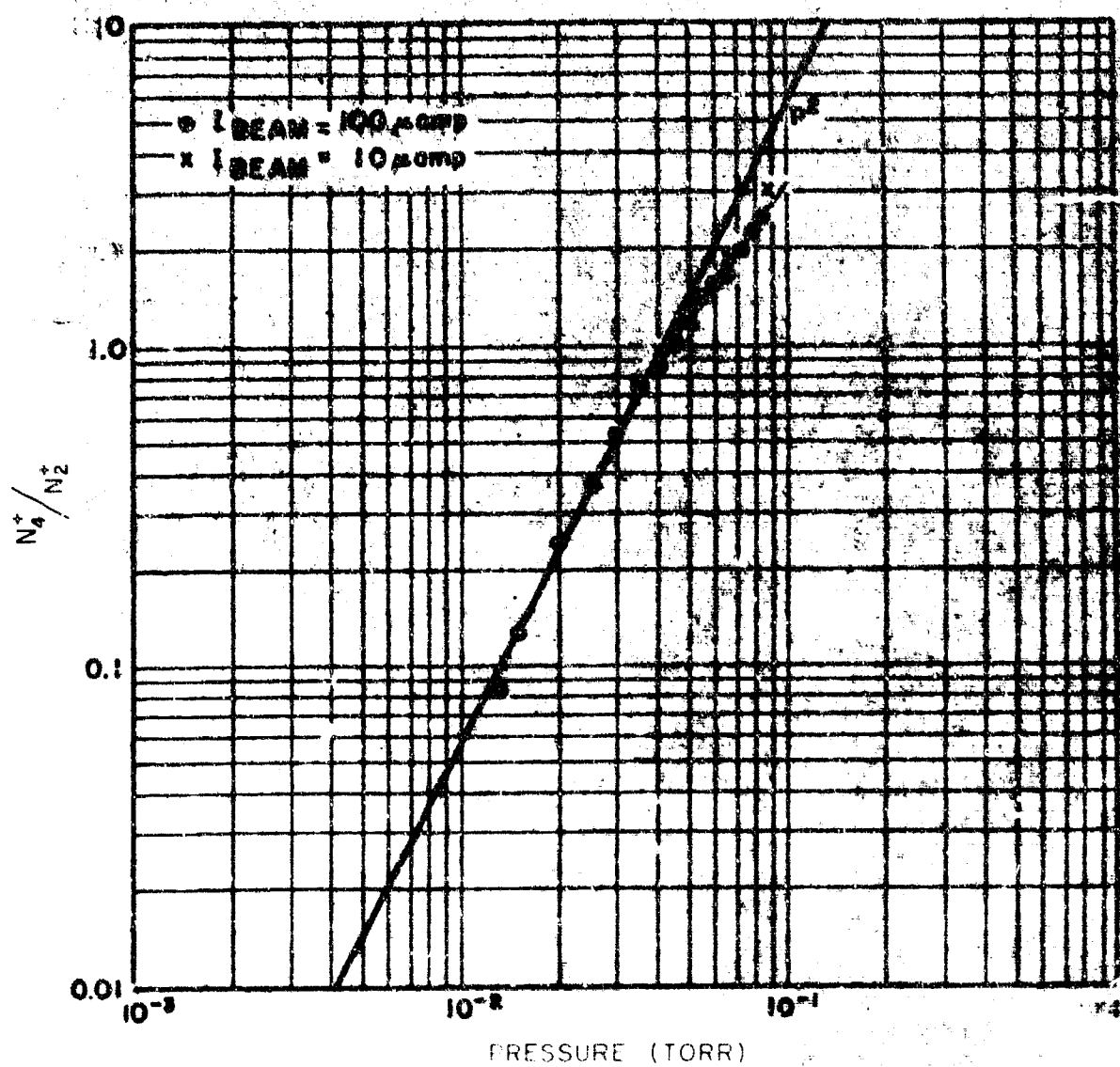
FIGURE 5.37- RATIO OF N_4^+ TO N_2^+ ION CURRENT VS. PRESSURE
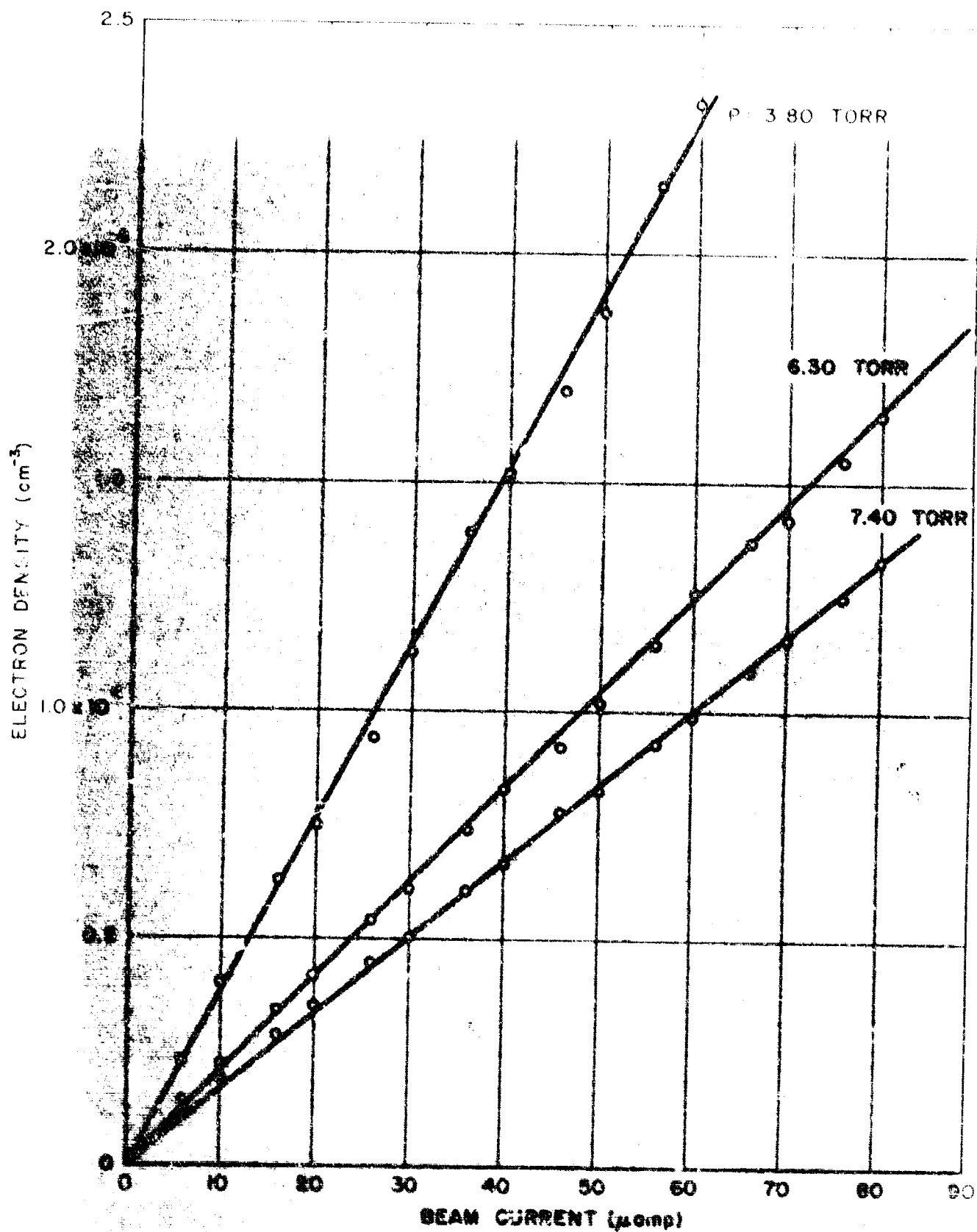
FIGURE 5.38 p^2/N_2 VS. ρ^2

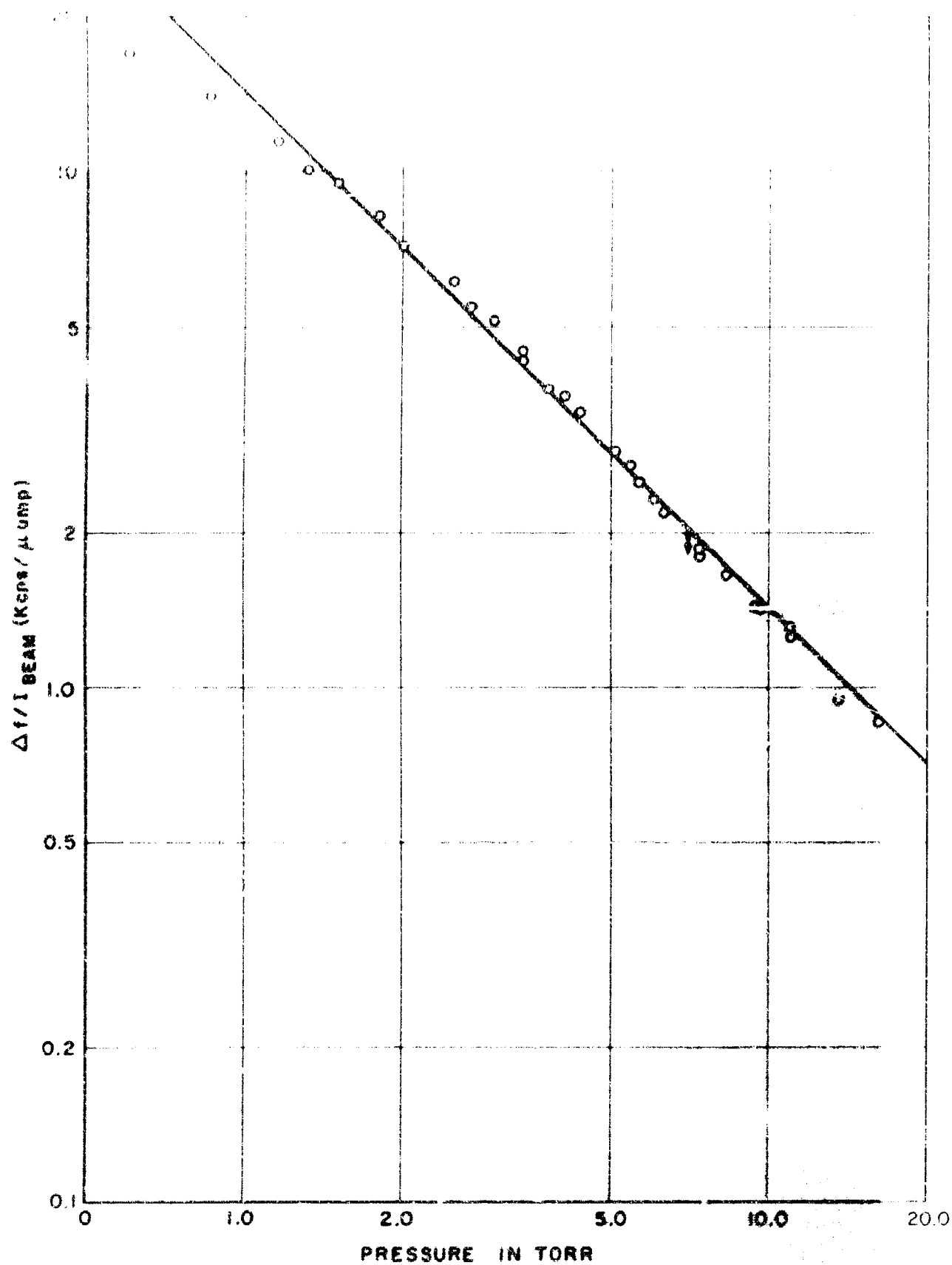FIGURE 5.39- ELECTRON DENSITY VS I_{BEAM} IN 4:1 $N_2:O_2$

FIGURE 5.40- SLOPES OF LINEAR PLOTS OF ELECTRON DENSITY
VS. I_{BEAM} AS A FUNCTION OF PRESSURE IN
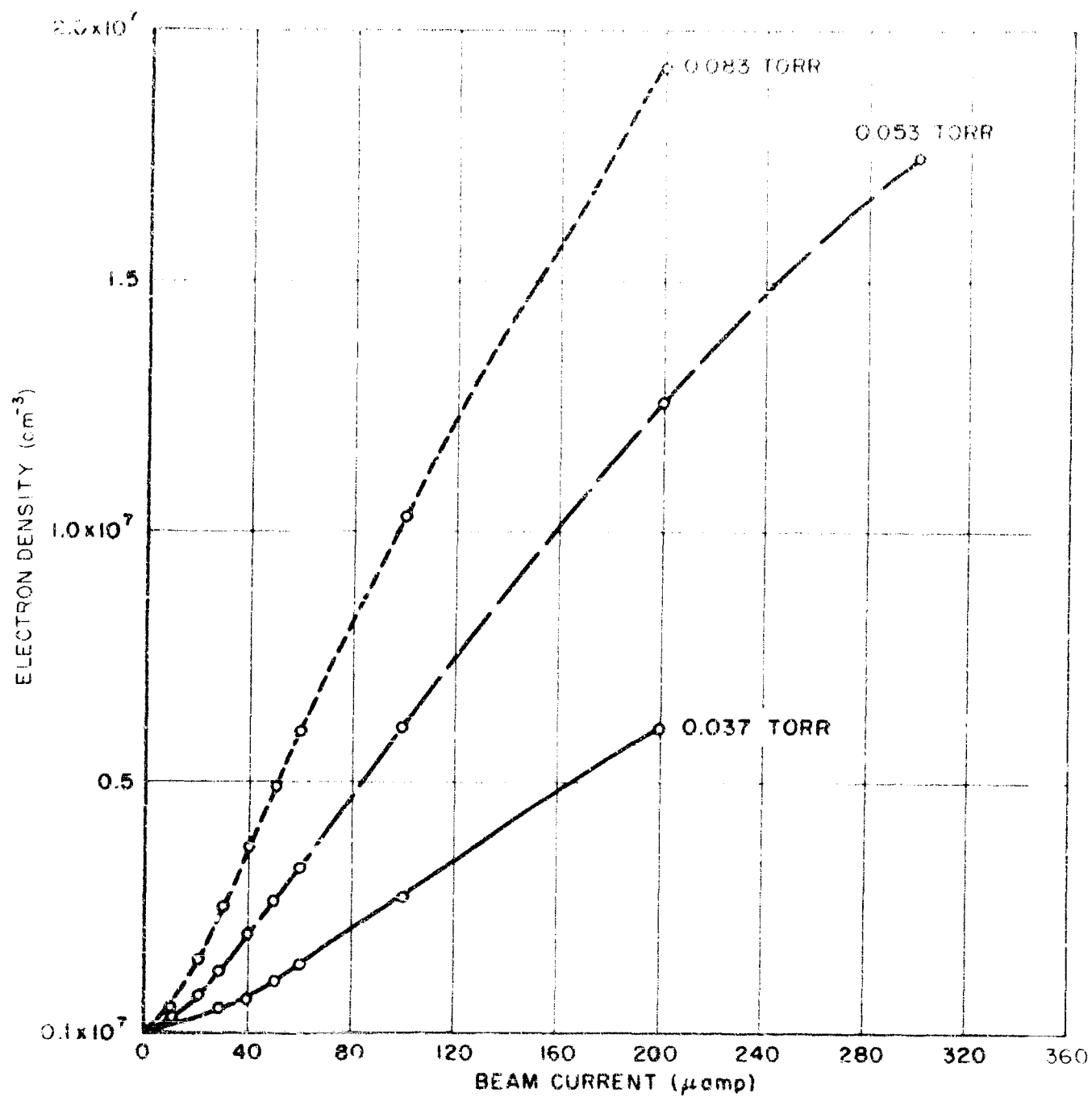$4:1$ N_2 O_2 MIXTURES

FIGURE 5.41- STEADY STATE ELECTRON DENSITY VS. BEAM
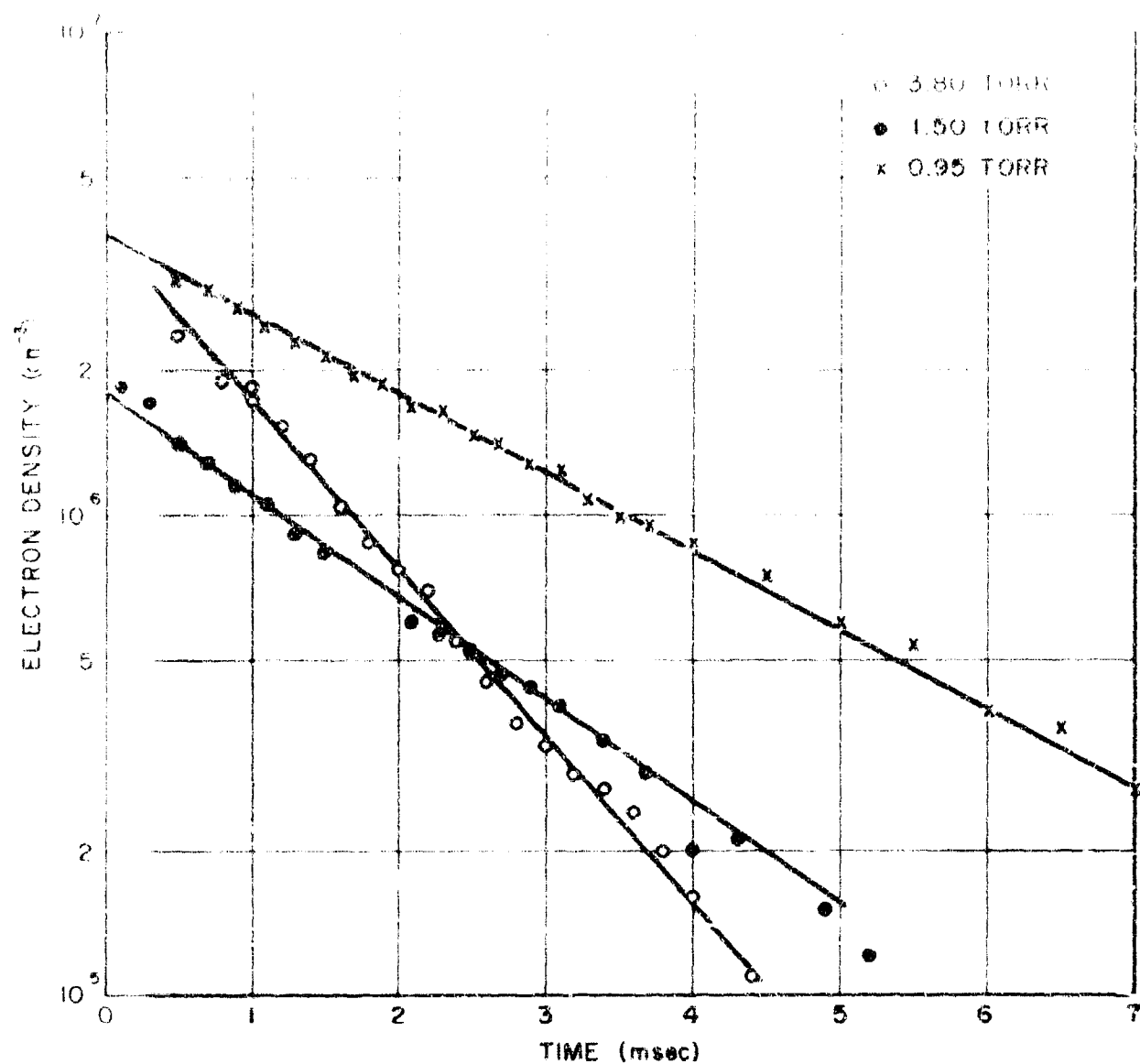CURRENT IN 4:1 $N_2:O_2$

FIGURE 5.42- AFTERGLOW DECAY OF ELECTRON DENSITY IN
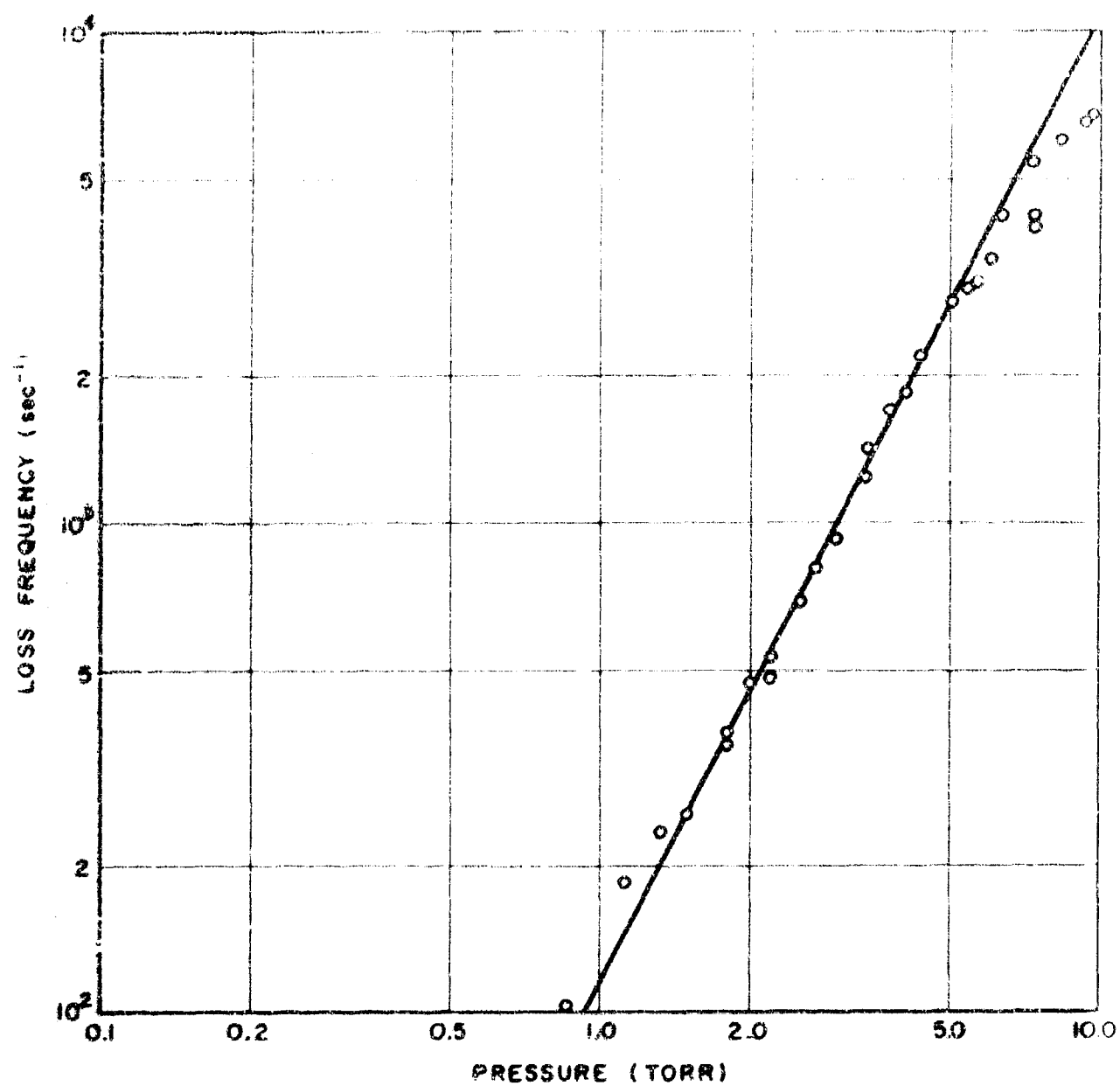4:1 $N_2:O_2$

FIGURE 5.43 - ELECTRON LOSS FREQUENCY VS. PRESSURE
IN 4:I $N_2:O_2$
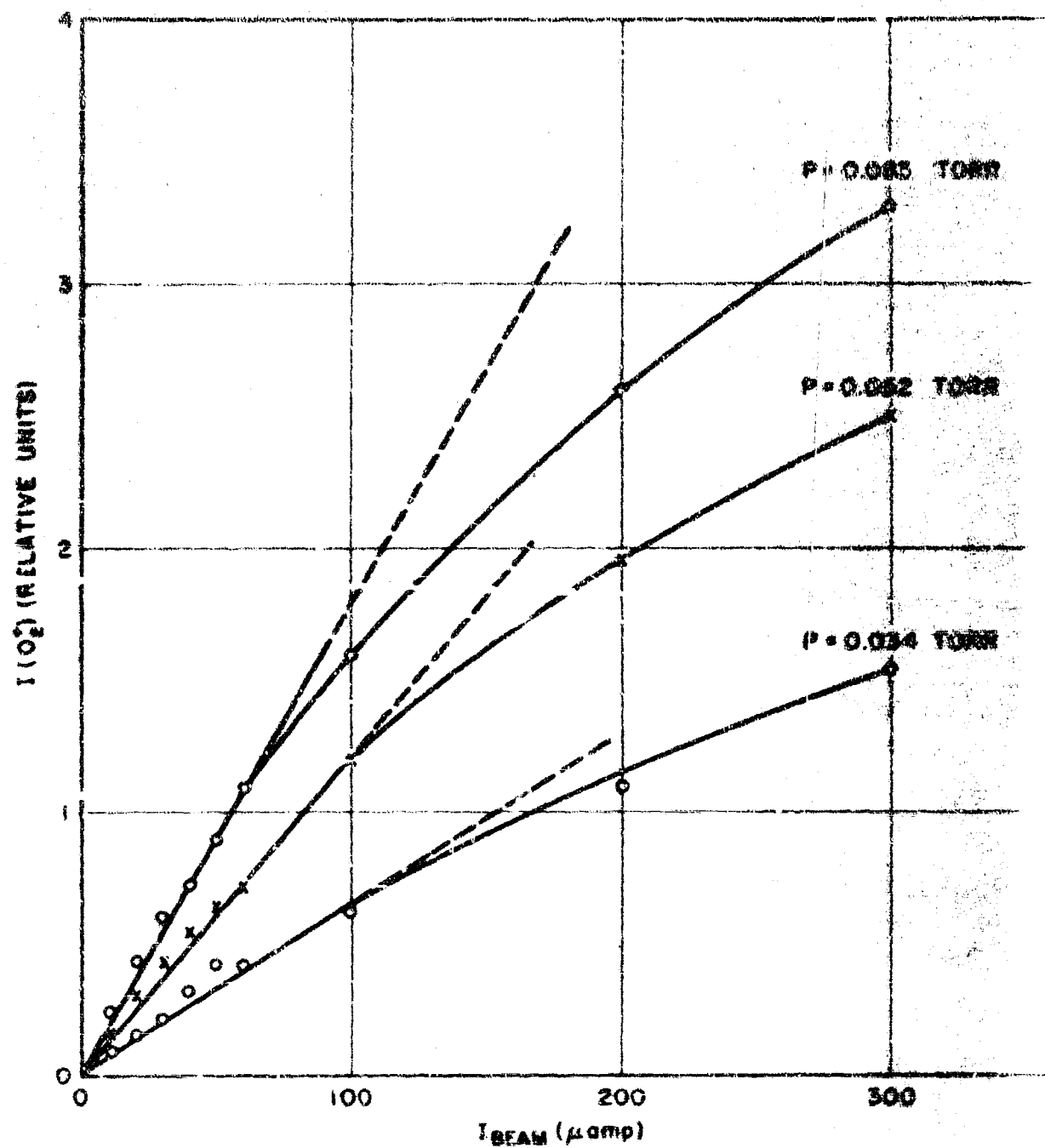
FIGURE 5.44- O_2^+ CURRENTS VS. I_{BEAM} IN 4:1 $N_2:O_2$
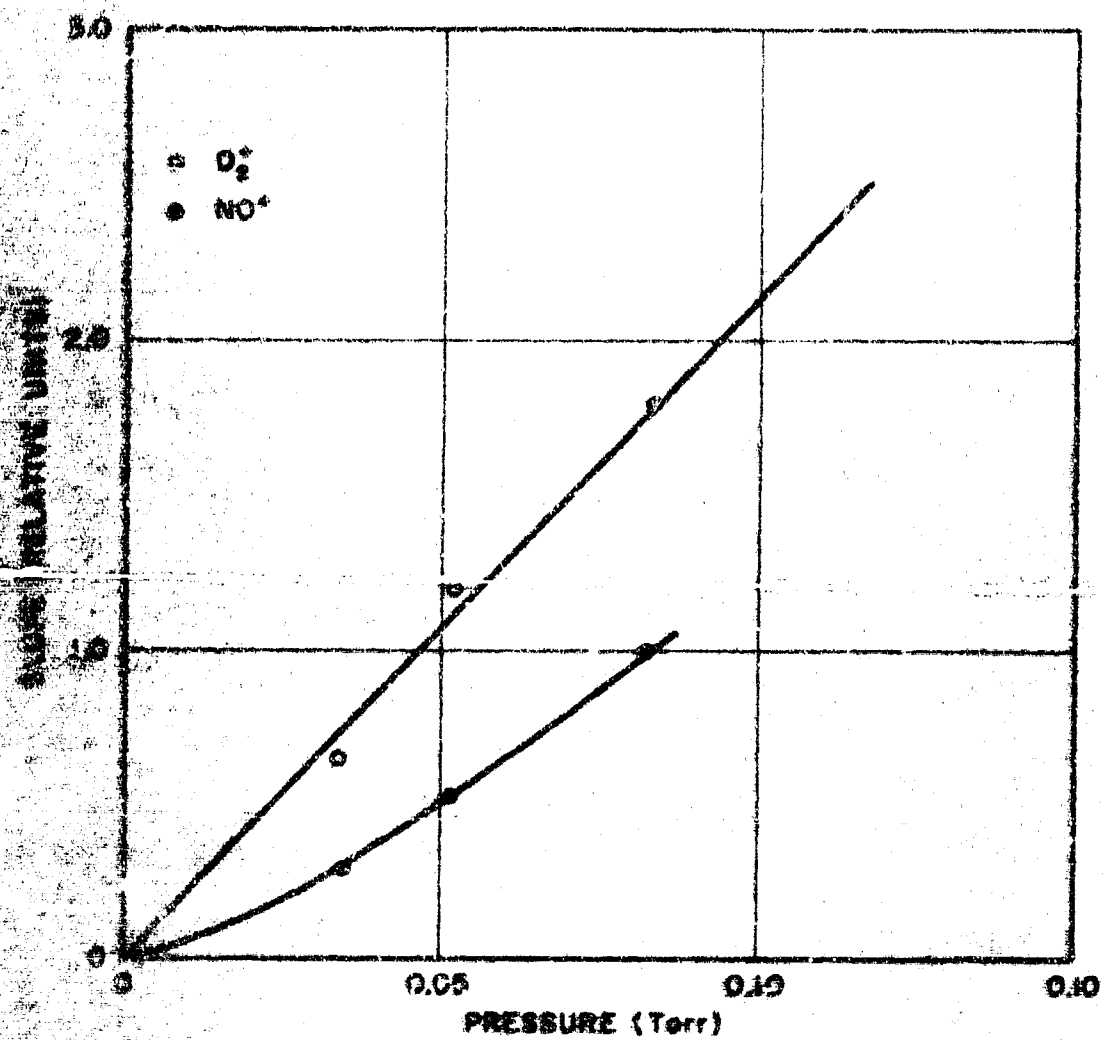
FIGURE 5.45- SLOPES OF LINEAR PORTION OF ION CURRENT VS. I_{BEAM} PLOT AS FUNCTION OF PRESSURE
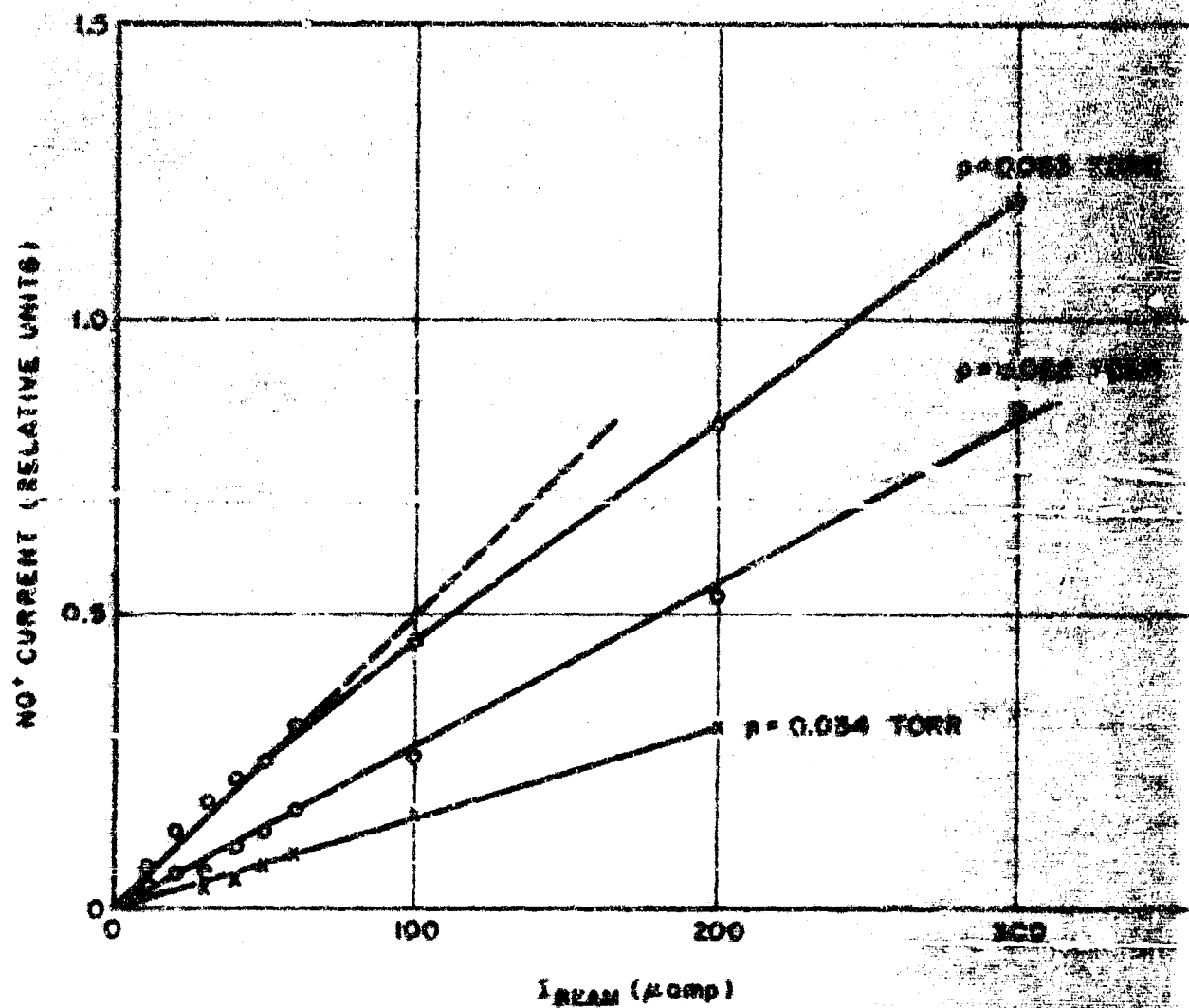
FIGURE 5.46— NO$^+$ ION CURRENT VS. I$_{BEAM}$ $N_2:O_2$
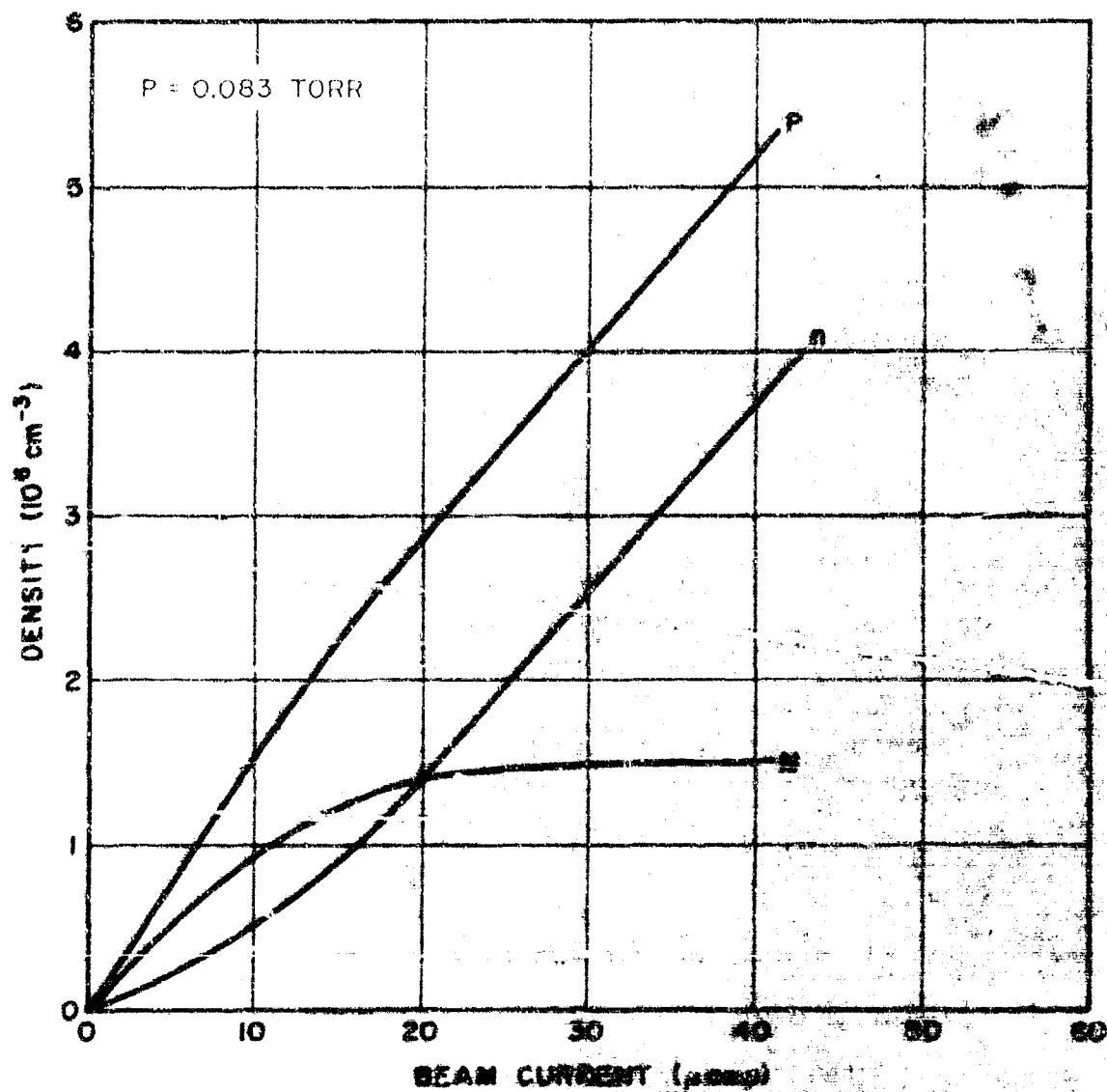
FIGURE 5.47- PARTICLE DENSITIES VS. BEAM CURRENT
IN 4:1 $N_2:O_2$ MIXTURE
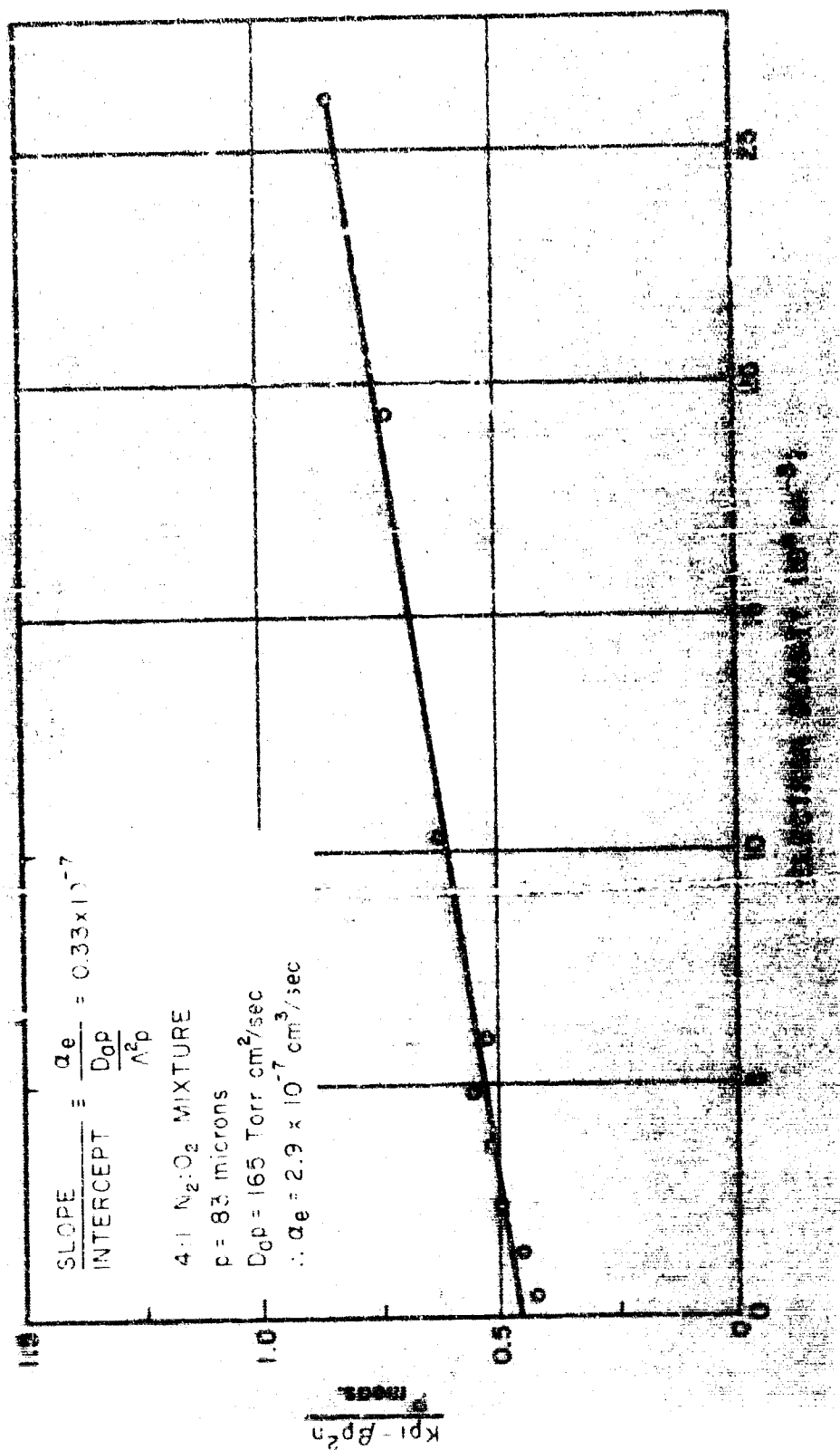
FIGURE 5.48 – EVALUATION OF a_e IN N_2O_2 MIXTURES

$$\frac{SLOPE}{INTERCEPT} = \frac{a_e}{\frac{D_a p}{\Lambda^2 p}} = 0.33 \times 10^{-7}$$

4:1 N_2:O_2 MIXTURE

p = 83 microns

$D_a p$ = 165 Torr cm²/sec

∴ a_e = 2.9 × 10⁻⁷ cm³/sec

FIGURE 5.49- IONIZATION RATE OF AIR BY BETA PARTICLES
VS. ALTITUDE

FIGURE 5.50- THREE-BODY ATTACHMENT LOSS FREQUENCY AS
A FUNCTION OF ALTITUDE

FIGURE 5.51- TYPICAL ELECTRON PRODUCTION DISTRIBUTION
FOR HOMOGENEOUS FISSION DEBRIS LAYER
ABOVE 90 Km

FIGURE 5.52 — COMPUTED PARTICLE DENSITIES 1 HOUR AFTER
DETONATION OF NUCLEAR DEVICE AT HIGH
ALTITUDE

VI. SUMMARY OF RESULTS AND SUGGESTIONS FOR
FURTHER WORK

A.   Summary of Experimental Results

A laboratory experiment was developed to study the response
of atmospheric gases to ionizing radiation under conditions
resembling those in the D region of the ionosphere subjected to
beta particles from trapped fission debris. The experiment,
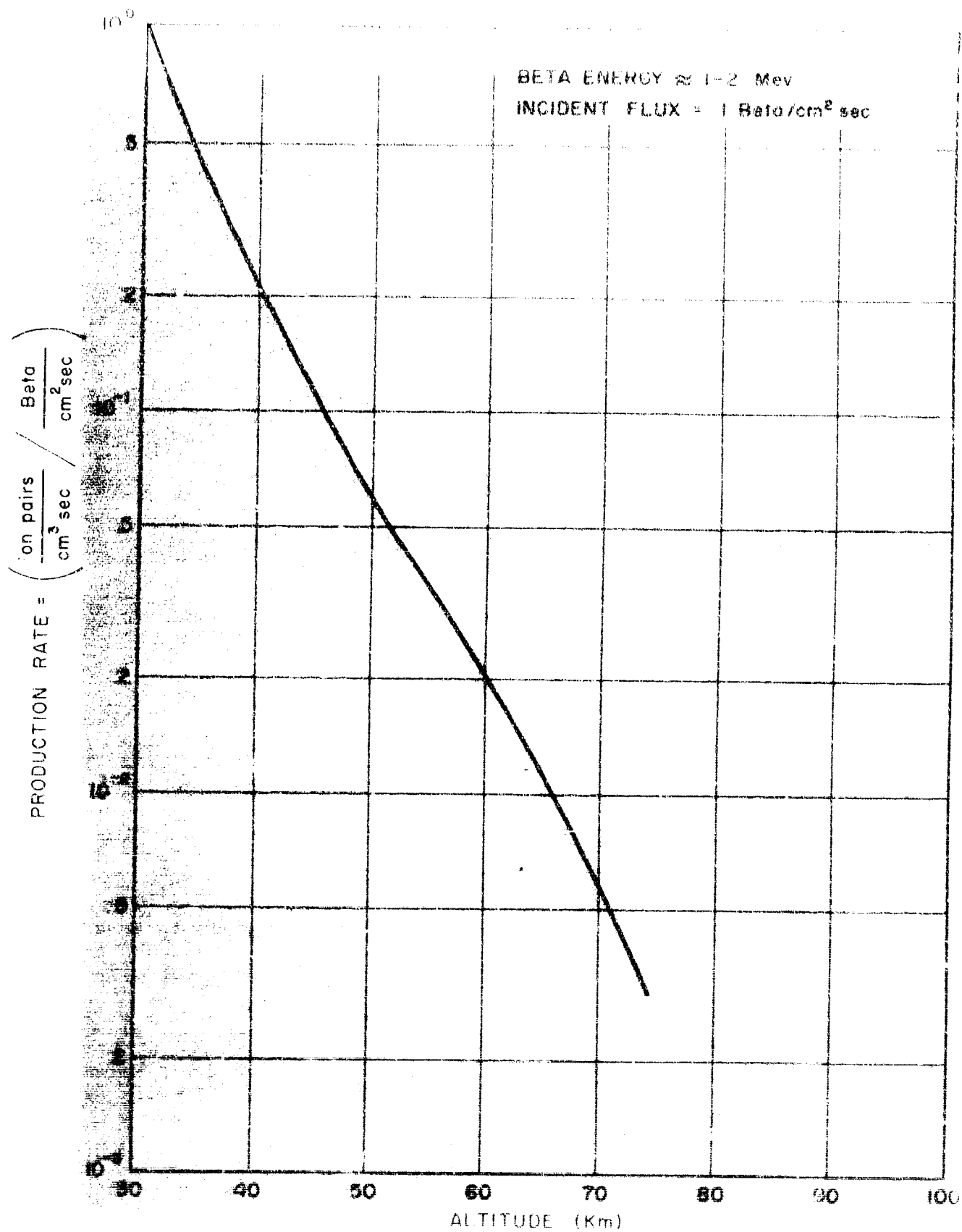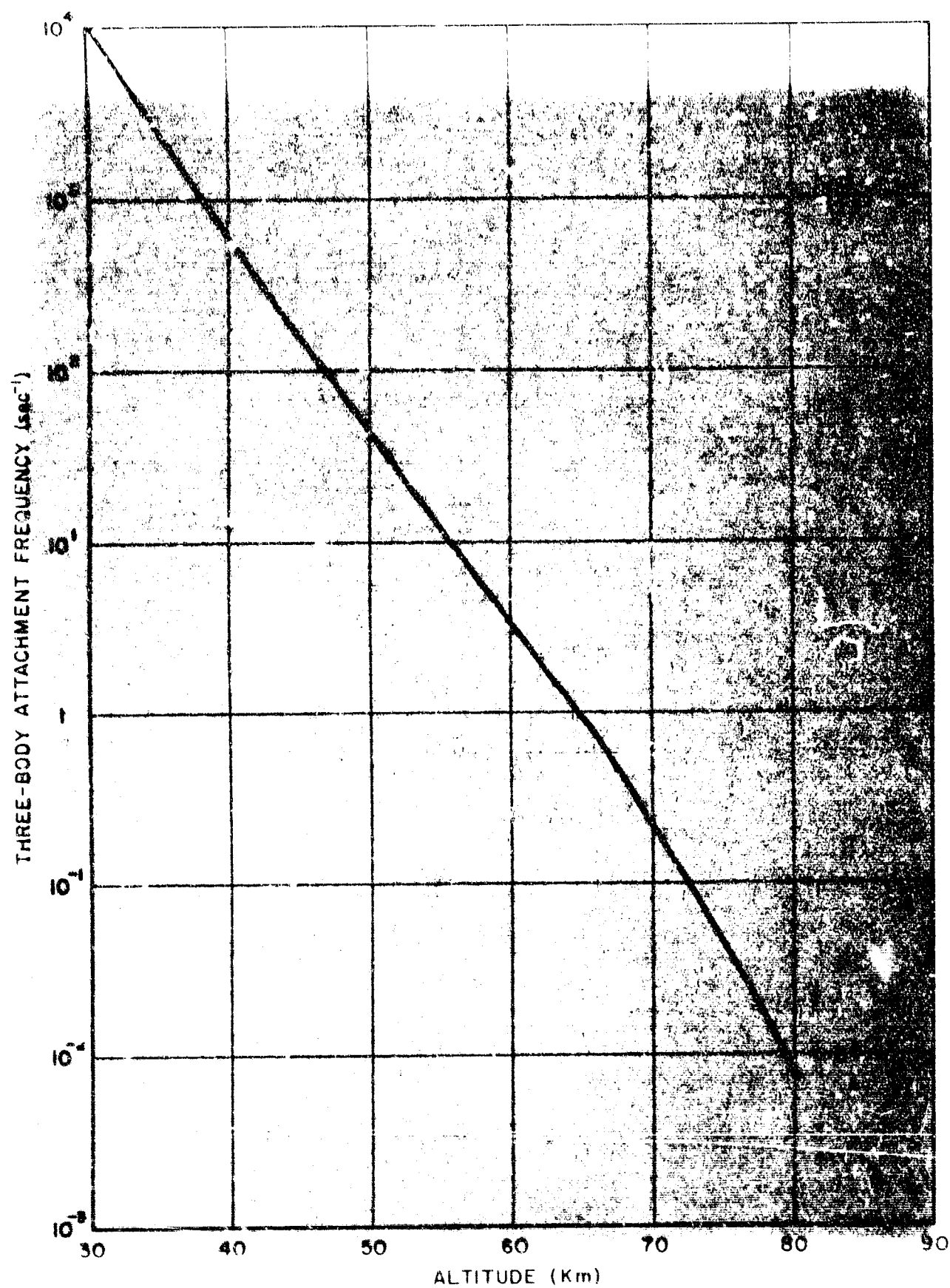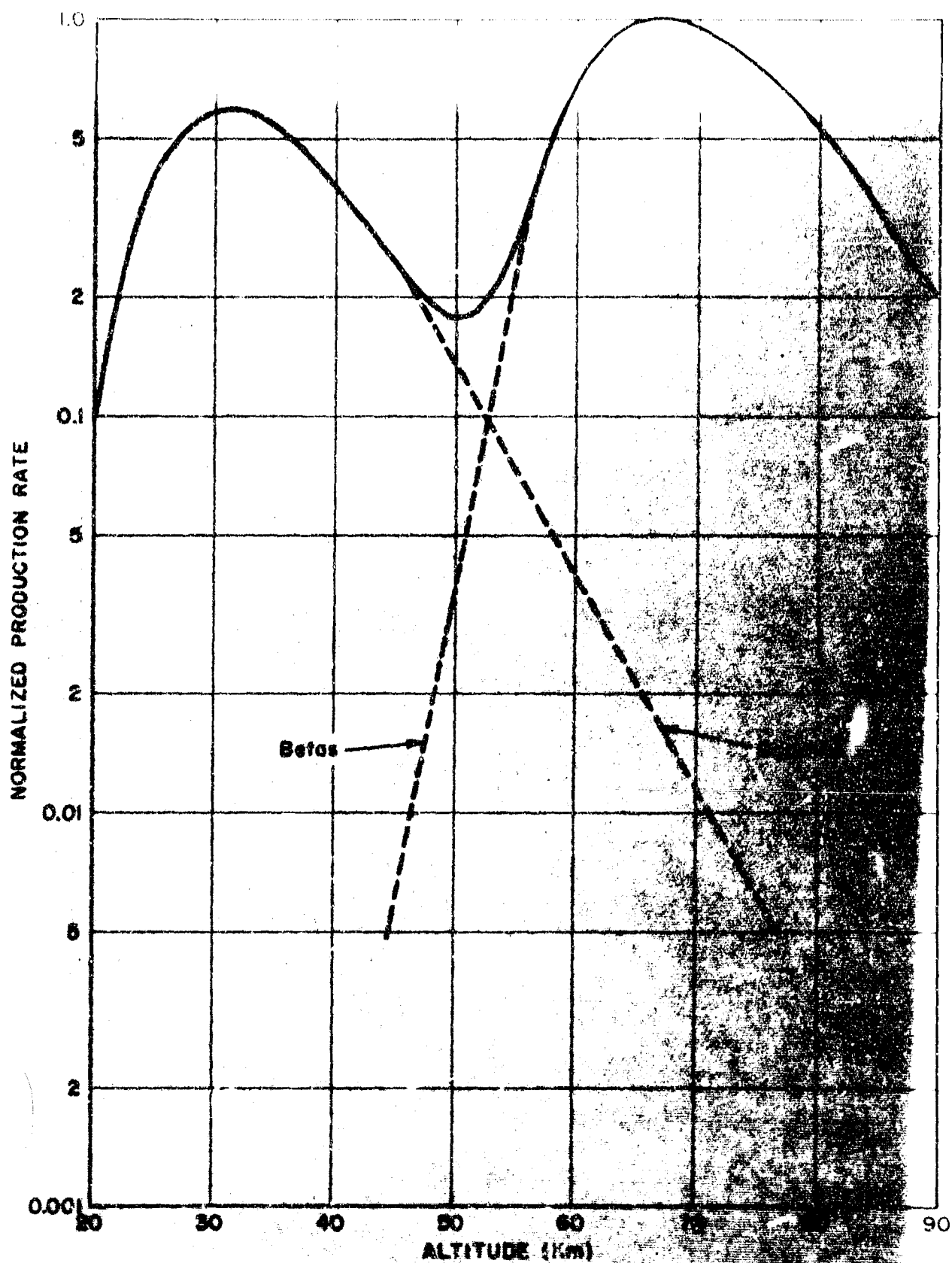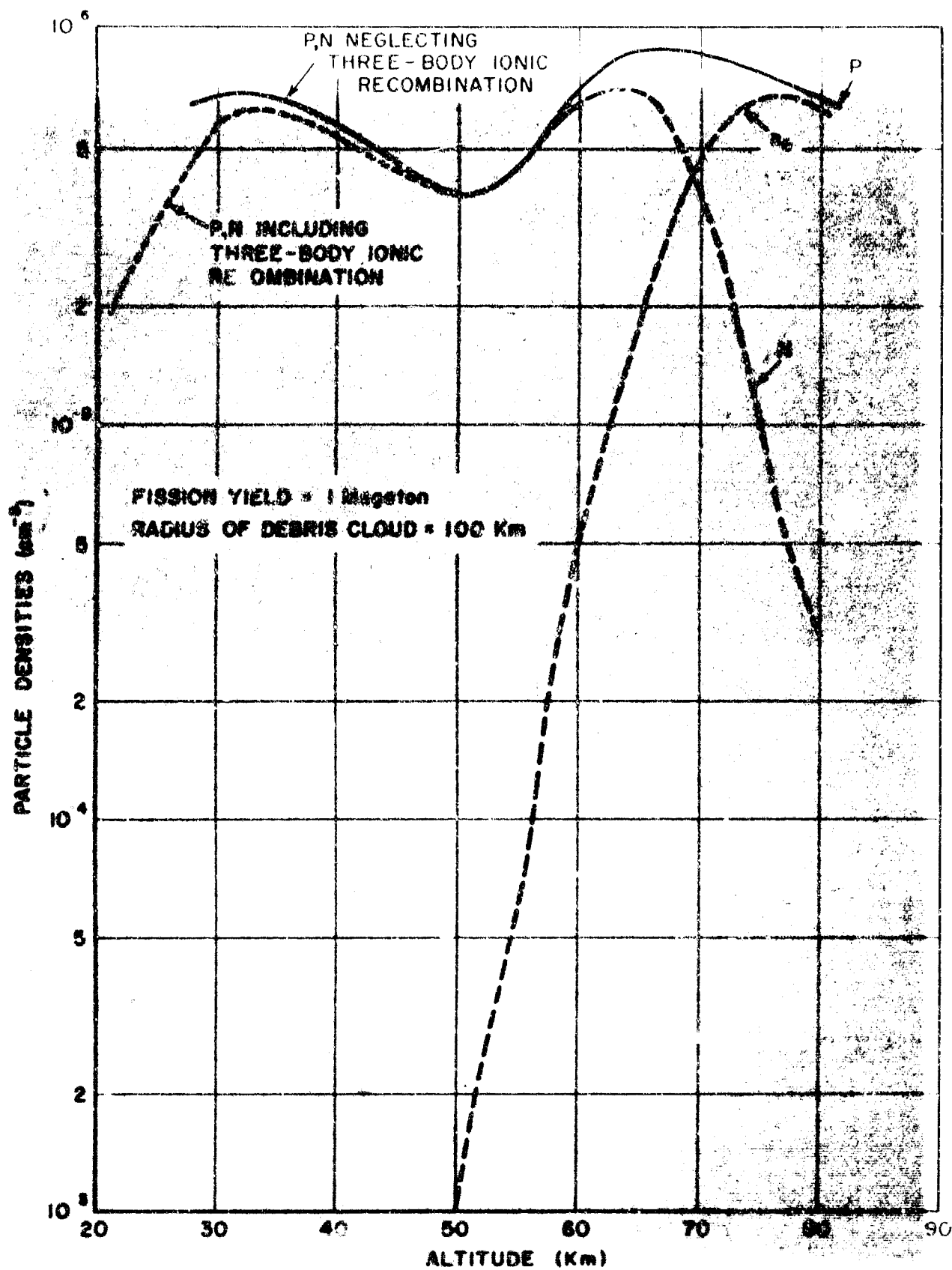described in Chapter II, uses a large reaction chamber to minimize
the effects of particle diffusion and wall-induced chemistry,
neither of which is pertinent to the atmospheric processes under
study. A spatially uniform beam of 1.5 Mev electrons, which
approximates the mean energy of the fission-debris betas, irradiates
the gas in the chamber. The subsequent behavior of the gas is
then determined from simultaneous electron density, ion analysis,
and optical emission measurements. As shown by the results
described in the body of the report (summarized below), the infor-
mation obtained from the laboratory measurements is in excellent
agreement with that deduced from the limited atmospheric data
which are currently available. In addition, one can study certain
processes, notably ionic recombination, more directly in the
experiment than can be done in the atmosphere or in other laboratory
apparatus. As a result of the similarity between this laboratory
environment and the disturbed upper atmosphere, which is borne out
by the measurements described in this report, the experiment
promises to provide detailed information concerning ionospheric
processes over a wide range of atmospheric conditions.

Measurements were performed in oxygen, nitrogen, and 4:1
airlike mixtures of $N_2:O_2$, over the pressure range 0.005 to 10 Torr.

206.

The principal processes observed include:

1. Production of electron-ion pairs by collisions
    of beam-electrons with neutral molecules; the
    rate equation is

    $$\left(\frac{\partial n_e}{\partial t}\right) = K p i$$

    where p is the gas pressure in Torr, i the
    current density of the incident beam in micro-
    amperes/cm^2. The values found for K in the
    three gases studied are

    $$\left.\begin{array}{l} K \text{(oxygen)} = (5.1 \pm 0.) \times 10^{\prime\prime} \\ K \text{(nitrogen)} = (5.7 \pm 0.) \times 10^{\prime\prime} \\ K \text{(air)} = (5.5 \pm 0.) \times 10^{\prime\prime} \end{array}\right\} \left(cm^3 \ sec \ Torr \ \frac{\mu amp}{cm^2}\right)^{-1}$$

    These are the first direct measurements of total
    ion production coefficients for 1.5 Mev electrons
    reported in the literature. They are in excellent
    agreement with theoretical predictions.

2. Three-body attachment of electrons to neutral O_2
    molecules; the rate equation is

    $$\left(\frac{\partial n_e}{\partial t}\right)_{3-body} = -\beta n_e [O_2][x]$$

    where $[O_2]$ is the number density of neutral O_2
    molecules, and $[X]$ is the density of molecules
    serving as third bodies. In pure oxygen, where
    $[X] = [O_2]$, and in airlike mixtures, where $[X] =$
    $[N_2] + [O_2]$, the measurements yield

$$\beta_{\text{OXYGEN}} = (2.12 \pm 0.15) \times 10^{-30} \text{ cm}^6/\text{sec}$$

$$\beta_{\text{AIR}} = (1.10 \pm 0.05) \times 10^{-31} \text{ cm}^6/\text{sec}$$

These values are in excellent agreement with
attachment rates deduced from atmospheric data
[Knapp, 1966] and from laboratory measurements
obtained with different ionization techniques
[Pack and Phelps, 1966] indicating that the
excitation technique does not critically affect
the observed rate.

3. Diffusion of electrons controlled by the presence
    of negative and/or positive ions; the rate
    equation is

$$\left(\frac{\partial n_e}{\partial t}\right)_{\text{diff.}} = D_{\text{eff}} \nabla^2 n_e$$

where the form of D_{eff} depends on the types and
densities of the ions present. In oxygen the
measurements are consistent with the value

$$\left(D_{\text{eff}} \, p\right)_{\text{OXYGEN}} = 110 \left\{1 + \frac{[O_2^-]}{n_e}\right\} \text{ Torr cm}^2/\text{sec}$$

in good agreement with the value derived from
the measured validity of O_2^+ [Sampson, 1965].
The diffusion measurements in oxygen are among
the few well-documented cases cited in the
literature for the influence of negative ions
on ambipolar diffusion. In air, the measure-
ments are consistent with $\left(D_{\text{eff}} \, p\right)_{\text{AIR}} = 165 \pm 15 \left\{1 + \frac{N}{n}\right\} \text{ Torr cm}^2/\text{sec}$
where N is the density of (unidentified)
negative ions. In nitrogen, the measurements

indicate that at low pressures, where N_2^+ is the dominant ion, $\left(D_{eff}\, p\right)_{NITROGEN} = (60 \pm 20)\; Torr\; cm^2/sec$ At high pressures, where the dominant ions are a mixture of N_3^+ and N_4^+,

$$\left(D_{eff}\, p\right)_{NITROGEN} = (130 \pm 20)\; Torr\; cm^2/sec$$

These are in general agreement with values computed from the best available mobility measurements [Keller, 1965].

4. Electron positive-ion recombination; the rate equation is

$$\left(\frac{\partial n_e}{\partial t}\right)_{RECOMB.} = -\alpha_e\, P\, n_e$$

where P is the density of recombining ions. A value for α_e was determined from the air measurements;

$$\alpha_e = (3 \pm 2) \times 10^{-7}\; cm^3/sec$$

This is in excellent agreement with the results obtained by other workers for individual ions

$$\alpha_e\,(O_2^+) \approx 2 \times 10^{-7}\; cm^3/sec\quad [Kasner, 1961]$$

$$\alpha_e\,(NO^+) \approx 4 \times 10^{-7}\; cm^3/sec\quad [Gunton, 1965]$$

5. Mutual neutralization of positive and negative ions by the reaction

$$X^+ + Y^- \longrightarrow X + Y$$
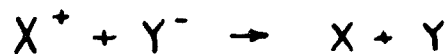
The rate equation is

$$\frac{dX^+}{dt} = \frac{dY^-}{dt} = -\alpha'_i\, X^+ Y^-$$

In pure oxygen at low pressures, where the ions O_2^+ and O_2^-, the measurements are consistent with

$$\left(\alpha_i\right)_{O_2} = 1 \times 10^{-7} \ cm^2/sec$$

to within a factor of two. This is believed
to be the first reported laboratory value for
$\alpha_i\left(O_2^+, O_2^-\right)$. In the airlike mixtures

$$\left(\alpha_i\right)_{air} = \left(3\pm2\right) \times 10^{-7} \ cm^2/sec$$

where the positive ions are O_2^+ and NO^+. The
negative ions have not yet been identified.

6. Quenching of optical radiation from the states
    $N_2(C^3\pi)$ and $N_2^+(B^2\Sigma)$ in binary collisions with
    ground-state N_2 and O_2 molecules. The observed
    two-body quenching cross-sections are:

	STATE	QUENCHER	CROSS-SECTION
N_2^*	$C^3\pi (v'=0)$	N_2	(1.2 ± 0.6) X $10^{-16} cm^2$
	$C^3\pi (v'=0)$	O_2	(39 ± 11) X $10^{-16} cm^2$
	$C^3\pi (v'=1)\dagger$	O_2	(52 ± 18) X $10^{-16} cm^2$
	$C^3\pi (v'=2)\dagger$	O_2	(81 ± 32) X $10^{-16} cm^2$
$(N_2^+)^*$	$B^2\Sigma (v'=0)$	N_2	(69 ± 10) X $10^{-16} cm^2$
	$B^2\Sigma (v'=0)$	O_2	(123 ± 21) X $10^{-16} cm^2$

Measurements for states labelled with a dagger
have not previously been reported in the
literature. For the other states, the results
for quenching by N_2 are in excellent agreement
with values reported in the literature
[Davidson, 1964; Brocklehurst, 1964]. The cross-
sections for quenching by O_2 are about a factor

of two higher than reported by Brocklehurst,
but appear to be in better agreement with
atmospheric data [Hoerlin, 1966]

7. Ion-molecule reactions have been studied in
    nitrogen and airlike mixtures. The measure-
    ments suggest the following reactions and rate
    coefficients referred to total N_2^+ density:

a) $(N_2^+)^* + N_2 \longrightarrow N_3^+ + N$; $k \stackrel{\sim}{\sim} 1 \times 10^{-14} cm^3/sec$

b) $(N_2^+)^* + N_2 \longrightarrow N_4^+ + N$; $k \stackrel{\sim}{\sim} 5 \times 10^{-14} cm^3/sec$

c) $(N_2^+)^* + O_2 \longrightarrow O_2^+ + N_2$

d) $(N_2^+)^* + O_2 \longrightarrow NO^+ + NO$
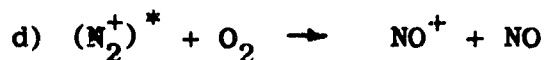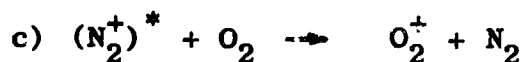
Tentative assignments have been made of the
excited states of N_2^+ participating in the
various reactions. These are

$$(N_2^+)^* = N_2^+ (^4\Sigma) \quad \text{for reactions a and c}$$

$$(N_2^+)^* = N_2^+(A^2\pi) \text{ and } N_2^+(B^2\Sigma) \text{ for reactions}$$
$$\text{b and d}$$
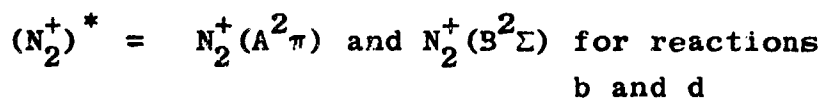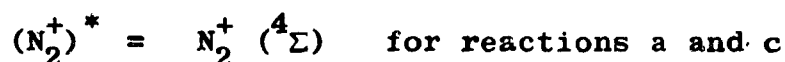
Reactions b and d appear to account for the
observed quenching of optical radiation from
$N_2^+(B^2\Sigma)$

The experimental results cited above show broad areas of agreement with <u>in situ</u> measurements of the properties of the disturbed ionosphere. The situation is not so straightforward with regard to the agreement of this work with that of other laboratories using different modes of excitation of the gas. Several reactions, notably three-body attachment and positive ion-electron recombination, appear to have the same rates as are found in electron swarm and microwave afterglow studies. Ion-molecule reactions, however, which are strongly dependent on the excited state configuration of the ion, are qualitatively different in this experiment from those observed by other workers using low-energy electrons. Some reactions, such as ion-ion two-body recombination, have not been studied in sufficient detail by other workers to permit comparison with the present results.

The lumped-parameter experiment thus appears to serve three functions which are of great importance to DASA's overall program. First, it provides a good approximation to the phenomenology of the disturbed upper atmosphere, at least at altitudes between 30 and 80 kilometers. Second, by taking advantage of the unique characteristics of this experimental facility (such as the large size of the chamber and the variety of available diagnostic techniques) one can use the experiment to study individual reactions in detail. Finally, by virtue of the similarity of the excitation employed here to that occurring in the beta-irradiated upper atmosphere, the lumped-parameter experiment will be useful in determining which reactions observed under various laboratory conditions are likely to be important in the disturbed ionosphere.

B. Suggestions for Further Work

Several modifications could profitably be made to the program which would improve the accuracy of the measured reaction rates and extend the range of atmospheric conditions which can be studied by the lumped-parameter experiment.

The single greatest improvement in the accuracy of the measured reaction rates can be brought about by the use of a numerical computation of the complete set of reaction equations. By taking proper account of the spatial distributions of the charged particles, one can expect to obtain better fits to the low pressure data, both in-beam and afterglow. The rate coefficients deduced from complete solutions will be more accurate than those derived in the report from an approximate analysis. From these solutions, it will be possible to determine the error introduced by the spatial congruence assumption in specific laboratory situations.

Future experiments should be performed on gas mixtures which more closely approximate the neutral composition of the D region. The inclusion of CO_2, water vapor, and the nitrogen oxides should yield particularly interesting results in their effect on attachment and detachment, on ionic composition, and on the effective rates for ion-ion and ion-electron recombination. The termperatures at which the experiments are performed should be varied between 200 and 500^OK. This will permit the observation of collisional detachment, as well as the evaluation of temperature dependences of the various rate coefficients in a range directly comparable to ionospheric conditions. More effort should be spent measurements at high beam fluxes to evaluate electron-positive ion recombination coefficients with greater accuracy.

Two modifications should be made to existing experimental apparatus which would increase the detail with which the state of the gas can be determined. First, time resolved mass spectrometric measurements should be made available, so that the transient production and loss of mass-analyzed ions can be studied in detail. This will permit the assignment of a diffusion coefficient to each ionic species. It will also permit the observation of gross differences in the ionic constitution of the gas during and after irradiation. Time-resolved optical absorption studies should also be made to determine the densities of those excited states of the neutral and ionized molecules which are believed to participate in ion-molecule reactions.

The lumped-parameter experiments should also be repeated in chambers of vastly different sizes from the one used here. With a chamber of linear dimensions some ten times smaller than the one used in this work, it should be possible to study electron densities in diffusion-controlled situations up to pressures of 10 Torr in air. From measurements of this type at low beam currents, one can evaluate ion-ion recombination coefficients in a pressure region where the three-body process dominates. Conversely, a much larger chamber could make that altitude range above 80 km, in which atomic oxygen is an important neutral constituent, accessible to laboratory study. This would permit the study of associative detachment, radiative attachment to O, and various ion-molecule reactions which depend on atomic oxygen.

BLANK PAGE

DOCUMENT CONTROL DATA - R&D

(Security classification of title, body of abstract and indexing annotation must be entered when the overall report is classified)

1. ORIGINATING ACTIVITY (Corporate author)	2a. REPORT SECURITY CLASSIFICATION
The G. C. Dewey Corporation 331 East 38th Street New York, New York 10016	Unclassified
	2b. GROUP --

3. REPORT TITLE

Ionization and Electron Loss Simulation in Atmospheric Gases

(65)

4. DESCRIPTIVE NOTES *(Type of report and inclusive dates)*

Final Report - 1 December to 1 March 1966

5. AUTHOR(S) *(Last name, first name, initial)*

Hirsh, M. N.   Slevin, J.
Halpern, G. M.   Wolf, N.

6. REPORT DATE	7a. TOTAL NO. OF PAGES	7b. NO. OF REFS
September 1966	To be numbered	--

8a. CONTRACT OR GRANT NO. DA28-043 AMC-01354(E) b. PROJECT NO. 5900-21-830-4600 c. d.	9a. ORIGINATOR'S REPORT NUMBER(S) R-199-3 9b. OTHER REPORT NO(S) *(Any other numbers that may be assigned this report)* ECOM-01354(F)

10. AVAILABILITY/LIMITATION NOTICES

This document is subject to special export controls and each transmittal to foreign governments or foreign nationals may be made only with prior approval of CG, U.S. Army Electronics Command, Fort Monmouth, N.J. ATTN: AMSEL-HL-CT-P

11. SUPPLEMENTARY NOTES --	12. SPONSORING MILITARY ACTIVITY U. S. Army Electronics Command ATTN: AMSEL-HL-CT-P Fort Monmouth, New Jersey 07703

13. ABSTRACT

(To be inserted)

DD FORM 1 JAN 64 **1473**   (1)

KEY WORDS	LINK A		LINK B		LINK C	
	ROLE	WT	ROLE	WT	HOLE	WT

INSTRUCTIONS

1. **ORIGINATING ACTIVITY:** Enter the name and address of the contractor, subcontractor, grantee, Department of Defense activity or other organization (*corporate author*) issuing the report.

2a. **REPORT SECURITY CLASSIFICATION:** Enter the overall security classification of the report. Indicate whether "Restricted Data" is included. Marking is to be in accordance with appropriate security regulations.

2b. **GROUP:** Automatic downgrading is specified in DoD Directive 5200.10 and Armed Forces Industrial Manual. Enter the group number. Also, when applicable, show that optional markings have been used for Group 3 and Group 4 as authorized.

3. **REPORT TITLE:** Enter the complete report title in all capital letters. Titles in all cases should be unclassified. If a meaningful title cannot be selected without classification, show title classification in all capitals in parenthesis immediately following the title.

4. **DESCRIPTIVE NOTES:** If appropriate, enter the type of report, e.g., interim, progress, summary, annual, or final. Give the inclusive dates when a specific reporting period is covered.

5. **AUTHOR(S):** Enter the name(s) of author(s) as shown on or in the report. Enter last name, first name, middle initial. If military, show rank and branch of service. The name of the principal author is an absolute minimum requirement.

6. **REPORT DATE:** Enter the date of the report as day, month, year; or month, year. If more than one date appears on the report, use date of publication.

7a. **TOTAL NUMBER OF PAGES:** The total page count should follow normal pagination procedures, i.e., enter the number of pages containing information.

7b. **NUMBER OF REFERENCES:** Enter the total number of references cited in the report.

8a. **CONTRACT OR GRANT NUMBER:** If appropriate, enter the applicable number of the contract or grant under which the report was written.

8b, 8c, & 8d. **PROJECT NUMBER:** Enter the appropriate military department identification, such as project number, subproject number, system numbers, task number, etc.

9a. **ORIGINATOR'S REPORT NUMBER(S):** Enter the official report number by which the document will be identified and controlled by the originating activity. This number must be unique to this report.

9b. **OTHER REPORT NUMBER(S):** If the report has been assigned any other report numbers (*either by the originator or by the sponsor*), also enter this number(s).

10. **AVAILABILITY/LIMITATION NOTICES:** Enter any limitations on further dissemination of the report, other than those imposed by security classification, using standard statements such as:

(1) "Qualified requesters may obtain copies of this report from DDC."

(2) "Foreign announcement and dissemination of this report by DDC is not authorized."

(3) "U. S. Government agencies may obtain copies of this report directly from DDC. Other qualified DDC users shall request through

_____ ."

(4) "U. S. military agencies may obtain copies of this report directly from DDC. Other qualified users shall request through

_____ ."

(5) "All distribution of this report is controlled. Qualified DDC users shall request through

_____ ."

If the report has been furnished to the Office of Technical Services, Department of Commerce, for sale to the public, indicate this fact and enter the price, if known.

11. **SUPPLEMENTARY NOTES:** Use for additional explanatory notes.

12. **SPONSORING MILITARY ACTIVITY:** Enter the name of the departmental project office or laboratory sponsoring (*paying for*) the research and development. Include address.

13. **ABSTRACT:** Enter an abstract giving a brief and factual summary of the document indicative of the report, even though it may also appear elsewhere in the body of the technical report. If additional space is required, a continuation sheet shall be attached.

It is highly desirable that the abstract of classified reports be unclassified. Each paragraph of the abstract shall end with an indication of the military security classification of the information in the paragraph, represented as (*TS*), (*S*), (*C*), or (*U*).

There is no limitation on the length of the abstract. However, the suggested length is from 150 to 225 words.

14. **KEY WORDS:** Key words are technically meaningful terms or short phrases that characterize a report and may be used as index entries for cataloging the report. Key words must be selected so that no security classification is required. Identifiers, such as equipment model designation, trade name, military project code name, geographic location, may be used as key words but will be followed by an indication of technical context. The assignment of links, rules, and weights is optional.

(2)